Magnetism of topological materials: insights from bulk and local probes

Dissertation zur Erlangung des akademischen Grades

Doctor of Philosophy (Ph.D.)

vorgelegt der Fakultät Mathematik und Naturwissenschaften
Technische Universität Dresden
and
Università Di Parma

von

Manaswini Sahoo

31.1.2025

Thesis supervised by Prof. Bernd Büchner and Prof. Roberto De Renzi prepared at Leibniz Institute for Solid State and Materials Research (IFW) as co-tutelle between the University of Parma and the Technical University Dresden.

Co-supervisors:

- Dr. Anja Wolter-Giraud: IFW Dresden, Germany
- Dr. Laura Corredor Bohorquez: IFW Dresden, Germany
- Prof. Giuseppe Allodi: University of Parma, Italy

Abstract

Magnetism in 2D materials promises many applications in future technologies; simultaneously, robust topological materials have opened a new path in the quantum world in recent decades. Then combining these two, the interplay between nontrivial topology and magnetism offers numerous applications in spin-based technologies, driven by innovative quantum phenomena such as the quantum anomalous Hall effect (QAHE) and axion insulators. These phenomena are manifested in materials like magnetic Weyl semimetals, magnetic topological insulators, skyrmions, or similar spin-textured materials, etc. This thesis mainly deals with the bulk and local magnetic properties of 2D/quasi-2D van der Waals materials which also host topologically non-trivial states. Importantly, it focuses on understanding the fundamental magnetic properties of these materials and on shedding light on the impact of the crzstalline disorder on local and bulk magnetic properties. The thesis has been divided into two parts based on the materials.

The $MnBi_2Te_4$ family of compounds holds promise for realizing the QAHE; however, achieving full quantization in antiferromagnetic $MnBi_2Te_4$ still requires an external magnetic field. Therefore, increasing the interlayer distance between the septuple layers of $MnBi_2Te_4$ and substituting Bi with Sb are considered as viable strategies to achieve net spin polarization without a magnetic field. These intrinsic magnetic topological insulator candidates $(MnBi_2Te_4)(Bi_2Te_3)_n$, n=0,1,2 and $MnSb_2Te_4$ are thoroughly investigated in the fourth and fifth chapters. The fourth chapter primarily focuses on the bulk magnetic characterization of the $MnSb_2Te_4$ single crystalline samples, aiming to verify the presence of a ferromagnetic ground state and explore different routes to enhance the magnetic transition temperature that is crucial for achieving QAHE at an elevated temperature. The major finding of this chapter is that Mn overstoichiometry, combined with a specific Mn/Sb intermixing pattern and the resulting increasing three-dimensional nature of the magnetic order, drives the ferromagnetic transition temperature upwards. Further shifting the attention to the local magnetic ordering of Mn atoms in all the compounds, investigating the (Mn/Bi, Sb) site intermixing inherently present due to the similar ionic radii of the atoms. Powerful local techniques, such as nuclear magnetic resonance (NMR) and muon spin relaxation (μSR), are employed to identify these native defects and further confirm that they also undergo an order-disorder transition well below the magnetic ordering temperature. This comprehensive investigation provides a microscopic understanding of the crucial role played by intermixing and suggests pathways for optimizing the magnetic gap in its surface states necessary for the observation of the QAHE.

In the second part of this thesis, the chiral soliton lattice candidates $Cr_{1/3}NbS_2$ and its analogous compound $Mn_{1/3}NbS_2$ are studied through NMR measurements in the sixth chapter. While topologically nontrivial spin textures have already been observed in $Cr_{1/3}NbS_2$ via Lorentz TEM, distinguishing between trivial domains and nontrivial periodic spin textures in $Mn_{1/3}NbS_2$ has proven to be challenging. In this thesis, NMR

investigations of ^{53}Cr and ^{55}Mn nuclei, supported by theoretical calculations, provide an in-depth analysis of both compounds. The $Cr_{1/3}NbS_2$ compound exhibits all the signatures of a monoaxial chiral helimagnet (CHM) in a magnetic field. This detailed understanding allows for a comparison with $Mn_{1/3}NbS_2$ which, despite a much higher density of specific defects in its single crystal, demonstrates the presence of a predominant CHM phase, characterized by significantly higher upper critical magnetic fields for the phase transition to a forced ferromagnetic state.

Kurzfassung

Magnetismus in 2D-Materialien ist vielversprechend für zahlreiche Anwendungen in zukünftigen Technologien; gleichzeitig haben die Entdeckung von robusten topologischen Phasen in den letzten Jahrzehnten einen neuen Weg in der Quantenwelt eröffnet. Die Kombination dieser beiden Welten, das Zusammenspiel zwischen nichttrivialer Topologie und Magnetismus, bietet zahlreiche Anwendungen in spinbasierten Technologien. Besonders treibende Kräfte sind hier innovationsorientierte Quantenphänomene wie der quantenanomale Hall-Effekt (QAHE) oder Axion-Isolatoren. Diese Phänomene treten unter anderem in Materialien wie magnetischen Weyl-Halbmetallen, magnetischen topologischen Isolatoren, Skyrmionen- oder ähnlichen spintexturierten Materialsystemen auf. Diese Arbeit beschäftigt sich hauptsächlich mit den makroskopischen und mikroskopischen magnetischen Eigenschaften von 2D/quasi-2D-van-der-Waals-Materialien, die auch topologisch nichttriviale Zustände aufweisen. Ein besonderer Fokus liegt hierbei auf dem Verständnis der grundlegenden magnetischen Eigenschaften dieser Materialien und dem Herausarbeiten der Auswirkungen von kristalliner Unordnung auf die lokalen magnetischen Eigenschaften. Die Arbeit wurde basierend auf den Materialien in zwei Teile gegliedert.

Die Familie der $MnBi_2Te_4$ -Verbindungen verspricht die Realisierung des QAHE; allerdings ist für die vollständige Quantisierung des transversalen Hall-Widerstandes in antiferromagnetischem $MnBi_2Te_4$ immer noch ein externes Magnetfeld erforderlich. Hier gelten die Vergrößerung des Zwischenschichtabstands zwischen den Septupel-Schichten von $MnBi_2Te_4$ und die Substitution von Bi durch Sb als mögliche Ansätze, um eine Nettospinpolarisierung ohne Magnetfeld zu erreichen. Diese potenziellen intrinsisch magnetischen topologischen Isolatoren $(MnBi_2Te_4)(Bi_2Te_3)_n$, n=0,1,2 und $MnSb_2Te_4$ werden im vierten und fünften Kapitel eingehend untersucht. Das vierte Kapitel konzentriert sich auf die magnetische Charakterisierung der einkristallinen-$MnSb_2Te_4$ Proben, um die Existenz eines ferromagnetischen Grundzustandes zu überprüfen und weiterführend verschiedene Möglichkeiten zur Erhöhung der magnetischen Übergangstemperatur zu untersuchen. Dies ist entscheidend für das Auftreten des QAHE bei erhöhter Temperatur. Die wichtigste Erkenntnis dieses Kapitels ist, dass ein Überschuss von Mn, im Vergleich zum idealen stöchiometrischen Verhältnis, in Kombination mit spezifischer Mn/Sb-Vermischung und der damit zusammenhängenden zunehmenden dreidimensionalen Natur der magnetischen Ordnung zu einer Erhöhung der ferromagnetischen Übergangstemperatur führt. Das fünfte Kapitel richtet die Aufmerksamkeit auf die lokale magnetische Ordnung der Mn-Atome in allen bisher untersuchten Verbindungen und untersucht den Einfluss der (Mn/Bi, Sb)-Mischstörstellen, die aufgrund der ähnlichen Ionenradien der Atome inhärent vorhanden sind. Hier werden lokale Sonden-Methoden wie Kernspinresonanz (NMR) und Myonenspinrelaxation μSR eingesetzt, um diese intrinsischen Mischstörstellen zu identifizieren, die weit unterhalb der Bulk-Ordnungstemperatur einen Ordnungs-Unordnungs-Übergang durchlaufen. Meine umfassende Untersuchung liefert ein mikroskopisches Verständnis

der entscheidenden Rolle der Mischstörstellen und bietet neue Erkenntnisse für eine mögliche Optimierung der magnetischen Energielücke der Oberflächenzustände.

Im zweiten Teil dieser Arbeit wurden die chiralen Solitongitterkandidaten, $Cr_{1/3}NbS_2$ und die verwandte Verbindung $Mn_{1/3}NbS_2$, im sechsten Kapitel mittels NMR-Messungen untersucht. Während in $Cr_{1/3}NbS_2$ bereits mittels Lorentz Mikroskopie topologisch nichttriviale Spintexturen beobachtet wurden, erwies sich die Unterscheidung zwischen trivialen Domänen und nichttrivialen periodischen Spintexturen in $Mn_{1/3}NbS_2$ als schwierig. Die in dieser Arbeit durchgeführten ^{53}Cr und ^{55}Mn NMR Untersuchungen, unterstützt durch theoretische Berechnungen, liefern ein tiefgehendes Verständnis beider Verbindungen. $Cr_{1/3}NbS_2$ weist alle Signaturen eines monoaxialen chiralen Helimagneten (CHM) in einem Magnetfeld auf. Dieses detaillierte Verständnis ermöglicht einen Vergleich mit $Mn_{1/3}NbS_2$ das trotz einer viel höheren Dichte spezifischer Störstellen im Einkristall Charakteristika einer vorherrschenden CHM-Phase zeigt, die durch erheblich höhere obere kritische Magnetfelder gekennzeichnet ist.

Riassunto

I materiali magnetici bidimensionali offrono prospettive promettenti per future applicazioni tecnologiche. D'altro canto la robustezza intrinseca dei materiali topologici ha aperto una nuova prospettiva nella fisica quantistica degli ultimi decenni. Una combinazione delle due proprietà fisiche, che sappia sfruttare l'interazione tra caratteristiche topologiche e magnetismo offre un controllo diretto sullo spin dei portatori e stimola lo sviluppo di applicazioni spintroniche innovative, alla luce della attuale comprensione di fenomeni fondamentali quantistici come l'effetto Hall quantistico anomalo (QAHE) e la comparsa di isolanti assionici. Fenomeni legati allo spin elettronico e sfruttabili tecnologicamente si manifestano in materiali come i semimetalli di Weyl magnetici, gli isolanti topologici magnetici, oppure in materiali che presentano configurazioni di spin non collineari, come gli skyrmioni. Questa tesi si occupa principalmente della proprietá magnetiche macroscopiche e locali di materiali bidimensionali o quasi bidimensionali di van der Waals che possono presentare stati topologicamente non banali. Il mio lavoro si è concentrato sulla comprensione delle proprietà magnetiche fondamentali di questi materiali e sul ruolo del disordine nelle proprietá macroscopiche messo in luce dal comportamento locale dello spin. La tesi è divisa in due parti, distinte dalle famiglie di materiali indagati.

La famiglia di composti derivanti da $MnBi_2Te_4$ è promettente come isolante topologico magnetico che presenta QAHE; tuttavia lo sfruttamento di questo fenomeno in un antiferromagnete richiede ancora l'applicazione di un campo magnetico esterno, come nell'effetto Hall convenzionale. Per ovviare a ció e generare una polarizzazione di spin spontanea in strutture ferro o ferrimagnetiche (preservando il gap topologico), si é tentato di aumentanre la distanza tra i blocchi bidimensionali atomici antiferromagnetici tdi $MnBi_2Te_4$, chiamati strati settuplici, o di sostituire Bi con Sb. I composti risultatnti, $(MnBi_2Te_4)(Bi_2Te_3)_n$, n=0,1,2 e $MnSb_2Te_4$, sono possibili isolanti topologici magnetici e in quanto tali vengono indagati nei capitoli quarto e quinto. Il quarto capitolo è dedicato alla caratterizzazione magnetica di campioni monocristallini di $MnSb_2Te_4$, con l'obiettivo di determinare la presenza di uno stato fondamentale ferromagnetico ed esplorare diverse strategie di crescita per aumentare la temperatura di transizione magnetica, cruciale per lo sfruttamento applicativo del QAHE. Questo capitolo illustra il risultato principale della ricerca: la sovrastechiometria del Mn, combinata con un particolare livello di miscelazione Mn/Sb aumenta significativamente la temperatura critica d'ordine magnetico perché tende a favorire l'accoppiamento magnetico tridimensionale.

Il quinto capitolo sposta l'attenzione sull'ordinamento magnetico locale degli atomi di Mn nei composti di queste famiglie, studiando la auto-sostituzione di Mn/Bi (o di Mn/Sb), nota come fenomeno di anti-sito, intrinsecamente inevitabile a causa del raggi ionici simili delle coppie di atomi indicati. Abbiamo utilizzato spettroscopie avanzate, come la risonanza magnetica nucleare (NMR) e la spettroscopia di spin di muoni polarizzati (μSR), per identificare questi difetti nativi, e dimostrare che subiscono una

transizione ordine-disordine ben al di sotto della temperatura di ordinamento magnetico del reticolo. La nostra indagine completa fornisce una comprensione microscopica del ruolo cruciale svolto dalla auto-sostituzione e suggerisce una specifica strategia per ottimizzare il comportamento magnetico preservando il gap topologico caratteristico degli isolanti topologici magnetici.

Nella seconda parte di questa tesi ho studiato un'altra famiglia di materiali topologici. Il sesto capitolo introduce il composto $Cr_{1/3}NbS_2$ e il suo analogo $Mn_{1/3}NbS_2$, entrambi ritenuti possibili esempi di reticolo solitonico chirale e ne descrive l'indagine attraverso misure NMR. La struttura magnetica topologicamente non banale è già stata identificata nel $Cr_{1/3}NbS_2$ dal diagramma di fase magnetico e da misure di microscopia di trasmissione elettronica di Lorentz che distinguono domini convenzionali da configurazioni periodiche non convenzionali. Presentano fasi chirali che danno luogo a una fase di ferromagnete forzato al di sopra di campi critici distinti per la direzione di applicazione del campo. L'analoga indagine su $Mn_{1/3}NbS_2$ non ha peró portato a risultati conclusivi. Gli esperimenti di NMR sui nuclei ^{53}Cr e ^{55}Mn supportate da calcoli teorici, hanno consentito una descrizione approfondita dell'ordinamento locale di entrambi i composti. L'ottimo monocristallo di $Cr_{1/3}NbS_2$ presenta tutte le caratteristiche distintive di un elimagnete chirale monoassiale (CHM), sia in campo magnetico applicato nullo che nelle due principali orientazione del campo. La comprensione dettagliata delle sue risonanze magnetiche nucleari ha consentito un confronto con $Mn_{1/3}NbS_2$ che, nonostante la molto maggiore densità di difetti specifici esistenti nel monocristallo in nostro possesso, dimostra anch'esso la presenza di una fase CHM, caratterizzata da campi critici superiori per la transizione a ferromagnete forzato notevolmente più alti di quelli del composto di Cr.

Acknowledgements

To begin with, I express my gratitude to the almighty for providing guidance and protection throughout this journey. I would also like to extend my sincere appreciation to everyone who contributed to the completion of this thesis, including those whose names I may have forgotten to mention.

I am deeply grateful to my supervisors, Prof. Bernd Büchner and Prof. Roberto De Renzi, for giving me the opportunity and for their unwavering support, motivation, and guidance, which played a crucial role in the successful completion of this work. I also wish to thank Dr. Anja Wolter-Giraud and Dr. Laura Corredor Bohrquez for their guidance in co-supervising this thesis work in Dresden as well as agreeing to proofread this thesis. The regular discussions on magnetism during group meetings and one-on-one sessions significantly enriched my understanding.

I am particularly indebted to Roberto for his invaluable assistance, from helping me settle in Parma, including finding accommodation, to introducing me to NMR and μSR. His ideas, advice, and generous availability for scientific discussions were instrumental in shaping this thesis. I also thank Prof. Giuseppe Allodi for sharing his expertise in NMR and for his constant assistance with measurements. Additionally, I am grateful to Dr. Zaher Salman for his support with μSR measurements at PSI, even during the challenging times of COVID-19, and for his readiness for discussions and collaboration. To my colleagues in Parma, Ifeanyi John Onuorah, Pietro Bonfà, and Muhammad Maikudi ISAH, I appreciate the meaningful discussions, collaborations, and support throughout my time in Parma.

I also extend my thanks to Prof. Anna Isaeva, Prof. Geetha Balakrishnan, and their teams for providing the samples used in this research.

I would also like to express my gratitude to ct.qmat (Complexity and Topology in Quantum Matter), the cluster of excellence, for providing financial assistance for this thesis work and all business trips. This support made it possible for me to pursue my research and connect with the broader scientific community.

My heartfelt thanks go to my friends in Dresden, Kranthi, Matheus, Shailja, Soumen, and Anirudhha, and in Parma, Ratika, and Niyaz, for their patience and support during moments of frustration and discouragement. Your friendship, the lunchtime conversations, and the short weekend trips were invaluable. I would also like to acknowledge all the past and present members of our thermodynamics group, namely Francesco, Bastian, Börge, Killian, Felix, and Dr. Audrey, for always maintaining a healthy work environment and for always present at the time of need. A special mention goes to Sebastian Gass for his technical support in the lab and insightful discussions on unsuccessful measurements.

Finally, I express my deep gratitude to my family, especially Ankit, who has been my constant source of strength, and my friends back home for their unending support and motivation during this journey. I am truly thankful for all that you have done for me.

List of publications

Parts of the results of this dissertation have been published or are contained in manuscripts in preparation for future publication:

2022 L. Folkers, L. T. Corredor,F. Lukas M. Sahoo, A. U. B. Wolter, A. Isaeva. *Occupancy disorder in the magnetic topological insulator candidate* $Mn_{1-x}Sb_{2+x}Te_4$, Z. Kristallogr. 2022; 237(4–5):101–108

2023 M. Sahoo, M. C. Rahn, E. Kochetkova, O. Renier, L. C. Folkers, A. Tcakaev, M.L. Amigò, F.M. Stier, V. Pomjakushin, K. Srowik, V.B. Zabolotnyy, E. Weschke, V. Hinkov, A. Alfonsov, V. Kataev, B. Büchner, A. U. B. Wolter, J.I. Facio, L.T. Corredor, A. Isaeva. *Tuning strategy for Curie-temperature enhancement in the van der Waals magnet* $Mn_{1+x}Sb_{2-x}Te_4$, Materials Today Physics 38 (2023) 101265

2023 M. Sahoo, Z. Salman, G. Allodi, A. Isaeva, L. Folkers, A. U. B. Wolter, B. Büchner and R. De Renzi *Impact of Mn-Pn intermixing on magnetic properties of an intrinsic magnetic topological insulator: the μSR perspective,* Journal of Physics: Conference Series 2462 (2023) 012040

2024 M. Sahoo, I.J. Onuorah, L. C. Folkers, E. V. Chulkov, M. M. Otrokov, Z. S. Aliev, I. R. Amiraslanov, A. U. B. Wolter, B. Büchner, L. T. Corredor, Ch. Wang, Z. Salman, A. Isaeva, R. De Renzi, G. Allodi. *Ubiquitous order-disorder transition in the Mn antisite sublattice of the* $(MnBi_2Te_4)(Bi_2Te_3)_n$ *magnetic topological insulators,* Adv. Sci. 2024, 11, 2402753

2024 M. Sahoo, P. Bonfà, A. E. Hall, D. A. Mayoh, A. U. B Wolter, B. Büchner, G. Balakrishnan, R. De Renzi, and G. Allodi. *Helical to Conical ground state in* $M_{1/3}NbS_2$, *M=Cr, Mn through NMR,* arXiv:2410.01631v1

Publication not included in the thesis

2022 N. Pèrez, M Sahoo, G. Schierning, K. Nielsch, and G. S. Nolas. *Europium clustering and glassy magnetic behavior in inorganic clathrate-VIII* $Eu_8Ga_{16}Ge_{30}$. Materials 2022, 15, 3439

Manuscripts in preparation:

2025 E. Kochetkova, M. Tardieux, M. Sahoo, F. Pabst, L. Folkers, A. U. B. Wolter, L. T. Corredor, I. Aguilera, and A. Isaeva *Tweaking magnetism in the magnetic topological insulators $Mn_{1-x}Sb_{2-y}Te_4$ by adjusting the Mn/Sb ratio, under review (2025).*

2025 K.K Bestha, M. Sahoo, R. Morrow, A. Malyuk, B. B üchner, L. Corredor, and A. U. B. Wolter. *Revisiting anisotropic magnetic phase diagram of Kitaev Quantum Spin Liquid candidate $Na_3Co_2SbO_6$, in preparation (2025)*

2025 E. Kochetkova, M. Sahoo, M. C. Tardieux, F. Pabst, O. Renier, I. Aguilera, A. U. B. Wolter, L. T. Corredor, and A. Isaeva, *Mn Interstitials in Layered $Mn_{1+x}Sb_{2-2/3x}Te_4$: Structural Modification and Curie Temperature Boost, in preparation (2025).*

Conference Contributions:

- **M. Sahoo**, L.T. Corredor, L. C. Folkers, A. Tcakaev, A. Alfonsov, J. I. Facio, V. Hinkov, V.Kataev, B. Büchner, A. U. B Wolter, and A. Isaeva, *Impact of Mn/Sb intermixing on magnetic ground state and dimensionality of High-Tc $MnSb_2Te_4$ (poster)*, ct.QMAT Retreat 2022, Merseburg, Germany, 23-25.3.2022.
- **M. Sahoo**, L.T. Corredor, L. C. Folkers, A. Tcakaev, A. Alfonsov, J. I. Facio, V. Hinkov, V. Kataev, B. Büchner, A. U. B Wolter, and A. Isaeva, *Impact of Mn/Sb intermixing on the magnetic ground state and dimensionality of High-Tc $MnSb_2Te_4$ (poster)*, International Conference on Complexity and Topology in Quantum Matter 2022, Würzburg, Germany, 25-29.7.2022.
- **M. Sahoo**, G. Allodi, L.T. Corredor, Z Salman, A Isaeva, A. U. B Wolter, B. Büchner, R. De Renzi, *Insight into the magnetic properties of intrinsic magnetic topological insulators (poster)*, 15th International Conference on Muon Spin Relaxation, Rotation, and Resonance 2022, Parma, Italy, 28.8–2.9.2022.
- **M. Sahoo**, G. Allodi, L.T. Corredor, Z. Salman, A. Isaeva, A. U. B Wolter,B. Büchner, R. De Renzi, *Insight into the magnetic properties of intrinsic magnetic topological insulators (poster)*, Workshop on Topology in Magnetic Materials, 2022, Herzberg, Switzerland, 22–24.11.2022.
- **M. Sahoo**, G. Allodi, L.T. Corredor, Z. Salman, A. Isaeva, A. U. B Wolter, B. Bc̈hner, R. De Renzi, *Insight into the magnetic properties of intrinsic magnetic topological insulators, (talk)*, DPG Spring Meetings 2023, Dresden, Germany, 26–28.3.2023.
- **M. Sahoo**, G. Allodi, L.T. Corredor, Z. Salman, A. Isaeva, A. U. B Wolter, B. Büchner, R. De Renzi, *Insight into the magnetic properties of intrinsic magnetic topological insulators (talk)*, Topological matter conference 2023, Athens, Greece, 28–31.3.2023.
- **M. Sahoo**, G. Allodi, L.T. Corredor, Z. Salman, A. Isaeva, A. U. B Wolter,B. Büchner, R. De Renzi, *Insight into the magnetic properties of intrinsic magnetic topological insulators (poster)*, CMD FISMAT 2023, Milan, Italy, 4–8.9.2023.
- **M. Sahoo**, P. Bonafa, A. Hall, L.T. Corredor, A. U. B Wolter, B. B. Büchner, G. Balakrishnan, G. Allodi, R. De Renzi, *Helical to conical order in $M_{1/3}$ NbS_2 (M=Cr, Mn), detected by ^{53}Cr,^{55}Mn, and ^{93}Nb NMR (talk)*, CMD30 FISMAT 2023, Milan, Italy, 4–8.9.2023.
- **M. Sahoo**, G. Allodi, L.T. Corredor, Z. Salman, A. Isaeva, A. U. B Wolter,B. Büchner, R. De Renzi, *Insight into the magnetic properties of intrinsic magnetic topological insulators (poster)*, Workshop on Magnetic Resonance of Correlated Electron Material 2023, Dresden, Germany, 17–22.9.2023.
- **M. Sahoo**, P. Bonfà, A. Hall, L.T. Corredor, A. U. B Wolter, B. B. Büchner, G. Balakrishnan, G. Allodi, R. De Renzi, *Helical to conical order in $M_{1/3}$ NbS_2 (M=Cr, Mn), detected by ^{53}Cr,^{55}Mn, and ^{93}Nb NMR (talk)*, Workshop on Magnetic Resonance of Correlated Electron Material 2023, Dresden, Germany, 17–22.9.2023.

- **M. Sahoo**, G. Allodi, L. T. Corredor, Z Salman, A Isaeva, A. U. B Wolter, B. Büchner, R. De Renzi, *Insight into the magnetic properties of intrinsic magnetic topological insulators (poster)*, Second Fall School "Topological Quantum Matter" and Fourth QMA Retreat, Leipzig 2023, Germany, 25–29.9.2023.

- **M. Sahoo**, P. Bonfà, A Hall, L. T. Corredor, A. U. B Wolter, B. B. Büchner, G. Balakrishnan, G. Allodi, R De Renzi, *Helical to conical order in* $M_{1/3}\,NbS_2$ *(M=Cr, Mn), detected by* ^{53}Cr,^{55}Mn, *and* ^{93}Nb *NMR (talk)*, DPG spring meeting 2024, Berlin, Germany, 17–22.3.2024.

- **M. Sahoo**, M. C. Rahn, E. Kochetkova, O. Renier ,L. C. Folkers, A. Tcakaev, A. Alfonsov, V. Hinkov, V. Kataev, J. van den Brink, B. Büchner, A.U.B Wolter, J. I. Facio, L. T. Corredor, and A. Isaeva, *Tuning strategy for Curie-temperature enhancement in the van der Waals magnet* $Mn_{1+x}Sb_{2-x}Te_4$*, (Invited Poster)*, Ct. mat retreat 2024, Weimar, Germany, 25-27.3.2024.

Contents

List of Figures

List of Tables

List of Abbreviations

QAHE	Quantum Anomalous Hall Effect
AHE	Anomalous Hall effect
TIs	Topological Insulators
SQUID	Superconducting Quantum Interference Device
ARPES	Angle Resolved Photo Emission Spectroscopy
RKKY	Ruderman-Kittel-Kasuya-Yosida
SOC	Spin-orbit coupling
μ**SR**	Muon Spin Rotation, Relaxation and Resonance
AF/AFM	Antiferromagnet
DFT	Density Functional Theory
DOS	Density of States
EFG	Electric Field Gradient
FM	Ferromagnet
FIM	Ferrimagnet
NMR	Nuclear Magnetic Resonance
NQM	Nuclear Quadrupole Moment
ZF	Zero Field
ZFC	Zero Field Cooled
FC	Field Cooled

Introduction

Magnetism, a fundamental phenomenon of nature, is all around us, quietly driving the mechanics of modern society. From guiding ancient navigators through simple compasses to driving modern transportation like magnetic levitation (maglev) trains and innovative technology, magnetism's evolution over time showcases its remarkable adaptability and importance. The understanding of magnetism increased as technology progressed. Based on the principle of electromagnetism, electric motors and generators were used during the Industrial Revolution. Then, in the digital age, the fundamentals of magnetism are used to store data in hard drives and record them in magnetic disks. In the healthcare sector, magnetism also plays an important role, particularly in magnetic resonance imaging (MRI). Over time, magnetism has evolved in its applications, significantly impacting our daily lives. Though magnetism in bulk materials was discovered ages ago and used in traditional technologies, magnetism in atomically thin layers was understood only a few years ago. These days, magnetism in 2D materials has had a profound impact on society by enabling advancements in technology like spintronics, medicine such as biosensors and targeted drug delivery, and quantum computing. These materials offer the potential for smaller, more efficient devices and could lead to significant breakthroughs in various industries, contributing to a more innovative, sustainable, and interconnected world.

Simultaneously, topology in condensed matter physics got recognition in 2019 after the Nobel Prize in Physics was given to Thouless, Haldane, and Kosterlitz. Their work was based on topology, which is a branch of mathematics that studies the properties of objects that are invariant under continuous transformations such as stretching and bending without tearing. Then this mathematical approach was applied to condensed matter physics to describe new topological states of matter and their phase transitions. They made significant contributions to understanding topological phase transitions in two-dimensional systems, demonstrating that certain materials, under specific conditions, could exhibit unique topological properties that distinguished them from conventional phases of matter. Their work laid the foundation for exploring topological insulators and quantum Hall effects.

This thesis focused on understanding the interplay of these key concepts of topology and magnetism, particularly in 2D materials. Magnetic topological materials provide fertile ground for discovering new quantum states of matter. The presence of magnetism can lead to complex interactions and phenomena that do not occur in non-magnetic topological materials. This can result in novel quantum effects, such as the quantum anomalous Hall effect, axion insulators, and other exotic states, contributing to the advancement of condensed matter physics. These materials exhibit intriguing behaviors due to their unique electronic structure and spin textures. Investigating their

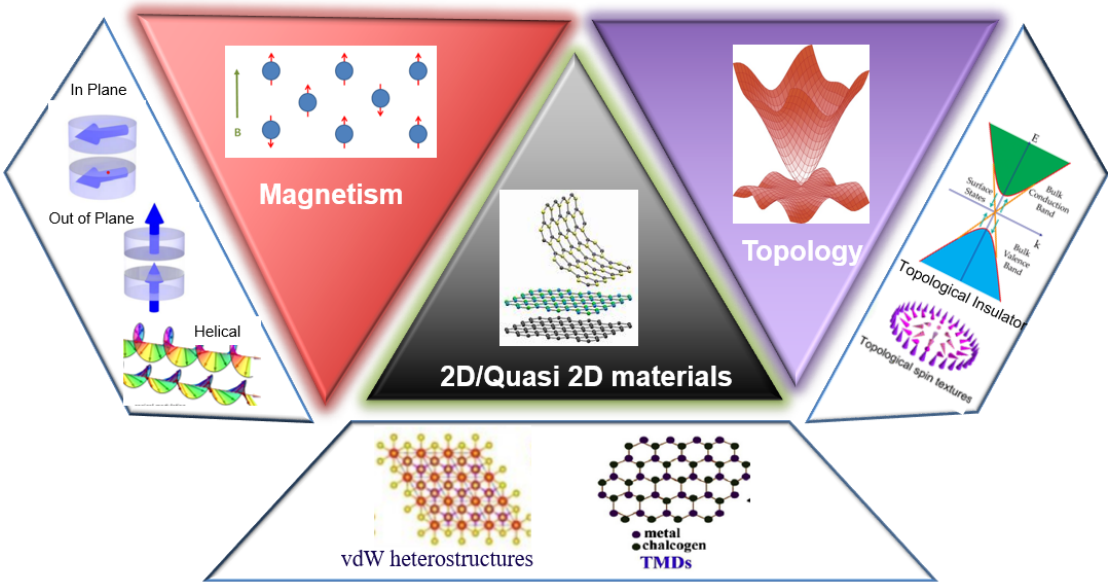

Figure 0.1: Schematic diagram of the key concept of the thesis

magnetism reveals not only fundamental principles but also promises revolutionary applications in spintronics and quantum computing. Most importantly, for future technological applications, the observation of these quantum phenomena at elevated temperatures is the biggest challenge. Unraveling the intricacies of this magnetism holds the key to harnessing these materials' full potential for future technological advancements [1–4]. Moreover, this thesis focuses on investigating both bulk and local magnetism of 2D/quasi 2D van der Waals candidates, which also host topologically non-trivial surface states, through local spectroscopic and bulk thermodynamic techniques.

This thesis is structured as follows:

Chapter 1 : An introduction to topology, magnetism, and 2D materials. This chapter briefly motivates the thesis work by explaining the basic concept of topology in condensed matter, magnetism in topology, and magnetism in 2D materials.

Chapter 2 : Experimental techniques. In this chapter, the theory and experimental setup of the techniques (SQUID magnetometry, NMR, and μSR) that have been utilized in this thesis have been described.

Chapter 3 : Literature review. This chapter presents a complete literature review on intrinsic magnetic topological insulators to identify the key challenges that were addressed in the thesis work.

Chapter 4 : Tuning the magnetic ordering of $MnSb_2Te_4$. This chapter initiates the exploration of the $MnSb_2Te_4$ compound, aiming to comprehend its ground state and the influence of Mn/Sb intermixing. Employing various techniques, a comprehensive experimental and theoretical investigation of this compound has been conducted. DC and AC magnetic studies, along with pressure-dependent magnetization experiments, were performed to understand the ground state of this compound and to identify a way to tune the transition temperature, a key

factor for observing the QAHE at higher temperatures. The findings from this chapter have been or will be documented in Ref. [5–7].

Chapter 5 : Role of Mn/P intermixing on the magnetism of MnP_2Te$_4$ (P=Bi, Sb). After the challenge of cationic intermixing was encountered in this compound family, Nuclear Magnetic Resonance (NMR) was used to characterize the magnetic nuclei, providing insights into magnetism at various sites. Another advanced local spectroscopic method, μSR, was also employed to investigate the intermixing phenomenon and its impact on thermodynamic magnetic transition. The results from both the NMR and μSR experiments are supported by theoretical calculations. The findings from this chapter have been or will be documented in Ref. [8–10]

Chapter 6 : Helical to conical order in M$_{1/3}$NbS$_2$ (M=Cr, Mn), detected by Cr, Mn NMR. This chapter investigates, a very well-known chiral soliton lattice host compound $Cr_{1/3}NbS_2$ though NMR and compares it with its isostructural compound $Mn_{1/3}NbS_2$ which is still debated to have topological nontriviality. Both of these compounds have been investigated through ^{53}Cr and ^{55}Mn nuclei NMR to identify commonalities and to map the phase transitions that occur when a magnetic field is applied in different orientations. The findings from this chapter will be communicated in Ref. [11]

Chapter 7 : Summary and Outlook. The thesis is summarised in this chapter.

Chapter 1

An introduction to topology, magnetism and 2D materials

1.1 Topological insulators

The field of condensed matter physics witnessed a significant paradigm shift in 1980 with the discovery of the Quantum Hall Effect (QHE), marking the start of a new and exciting chapter. Before this, explanations relied on the Landau theory of phase transitions, which fell short in elucidating the quantum Hall systems due to the absence of spontaneously broken symmetry rather than the classification based on topological order. Analogous to the classical Hall effect, K. v. Klitzing observed quantized plateaus in Hall conductivity and simultaneous zero longitudinal resistivity under high magnetic fields while measuring a 2D electron system [12]. This indicated an insulating bulk with dissipationless edge states, where electrons, constrained by the magnetic field, traveled one-way along the edges. This marked a new era in understanding quantum states attributed to the topology of electron wavefunctions. The pivotal concept of the Chern number $\mathcal{C}_\mathrm{n}$ or TKNN number, introduced by D. J. Thouless, M. Kohmoto, M. P. Nightingale, and M. den Nijs (TKNN) in 1982 [13, 14], provided a measure of the number of edge states which also corresponds to the occupancy of the Landau levels.

The Hall conductivity σ_{xy} is simplified as

$$\sigma_{xy} = \frac{\mathcal{C}_\mathrm{n} e^2}{h} \tag{1.1}$$

where e is the electron charge and h is Plank's constant. $\mathcal{C}_\mathrm{n}$, called the Chern number which is represented as the topological invariant where there is no deformation in the materials parameter. The hall conductance is quantized if the Fermi energy lies in a gap between Landau levels or an energy gap between the valency band and the conduction band[15]. symmetry plays a crucial role here and different symmetry groups consider different types of topological invariants. For instance, C is considered a topological invariant in case of broken time-reversal symmetry, $\mathcal{Z}_2$ is considered for the topological electronic structure in momentum space where time-reversal symmetry is present.

The Chern number could be understood as the surface integral of Berry curvature over the Brillouin zone[15],

$$\mathcal{C}_\mathrm{n} = \frac{1}{2\pi} \int d^2k \mathcal{B}_f \tag{1.2}$$

where $\mathcal{B}_f$ is the Berry curvature or Berry flux, expressed as $\mathcal{B}_f = \nabla \times \mathcal{Q}$ and $\mathcal{Q}$ is $\mathcal{Q} = i < U(k)|\nabla_k|U(k) >$, U(k) is the Berry wave function [16]. In the Gauss-Bonnet

theorem, the integral of the Gaussian curvature over a closed surface is a quantized topological invariant and is termed g, which is the number of holes. For instance, the number of holes in a basketball is 0, so g=0, but for a ring, g=1, shown in Fig. 1.1.

Figure 1.1: g=0 for basketball but g=1 for the ring.

This topological invariant changes while going from a gapped bulk state to a surface where gapless conducting states (for 2D, edge states) are present. In other words, the localized electrons at the bulk complete a closed cycle, but the electrons execute a skipping motion at the edges as their cyclotron orbits bounce off, as shown in Fig. 1.2. The transport of charge in these edge channels is characterized by non-dissipative behavior, with the direction—either clockwise or anticlockwise—uniquely determined by the charge's sign (electron or hole) and the orientation of the applied magnetic field (up or down). This could be referred to as bulk boundary correspondence [15].

Dirac point and Haldane model : In 1988, Haldane proposed a model to explain the QHE by breaking time-reversal symmetry through the introduction of a magnetic field. This magnetic field lifts the degeneracy at the Dirac points, which are points in the Brillouin zone where the conduction and valence bands cross. This is called band inversion [1]. At these Dirac points, the electronic dispersion resembles that of a massless relativistic particle, described by the Dirac equation. Typically, the degeneracy at the Dirac points is protected by inversion symmetry ($\mathcal{I}$) and time-reversal symmetry ($\mathcal{T}$). When $\mathcal{T}$ is perturbed, it induces a mass at the Dirac points. However, to maintain inversion symmetry, the masses at different points must be opposite. Haldane demonstrated that the resulting gapped state is equivalent to a Quantum Hall Effect state with a Hall conductivity (σ_{xy}) of e^2/h [15, 17].

[1] The conduction band has s-like symmetry and the valency band has p-like symmetry. The p level rises above the s level due to spin-orbit coupling, leading to inversion in band structure

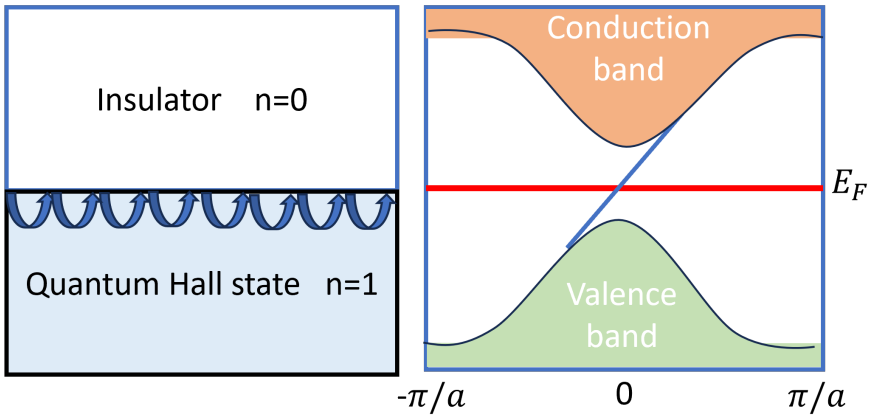

Figure 1.2: (a) Chiral edge mode is present at the boundary of the insulator and quantum hall state. A single-edge state connects the valence band to the conduction band (described by the Haldane model); taken from Ref. [15].

Haldane also emphasized that Dirac points should always come in pairs, and each pair contributes to a Hall conductivity of $\sigma_{xy} = e^2/(2h)$. This requirement ensures that the Hall conductivity is quantized to integer values and avoids the possibility of half-integer quantization. Hence, by solving the Haldane model in a semi-infinite geometry, these chiral edge states could be explicitly explained. Fig. 1.2 shows the energy levels as a function of the momentum k_x along the edge. The solid regions show the bulk conduction and valence bands, which form continuum states and show the energy gap near K and K'. A single band, describing states bound to the edge, connects the valence band to the conduction band with a positive group velocity[15, 17].

2D ($\mathcal{Z}_2$) topological insulators : The presence or absence of $\mathcal{T}$ could explain the new topological class, where the broken $\mathcal{T}$ would lead to topological non-trivial Hall conductivity but also unbroken $\mathcal{T}$ preserves insulating band structure. One of the important concepts is Kramers' theorem, which says the degeneracy of every energy level is twofold degenerate if it has a half-integer spin. That means every eigenstate, $|\eta>$ of a half-integer spin has another time-reversed eigenstate, $\mathcal{T}|\eta>$ of the same energy, with $\mathbf{T^2}$ = -1 and $\mathbf{T}$ represented by an antiunitary operator where, $\mathbf{TH(k)T^{-1}} = \mathbf{H(-k)}$ [15].

To prove this, consider a spin operator S that reverses under the operation of $\mathcal{T}$, $S \rightarrow \mathcal{T}S = -S$ The $\mathbf{T}$ is usually written as $\mathbf{T} = e^{i\pi S_y}K$, where S_y is the spin operator along the y direction and K is the complex conjugate. Afterward, $\mathbf{T^2} = e^{i\pi S_y}Ke^{i\pi S_y}K = (-1)^{2S}$. Hence, for half-integer spins ($S = \frac{1}{2}, \frac{3}{2}..$) $\mathbf{T^2}$ = -1. This Kramers degeneracy without spin-orbit coupling is simply the degeneracy between up and down spins; however, spin-orbit coupling leads to nontrivial consequences. Hence, similar to Fig. 1.2, the 2D TIs have states bound to the edge inside the gap of the valency band and conduction band. According to Kramers' theorem, they need to be doubly degenerate at the $\mathcal{T}$ invariant points at the Brillouin zone. If the bands intersect the Fermi level (E_f) an even number of times, the edge states can be eliminated; however, if they intersect an odd number of times between K_x =0 and π/a, the edge states cannot be eliminated. Hence, the number of Kramers pair of edge modes that intersect the E_f can be defined as $K_N = \Delta\nu$ mod 2 [15]. This changes the $\mathcal{Z}_2$ invariants

across the interface. Unlike the TKNN invariant which can take any integer value, $\mathcal{Z}_2$ topological invariant has values like ν_0 =0 for trivial insulators or vacuum and ν_0 =1 for TIs. Band inversion between the conduction and valence band rather than overlapping like in semimetals remains the most important criterion for TIs. The 2D Dirac fermion states correspond to an interface where the Dirac mass changes sign. This can also be compared to the surface states of 3D topological insulators (this will be discussed ahead). They have topologically protected edge states, which form 1D conductor-like states. They are also known as quantum spin Hall insulators (QSHI). This quantized surface or edge state was then realized more than three decades after Haldane's suggestion, and QHE was experimentally verified in topological insulators (TIs), specifically in strong spin-orbit-coupling HgTe/(Hg, Cd)Te heterostructures [18, 19] .

3D topological insulators: Following the theoretical investigation of the $\mathcal{Z}_2$ topological index, initially confined to quantum Hall systems such as HgTe in 2D, the analysis was subsequently extended to encompass three-dimensional (3D) scenarios. This expansion of the study unveiled the identification of the bulk phase characterized by topological nontriviality in 3D topological insulators. Generally, they are characterized by four $\mathcal{Z}_2$ topological invariants. The surface characteristics of the 3D crystal exhibit similarities to those of a 2D topological insulator. The surface Brillouin zone contains four points that are invariant under time reversal, and at these specific points, if any surface states exist, they must exhibit Kramers degeneracy. However, beyond these distinctive points, the degeneracy is lifted by the spin-orbit interaction. Consequently, these Kramers degenerate points give rise to 2D Dirac points in the surface band structure. The important point would be how these surface states intersect the Fermi energy. If they are odd, then they are topologically protected. The strong topological insulator always has an odd number of Kramers degenerate Dirac points enclosed by the surface Fermi circle. The Hamiltonian for a single Dirac point at the surface of the TI could be described as

$$\mathcal{H}_{\mathbf{S}} = -i\hbar v_F \vec{\sigma} \cdot \vec{\nabla} \tag{1.3}$$

where v_F is the Fermi velocity and $\vec{\sigma}$ is the Pauli matrix. The Hamiltonian explains the *spin-momentum locking* of the massless Dirac electrons, which means that the spin of the electrons is perpendicular to their momentum and opposite spins travel in opposite directions. The first 3D topological insulator, $Bi_{0.09}$ $Sb_{0.91}$, was experimentally discovered by Hasan et al. in 2008. [20] through ARPES measurements. They could observe doubly degenerate Kramers point in the Brillouin zone, and the surface states cross E_f five times between these Kramers points. This was, for the first time, established as the 3D TI with protected topological surface states. Then, in search of a large band gap 3D TI, Bi_2Se_3 was proposed as the next generation TI [21–23] also theoretically predicted to have a single Dirac cone. Subsequently, Bi_2Te_3 and Sb_2Te_3 had been confirmed to have similar topological band structures [24–26]. Apart from the similarities with the previous generation, these materials had a very large band gap of around 0.3 MeV in Bi_2Se_3 and could have potential for future applications. This class of materials also remains highly tunable; the Dirac node remains unperturbed by the non-magnetic disorder, but the magnetic impurity breaks time-reversal symmetry and opens the gap at the Dirac point. Most topological insulator applications require the chemical potential to lie at the Dirac point. However, for Bi_2Se_3, the Fermi energy does not lie in the gap due to vacancies. And by chemical tuning or doping, the

Fermi surface could be tuned to lie exactly at the Dirac point [26]. However, the primary challenge in this class of materials lies in differentiating between surface and bulk states through transport measurements.

1.2 Topology and magnetism

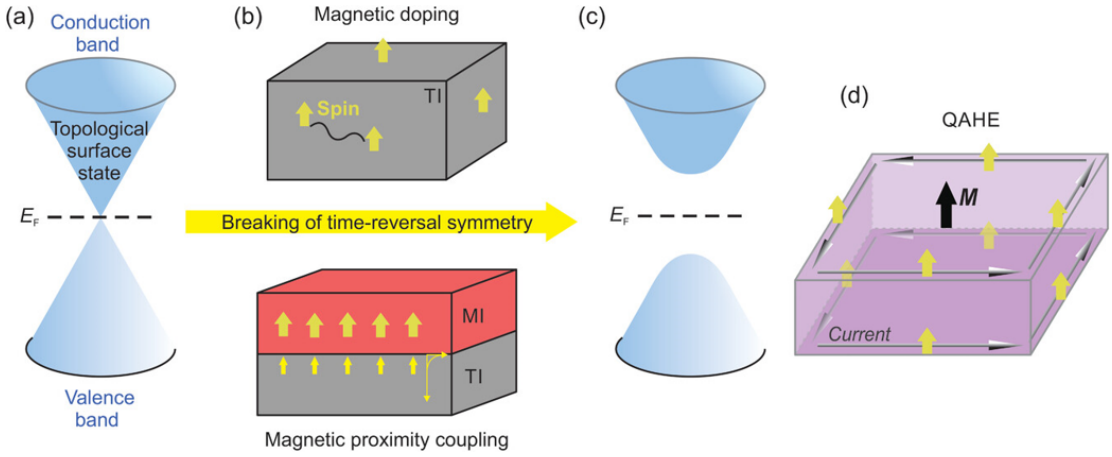

Figure 1.3: Schematic illustrates the transformation in the surface states of TIs when magnetic order is introduced: a) The topological surface state exhibits a linear dispersion relation b) Introducing magnetic order into the TI system, either through doping with magnetic impurities or proximity coupling to a magnetic insulator, breaks time-reversal symmetry c) bandgap opens in the surface state, with the Fermi energy positioned within this bandgap. d) Realization of the QAHE in a TRS-broken TI material, characterized by quantized edge conduction at the top and bottom surfaces of the film, with spin-momentum locking; taken from Ref. [27].

Following the development of the theory and experimental implementation of TIs and 3D TIs, along with the adjustment of surface states through nonmagnetic impurities, the focus shifted to exploring the impact of spontaneous magnetization. The incorporation of spontaneous magnetization into the electronic structure of surface states in TI results in the breaking of $\mathcal{T}$, leading to the coupling of conduction electrons with spontaneous magnetization through exchange interaction.[15, 28–30] Hence, the Hamiltonian in 1.3 could be rewritten as

$$\mathcal{H}_{\mathbf{S}} = -i\hbar v_F \vec{\sigma} \cdot \vec{\nabla} + m\sigma_z \tag{1.4}$$

where $m = -JN_sS_z$ and σ_z is the Pauli matrix, and J is the exchange coupling. Broken $\mathcal{T}$ would lead to the opening of the gap at the Dirac point in surface state, and the Dirac fermion would become massive. This could be realized in multiple ways: *(i) proximity effect*, i.e., a magnetic thin film on top of a TI. *(ii) introducing magnetic impurity*. This would result in Kramers degeneracy at the Dirac point due to exchange interactions. Then, if E_f is present at the mass gap, the Hall conductivity is quantized according to TKNN. This effect could be observed in the quantized anomalous Hall effect (QAHE). Analogous to the classical Hall Effect, AHE requires an external magnetic field or

spontaneous magnetization. Now, breaking $\mathcal{T}$ in TIs would simply drive the mechanism of AHE to the TKNN formula and Berry curvature expressed in equation 1.2. The discovery of the quantized Hall effect in 2D electron gases and topological insulators through the breaking of time-reversal symmetry using a strong external field encouraged further research into achieving similar quantized states through the spontaneous breaking of time-reversal symmetry. This was achieved by introducing magnetism into topological insulators, thereby reinforcing the principles outlined in the Haldane model. It was predicted that the QAHE could be realized in different ways, one of them being magnetic TIs [31]. Let's discuss three major ways of achieving this: (i) *Doping with magnetic impurities into TIs*, (ii) *Proximity effect with Ferromagnetic layer and TIs.* (iii) *Intrinsic Magnetic topological insulators*. This QAHE further would give rise to the chiral edge mode, whose direction directly depends on the Chern number and direction of the magnetization.

1.2.1 Magnetic topological insulators

The formation of an exchange gap at the surface state is the most important aspect of magnetic TI. Essentially, the exchange interaction between the Dirac electron at the surface states and the localized spin is responsible for the opening of the mass gap (Fig. 1.3). Let's discuss the possible methods to achieve this.

Proximity effect :

The magnetic proximity effect between a magnetic thin film on top of a TI was one of the mechanisms for realizing this effect. Despite several attempts on different heterostructures, like (Bi, Sb)$_2$Te$_3$/YIG and (Bi, Sb)$_2$ Te$_3$/EuS [32, 33], it was not easy to observe any QAHE or spontaneous magnetization. Another attempt by Watanabe et al. was partially successful in realizing QAHE in (Zn, Cr)Te/ (Bi, Sb)$_2$ Te$_3$/(Zn, Cr)Te heterostructures. However, they also observed a large gap due to Te present in both the Ferromagnetic Insulator (FI) and TI layer; the surface state might penetrate into the FI layer. [34] Although this way of realizing QAHE was noteworthy, the process is not irreversible, and the surface states might be destroyed due to too many complicated layer structures. Hence, it was essential to have a controllable way of maneuvering the surface states.

Doping with magnetic impurities into TIs :

Another effective way to control the surface states by doping TIs with 3d transition metal into the TIs was predicted decades ago [35–37]. In general, there are two mechanisms responsible for ferromagnetism in doped TIs. The first one is the Ruderman-Kittel-Kasuya-Yosida (RKKY) mechanism, which describes the indirect exchange interaction between the local magnetic moment and the conduction electrons. This may induce spin polarization in the conduction electrons and change the spin polarization of neighboring magnetic ions. This RKKY interaction is characterized by spatial oscillation, whose strength depends on the separation of magnetic impurities or ions. The general RKKY form is [38]

$$E_{ab} = \frac{2k_F r_{ab}\cos(2k_F r_{ab}) - \sin(2k_F r_{a,b})}{{r_{ab}}^4} \tag{1.5}$$

where r_{ab} is the distance between magnetic impurities and k_F is the Fermi wave vector. This mechanism was initially given for diluted systems where the direct exchange interaction was difficult to realize, but because of this RKKY interaction, the itinerant electrons can have finite coupling. And the strength here depends on the distance between doped magnetic impurities. This knowledge was then transferred to the transition metal doping in TIs and verified experimentally in Mn-doped Bi_2 Se_y Te_{3-y} [39] as RKKY interaction would develop ferromagnetic order on the doped Mn impurities present on the surface of the TI. Another report suggests carrier density-dependent ferromagnetism, where magnetic order like T_C could be tuned by tuning the carrier density [40]. The T_C was drastically increased by decreasing the carrier density, as shown in Fig. 1.4. However, usually, in RKKY interactions, the effective carrier-mediated ferromagnetism is enhanced by the increased carrier density. In this light, the author's explanation of Dirac fermion-mediated ferromagnetism was accountable. This was also further confirmed by STM experiments [41].

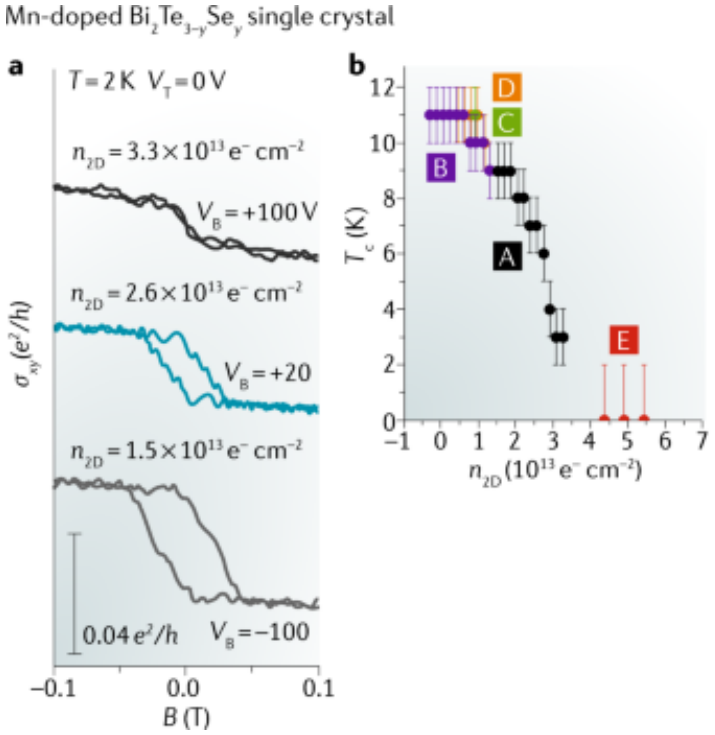

Figure 1.4: (a) Different gate bias V_B applied to $Mn_xBi_{2-x}Se_yTe_{3-y}$ single crystal flakes that controls the AHE. (b) Ferromagnetic Curie temperature T_C as a function of n_{2D} observed for five samples (A–E); taken from Ref. [30].

In contrast to the concept of carrier-mediated ferromagnetism, another mechanism known as Van Vleck paramagnetism provides an alternative explanation for the exchange interaction between the local moment leading to ferromagnetic order. This phenomenon is mediated by valence band electrons and plays a role in the magnetic ordering observed in TIs doped with chromium and vanadium. In general, diluted magnetic semiconductors lack reasonable electron spin susceptibility, making it necessary to have a finite carrier concentration for effective coupling between magnetic local moments. However, a notable exception arises in the context of TIs such as Bi_2Te_3

and Bi_2Se_3, where the presence of spin-orbit coupling (SOC) significantly enhances electron spin susceptibility through the Van Vleck mechanism. In these materials, SOC induces a strong coupling between the electron spin and its orbital motion, leading to an increased magnetic response. Furthermore, the electronic band structure of Bi_2Se_3 exhibits band inversion, a signature of TI, which further amplifies the Van Vleck susceptibility. It has been proposed that doping with 3d transition metals, including chromium, iron, vanadium, and titanium, could lead to a ferromagnetic insulating or metallic state. This is because these metals typically replace the Bi^{3+} ion in the lattice structure, and each of these transition metals maintains a stable 3+ oxidation state, thereby not introducing additional free carriers into the system. In order to have the ferromagnetic order and sizable T_C, it is essential to have the electron susceptibility larger than the susceptibility of the local moment. It was predicted that the presence of these magnetic dopants would encourage out-of-plane anisotropy in these ferromagnetic insulators [31].

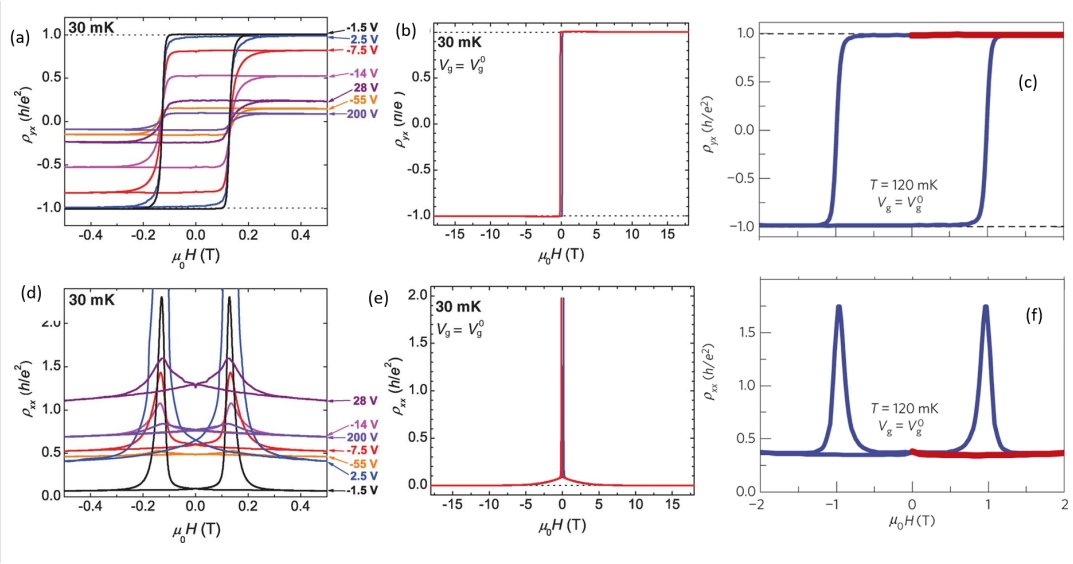

Figure 1.5: QAHE observed in Cr: BST and V: BST (a) Quantized transverse resistivity observed at different gate voltage and (b) Zero voltage at 30 mK for Cr: BST (c) at 120 mK for V: BST (d) corresponding zero longitudinal resistivity observed at different gate voltage and (e) Zero voltage at 30 mK for Cr: BST (f) at 120 mK for V: BST; taken from Ref. [42, 43].

In 2013, the prediction was then finally experimentally realized on $Cr_{0.15}(Bi_{0.1}Sb_{0.9})_{1.85}Te_3$ (Cr:BST) MBE-grown thin films on dielectric STO substrates with 5 quintuple layer thickness (QL) [42]. They observed an unprecedented transition temperature of 15 K, along with a square-shaped hysteresis curve exhibiting a coercivity of 97 Oe at 1.5 K. This pattern indicates ferromagnetic order with out-of-plane anisotropy and a distinctive AHE signature. Subsequently, they conducted measurements of both transverse and longitudinal resistivity at the lowest temperature of 30 mK, sweeping external magnetic fields, and varying gate voltage. The robust hysteresis shape persisted, attributed to Van Vleck-mediated ferromagnetism, and the quantized resistivity reached its peak at -1.5 eV, as illustrated in Figure 1.5 (a,b).

Furthermore, at zero fields, the transverse resistivity peaked at -1.5 eV, while the longitudinal resistivity approached almost zero (0.098 h/e^2) as shown in Fig. 1.5 (d,e),

marking the successful realization of the QAHE in this system. Additional confirmation was obtained by measuring both resistivities up to 15 T without applying any gate voltage, revealing that the longitudinal resistivity became perfectly zero beyond 10 T. Simultaneously, the transverse resistivity remained quantized, indicating the existence of a pristine quantum Hall state without any quantum phase transition. This groundbreaking work represents the first experimental validation of existing theories, paving the way for dissipation-less edge states in topological electronics with low power consumption.

Following the achievement of the quantum anomalous Hall state in Cr: BST, within the subsequent two years, another thin film composed of $(Bi_{0.29}Sb_{0.71})_{1.89}V_{0.11}Te_3$ (V: BST) with a thickness of 4 QL was documented to exhibit nearly perfect quantized transverse resistivity ($1.00019 \pm 0.00069 h/e^2$) and longitudinal resistivity ($0.00013 \pm 0.00007 h/e^2$) at 25 mK [43]. The observation of the QAH state was also noted at a relatively elevated temperature of 120 mK (see fig 1.5 c,f), accompanied by a nearly one order of magnitude higher coercivity (H_c) at 1.3 T. The primary distinction arose from the substitution of V, which possesses a smaller magnetic moment of $1.5\mu_B$ compared to Cr ($3\mu_B$). The V ion exhibits a mixed valency state of 3+ and 4+, replacing the Sb atom, and the additional electron from V^{4+} neutralizes p-type carriers, thereby reducing the electron density at the Fermi energy. Additionally, V has a lower magnetic moment, leading to larger (and fewer) domains than Cr, resulting in a higher H_c [43]. Several analogous compounds have also been reported, such as a single crystal of $Cr_{0.08}(Bi_{0.1}Sb_{0.9})_{1.92}Te_3$ demonstrating a gap opening (ranging from 9 mV to 48 mV) at the surface state, measured through surface-sensitive spectroscopic imaging STM (SI-STM) technique [44]. Furthermore, in Se-rich bulk crystal $(Bi_{0.84}Fe_{0.16})_2Se_{3.7}$, through ARPES [45], an exchange gap of 50 mV was identified in the crystal precisely at the Dirac point.

While advancements in achieving the quantum Hall state and a substantial exchange gap at the Dirac point in crystal and thin-film structures doped with magnetic impurities are noteworthy, there were some constraints. The uneven distribution of these doped impurities leads to a non-uniform band gap across the entire surface of the topological insulator (TI). Additionally, variations in the local density of these dopants result in differences in magnetic order. The crystals doped with manganese are insufficient for establishing the Dirac point at the exchange gap due to the narrow gap opening. Moreover, the observation of these quantum Hall states is confined to very low temperatures, limiting their potential for future applications.

Intrinsic Magnetic Topological Insulator:
To overcome these limitations, there was a need to identify a material possessing intrinsic magnetism and SOC, preferably ferromagnetic, exhibiting out-of-plane anisotropy, and high Curie temperatures to open the exchange gap. In this light, it was predicted in 2017 that antiferromagnetic topological insulators with broken $\mathcal{T}$ and primitive lattice translational symmetry ($\mathcal{S}$) with preserved C $=\mathcal{T}\,\mathcal{S}$ could be promising to achieve this goal [46]. This was similar to the previous $\mathcal{T}$ symmetry-broken strong topological insulator and could open an exchange gap at the Dirac points and could have Kramers degeneracy. It was predicted to have quantized magnetoelectric coupling, and it had the potential to realize the QAH state as well. Due to its layered behavior, the magnetic and electronic properties could be easily tuned without any doping or substitutions. Hence, it was promising for large exchange gaps and homogeneous surface magnetic ordering.

Realizing this in a real single crystal took another decade, and in 2019, it was first reported in a layer 2D van der Waals material candidate. $MnBi_2Te_4$ was proposed to be the first antiferromagnetic topological insulator in early 2017 by Otrokov et al. [47] and first experimentally realized by them in 2019 [48]. The main focus of my thesis would be focused to only this kind of magnetic TIs.

1.2.2 Real space topology: Skyrmions and Solitons

After exploring the topology associated with momentum space, denoted as **k** space, in the previous discussions, this thesis also addresses various magnetic systems that harbor real-space topological defects, such as chiral solitons. These defects cannot be eliminated through gradual deformations. In the realm of magnetism, two magnetic configurations are considered topologically inequivalent or non-trivial if they cannot be continuously transformed into one another without encountering an infinite energy barrier. There are two potential types of topological defects: (i) *singular topological defects*, including Ising-type domain walls, vortices, and hedgehogs where magnetization disappears at a point or along a line; and (ii) *smooth topological textures*, such as skyrmions and chiral solitons, where magnetization is smooth and continuous at all points [49], which is the focal point of our investigation.

These topological characteristics are contingent on two factors: the system's dimensionality (D) and the spin dimensionality (d). Solitons (d = 3, D = 1), where the magnetic moments are arranged in a line and can point in any direction, are nothing but the reduced-dimensional analog of the skyrmions (d = 3, D = 2), where the magnetic moments are in a plane. Compared to the skyrmions, solitons have similar and also distinct properties, like the ability to form lattices in bulk materials with periodicity depending on the external field[50, 51].

Solitons are the solutions of the sine-Gordon equation, defining the namesake simple model, initially studied surfaces of constant negative curvature in geometry, given as [52, 53]

$$\partial^2\varphi + \sin^2\varphi = 0 \tag{1.6}$$

where $\partial^{\equiv}\partial^{\mu}\partial_{\mu}$ denotes the d'Alembert operator and φ is the scalar field variable. They are characterized by how many times they wrap around the easy-plane circle as one proceeds along the sample. The number of times the field that wraps around the unit circle is known as the winding number

$$w_S = \frac{1}{2\pi}\int dx\partial_x\phi \tag{1.7}$$

For an easy-plan soliton, wrapping around exactly once corresponds to one soliton ($w_S = \pm 1$). Analogous to that, the skyrmions (D = 2, d = 3) of the isotropic spins on a 2D plane are topologically nontrivial. If the spin structure rotates tangentially, it forms a Bloch skyrmion. This could again be understood from the hedgehog (D = 3, d = 3) but with a finite size. They cannot be continuously transformed into a ferromagnetic state. The winding number could be written as

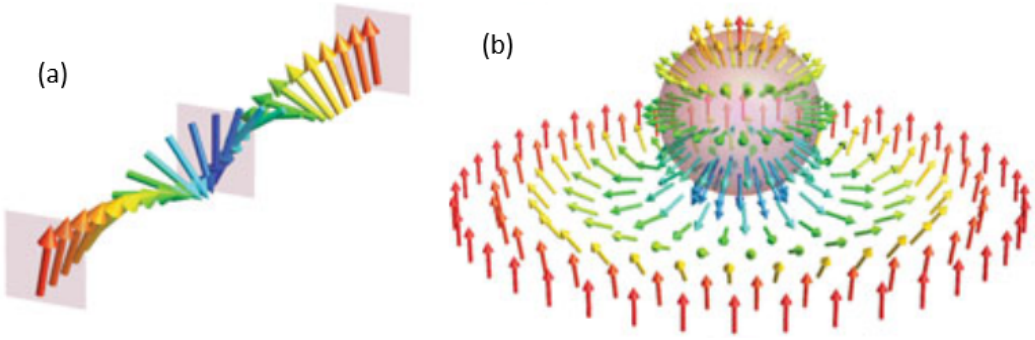

Figure 1.6: Soliton and stereographic projection of Skyrmion; taken from Ref. [49].

$$w_{Sky} = \frac{1}{4\pi}\int_0^{2\pi} d\Phi \partial_\Phi \phi [m_z(0) - m_z(\infty)] \tag{1.8}$$

where $\Phi = \phi \pm \zeta$, $\zeta = \frac{\pi}{2}$ for Bloch type skyrmions, and $\zeta = 0, \pi$ for Neel skyrmion, confining our focus to solitons [2]. and further discussing the energy that is required to stabilize this state and the candidate hosting solitons in chapter 6. Unlike skyrmions, solitons are infrequently observed in actual materials because they necessitate a magnetic moment that exists only in 1D spin chains. $Cr_{1/3}NbS_2$ stands out as one of the extensively studied compounds hosting this soliton lattice.

This summarizes the theory of two important pillars in my thesis work: topology and magnetism. Then let's move on to the materials, specifically 2D and quasi-2D materials, that host both long-range magnetic order and topological non-triviality. One would briefly discuss 2D magnetic materials, specifically van der Waals materials, and their magnetism.

1.3 Two dimensional (2D) van der Waals magnets

Two-dimensional (2D) materials, typically a few atomic layers thick, are weakly coupled by van der Waals forces between the layers, often exhibit different properties than their 3D counterparts, and offer the most flexibility in tuning their magnetic, electronic, and optical properties. The weak interlayer interaction makes it easier to exfoliate thin flakes and deposit them into various substrates, which makes them excellent for device applications. For the first time, reported by K. S. Nonvoselv et al. in 2005 [54], Four different 2D materials (hexagonal boron nitride hBN, molybdenum disulfide MoS_2, graphene, and dichalcogenides NbS_2) ranging from single monolayer to a few atomic layers of different electronic properties (insulating, semiconductor, metallic, and semimetallic) were obtained by just cleaving the strongly layered 3D materials. This paved the way for new-generation technological applications, including electronics, optoelectronics, energy conversion, and data storage. Further going ahead, apart from just exfoliation, several different methods were used to prepare or grow these 2D materials [55]. This thesis will deal with mostly magnetic 2D van der Waals materials,

[2] Soliton is often used to refer to all the topological objects; referring to only the topological texture with D=1,d=3

hence it is important to describe the magnetism in 2D materials. However, basic concepts such as exchange interaction and magnetic orders will be briefly discussed first. This particular section is taken from Ref. [56], hence recommended for more details.

1.3.1 Exchange interaction and magnetic order

The macroscopic magnetic properties of a material are primarily influenced by the interactions between its magnetic moments. Magnetism is inherently a quantum phenomenon, emerging from the combination of electrostatic Coulomb interactions, electron spin, and the Pauli exclusion principle for fermions. Central to the phenomenon of long-range magnetic order are exchange interactions, which are essentially electrostatic interactions. These arise because similar charges cost energy when close together and save energy when they are farther apart.

Considering a simple model with just two electrons, the spin-dependent term in the effective Hamiltonian can be written as [56]

$$\mathcal{H}^{spin} = -2JS_1 \cdot S_2 \tag{1.9}$$

where J is the exchange constant. By further applying this to all the neighboring atoms, the Hamiltonian of the Heisenberg model could be written as

$$\hat{\mathcal{H}} = -\sum_{ij} J_{ij} S_i \cdot S_j \tag{1.10}$$

where J_{ij} is the exchange constant between i^{th} and j^{th} spins. The factor of 2 is omitted because the summation includes each pair of spins twice. This measures the energetic difference between different spin configurations. Whereas for $J_{ij} > 0$, a parallel spin arrangement is preferred, $J_{ij} < 0$ favors an antiparallel arrangement of S_i and S_j.

Direct exchange: Electrons on adjacent magnetic atoms interact through an exchange interaction called direct exchange. While this appears to be the simplest mechanism for exchange interaction, real physical scenarios are often more complex. The Heisenberg model describes a direct exchange between two neighboring atoms with overlapping electronic densities. However, direct exchange often does not play a significant role in determining magnetic properties due to insufficient direct overlap between neighboring magnetic orbitals. Consequently, many magnetic materials require consideration of indirect exchange interactions. *Superexchange*: Superexchange is defined as an indirect exchange interaction between non-adjacent magnetic ions, mediated by a non-magnetic ion positioned between the magnetic ions. [56].

Types of magnetic order

The different ground states include *ferromagnets*, where all magnetic moments align parallel; *antiferromagnets*, where adjacent magnetic moments align antiparallel; spiral and *helical* structures, where the magnetic moment direction rotates around a cone or circle from one site to the next; and *spin glasses*, where magnetic moments are fixed in random arrangements. These types of magnetic ground states will be the primary focus

of this thesis. A ferromagnet exhibits spontaneous magnetization even without an external magnetic field, with all magnetic moments aligned in a single direction. This phenomenon is typically driven by exchange interactions, as previously described. When a ferromagnet is subjected to an external magnetic field B, the relevant Hamiltonian to consider is [56]

$$\hat{\mathcal{H}} = -\sum_{ij} J_{ij} S_i \cdot S_j + g\mu_B \sum_j S_j \cdot B \tag{1.11}$$

In this scenario, the exchange constants for nearest neighbors are positive to ensure ferromagnetic alignment. Conversely, if the exchange interaction is negative (J<0), the molecular field favors nearest neighbor magnetic moments aligning antiparallel to each other, resulting in antiferromagnetism. In some cases, the magnetization of the two sublattices may not be equal and antiparallel, leading to a net magnetization in the material, known as *ferrimagnetism*.

All materials exhibit some level of diamagnetism, characterized by a weak, negative magnetic susceptibility. In diamagnetic substances, an applied magnetic field induces a magnetic moment that opposes the field that generated it. Paramagnetism corresponds to a positive susceptibility so that an applied magnetic field induces a magnetization that aligns parallel with the applied magnetic field that caused it. In addition to conventional systems, there are inherently random systems that exhibit behavior similar to a phase transition at a specific temperature. This transition leads to a state that, while not ordered, is markedly different from the disordered state at high temperatures. A spin glass can be defined as a random magnetic system with mixed interactions, characterized by random but cooperative freezing of spins at a specific temperature, T_f (the freezing temperature).

The glassy behavior arises from the competing interactions between individual magnetic moments, resulting in a highly degenerate ground state. Slow relaxation occurs as these magnetic moments begin to reorient, causing additional frustrations and prompting further reorientation of other moments. This process is highly complex because each magnetic moment exists in a unique environment and may experience different types of frustration due to the random distribution of sites and exchanges. As the system cools and approaches the freezing temperature T_f from higher temperatures, some magnetic moments start to form clusters rather than acting independently. These clusters vary in size, leading to a broad range of relaxation times [57].

1.3.2 Magnetism in two-dimensional materials

Two-dimensional (2D) magnetism involves the study of magnetic moment configurations and their collective magnetic excitations in materials and structures that are atomically thin. This phenomenon results from magnetic interactions and spin fluctuations confined to the 2D limit. In this subsection, the early theoretical research on 2D magnetism focuses on studies that use the spin Hamiltonian will be reviewed. To keep things simple, the discussion is limited to spin Hamiltonians that include only nearest-neighbor interactions [58]

$$\hat{\mathcal{H}} = -\sum_{i<j} J(\hat{S}_i^x \hat{S}_j^x + \hat{S}_i^y \hat{S}_j^y + \alpha \hat{S}_i^z \hat{S}_j^z) \tag{1.12}$$

where J is the exchange coupling, $S_{i,j}^{\hat{x},\hat{y},z}$ are the x-, y-, and z- components of the spin operators at the i and j sites; and α is the dimensionless parameter to tune the magnetic exchange anisotropy between the in-plane xy-component and the out-of-plane z-component. If it is 1, (α = 1), then spin Hamiltonian is isotropic, α > 1 easy axis, α < 1: easy plane. Considering the extreme conditions, $\alpha \gg 1$ for the easy axis can be considered as the Ising type spin Hamiltonian with spin dimension $d = 1$, which could be written as

$$\mathcal{H}_{\text{Ising}} = -\sum_{i<j} J_z \hat{S}_i^z \hat{S}_j^z. \tag{1.13}$$

In this case, the spin at each site is restricted to only two spin states, up or down along the z-axis (shown in Fig. 1.7 a). $\alpha \approx 0$ for the easy plane as the case of xy type with $d = 2$, shown in Fig. 1.7 b, written as the Hamiltonian

$$\mathcal{H}_{\text{XY}} = -\sum_{i<j} J_{x-y} \hat{S}_i^x \hat{S}_j^x + \hat{S}_i^y \hat{S}_j^y. \tag{1.14}$$

Here, the spin can only point to any direction within the xy- plane. As the thermal and quantum fluctuations are stronger in 2D, it is easy to rotate the spin alignment with the xy- plane at zero temperature, hence unfavorable for long-range order formation.

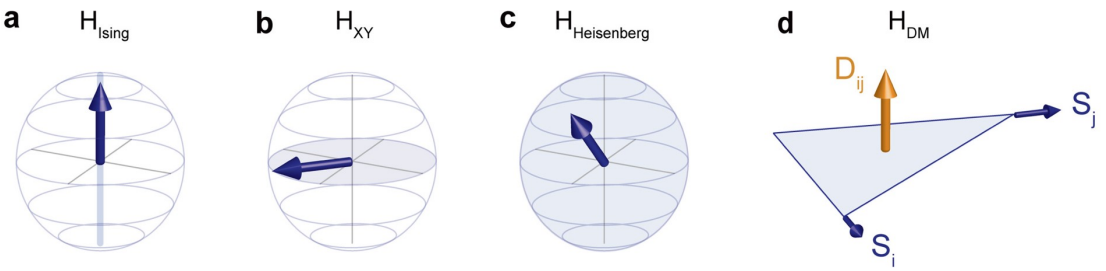

Figure 1.7: Sketch to highlight four types of spin interactions. (a) Ising-type; (b) XY-type; (c) isotropic Heisenberg-type; shaded areas correspond to the preferred spin orientations; (d) DM interaction; taken from Ref. [58].

However, the 2D systems studied in the thesis are mostly based on the $d = 3$ spin dimension, which is understood by the 2D isotropic Heisenberg model where all the three spin components are involved and one can write the Heisenberg Hamiltonian as

$$\hat{\mathcal{H}}_{\text{Heisenberg}} = -\sum_{i<j} J(\hat{S}_i^x \hat{S}_j^x + \hat{S}_i^y \hat{S}_j^y + \hat{S}_i^z \hat{S}_j^z) \tag{1.15}$$

In this case, the spin at each site can take any orientation within the 3D space without costing any extra energy.

The Mermin-Wagner theorem demonstrates the absence of magnetism in $D \leq 2$ isotropic Heisenberg systems with finite-range exchange interaction at temperatures above zero. According to the theorem, thermal fluctuations are gapless long-wavelength

spin excitations and disrupt long-range order, hindering spontaneous symmetry breaking [3][59]. In contrast, in the case of 3D samples the phase transition from an ordered state to a disordered state where the effect of thermal fluctuation dominates, occurs at a finite temperature. Going back to lower than 3 spatial dimensions, Heisenberg systems cannot order, unless, both in 1D [60], and 2D systems, the spherical invariance of the Hamiltonian is removed, which brings to the Ising model of eq. 1.13 as the opposite limit to the Heisenberg model. In real-world bulk 2D systems spontaneous magnetization is achieved either because their 2D character implies neglecting tiny 3D interactions that eventually come into play at low temperatures or by considering the effect small anisotropic interactions, again negligible at higher temperatures [61]. The stability of the spin is more strongly reduced by spin fluctuations as the spatial dimension is lowered from 3D to 2D materials. However, magnetic anisotropy, which depends on SOC and dipole-dipole interactions, eventually contributes to magnetocrystalline anisotropy. Shape anisotropy is also an important factor for magnetism in 2D materials, favoring in plane spin orientation. But exchange interactions are not limited to the isotropic Heisenberg and Ising terms, that can be summed up in the symmetric terms of a tensor. Spin-orbit coupling introduces also antisymmetric terms, also important in quantum magnetism.

The Dzyaloshinskii-Moriya interaction The antisymmetric exchange coupling between two neighboring spins is described by the DM interaction and the Hamiltonian can be written as

$$\mathcal{H}_{\mathrm{DM}} = -\mathbf{D} \cdot \mathbf{S_i} \times \mathbf{S_j} \tag{1.16}$$

where $\mathbf{D}$ is the Dzyaloshinskii vector pointing along a high-symmetry direction of the magnetic crystals; shown in Fig. 1.7 d. In systems where the Dzyaloshinskii-Moriya (DM) interaction significantly contributes to the total spin Hamiltonian, the spin alignments are not collinear, like in simple ferromagnets and antiferromagnets. More details will be discussed in the last chapter.

The breakthrough happened after magnetization confirmation of CrI_3 [62] and $Cr_2Ge_2Te_6$ [63] down to monolayer and bilayer, which were ferromagnetic insulators with transition temperatures of 45K and 28K, respectively. Following this, Fe_3GeTe_2 was also reported to be a conductor, and its T_C could be tuned to room temperature by ionic gating [64]. Then observation of antiferromagnetism in 2D materials was in $FePS_3$ [65, 66] and $NiPS_3$ [67]in 2016, where magnetic order was preserved even after exfoliation into monolayer or a few layers. A few other candidates were also reported $CrBr_3$ [68], CrSBr[69], MSe_2, M=Mn,V [70, 71], MnSn[72], $FeTe_2$ [73] to have long-range order.

[3]Spontaneous symmetry breaking refers to the phase transition of an invariant Hamiltonian, whereby the ground state is degenerate and the order parameter vanishes above the transition, but below it is different from zero, selecting one ground state; for instance, eq.1.15 is spherically symmetric, as well as its paramagnetic ground state above the Curie temperature, but the ferromagnetic ground state below must be aligned in a chosen direction, despite the invariant Hamiltonian, thus breaking its symmetry.

Chapter 2

Experimental techniques

Experiments serve as a foundation for evidence-based decision-making, theory development, and the advancement of knowledge across various fields including science and research. Various techniques are used for different purposes, and the appropriate technique depends on the specific material under investigation and the energy and time scale involved. This chapter presents an overview of the techniques adopted (the focus has been given on the study of bulk magnetic properties using macroscopic and microscopic techniques) and their relevance to the systems investigated. Fig. 2.1 shows the schematic diagram comparing the frequency winodows that can be explored by local microscopic techniques like Nuclear Magnetic Resonance (NMR), Muon Spin Spectroscopy (μSR), and macroscopic technique, such as Superconducting Quantum Interference Device (SQUID) magnetometer.

To observe the macroscopic magnetic properties like magnetic ordering and transition temperatures of topological and other quantum magnetic materials investigated in this thesis work, SQUID-VSM has been used at the same time NMR and μSR have been used to understand the local microscopic magnetism and gain more insight into intermixing and local spin textures.

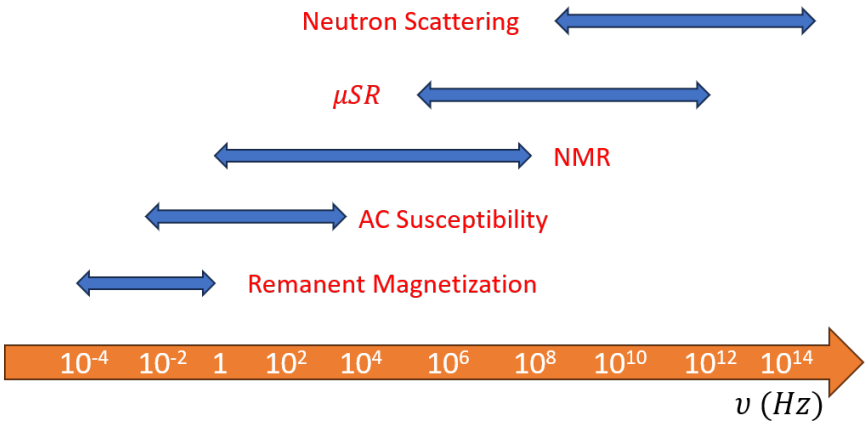

Figure 2.1: Approximate frequency range available for different techniques; taken from Ref. [57]

2.1 SQUID- magnetometry

As explained in the above paragraph, this thesis work focuses on investigating the bulk and local magnetic properties of various topological magnetic materials. To delve into

the bulk magnetism aspect, precise measurements were conducted using an experimental technique known as the superconducting quantum interference device (SQUID) magnetometer. This advanced device boasts exceptional sensitivity and is capable of detecting magnetic signals as low as 10^{-8} emu.

The experimentation includes a range of measurements, such as DC susceptibility, AC susceptibility, relaxation, and memory effects, all carried out utilizing the commercially available SQUID system from Quantum Design (SQUID-VSM, MPMS 3). Additionally, pressure-dependent magnetization data was gathered using an MPMS XL, with a custom pressure cell setup designed for this purpose, the intricate details of which will be presented later in the discussion.

For temperature-dependent investigations, all SQUID devices were equipped with He^4 flow cryostats, enabling precise temperature control spanning from 1.8 K to 400 K. Moreover, the experiments allowed for applying external magnetic fields (ranging $\pm$ 7 T) and frequencies (from 0.1 Hz to 1000 Hz).

In the following sections, the concept of SQUID fundamentals and working principles will be introduced, which will give us a base for understanding the bulk magnetization results and how they are obtained. The theory and concepts presented in this section are mainly based on Refs. [74, 75].

2.1.1 SQUID fundamentals

The SQUID magnetometer serves as a transducer, converting changes in magnetic flux into voltage output. Its operation relies on the superconducting quantum interference phenomenon occurring within a SQUID sensor containing two parallel-connected Josephson junctions (see Fig. 2.2). In this setup, the presence of magnetic flux in the junction area modulates the phase of the superconducting order parameter. This modulation leads to a 2π change in phase whenever the magnetic flux undergoes a variation equivalent to the flux quantum

$$\phi_0 = \frac{h}{2e} = 2.07 \times 10^{-15} Tm^2. \tag{2.1}$$

This SQUID sensor is then inductively coupled to a second derivative gradiometer, which is a closed circuit of four identical, oppositely wound (to cancel out the external signal that does not come from the sample), superconducting coaxial coils, and is generally located in a complete superconducting shield to prevent magnetic flux from the magnet or environment from creating noise. The sample is then moved through the gradiometer to induce a current in the coils through the stray field produced by its magnetization (M) in response to the external magnetic field H_{ext}. Assuming the sample dimensions are much smaller than the dimensions of the detection coils, the current induced in the detection coils is a function of the sample position. The approximate shape of this function is shown in Fig. 2.2. The current in the detection coils is inductively coupled to the SQUID sensor, which serves as an extremely sensitive current-to-voltage converter.

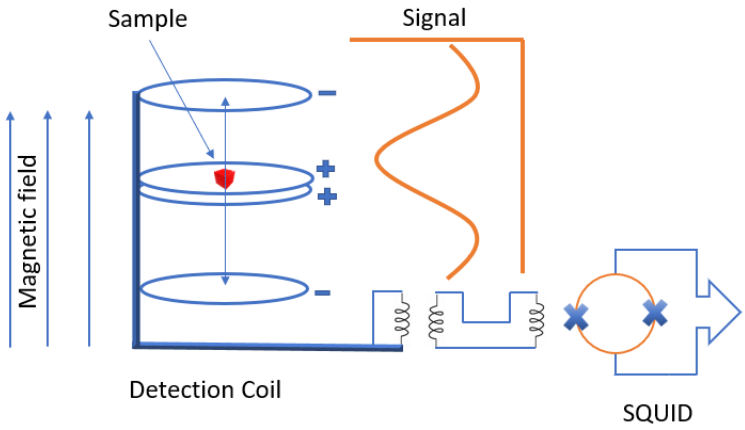

Figure 2.2: Schematic diagram of SQUID detection

While measuring in the DC mode, the sample is moved through the pickup coils in the region of maximum field homogeneity to produce a voltage signal as a function of position (z). The signal is then fitted through control software to an expected shape function, whose amplitude is proportional to the magnetic moment of the sample. The fitting function is used generally assuming the sample is a point-like magnetic field source. The measurements conducted in this thesis work primarily utilize vibrating sample magnetometry mode (VSM), offering superior resolution compared to DC mode. In this mode, the sample oscillates within a narrow range around the center of the detection coils. Consequently, the dipolar signal generated is modulated by a sinusoidal signal of constant frequency. This modulated signal is subsequently demodulated using a lock-in amplifier, effectively eliminating low-frequency noise through a low-pass filter. As a result, the magnetic moment of the sample is accurately retrieved with enhanced resolution.

Accurate calibration of the instrument using a standard reference material, such as palladium in our case, is crucial to obtain reliable magnetization values. Additionally, geometric effects resulting from differences in the sample's lateral dimensions compared to the calibration standards must be considered. These differences can lead to either underestimation or overestimation of the absolute moment. In this study, the samples were affixed to a quartz rod (acting as a sample holder) using GE-Varnish. The use of a long, pure quartz rod ensures that no additional magnetic contribution is introduced to the sample signal. However, the small, mostly diamagnetic signal (around 10^{-7} emu) from the glue was separately measured concerning temperature and field variations. This signal was subtracted from the magnetization curves when necessary, specifically when the sample signal was comparable to the background and couldn't be ignored.

2.1.2 DC and AC magnetic susceptibility

In the SQUID magnetometer, the measurement of DC magnetic susceptibility is possible under the condition that the sample properties remain unchanged without any detectable dynamic response. This condition can be reframed as either the dynamics being significantly faster or slower than the experimental timescale.

In general, the magnetic susceptibility can be defined by the equation [57]

$$\chi = \frac{\delta M}{\delta H} \tag{2.2}$$

where M is the sample magnetization and H is the applied magnetic field. In the common cases when $\chi \ll 1$

$$B = \mu_0(H + M) \simeq \mu_0 H, \tag{2.3}$$

for real experiments, one can define susceptibility as

$$\chi_{exp} = \frac{\delta M}{\delta H} \simeq \mu_0 \frac{\delta M}{\delta B} \tag{2.4}$$

where δB is the finite applied field.

In DC susceptibility measurements, the small magnetic field variation δB typically falls within the range of a few Oersteds to a few thousand Oersteds. χ_{dc} is commonly studied across various temperature cycles. The process involves cooling the system without any magnetic field, known as the Zero Field Cool (ZFC) procedure, to record the magnetic moment. Subsequently, during a warming cycle, the magnetic moment is recorded with the applied magnetic field, Field Cooled Warming (FCW). Lastly, the system is cooled again with the applied field to record the magnetization, a method referred to as field-cooled cooling (FCC). More information could be extracted from the DC susceptibility in the paramagnetic region at a relatively high temperature using the *Curie-Weiss law*, [76]

$$\chi = \frac{C}{T - \theta_{CW}} \tag{2.5}$$

where C is the Curie constant and θ_{CW} is referred as the Curie Weiss temperature. the alignment of the moments in a paramagnet at an external field is explained by this equation as the susceptibility increases by lowering the temperature, shown in Fig. 2.3 a

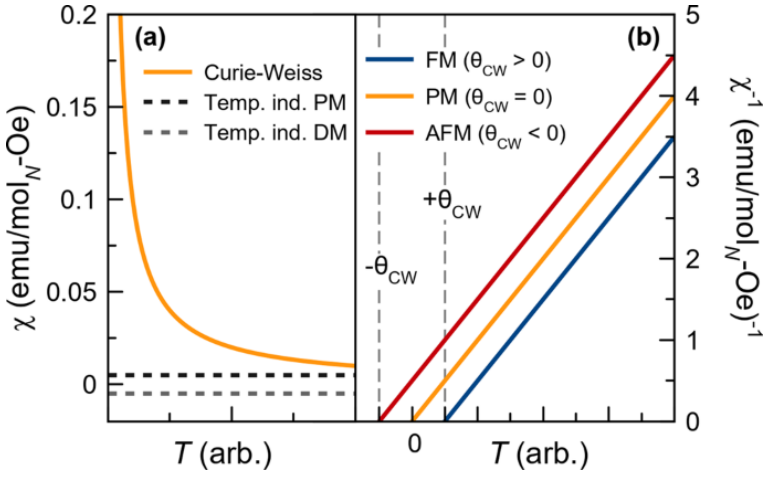

Figure 2.3: (a) Curie–Weiss susceptibility due to paramagnetic local moments go as 1/T. (b) The inverse susceptibility of a material that follows the Curie–Weiss law; taken from Ref. [76].

The C is directly related to the number of unpaired electrons and, can be used to calculate the effective magnetic moment per ion in units of Bohr magnetons,μ_B

$$\mu_{eff} = \sqrt{8C}\mu_B \tag{2.6}$$

the effective moment then, can be compared to the calculated value for the ion, given by

$$\mu_{cal} = g\sqrt{\mathrm{J(J+1)}}\mu_B \tag{2.7}$$

where Jj is the the total angular momentum.

Then the Curie temperature θ_{CW} is an indicator of the strength of the magnetic correlations between ions as its strength depends on the molecular field. For FM interactions, the molecular field aligns with the external field hence giving rise to positive θ_{CW} and close to the transition temperature ($\theta_{CW} \approx T_C$), whereas negative values of θ_{CW} imply antiferromagnetic interactions with larger deviation from the T_N (shown in Fig. 2.3 b).

In AC magnetic susceptibility measurements, a small-amplitude sinusoidal magnetic field (H_{AC}) that varies over time is introduced alongside the static magnetic field (H_{DC}), usually ranging from 0 to 10 Oersted and applied parallel to the H_{AC}. The static magnetic field is deliberately kept low to exclusively capture the immediate induced response caused by H_{AC}. This approach is especially valuable for investigating the fundamental state of the spin system. Hence the effective applied field becomes [57]

$$H = H_{DC} + H_{AC}\cos\omega t \tag{2.8}$$

where ω is the frequency of the oscillating field.

The oscillating response of the magnetization (M_{AC}) is recorded and the AC susceptibility is defined as

$$\chi_{AC} = \frac{M_{AC}}{H_{AC}} \tag{2.9}$$

The graphical representation of the DC and AC susceptibility is presented in Fig. 2.4.

The relaxation time (τ) is a measure of how quickly or slowly the magnetic moments can align with the external magnetic field. So depending upon the relaxation time of the magnetic moment of the material, three regions could be identified: $\omega << \frac{1}{\tau}$, $\omega >> \frac{1}{\tau}$, and $\omega \approx \frac{1}{\tau}$. The initial two regions correspond to isothermal susceptibility χ_T and adiabatic susceptibility χ_S. In $\omega << \frac{1}{\tau}$, the system responds immediately to the external perturbation. The moments easily exchange their energy with the lattice, obtaining an equilibrium position. Following, the second regime ($\omega >> \frac{1}{\tau}$), the moments cannot not respond to the external perturbation as the AC and DC field oscillates too quickly. Finally, in the third regime, $\omega \approx \frac{1}{\tau}$, the time scale of both the oscillating frequency and relaxation time are comparable and the response is usually complex.

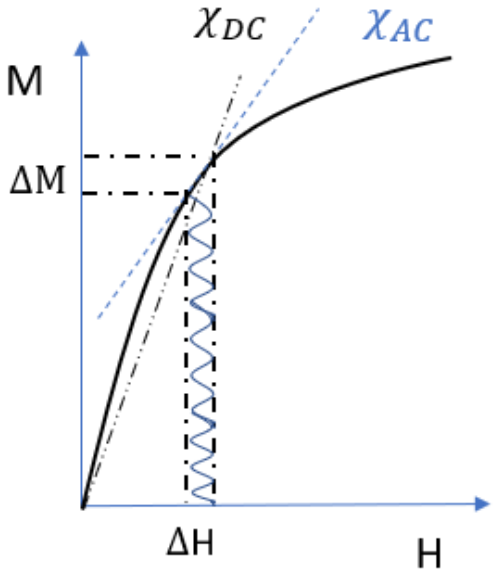

Figure 2.4: Graphical representation of the DC and AC susceptibility; taken from Ref. [57].

There is a finite chance of phase lag between the ω and τ in this regime so the response is usually reported in two parts: real and imaginary part. Hence the AC susceptibility could be represented as

$$\chi_{AC} = \chi' + i\chi'' \tag{2.10}$$

where χ' is the real part and represents the reversible magnetization process. and χ'' is the imaginary part representing the losses due to the irreversible magnetization process. Various theoretical models have been used to explain the Ac susceptibility, some of them are summarized below. For simplicity reasons, complex mathematical calculations will be avoided, focusing on the physical interpretation of the equation. Further reading is recommended from [57, 77]. This measurement could be useful for various experimental systems, however, used for mostly explaining spin glass. AC susceptibility measurements of spin glasses identified a distinctive cusp in the in-phase component, χ' at T_f, and associated imaginary part χ'' becomes non-zero as a result of the dissipation/loss of energy. Further details will be discussed in Chapter 4.

2.1.3 Non equilibrium phenomena

Apart from the susceptibility measurements one could also perform different experiments in a SQUID magnetometer such as Magnetic relaxation measurement and Memory effect measurement to slow relaxation. These particular experiments were chosen for this thesis work. Here the theoretical background behind these experiments will be explained.

Magnetic relaxation

Magnetic relaxation is a complex but well-known method for studying the slow spin dynamics in magnetic systems. Hence many models have been proposed to describe the phenomenon [78].

Logarithmic relaxation

Let us consider a single magnetic particle that has a fixed magnetic moment. and apply an external magnetic field opposite to the initial magnetization direction, the spins will turn towards the field to minimize the energy. Now, the time dependence of this magnetization could be described as

$$M(t) = M_0(2\exp(-t/\tau) - 1) \tag{2.11}$$

where τ is the time required for the magnetization reversal. This could be expressed as

$$\tau = \nu_0^{-1} \exp \Delta E/k_B T \tag{2.12}$$

Of course, this doesn't satisfy real systems with many interacting and non-interacting magnetic particles, so if one extends this for many non-interacting particles the Magnetization will become

$$M(t) \simeq M_0 - V(H,T)ln(t/t_0) \tag{2.13}$$

where V(H,T) magnetic viscosity coefficient. Unfortunately, this model is not realistic as it diverges at t-0 and t-∞ and the physical meaning of the parameters is not clear.

Kohlrausch–Williams–Watts relaxation [79]

For the systems with non-interacting particles and grains where the energy barrier is large, the previous equation holds. However, where the energy barrier is narrow, the time-dependent magnetization could be fitted to a general stretched exponential function

$$M = M_0(\exp(t/\tau)^{\beta} - 1), 0 < \beta < 1 \tag{2.14}$$

This equation holds for a wide variety of materials and explains slow relaxation in Spin glass and cluster spin glass phenomena. This is known as Kohlrausch–Williams –Watts (KWW) relaxation.

For experimentation purposes, the magnetic relaxation could be measured both with H_{DC} and H_{AC}. Cool down the system after applying any magnetic field, then suddenly remove the field and record magnetization M(t) over the time period. This is also called thermoremanent magnetization. Parameters like β and τ give the relaxation time (typically orders of a few seconds to a few Hours).

Memory and Chaos

Somewhat similar to the process of human Aging [80, 81], one could measure the aging behavior of the sample if they possess some spin glass behavior. It corresponds to the slow evolution of the system towards equilibrium, starting at the time of the quench below the spin glass transition T_f, and is fully reinitialized by heating the sample above the glass temperature. In the spin-glass phase, the system is out of equilibrium so the effect of small temperature cycles, especially at low temperatures or near T_f would be

considerable. Higher temperatures tend to stabilize the activation energy of the system and bring the system to equilibrium. Hence, one could observe a difference in the magnetization while scanning the temperature with and without a magnetic field. This memory and chaos effect (Fig :2.5) could be measured using the SQUID magnetometer. The following process has to be followed:

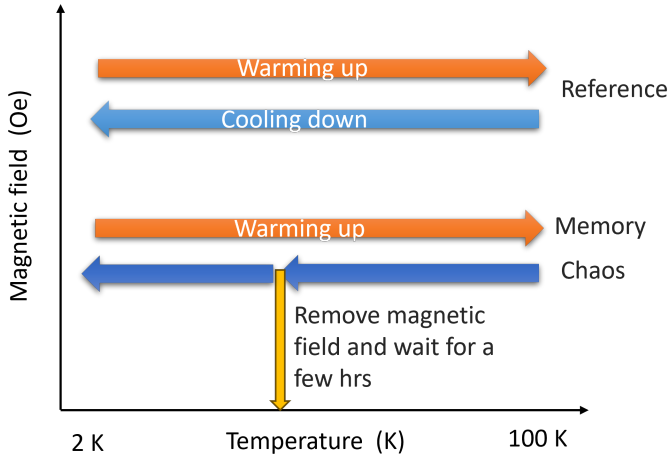

Figure 2.5: Schematic diagram explaining memory and chaos process

- Cooldown the system gradually above the transition temperature while applying a magnetic field until it reaches the base temperature. Then, warm it up steadily at the same rate, creating what is commonly known as the reference curve.
- Cool down the system once more, but this time pause at specific temperatures and remove the magnetic field. If there's any non-equilibrium behavior, the resulting curve may differ; this phenomenon is referred to as the chaos effect..
- Warm the system again without any pauses. The system is expected to memorize the previous halt period and follow the same trajectory, which is known as the memory effect.

The memory and chaos effects have been explained by organizing the metastable states hierarchically based on temperature [82, 83]. This framework allows for a quantitative characterization of the increase in free-energy barriers as the temperature decreases. This measurement is particularly interesting to study the spin glass-like behavior where a cluster of spins flips together. On a larger scale, aging refers to the system becoming less responsive over time. This means that its reaction to changes in a magnetic field becomes progressively slower as it gets older. A slower response indicates the presence of larger energy obstacles, and consequently, more spins need to flip simultaneously in the system.

2.1.4 Pressure dependent magnetization

Pressure-dependent magnetization was measured using a custom-built CuBe cell (shown in Fig. 2.6 a) that can be fitted in the sample chamber of the quantum design MPMS XL SQUID magnetometer. The technical details of the details of the cell is provided in

[84–87]. The bulk magnetization data under varying pressure conditions were obtained using a custom-built pressure cell compatible with a commercial SQUID magnetometer (MPMS-XL). Within the copper-beryllium (CuBe) cell, two opposing cone-shaped ceramic anvils compress a CuBe gasket featuring a cylindrical hole designed as a sample chamber glued using stycast [84, 86]. After drying for a day, a thin flake-like single-crystalline sample of $MnSb_2Te_4$, oriented with the c axis perpendicular to the gasket, was placed into the gasket hole (with a diameter ⌀ = 0.6 mm and a height h = 0.8 mm) and positioned on the flat surface of the ceramic anvil. Along with the sample, a piece of pb of similar size is also positioned in the same sample space to record its superconducting transition T_C which depends on the applied hydrostatic pressure via a linear equation.

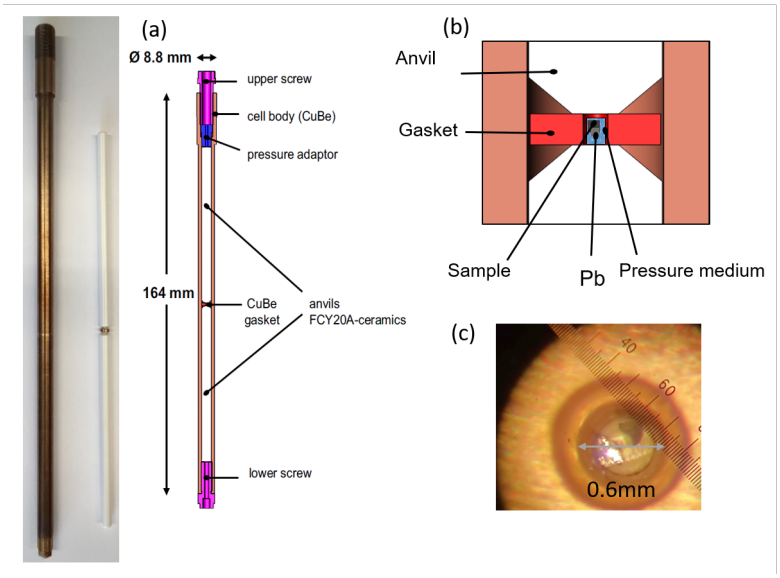

Figure 2.6: (a) Custom built pressure cell with its schematic diagram (b) schematic diagram of the sample space (c) Image of the gasket containing the sample and a Pb.

This way, the superconducting lead serves as a pressure monitor. The pressure value could be monitored by comparing the change in T_C. Daphne oil 7575 is used as the pressure-transmitting medium to transform a uniaxial force at room temperature and into hydrostatic pressure within the sample chamber. Additional comprehensive details regarding the technical details of the pressure cell can be accessed in Refs. [84, 85, 87].

2.2 Nuclear Magnetic Resonance

2.2.1 Introduction

Nuclear Magnetic Resonance (NMR) stands as a versatile and proficient technique, utilized not only in condensed matter physics but also in various scientific disciplines such as chemistry and biology. In modern times, its application has expanded to include medicine through Magnetic Resonance Imaging (MRI), a pivotal component of contemporary healthcare, offering a secure and detailed method to visualize internal

bodily structures and functions without invasive procedures. Our primary focus is on its utilization in fundamental condensed matter physics, particularly in the examination of the electronic spin ensemble. This entails investigating both its static properties, such as the expectation value of the local magnetic moment manifested in the resonance spectrum, and its dynamic facets, including spin fluctuations, discerned through the relaxation of nuclear magnetization. Resonance occurs through the synchronized precessions of the moment, stimulated by a fluctuating magnetic field whose frequency aligns with that of the spins. In the electromagnetic spectrum, the resonance frequencies for most nuclei with non-zero spin commonly fall within the radio-frequency (rf) range. In a standard NMR procedure, atomic nuclei within an external magnetic field (H_0) are stimulated by a resonant rf pulse, and the ensuing spin dynamic of atomic nuclei is captured, providing insights into the localized spin-charge environment surrounding the probed nuclear spin, as influenced by hyperfine and quadrupole couplings.

In the following sections, we'll briefly introduce the concept of magnetic resonance in the quantum mechanical and classical approaches and how it naturally leads to the concept of nuclear spin relaxation. We briefly describe the instrumentation. The NMR theory and concepts presented in this section are mainly based on [88–91].

2.2.2 The quantum mechanical description

The nucleus consists of one or more isotopes, each with a total magnetic moment μ_N, which is proportional to the total angular momentum I, could be written as

$$\boldsymbol{\mu}_n = \gamma \mathbf{I} \tag{2.15}$$

where γ is the nuclear gyromagnetic ratio [1]. Quantum mechanically, the vector quantities $\boldsymbol{\mu}_n$ and $\mathbf{I}$ can be expressed as dimensionless angular moment operator $\hat{\mathbf{I}}$ in the following manner:

$$\mathbf{I} = \hbar \hat{\mathbf{I}} \tag{2.16}$$

If one applies an external magnetic field $\mathbf{B} = B_0 \hat{z}$ along the z direction, the energy levels will be split by the Zeeman interaction, and the Hamiltonian will be given by [2]

$$H_Z = -\boldsymbol{\mu}_n \cdot \mathbf{B} = \gamma B_0 \hbar I_z \tag{2.17}$$

and now by solving this one can get the eigenvalues as

$$E_m = -\gamma \hbar B_0 m, \quad m = -1, ..., +1 \tag{2.18}$$

that can be experimentally observed by inducing transitions among the corresponding eigenstates. For magnetic resonance conditions, an alternating magnetic field is applied perpendicular to the static magnetic field, adding a time dependent perturbation term to the Hamiltonian

$$\mathrm{H_{rf}}(t) = \gamma B_{rf} \cos \omega t \, I_x \tag{2.19}$$

[1] It is given as $\gamma = g_n \mu_n / \hbar$ where μ_n is the nuclear magnetic moment and g_n is the Lande g-factor of the nucleus.

[2] We skip the hat on the dimensionless spin operators in the following.

where B_{rf} is the amplitude of the oscillating field and its frequency ω produces resonant effect when the photon energy $\hbar\omega$ exactly matches the energy difference between the nuclear levels

$$\omega = \gamma B_0 \stackrel{\text{def}}{=} \omega_0 \tag{2.20}$$

Here ω_0 is the frequency of the Larmor precession, explained in the next section through the classical description.

2.2.3 The classical description: Bloch equation

In NMR, the observable which is measured is nuclear magnetization and its evolution over time. In this section, we'll discuss this from the basics. From Newton's law, one can write the rate of change of the angular momentum as

$$\frac{\mathrm{d}}{\mathrm{d}t}\mathbf{L} = \mathbf{T} \tag{2.21}$$

where $\mathbf{T}$ is the torque. This classical equation of motion holds both for the angular momentum of an individual spin, for its magnetic moment

$$\boldsymbol{\mu} = \gamma\mathbf{I} \tag{2.22}$$

and for the bulk nuclear equilibrium magnetization that corresponds to the density of magnetic moments. Notice that this must be produced by a large magnetic field, either external or internal, thanks to the nuclear Curie susceptibility $\rho\mu_0\mu_n^2/3T$, where ρ is the density of nuclei and μ_0 the permeability of vacuum. Therefore, the NMR signal is proportional to magnetic field, density of nuclei and inversely proportional to temperature, T.

$$\mathbf{M} = \gamma\mathbf{L} \tag{2.23}$$

Hence, substituting in eq. 2.21

$$\frac{\mathrm{d}}{\mathrm{d}t}\mathbf{M} = \gamma\mathbf{T} \tag{2.24}$$

we can rewrite the total torque applied to the bulk magnetization by the static magnetic field as the cross product $\mathbf{T} = \mathbf{M} \times \mathbf{B}$. This describes the free precession of the magnetization $\mathbf{M}$ under the influence of a static magnetic field in the z-direction ($\mathbf{B} = B_0\hat{z}$)

$$\frac{\mathrm{d}}{\mathrm{d}t}\mathbf{M} = \omega_0\mathbf{M} \times \hat{z} \tag{2.25}$$

In Cartesian components

$$\begin{aligned}
\frac{\mathrm{d}}{\mathrm{d}t}M_x &= \omega_0 M_y \\
\frac{\mathrm{d}}{\mathrm{d}t}M_y &= -\omega_0 M_x \\
\frac{\mathrm{d}}{\mathrm{d}t}M_z &= 0
\end{aligned} \tag{2.26}$$

Solving these equations we get

$$\begin{aligned} M_x(t) &= M_x(0)\cos\omega_0 t + M_y(0)\sin\omega_0 t \\ M_y(t) &= -M_x(0)\sin\omega_0 t + M_y(0)\cos\omega_0 t \\ M_z(t) &= M_z(0) \end{aligned} \tag{2.27}$$

where $\omega_0 = \gamma B_0$ is the same Larmor frequency identified in the quantum mechanical description of Sec. 2.2.2. These equations describe the procession of the magnetization vector about the z-axis in the cone. It can be shown that this corresponds to the dynamics of the quantum observables.

The same motion can be described as a static spin in a frame rotating at the Larmor frequency. Its Newton equation then must contain an apparent torque $-\omega_0/\gamma \mathbf{M} \times \hat{z}$, i.e an apparent field $\mathbf{B}_a = -\omega_0/\gamma \hat{z}$ that cancels exactly $\mathbf{B}$, justifying the static state.

Now, if a rotating rf field (B_{rf}) is applied at the resonance condition of eq. 2.20, perpendicular to the static magnetic field (i.e. x-y plane), say in the x direction, in the rotating frame it will appear as static and the only net field.[3]. By the same eq. 2.24 this produces a precession of the nuclear magnetization around x in the rotating frame, which, coupled to the precession around the static field, results in a *nutation* in the laboratory frame. A pulse of appropriate duration flips the nuclear magnetization out of its equilibrium along the applied field (M_z) onto the y direction (M_y). After switching B_{rf} off, the nuclear magnetization will continue processing around the applied field according to eq. 2.27.

The coherent precession of $\mathbf{M}$ is detected in NMR since it induces an electromotive force in the same NMR coil that is used to produce B_{rf}. However, the signal decays in time (Free Induction Decay, or FID) and it does so with two different relaxation mechanisms, one for the decay of coherence (transverse relaxation) and one for the return of the magnetization to equilibrium (longitudinal relaxation).

Longitudinal relaxation

Longitudinal relaxation arises from the interaction between a spin and its environment, called the *lattice*. As a result of this interaction, the energy of the rotated magnetization in the magnetic field, $-\mathbf{M}\cdot\mathbf{B}$ will dissipate to the lattice until equilibrium is recovered, with $\mathbf{M}$ back again along $\mathbf{B}$.

A phenomenological description is provided by Bloch equations that introduce a viscous term for the M_z component in eq. 2.26 :

$$\frac{\mathrm{d}}{\mathrm{d}t}M_z = \frac{M_z - M_0}{T_1} \tag{2.28}$$

Where M_0 is the equilibrium Magnetization and T_1 is the longitudinal relaxation time.

Transverse relaxation

Independent of equilibrium recovery the precession can loose coherence due to both reversible processes, typically arising from the interactions among nuclear spins, and

[3] A pulsed rf field has the same effect.

irreversible, energy conserving processes. As a result of these processes the magnetization in the xy-plane decays to zero. In the Bloch equations this is a distinct viscous term for the x an y components

$$\frac{\mathrm{d}}{\mathrm{d}t}M_x = -\frac{M_x}{T_2} \tag{2.29}$$

$$\frac{\mathrm{d}}{\mathrm{d}t}M_x = -\frac{M_y}{T_2} \tag{2.30}$$

Hence, the full Bloch equations read

$$\begin{aligned}
\frac{\mathrm{d}}{\mathrm{d}t}M_x &= \gamma(\mathbf{M}\times H_0)_x - \frac{M_x}{T_2} \\
\frac{\mathrm{d}}{\mathrm{d}t}M_y &= \gamma(\mathbf{M}\times H_0)_y - \frac{M_y}{T_2} \\
\frac{\mathrm{d}}{\mathrm{d}t}M_z &= \gamma(\mathbf{M}\times H_0)_Z + \frac{M_z - M_0}{T_1}
\end{aligned} \tag{2.31}$$

NMR can probe this time evolution of magnetization by applying suitable pulse sequences.

2.2.4 The echo sequence

Simple description in terms of ants running faster and slower, reversing time, and formation of the echo. Discussion of the fact that echo intensity vs time between pulses distinguishes reversible decay T_2^* (eg inhomogeneity of local field) from irreversible decay T_2 We measure therefore T_2, the irreversible part by the spin echo. Spin echo sequence is often used in NMR to reduce the effects of magnetic field variations. It involves two main pulses: a π /2 pulse that tips nuclear spins into the transverse plane and a π pulse that refocuses the spins after a certain time delay. This refocusing creates a coherent signal called an echo, which helps improve signal quality, and measure relaxation times. It always needs to be much higher than T_2 relaxation and slightly longer than the dead time. Phase delay (Phi) represented in numbers 0 means no flip and 2 means flip of the carrier rf frequency.

More on the pulse sequence

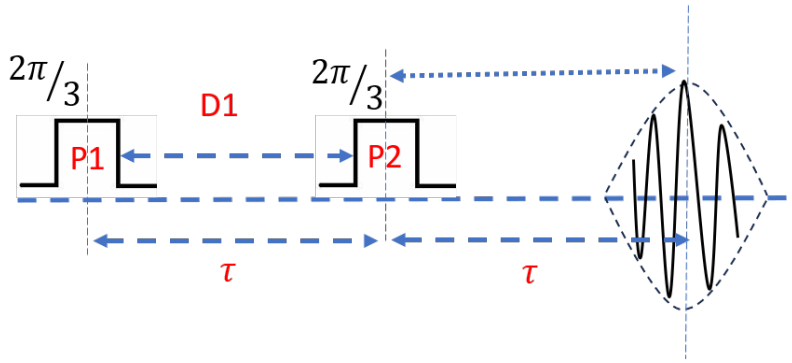

Figure 2.7: A typical Hahn echo pulse sequence

To conclude the NMR method section, it's worth mentioning a few more details on the employed pulse sequences, referring to Fig. 2.7. The NMR detection was always performed using one of the Hahn-spin echo sequences [92] where typically two pulses of nutation $\theta_{1,2}$ whose centers are separated by a delay $\Delta t = D1$ are employed and the echo is produced at time Δt after the center of the second pulse. The FID signal produced by each pulse decays very quickly, with T_2^*, much shorter than the instrument dead-time and cannot be measured directly. If the irreversible T_2 itself is not shorter than $D1$, the echo can be produced after the dead time. The better known Hahn echo is produced with $\theta_1 = \frac{\pi}{2}, \theta_2 = \pi$. However, with $I > \frac{1}{2}$ a more uniform spectral excitation is obtained with $\theta_1 = \theta_2 = \frac{2\pi}{3}$.

2.2.5 Saturation recovery

Describe that by suitable random duration resonant pulses separated by T_2 we reach another out-of-equilibrium state where the magnetization is spread over 4π. Then measuring a spin echo at a given delay t traces how much magnetization was recovered in t,i.e. measures T_1.

2.2.6 Nuclear Spin Hamiltonian

Until now, the Zeeman splitting, which is due to the interaction of the spin with the external magnetic field, was discussed. However, there are several other interactions possible for magnetic systems between the nucleus and the surrounding electron cloud, and it can affect nuclear energy levels as well as induce spontaneous nuclear transitions.

A general nuclear Hamiltonian containing all the interactions among the nuclear spins and with their surrounding electron cloud, in the presence of a magnetic field can be written as

$$\mathcal{H}_\mathcal{T} = \mathcal{H}_\mathcal{Z} + \mathcal{H}_\mathcal{E} + \mathcal{H}_\mathcal{N} + \mathcal{H}_\mathcal{Q} \tag{2.32}$$

where$\mathcal{H}_\mathcal{Z}$is the Zeeman interaction,$\mathcal{H}_\mathcal{E}$ is the nuclear dipolar interaction, $\mathcal{H}_\mathcal{N}$ is the hyperfine interaction and $\mathcal{H}_\mathcal{Q}$ is the quadrupole interaction. The dipolar interaction is

negligible for the samples studied in the thesis and the Zeeman interaction has been discussed before. Hence let's discuss briefly the third and fourth terms.

Hyperfine interaction

This thesis work deals with magnetic materials, and NMR has been performed in the ordered state. Hence, all the descriptions here are for magnetically ordered materials. As discussed above, hyperfine interaction comes from atomic physics and is described as the interaction between electron magnetic moment and nuclear magnetic moment. The hyperfine interactions $\mathcal{H}_{\mathcal{N}}$ generate additional magnetic fields at the nuclei, leading to a shift in NMR lines compared to the resonance frequencies of nuclei without these interactions. The electron-nuclear hyperfine Hamiltonian is given by [91]

$$\mathcal{H}_{\mathcal{N}} = \gamma\gamma_e\hbar^2\mathbf{I}\cdot\left[\left(3\frac{(\mathbf{S}.\mathbf{r})r}{r^5}-\frac{\mathbf{S}}{r^3}\right)+\frac{8\pi}{3}\mathbf{S}\delta(r)+\frac{\mathbf{L}}{r^3}\right] \tag{2.33}$$

where $\mathbf{S}$ is the spin, $\mathbf{L}$ is the orbital angular momentum of the electron, and $\mathbf{r}$ is the distance between the electron and nucleus. Therefore, the electronic magnetic moment is influenced by both spin and orbital angular momenta, but in solid materials, the orbital component is often quenched by the crystal field, and the third term doesn't play a significant role in the NMR experiments reported in this thesis. More generally, there are exceptions to this rule. There are two remaining parts to eq. 2.33: the first term is the point-dipolar interaction between nuclear spin and electron spin. Let's separate the electron of neighbor atoms, which we neglect at this stage, from the on-site electrons (the same atom of the nucleus). The retained term is called pseudo-dipolar, to distinguish it from nuclear dipolar interactions, and it vanishes for s-electrons due to spherical symmetry. The second term is named the Fermi contact term, and it vanishes for electrons with nodes at the nucleus (p-,d-,f-electrons). The Fermi contact contribution is isotropic while the dipolar term is anisotropic (traceless) because it depends on the wave function, i.e. the crystal orientation relative to the applied magnetic field. Equation 2.33 accounts only for a single electron coupling with a nucleus. To derive an effective hyperfine Hamiltonian of the nucleus summed over all electrons, one needs to average over the electron wave functions.

The resulting pseudo-dipolar plus contact terms correspond to a hyperfine tensor $\mathcal{A}$ and the Hamiltonian can be written as [93]

$$\mathcal{H} = \mathbf{I}\cdot\mathcal{A}\cdot\langle\mathbf{S}\rangle \tag{2.34}$$

where $\mathbf{I}$ is the nuclear spin, $\langle\mathbf{S}\rangle$ is the average electron spin. $\mathcal{A}\cdot\langle\mathbf{S}\rangle$ may be written as hyperfine field B_{hf}. Thus, the hyperfine Hamiltonian can be represented by the Zeeman Hamiltonian. Notice that the contact contribution to the hyperfine coupling $\mathcal{A}$ is proportional to the square modulus of the wave function, i.e. it is positively defined. However, if the electron magnetic moment aligns parallel to the field, the spin aligns in the opposite direction, because of its negative charge (see eq. 2.35 below). In this case, the contact hyperfine field is opposite to the external field.

When magnetic moments are ordered, the hyperfine interaction gives rise to a static field, which may be very large for the nuclei of the magnetic ions. For instance, in the case of ^{55}Mn and ^{53}Cr, the two nuclei utilized in this thesis, they are 45 T for a valence state close to Mn^{2+} and 30 T for a valence state close to Cr^{3+}, respectively. These

values exceed those of normal NMR magnets and enable us to perform NMR in zero applied field (ZFNMR).

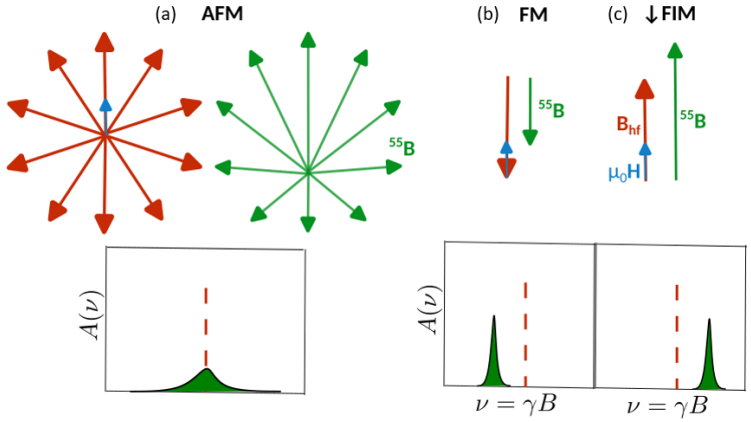

Figure 2.8: Polycrystal vector composition ${}^{55}B = \mu_0 H + B_{hf}$ and their resulting spectral shifts for three simple cases: antiferromagnet (AFM, a); soft ferromagnet (FM, b), soft ferrimagnet, minority spin (↓FIM, c).

In the presence of magnetic order, the external magnetic field couples to a ferromagnet and to a ferrimagnet, but not to an antiferromagnet. In this way, one can easily distinguish them by the behavior of the NMR Larmor frequency shift. In the case of ^{55}Mn, for example, the hyperfine field (B_{hf}) couples the magnetic moment in the following way:

$$ {}^{55}\nu(H) = \nu_{\mathrm{hf}} \begin{cases} -{}^{55}\gamma\,\mu_0 H & \mathrm{FM} \\ +{}^{55}\gamma\,\mu_0 H & \downarrow \mathrm{FIM}, \\ +0\left(\left[\frac{\mu_0 H}{B_{\mathrm{hf}}}\right]^2\right) & \mathrm{AFM} \end{cases} \tag{2.35} $$

In the collinear antiferromagnetic (AFM) case, the moments do not align to the external field, resulting in broadening without a discernible first-order shift, as shown in 2.8 a. In the ferromagnetic (FM) scenario, the magnetic moments consistently align with the applied field, given the negative nature of B_{hf} due to positive $\mathcal{A}$ for ^{55}Mn(i.e., opposite to H, as discussed below eq. 2.34). Consequently, the frequency decreases as the field strength increases, as shown in Fig. 2.8 b. However, in the case of a ferrimagnet (FIM), where one majority sublattice has larger magnetization and aligns along the field, its spins are antiparallel, and the minority sublattice has an opposite spin alignment, parallel to the field, hence its frequency shifts to higher frequencies since $\mathbf{B}_{\mathrm{hf}} \parallel \mathbf{H}$.

Nuclear Quadrupole Interaction

For nuclei with $I > \frac{1}{2}$ the nuclear charge distribution is not spherical and has a non-vanishing electric quadrupole moment eQ which interacts with the electric field gradient (V) due to the electron cloud, a rank two tensor.

$$\mathrm{V} = \begin{pmatrix} V_{XX} & 0 & 0 \\ 0 & V_{YY} & 0 \\ 0 & 0 & V_{ZZ} \end{pmatrix} \tag{2.36}$$

We assume $|V_{xx}| \leq |V_{yy}| \leq |V_{zz}|$) and by the Laplace equation, V_{xx} + V_{yy}+ $V_{zz} = 0$.

By defying a quadrupole frequency,

$$\nu_Q = \frac{3eV_{ZZ}Q}{2I(2I-I)h} \tag{2.37}$$

the nuclear spin Hamiltonian in an external field may be written as

$$\begin{aligned} \mathcal{H} &= \mathcal{H}_\mathrm{Z} + \mathcal{H}_\mathrm{Q} \\ &= h\nu_0 I_\mathrm{Z} + \frac{h\nu_\mathrm{Q}}{3V_{zz}} \mathbf{I}\cdot\mathbf{V}\cdot\mathbf{I} \end{aligned} \tag{2.38}$$

Spin I implies 2I +1 eigenvalues $\mathrm{E_m}$, with $-I \leq m \leq I$ and since NMR detects Δm =1 transitions, one would expect 2I frequencies , as shown in Fig. 2.9 for I=$\frac{3}{2}$

$$\nu_m = \frac{\mathrm{E_{m-1}} - \mathrm{E_m}}{h} \tag{2.39}$$

The magnitude of the quadrupole coupling constant is usually the size of a few KHz to MHz, hence the main line splits into satellites (Fig. 2.9), and depending upon the size of other interactions (mostly hyperfine in our case) one can see this in the NMR spectra. An illustrative figure Fig.. 2.9 shows how the energy levels change according to the Zeeman and the quadrupolar interactions for a spin 3/2 nucleus. The latter is much smaller than the former and it is sketched here in first-order perturbation, Interestingly, the first-order approximation does not affect the central transition, and the second-order correction is inversely proportional to the Larmor frequency so that With increasing field, the second-order effect on the central transition decreases.

Notice that the principal axis Z of V does not in general coincide with the field direction $\hat{z}$. Therefore we may write the Zeeman term in the electric field gradient frame using

$$I_z = I_Z \cos\theta + I_X \sin\theta \tag{2.40}$$

considering that, inn general, the asymmetry coefficient,

$$\eta = \frac{V_{YY} - V_{XX}}{V_{ZZ}} \tag{2.41}$$

is not zero.

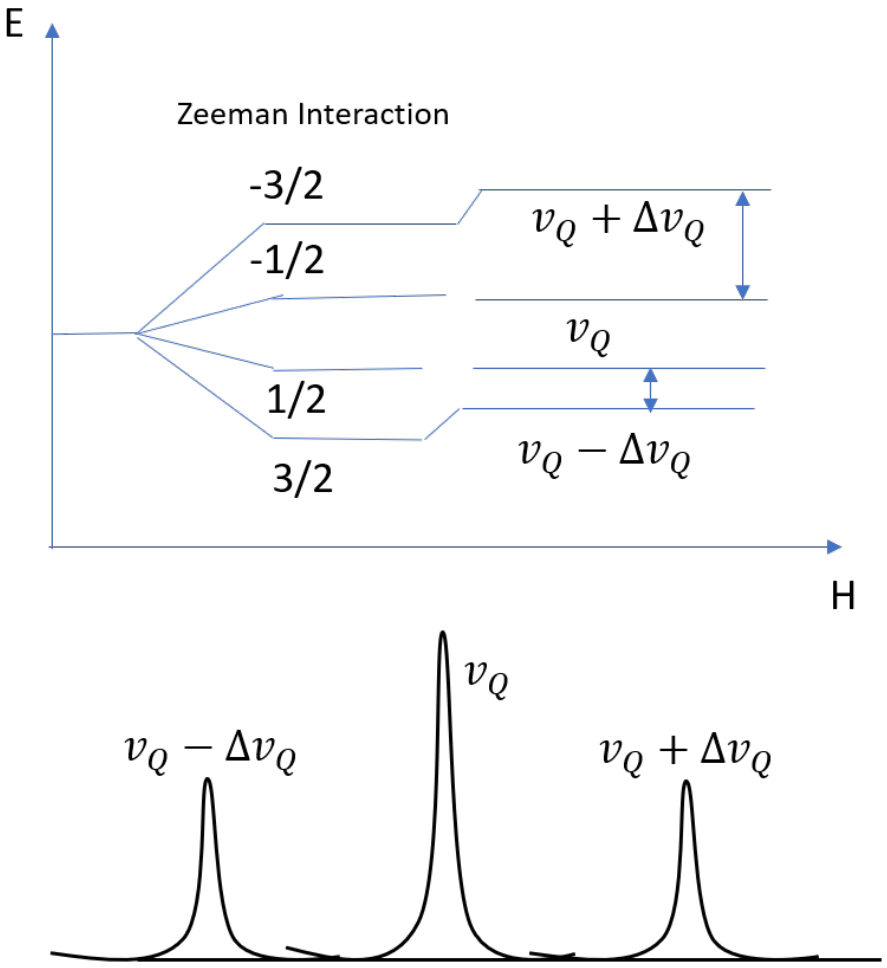

Figure 2.9: First order quadrupole Interaction

However, for simplicity, consider here η =0, i.e. assume that the quadrupole gradient has cylindrical symmetry. In this approximation, the transitions are, in first-order perturbation,

$$\nu_m^{(1)} = \nu_L + \nu_Q(m-1)\frac{3\cos^2\theta - 1}{2} \tag{2.42}$$

The data analysis provided in the thesis requires considering $\eta \neq 0$, and the quadrupolar interaction up to second order. This will be discussed in the appendix.

2.2.7 Instrumentation: HyResSpect

NMR is a powerful tool to investigate the local environment and the interaction of nuclei in a material however, magnetic nuclei are often complicated and challenging to inspect through this. A few factors responsible are briefly discussed below. This section is mainly taken from Ref. [88, 89, 94].

Distribution of local magnetic fields: magnetic materials often have heterogeneous local spin structures connected with defects and large hyperfine couplings, which leads to a distribution of local nuclear magnetic environments. This results in very broad NMR peaks, sometimes making it difficult to resolve and identify individual peaks accurately. *Short T_2 Relaxation Times*: magnetic materials often have short T_2 relaxation

times. This results in rapid signal loss and reduced signal-to-noise ratio, making it challenging to acquire high-quality NMR spectra. Relaxation is typically too short to measure NMR from nuclei of magnetic ions in the paramagnetic phase, due to the large fluctuating hyperfine fields. *Large magnetic coupling*. This leads to enhanced signal, since both the large external fields and the tiny nuclear magnetization couple to the huge hyperfine fields, which is a bonus. However this results in signal amplitude not simply proportional to number of resonating nuclei, as in the non magnetic case. *Instrumentation Limitations*: NMR instruments need different characteristics from the usual commercial high resolution spectrometers used in chemistry, in order to accommodate magnetic materials. They require a much wider frequency tunability, a flat frequency response, the shortest instrument dead time, and a large receiver bandwidth.

All the NMR measurements in this thesis were measured by a home-built broadband NMR spectrometer: HyResSpect [95] covering a 5-800MHz frequency range. The rf heterodyne design employs an external signal generator mixed with a fixed high frequency, that can be easily controlled in phase. Fast-averaging, capable of more than 10,000 repetitions per second, may be exploited when relaxation times are very short, as it is often the case in magnetic materials. Short dead times may be achieved by optimized probe resonating circuit design, used both for transmitting the radio-frequency and acquiring the nuclear induction. This is obtained by reducing the typical very large Q factors which would imply narrow excited bands and long delays between excitation and acquisition. At the high frequencies typical of many transition metal nuclei in their hyperfine field dead time of less than 2 μs may be achieved.

In this section, the main components of HyResSpect have been briefly discussed, including the probe head, and the pulse sequence relevant to our study.

Cryogenics

Superconducting magnets play a vital role in NMR measurements. In our study, a Maglab EXA cryo-magnet was employed, manufactured by Oxford Instruments, which offers variable temperature capabilities. This cryo-magnet enables rapid adjustments of the magnetic field within the 0-9 T range, at a rate of 1T/min, all controlled by software. Although the field homogeneity does not meet typical NMR standards, this limitation does not significantly impact NMR studies on magnetic materials due to their broader resonance lines. In return the fast field sweep rate allows quick experiment turn-around. To ensure stable temperature control ranging from 250 K down to 1.4 K, with accuracy and precision better than 0.1 K, a variable temperature insert (VTI) cryostat was utilized, utilizing helium flow from the same bath as the superconducting solenoid. This stability is crucial for our experiments. The sample is positioned within a coil in a resonant LC circuit housed by the VTI. Further details regarding this setup are provided in the subsequent section. Additionally, for zero-field measurements at liquid nitrogen temperature, a Cryomagnetics warm 89mm bore 7.96T fixed-field superconducting magnet with an Oxford CF flow cryostat was employed. The Oxford ITC 4 temperature controller was employed to regulate the heater and temperature sensor of the VTI and CF cryostats in both setups.

The Hardware: excitation and acquisition

A simplified block diagram of our NMR hardware is shown in Fig. 2.10. Let's start from the top left side, which is a synthesizer that produces a continuous wave signal, mixed with a fixed frequency ν_1, greater than the maximum Larmor frequency, with four possible phases at 90 degrees with respect to each other. These are required for phase cycling, that, together with 0, 180 degree phases in the receiver mixer, can removes constant offsets from the acquisition.

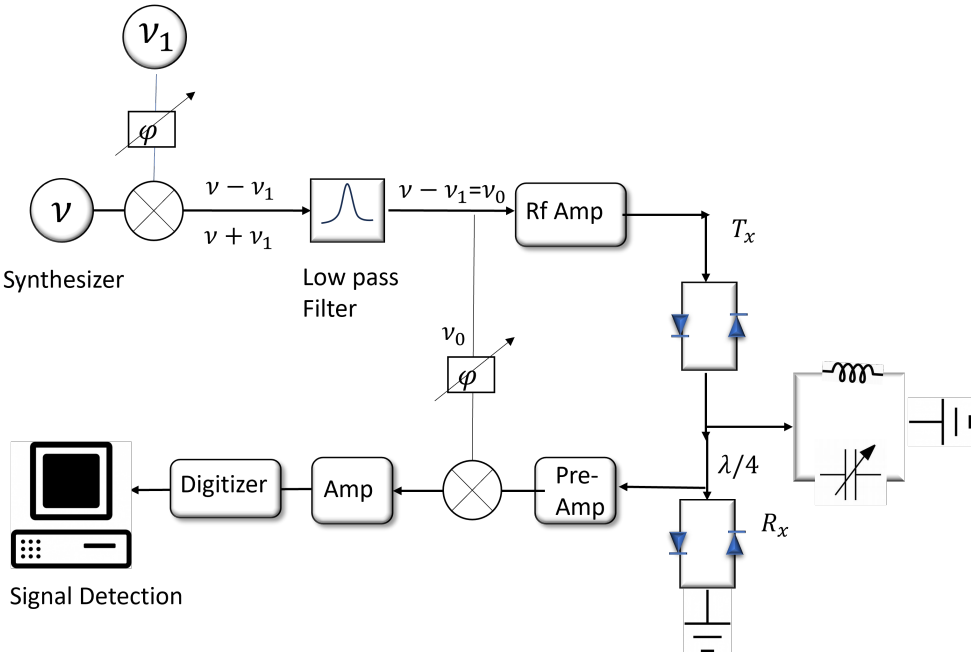

Figure 2.10: NMR block diagram

The mixer produces $\cos 2\pi(\nu + \nu_1)t + \cos 2\pi(\nu - \nu_1)t$ and a low-pass filter selects the Larmor frequency $\nu_0 = \nu - \nu_1$. Next to it a fast switch (rising time less than 10 ns) cuts rectangular pulses of variable time length and timing. The phase of the sinusoidal wave must be stable in order to preserve coherence for the duration of the NMR signal detected in the receiver.

Since the NMR spectrum in solids is broad (nuclei resonate at different frequencies) one needs to produce short pulses to irradiate a large fraction of them (the shorter the pulse duration τ, the broader the width of the irradiated spectrum). In order to nutate the nuclear spin to the xy plane (see the description below eq. 2.27), one must adjust the pulse duration and the amplitude of the rf field (e.g. $\pi/2 = \gamma B_{rf}\tau$).

A linear power amplifier is required to produce short $\pi/2$ rf pulses (peak power of several hundred W). Amplification results in a significant voltage, further increased by the large Q of the resonant circuit, leading to a substantial coil current and, consequently, generating a sizeable radio-frequency field. The linearity of the amplifier preserves the pulse shape.

This large pulse is then transmitted by low loss 50 Ohm coaxial cables to the sample coil (far right) which is the L of a tuned LC resonator (discussed in the next section). The nuclear magnetization precesses at a slightly different frequency $\nu_0 + \Delta\nu$ from the transmitter, inducing a tiny NMR signal in the same coil.

The three main components of the circuit including the probe head (discussed in the next section), the transmitter (T_x), and the receiver (R_x) are coupled and decoupled through simple passive circuits based on diode bridges, consisting of two parallel diodes with opposing polarities. One is in series with the transmitter cable (one diode lets the positive half through and the other the negative half of the waveform). The signal waveform passes through the bridge only if it exceeds the diode threshold voltage (typically 0.7 V), while the bridge operates as an open circuit for the sub mV NMR signals.

Conversely, the R_x terminal acts as an open circuit during transmission of the amplified rf pulse, protecting the preamplifier. This is achieved by a similar diode bridge connected to ground at the end of a coaxial cable of approximately one-quarter wavelength of the working radio-frequency, whereby the short circuit is transformed into an open circuit by the quarter lambda transmission line. In contrast, the tiny NMR signal does not activate conduction to ground and reaches the high-quality, wideband pre-amplifier with excellent linearity characteristics and a specific gain factor. Finally, the signal $\nu_0 + \Delta\nu$ is mixed in quadrature with the reference Larmor frequency ν_0 (i.e. it is mixed with two references, with $\pi/2$ phase difference, so that both phase and amplitude of the signal are produced) to be low-pass filtered and recorded as the so-called *audio* frequency $\Delta\nu$ signal. The computer produces an average by adding coherently many NMR signals.

The simple mixing scheme is called homodyne detection, when the synthesizer frequency directly provides the reference sinusoidal signal at the Larmor frequency. HyReSpect works on the slighlty more complex heterodyne detection describe above. The advantage is that the signal may be reproduced with different phase conditions. Specifically a signal can be produced with opposite phase and subtracted in the computer memory to be accumulated coherently, whereas any phase insensitive offset averages to zero.

The software control: gtknmr

The HyReSpect spectrometer is controlled through a graphical user interface (GUI) based program called "gtknmr" controlled through Linux scripting language. One needs to control several parameters in order to set up an NMR experiment and these parameters can be optimized in gtknmr. The main ones are discussed below,

- The initial parameters which need optimization are pulse duration (P1, P2..., usually presented in μs) and radio-frequency attenuation T_xAtt to get the desired θ pulse /θ is the nutation angle). T_xAtt is the attenuation expressed in dB, the larger the number, the weaker the pulse.

- D1 represents the delay between pulses for a spin echo sequence.

- The receiver must be switched off during transmission and the Receiver Inhibition Time (Rinh) is the time after the last pulse when the receiver is switched back on. Acquisition Delay (AcqD) is the further delay before the acquisition trigger. The sum of both parameters (AcqD+Rinh) must always be less than D1. The Relaxation Delay (RlxD) is the interval between sequence repetitions, which must be of order 5 times T_1.

- Receiver gain or Receiver attenuation(R_xAtt). Initially, the NMR signal undergoes substantial amplification, and this parameter dictates a subsequent reduction in intensity, regulating the highest permissible overall amplification to prevent receiver saturation.
- Maximum scans (MxScans), number of sequence+acquisition repetitions, the signal is summed (averaged) for better signal-to-noise ratio, NScan is the number of scans actually recorded and the block size (BlkSiz) represents the total number of digitized points.

The probe head

The above-mentioned probe head in the block diagram is an RLC circuit(shown in Fig. 2.11), made with a variable capacitor (C) to tune with the resonant frequency and make a resonator with variable frequency, an Inductor (L), essentially a copper coil to wind around the sample (for maximum efficiency), plus an optional parasite Resistor (R) connected in series. The circuit must be tuneable in the required frequency range ($\omega = (LC)^{\frac{1}{2}}$) in order to match the nuclear Larmor frequency. A high current gain is produced by a large quality factor $Q = \frac{\omega L}{R}$), i.e. without the optional R, producing rf magnetic field up to a few mT. A high Q factor results in a larger NMR signal. Nonetheless, an excessively high-quality factor could result in an undesirable rise in receiver dead time, which may be conflict with short T_2 relaxation times. As a result, a balance or compromise needs to be sought.

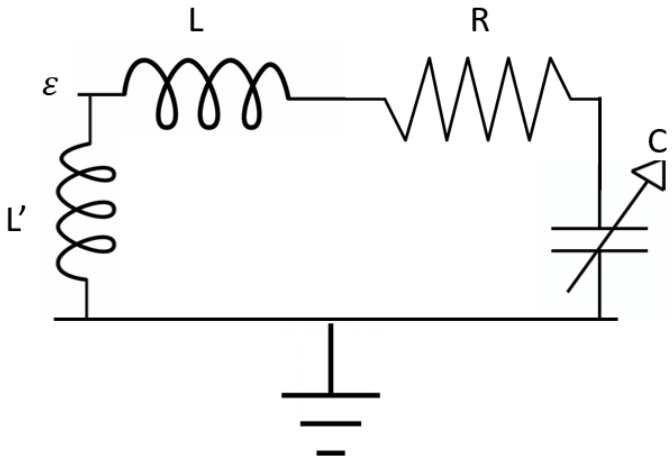

Figure 2.11: NMR probehead

It is essential to carefully design the inductor coil. This involves minimizing the space around the sample to maximize the induced nuclear EFM. Additionally, the number of turns in the coil should be adjusted based on the desired frequency, with fewer turns for higher frequencies. To achieve maximum power transfer to the sample, the impedance of the transmission circuit (50 Ohms) should be matched with that of the RLC circuit. This is accomplished by connecting an inductor L' in parallel to the RLC circuit, or else by connecting the inner conductor of the coaxial cable (the ε point in Fig..2.11) a fraction of a turn past the beginning of the coil, which is connected to ground. This makes a self-transformer of the full coil. In both cases, careful matching

by the value of L' or by the self-transformer ratio, results in a 50 Ohm impedance of the resonant circuit.

Whenever this type of high Q probe head is employed at high frequency, above 400 MHz, the recording of a broad NMR spectrum becomes a tedious sequence of frequency change, manual probe tuning, and restarting acquisition. At lower frequencies an automated tuning implements a stepper motor and a multifrequency detection of the probe reflected wave to optimize the variable capacitance.

The resistive probe

Materials exhibiting magnetic order, particularly ferro- and ferri-magnets, where both the radiofrequency field B_{rf} and the precessing nuclear magnetization modulate the huge B_{hf}, experience a very large amplification of B_{rf}, referred to as rf enhancement. In these unique instances, a resonant circuit for NMR transmission and detection might not be strictly necessary, as the enhanced rf power alone can produce short enough pulses and a strong NMR signal. Consequently, the NMR coil can be straightforwardly connected in series with a 50-ohm resistor to match the cable and transmitter's impedance.

This simplifies data acquisition significantly, as such a probe head enables the recording of NMR signals across a wide frequency range without requiring circuit tuning at each new frequency, unlike the previous LC probe head setup.

The spectra are typically reconstructed by plotting the central amplitude of the Fourier Transform of each echo, taken from its center, filtered by a decay function for noise reduction and apodization, vs. the excitation frequency. When several broad peaks are visible the best fit of each peak is obtained by fitting one or more Gaussian components, according to

$$G_\alpha(\nu) = \sum_{i=1}^{n} \frac{A_{\alpha,i}}{\sqrt{2\pi}\sigma_{\alpha,i}} \exp\left[-\frac{1}{2}\left(\frac{\nu-\nu_{\alpha,i}}{\sigma_{\alpha,i}}\right)^2\right] \tag{2.43}$$

whose mean frequency may be computed as its first-moment $\overline{\nu_\alpha}$ by the weights $w_{\alpha,i}$:

$$\overline{\nu_\alpha} = \sum_i w_{\alpha,i}\nu_{\alpha,i}, \quad w_{\alpha,i} = \frac{A_{\alpha,i}}{\sum_k A_{\alpha_k}} \tag{2.44}$$

A final comment is due to the temperature dependence of the spectra, where the ZF NMR frequency vs. temperature follows the order parameter. In second-order transitions, this is typically possible only for nonmagnetic nuclei, since relaxation rates tend to diverge at the critical point and the signal is lost.

2.3 Muon Spin Spectroscopy

2.3.1 Introduction

Muon spin relaxation, rotation, and resonance, depending on the specific experimental context, frequently denoted just as μSR, encompass the method where an unstable elementary particle, called a muon, is implanted spin-polarized into the target system to investigate both electronic and local magnetic properties. Its spin precession can be

revealed by exploiting particle detection techniques, hence its principle is similar to NMR. It is thus complementary to NMR since it also provides important static and dynamic magnetic information about the environment of the local muon sites. The main disadvantage with respect to NMR is that the implantation sites are unknown. However, it has certain advantages over NMR. Here a few of them are listed, specific to magnetic materials

- Muons are implanted 100% spin-polarized in any material. They do not require internal or external magnetic fields to achieve this polarization and thanks to their large gyromagnetic ratio $\gamma = 135.5$ MHz/T they can detect very weak internal magnetic fields, hence tiny electronic magnetic moments
- Zero Field (ZF) measurements are possible and help to identify the ground state of the magnetic system.
- Unlike the NMR of magnetic nuclei, the relaxation rate may be followed very closely to second-order transitions, accurately measuring the order parameter.
- NMR cannot be employed with samples composed of non-active NMR nuclei, that is with $I = 0$, or too small gyromagnetic ratio γ, or too small natural abundance, whereas μSR experiments can be performed on any sample.
- In a homogeneous magnetic polycrystal, fixed proportions of precessing and non-precessing signals are expected. As discussed in Sec. 2.3.3, the experiment yields a very precise determination of the magnetically ordered sample volume, showing the sharpness of the transition.

μSR provided complementary information to our macroscopic measurements by SQUID-magnetometer as well as microscopic measurements by NMR. In this section, I will discuss the characteristics of muon and the experimental guide for μSR. The μSR theory and concepts presented in this section, are mainly based on [89, 94, 96, 97]

The muon discovery and its properties

The accidental discovery of muons by Carl David Anderson and Seth Neddermeyer in 1936, studying cosmic rays in a cloud chamber in California, prompted the remark from the scientist Isidor Rabi, "Who ordered that?". The particle was initially mistaken for the π meson, the mediator of nuclear interaction, already predicted by Hideki Yukawa. The muon was later correctly identified as a heavy lepton by Cecil Powell. Initially, the potential of utilizing the muon for investigating condensed matter systems went unnoticed by scientists until T.D. Lee postulated the violation of parity in weak decays, and Garwin et al. [98] demonstrated this violation both in the muon production from the pion and in the decay of the muon, already stating that muon beams would become relevant for probing magnetic fields inside a solid upon its implantation. This led to the birth of muon spin spectroscopy as an experimental technique to study condensed matter systems.

	Spin	Charge	Mass	Lifetime	$\gamma/_{2\pi}$ $(\frac{MHz}{T^{-1}})$
e	1/2	-e	m_e	∞	28000
μ	1/2	$\mp e$	$207m_e$	2.2 μS	135.538
p	1/2	+e	$1836m_e$	∞	42.6

Figure 2.12: Muon properties

Coming to the muon properties, summarized in Fig. 2.12, muon is a relatively long-lived radioactive particle, with an average lifetime of $2.2\mu s$[4]. Once implanted, it chemically behaves as hydrogen (a light unstable isotope). Due to its comparatively large gyromagnetic ratio (γ_μ) (3.2 larger than hydrogen, the largest common γ in NMR), it can detect tiny internal magnetic fields. The implanted muon can exist in three different charge states. It can exist on its own as a positively charged particle μ^+ like hydrogen cation H^+. [5] It can acquire an electron and form an electrically neutral state called muonium, Mu^0, analogous to the H atom. Finally, sometimes, it can pick two electrons and form a negatively charged Mu^-). In the magnetic materials that we investigated, DFT shows that only Mu^+ is formed. We shall refer to it as muon, for brevity.

The muon production and impantion

Muons occur naturally as a result of high-energy particle interactions with atmospheric gas nuclei. In laboratory settings, their creation involves the collision of high-energy protons (p) sourced from particle accelerators with carbon targets. This collision leads to the emission of the more unstable pions (π, mean lifetime $\tau_\pi = 26$ ns). To attain the specific desired charge (positive pions) and momentum, emitted pions are selected using a dipole magnet and decay in flight,due to their short lifetime, giving rise each to a positive muons (μ^+) and a neutrino (ν_μ). These processes can be depicted as follows:

$$p^+ + p^+ \longrightarrow \pi^+ + p^+ + n \tag{2.45}$$

$$\pi^+ \longrightarrow \mu^+ + \nu_\mu \tag{2.46}$$

Fig. 2.13 shows the decay of $I = 0$ pion into an antimuon (μ^+) and a neutrino (ν_μ) with negative helicity and $S = \frac{1}{2}$ (this is parity violation: the neutrino with positive helicity does not exist in nature). In order to conserve momentum spin $S = \frac{1}{2}$ μ^+ should also have negative helicity [99], hence spin-polarized muons are produced when pions decaying at rest are selected by means of the beam transport momentum.

[4] We use the positive antimuon, since the negative muon undergoes K-capture by the nucleus, and also probes nuclear matter, making the data analysis more complex.

[5] Like hydrogen, this is most often a covalent bond, or a hydrogen bond, both having zero net hyperfine field from a single pair of electrons.

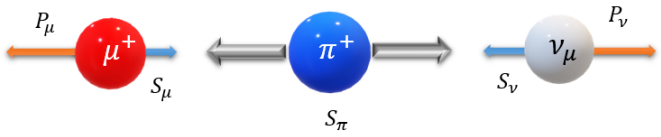

Figure 2.13: A Schematic plot of production of the muon, in the pion rest frame. This coincides with the laboratory frame for pions decaying at rest. The blue and orange arrows indicate the spin and momentum direction of each particle respectively. The figure is taken from Ref. [100].

After a mean lifetime of 2.197 μs, the muon decays into positron (e^+) and two neutrinos (ν_e and $\bar{\nu}_\mu$). This process is written as;

$$\mu^+ \longrightarrow e^+ + \nu_e + \bar{\nu}_\mu \tag{2.47}$$

Now, a beam of 100% spin-polarized muons is transported to the sample and implanted. They lose their excess kinetic energy (4 MeV at the π decay), i.e. they thermalize by scattering on the atoms and they end up occupying a site (typically forming chemical bonds). This process occurs in hundreds of ps, and is negligible with respect to their mean decay time τ_μ. In the three-body decay, positrons emerge with an energy spectrum. However, due to parity violation, their average linear momentum of emission is asymmetric, more probable in the muon spin direction. This can be exploited in the positron detection to extract the ensemble average of the muon spin dynamics in time, the working principle of μSR, as this will be discussed in the next section. Before that let us understand the asymmetry of positrons.

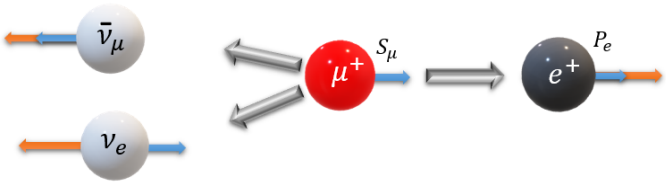

Figure 2.14: A Schematic plot of muon decay The blue and orange arrows indicate the spin and momentum direction of each particle respectively.

The muon asymmetry

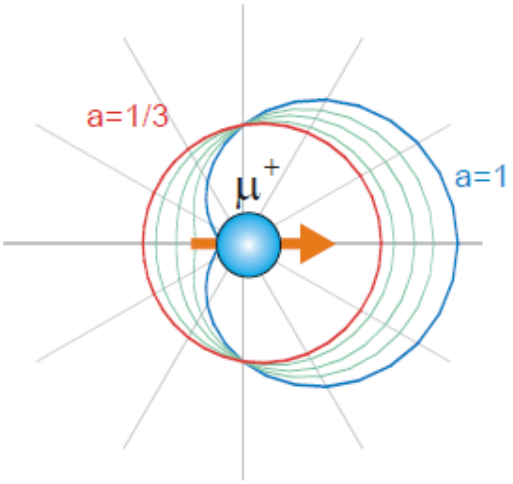

Figure 2.15: Angular distribution of the positrons from the muon decay.
Taken from [101]

With a fixed muon spin direction, the probability of emission is given by the asymmetry lobe shown in Fig..2.15 for different energies and given by

$$\mathcal{E}(\theta) = \frac{N(\eta)}{2\pi}\big(1 + A(\eta)\cdot\cos\theta\big) \tag{2.48}$$

where $A(\eta)$ is the asymmetry factor that depends on the positron energy. In the three body decay there is a maximum energy $E_{\max}$ for positron and a fraction

$$\eta = \frac{E}{E_{\max}} \tag{2.49}$$

which follows a distribution function given by

$$N(\eta) = 2\eta^2(3 - 2\eta) \tag{2.50}$$

The asymmetry is then

$$A(\eta) = \frac{2\eta - 1}{3 - 2\eta} \tag{2.51}$$

and when all positron energies are sampled with equal probability the asymmetry parameter has the value $A_0 = \frac{1}{3}$ (red curve).

Ensemble averages are possible since all implanted muons spin start from the same direction and a clock is restarted at each incoming muon. If for instance, they undergo identical precessions at frequency ω_μ in the xy plane, they will be pointing in the same direction $\theta = \omega_0 t$ at any clock time t. This time-dependent direction is the axis of the asymmetry lobe of Fig. 2.14 at that time. For instance, placing a positron detector in

the initial spin direction, say x, its positron counts will be modulated by the precession

$$\begin{aligned} N(t) &= N_0 e^{-\frac{t}{\tau_\mu}} [1 + A_0 P(t)] \\ &= N_0 e^{-\frac{t}{\tau_\mu}} [1 + A_0 \cos \omega_\mu t] \end{aligned} \tag{2.52}$$

where N_0 is the rate at $t = 0$, A_0 is the experimental average asymmetry over all positron energies, somewhat lower than the theoretical value. $P(t)$ is the time-dependent spin polarization, defined as

$$P(t) = \langle \sigma_x(t) \rangle \tag{2.53}$$

where σ is the muon Pauli operator in the $\hat{\xi}$ direction. Clearly, if A_0 vanishes the probability becomes isotropic and the counts are those expected of the radioactive decay.

2.3.2 Experimental setup

In this section, I will discuss the experimental setup and the basic principle of μSR, having in mind the GPS spectrometer at the Paul Scherrer Institut, where the experiments were performed.

The principle

The muon undergoes the Larmor precession around the direction of the local field, at the Larmor frequency $\omega_\mu = \gamma_\mu |\mathbf{B}_\mu|$, determined by the muon gyromagnetic ratio γ_μ and the modulus $|\mathbf{B}_\mu|$ of the total magnetic field at the muon site, exactly like in NMR, as described in Sec.. 2.2.2 and 2.2.3.

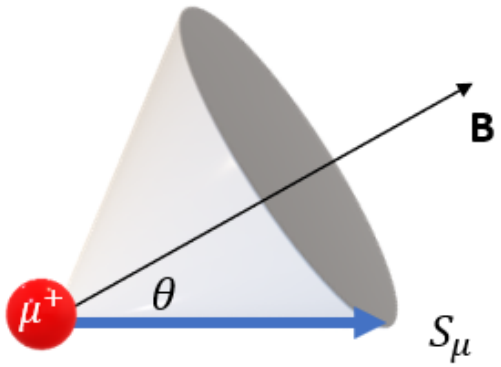

Figure 2.16: Muon precession around a field in a random direction. The blue arrow represents the initia spin direction

This figure will be discussed more in Sec. 2.3.3 in the context of randomly oriented fields in polycrystals.

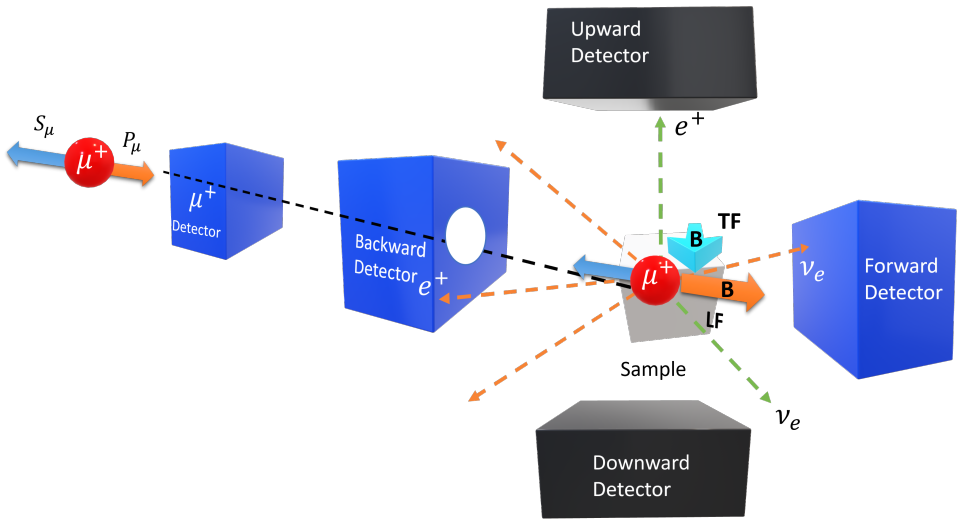

Figure 2.17: Schematic illustration of μSR experiment with a beam of spin-polarized μ^+ implanted in a sample

In the present simplified description, we assume that the initial muon spin direction is antiparallel to the beam momentum[6]. In this case the direction of the magnetic field may be Transverse or Longitudinal with respect to the initial muon spin direction. A schematic diagram similar to that of the GPS experiment, involving both Transverse field and Longitudinal field geometry, is shown in Fig. 2.17 (see Ref. [102–105] for details). I now describe the types of experiments relevant for the present thesis.

Zero field (ZF): This experiment involves the study of muon polarization without any applied magnetic field. However, in our case there is magnetic field at the muon, due to ordered electronic moments below the magnetic transition. For the sake of simplicity, here is a simple geometry where only the Backward (B) and Forward (F) detectors reveal an asymmetry is discussed.

Weak Transverse field (wTF): In this case a small external magnetic field (typically 100 G) is applied perpendicular to the initial muon spin polarization. In GPS it is applied orthogonally to the plane of the detectors, see the blue arrow in Fig. 2.17, and the asymmetry is revealed in all detectors. This is a quick way to determine the magnetic volume fraction, as mentioned in the introduction: above the transition, all muons precess with negligible relaxation at the frequency appropriate for the low applied field; below the transition, this signal should disappear, apart from muons stopping outside the sample. The sharpness of the jump tells the sharpness of the transition.

Longitudinal field (LF): The magnetic field is applied parallel to the muon spin polarization in (See Fig. 2.17) the orange arrows show the field direction and like ZFμSR the positrons are counted in the F and B detectors. This experiment may discriminate whether the longitudinal component undergoes static or dynamic relaxation.

[6]On GPS the spin may be turned at $\approx$ 60 degrees from the beam direction by a spin rotator (Wien filter)

Total internal field at the muon sites

In the magnetically ordered state, the total local magnetic field experienced at the muon site B_μ may be written as

$$\mathbf{B}_\mu = \mu_0\mathbf{H} + \mathbf{B}_c + \mathbf{B}_{dip} \tag{2.54}$$

where $\mu_0\mathbf{H}$ is the external applied field, and the other two terms are the contact hyperfine and dipolar contributions, arising from the interaction between the muon spin polarization and the local electronic spin surrounding the muon site. They give rise in principle to the same type of Hamiltonian of eq. 2.33, but $\mathbf{B}_{dip}$ is more relevant for the muon, that is on average farther from the ordered electronic moment than the ^{55}Mn and the ^{53}Cr nuclei. The explicit expression is

$$\mathbf{B}_{dip} = \frac{\mu_0}{4\pi}\sum_i \left[\frac{3\mathbf{r}_i(\mathbf{m}_i\cdot\mathbf{r}_i)}{r_i^5} - \frac{\mathbf{m}_i}{r_i^3}\right] \tag{2.55}$$

where $\mathbf{m}_i$ is the magnetic moment of atom i and $\mathbf{r}_i$ is the vector connecting atom i and the muon site, at the origin of the reference frame. Usually, it is calculated by the Lorentz construction: a *Lorentz sphere* of radius R is centered at the origin, and $\mathbf{B}_{dip}$ is calculated ab initio inside it, whereas the rest is approximated with uniform magnetization, i.e. ignored for an antiferromagnet. For a ferro or ferrimagnet, the outer space cannot be ignored, as magnetic poles appear on the boundaries. In zero field, one usually assumes that the outer boundary is demagnetized while the inner spherical boundary shares the same moment direction of the Lorentz sphere, producing a further contribution

$$\mathbf{B}_{FM,dip} = \mathbf{B}_{dip} + \mathbf{B}_L = \mathbf{B}_{dip} + \mu_0\frac{\mathbf{M}}{3} \tag{2.56}$$

The contact hyperfine field $\mathbf{B}_c$ can be expressed for a spherical electronic cloud surrounding the muon at the muon position, i.e. $r = 0$, with the position vector defined above

$$\mathbf{B}_c = -\frac{2}{3}\mu_0\mathbf{m}, \rho_s(0) \tag{2.57}$$

where $\mathbf{m}$ is the moment of the electron providing the local spin density $\rho_s(0) = \rho_{s\uparrow}(0) - \rho_{s\downarrow}(0)$ at the muon site. The site must be assigned in order to calculate the total internal field $\mathbf{B}_\mu$. The DFT calculation was not my direct contribution, and I limit myself to explaining the main results in Ch. 5.

Anisotropy from the positron detector counts

Let's consider ZF μSR for the time being. The time-dependent count rate $N_{F,B}(t)$ in the F and B detectors is given by eq. 2.52, with distinct initial count rates $N_{0F,B}$[7] These count rates are ensemble average, accumulating millions of muon decays per experiment (run, in the μSR parlance). The time-dependent asymmetry $A(t) = A_0P(t)$ may be obtained experimentally as the normalized difference of these count rates

$$A(t) = \frac{N_F(t) - \alpha N_B(t)}{N_F(t) - \alpha N_B(t)} \tag{2.58}$$

[7]In general, the sample position is not perfectly centered between the two, the detector efficiency and geometry may not be exactly the same.

where the constant $\alpha = N_{0F}/N_{0F}$ may be experimentally determined. The polarization function $P(t)$ deviates from the simple cosine of eq. 2.52 for two reasons: *i)* spin relaxation, which follows from the same phenomenological discussion of Sec. 2.2.3 and leads to the decay of $A(t)$; *i)* the presence of more muon stopping sites. For this reason, a more general expression is

$$A(t) = A_0 \sum_i f_i [P_{iT}(t) + P_{iL}(t)] \tag{2.59}$$

where the subscript i labels distinct muon sites, f is a fraction ($\sum_i f_i = 1$) and the subscripts T, L distinguish longitudinal components, relaxing as $1/T1$, from precessing transverse components, relaxing as $1/T_2^*$.

2.3.3 Muon polarization functions

Consider again the precession cone of Fig. 2.16 where the field $\mathbf{B}_\mu$ is in a random direction, making an angle θ with the initial muon spin direction, say $\hat{x}$. This may be the case of the internal field in a polycrystal grain below the magnetic transition temperature. For the sake of simplicity imagine a detector with an axis along $\hat{x}$. Following eq. 2.59 and assuming for simplicity a single stopping site, the muon spin polarization $P_x(t)$ may be expressed as

$$P_x(\theta, t) = \cos^2\theta \exp\left(-\frac{t}{T_1}\right) + \sin^2\theta \exp\left(-\frac{1}{2}\sigma^2 t^2\right) \cos\gamma_\mu B_\mu t \tag{2.60}$$

where $B_\mu = |\mathbf{B}_\mu|$, the $\cos^2\theta$ projection represents muons experiencing local field components along $\hat{x}$, longitudinal with respect to the spin, that relax with T_1, the $\sin^2\theta$ projection represents muons experiencing local field components perpendicular to $\hat{x}$, transverse with respect to the spin and we assume that their T_2^* relaxation is dominated by Gaussian inhomogeneous broadening, as in the case of the NMR lineshapes of eq. 2.43. The powder average of $P_x(\theta, t)$ is obtained by integrating this expression over the full solid angle and it represents the expected outcome of an experiment with a polycrystalline sample

$$P_x(t) = \frac{1}{3}\exp\left(-\frac{t}{T_1}\right) + \frac{2}{3}\exp\left(-\frac{1}{2}\sigma^2 t^2\right) \cos\gamma_\mu B_\mu t \tag{2.61}$$

Consider now an ideally sharp second order transition to the paramagnetic state at T_m. Below T_m the internal field $B_\mu(T)$ is proportional to the electronic moment $\mathbf{m}$, and it traces the temperature dependence of the order parameter. Above T_m the internal field B_μ disappears and the whole $P_x(t)$ becomes indistinguishable from the longitudinal polarization. Hence the amplitudes of P_L and P_T will undergo a step-like increase to 1 and decrease to zero, respectively, as shown in Fig.. 2.18. The experimental data will again show how sharp is the magnetic transition, complementing wTF data. This ability is unique to μSR.

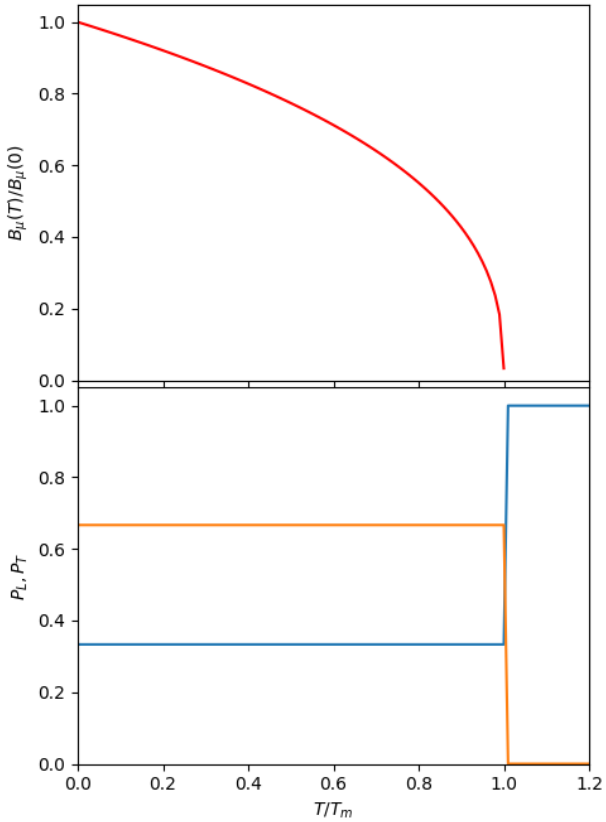

Figure 2.18: Disappearance of B_μ and step like transition of P_L and P_T at T_m

Chapter 3

Literature review of intrinsic magnetic topological insulators

3.1 Intrinsic magnetic topological insulators:$MnBi_2Te_4$

As already mentioned in the chapter 1, the introduction of spontaneous magnetization to the surfaces of topological insulators (TIs) results in the breaking of time-reversal symmetry ($\mathcal{T}$). This perturbation induces the opening of an exchange gap, specifically in the proximity of the Dirac point within the topological surface states. Consequently, this phenomenon facilitates the emergence of various novel topological states, like the quantum anomalous Hall effect (QAHE) and axion insulators, offering prospects for innovative technological applications in the future [30, 106]. The achievement of the QAHE has been notably advanced through strategies involving magnetic proximity and the introduction of 3d transition metal doping as magnetic impurities [31, 42]. These methodologies have demonstrated efficacy, marking significant progress toward the realization of the QAHE and introducing innovative avenues for attaining this objective. Nevertheless, the practical implementation has encountered limitations, particularly those attributable to the small and non-uniform distribution of the surface gap. Consequently, the observation of the QAHE has been constrained to ultra-low temperatures. To overcome these limitations and elevate the operational temperature of the QAHE, it became imperative to explore new magnetic topological insulators that have intrinsic magnetism as well as non-trivial topology.

Intrinsic magnetic topological insulators, more precisely antiferromagnetic topological insulators, were predicted way early in 2010[46] but far from realizing the required topological properties until 2019 in **$MnBi_2Te_4$** [48]. Though it was long reported as a new layered chalcogenide semiconductor in 2013 [107], its topological properties and possible realization of the QAHE were not explored for several years. It was predicted to have the necessary intrinsic magnetization and a large magnetic gap at the surface states in the heterostructures [47] and for the first time, it was observed in the $MnBi_2Te_4$ single crystals, as confirmed by various experiments [48]. The same year, Rienks et al. reported a large magnetic gap of 90 mV in the Mn-doped Bi_2Te_3 developed as a heterostructure of $MnBi_2Te_4$ septuple and Bi_2Te_3 quintuple layers[107]. Subsequently, many predictions appeared in 2019 [68, 108, 109]. In this literature review, the crystal and magnetic structure of the $MnBi_2Te_4$ are discussed first, followed by the topological and transport properties reported until now [106, 110].

3.1.1 A-type antiferromagnetism and crystal structure

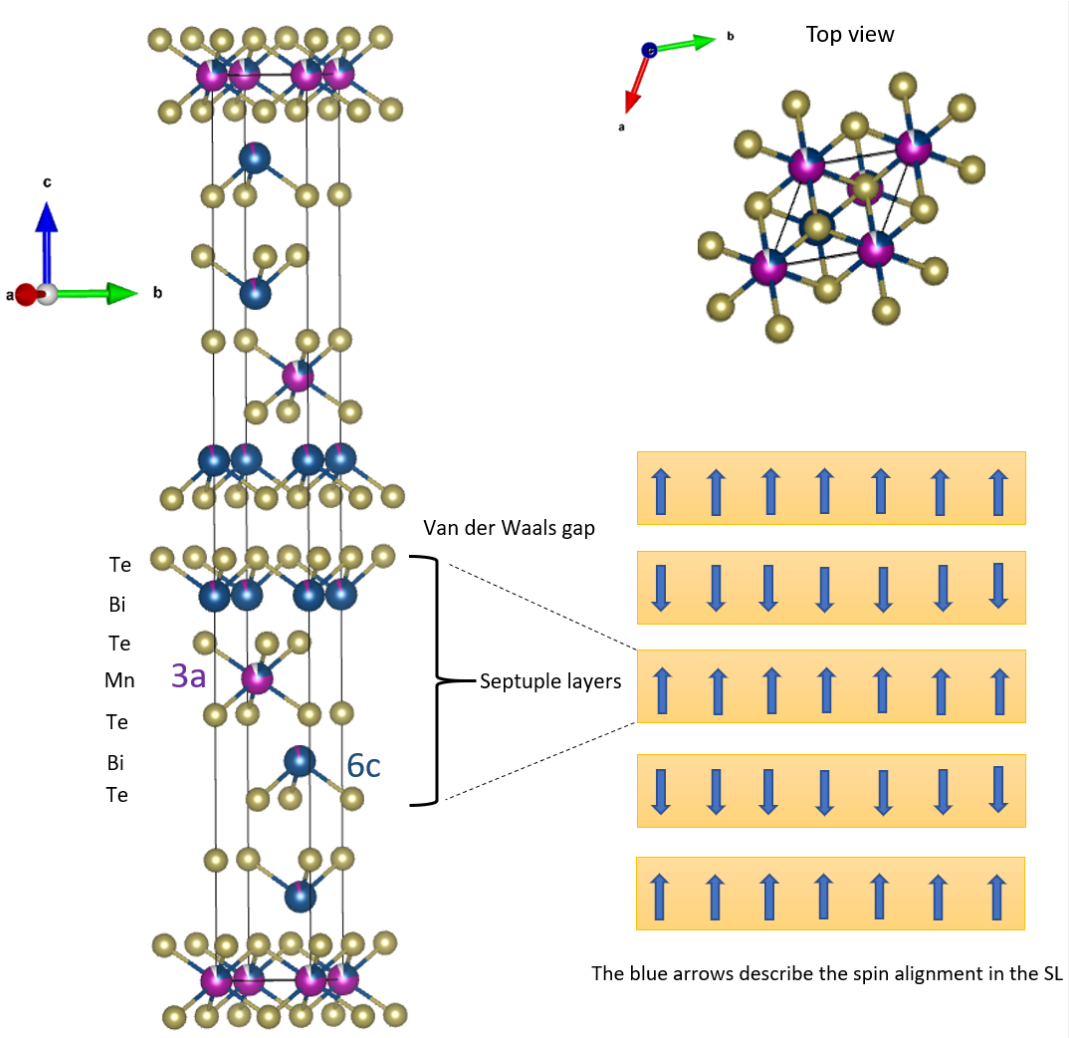

Figure 3.1: The crystal structure of $MnBi_2Te_4$ grey circles - tellurium, blue circles - bismuth, pink circles - manganese, top right corner shows the view from ab-plane.

$MnBi_2Te_4$ possesses the $GeAs_2Te_4$ type trigonal structure and adopts a centrosymmetric space group $R3\bar{m}$ (number 166), featuring lattice parameters a = 4.3314(2) Å and c = 40.932(2) Å [111]. The material exhibits a layered structure composed of septuple layers, forming a rhombohedral (ABC) stack along the *c* axis. These septuple layers (SL) consist of seven atomic layers arranged as Te-Bi-Te-Mn-Te-Bi-Te, with well-defined van der Waals gaps between them (see Fig.3.1). In contrast to doped $MnBi_2Te_3$, $MnBi_2Te_4$ grows with an alternating pattern of Bi_2Te_3 and Mn-Te layers which can be described as an intercalation of the Mn-Te layer into the Te-Bi-Te-Bi-Te quintuple layer (QL). This results in a stoichiometric crystal structure and a uniform magnetic arrangement. Considering the tendency for cation intermixing in similar $GeBi_2Te_4$ semiconductor structures, cation intermixing is taken into consideration at the Bi (6c) and Mn (3a) sites in the samples[111]. Notably, the degree of cation intermixing in $MnBi_2Te_4$ is relatively smaller compared to other compounds in the same family; this distinction will be explored in further detail below.

The Mn atoms responsible for the magnetism in the system are ferromagnetically coupled within the same layer, while the coupling between adjacent layers is antiferromagnetic (AFM). This behavior has been deduced through first-principle calculations, where the exchange coupling parameter ($j^{\parallel}$) indicates dominant ferromagnetic coupling with nearest neighbors and weaker coupling with more distant interactions [48]. On the other hand, $j^{\perp}$ values are largely negative, signifying antiferromagnetic coupling between layers and establishing an overall A-type antiferromagnetic configuration as the ground state. The positive magnetic anisotropy implies an out-of-plane easy-axis anisotropy with a local magnetic moment of $\pm 4.7 \mu_B$. Monte Carlo simulations further predicted the transition temperature for the onset of antiferromagnetic ordering (T_N) to be approximately 25.4 K [48].

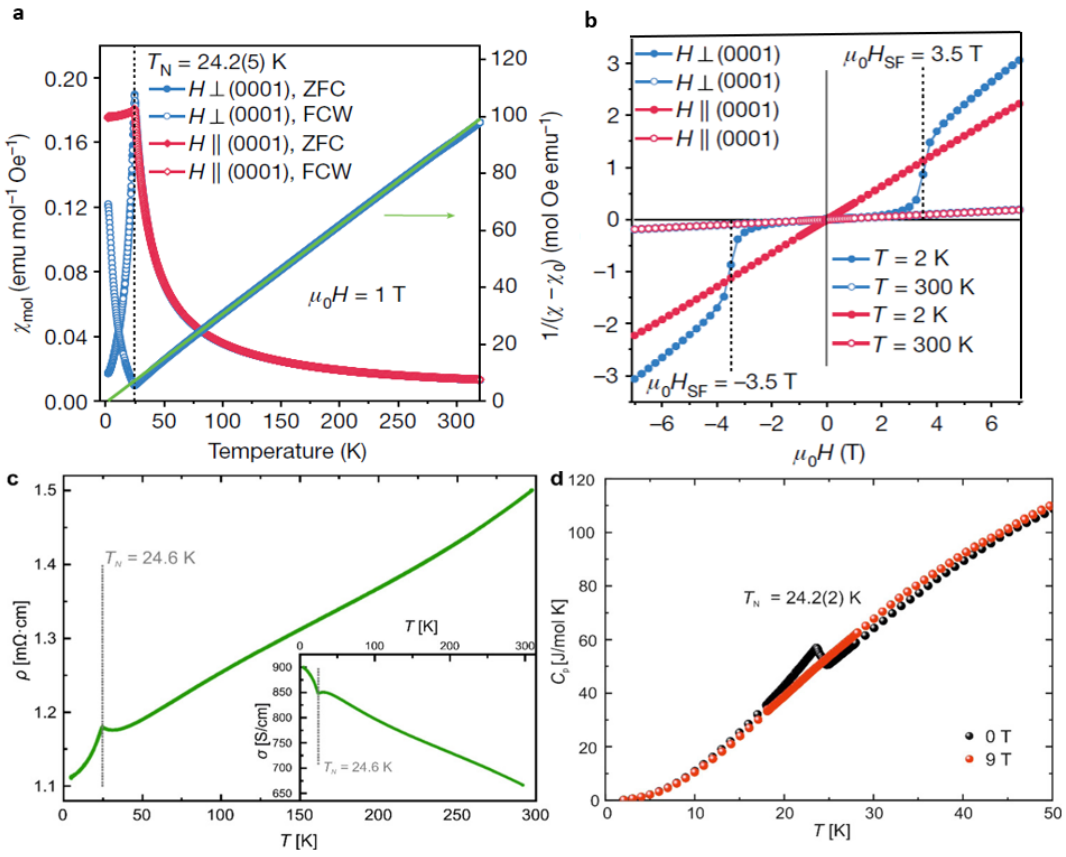

Figure 3.2: (a) Magnetic susceptibility along both $H \parallel c$ and $H \perp c$, (b) Isothermal magnetization in both directions; (c,d) Resistivity and specific heat of $MnBi_2Te_4$, for zero fields and $H \parallel c$; taken from Ref. [48, 111].

The consistent magnetic behavior has been experimentally validated through X-ray magnetic dichroism, where the polarization of the Mn atom is observed, suggesting AFM order along the easy axis. This confirmation is further supported by bulk magnetic SQUID measurements, as evidenced by the cusp in both the zero-field-cooled (ZFC) and field-cooled (FC) curves, indicating a magnetic transition at T_N of 24.2(5) K (see Fig. 3.2 a. When measured along $H \parallel c$ below T_N, the magnetization exhibits a more rapid decrease and consistently lies well below the susceptibility curve measured in the

$H \perp c$ direction, indicating an out-of-plane anisotropy (Fig. 3.2a). The Curie-Weiss fit gives a small positive value of θ_{CW} = 3(3) K. This anisotropy is further confirmed by isothermal magnetization measurements (Fig. 3.2b), where applying the magnetic field along both directions ($H \parallel c$ and $H \perp c$) reveals a clear anisotropic response. Furthermore, a spin-flop transition occurs at approximately 3.5 T only along $H \parallel c$, altering the AFM ground state to a canted AFM state[112–114]. The AFM transition temperature at $T_N \approx$ 24–25 K is further confirmed by different techniques: [112, 115–121] such as resistivity measurements shown in Fig. 3.2c [111, 112, 120–123] and specific heat (Fig. 3.2d) [111]. Furthermore, the magnetic structure has been probed through neutron diffraction, confirming the A-type AFM structure with an ordered magnetic moment per Mn atom of approximately $4.04\mu_B$ at 10 K [116]. Additionally, neutron scattering experiments reveal a much stronger exchange coupling between the interlayers ($j^{\perp} \approx 0.3$) compared to the intralayer coupling ($j^{\parallel} \approx 0.1$) [118].

3.1.2 Band gap and quantum Hall state

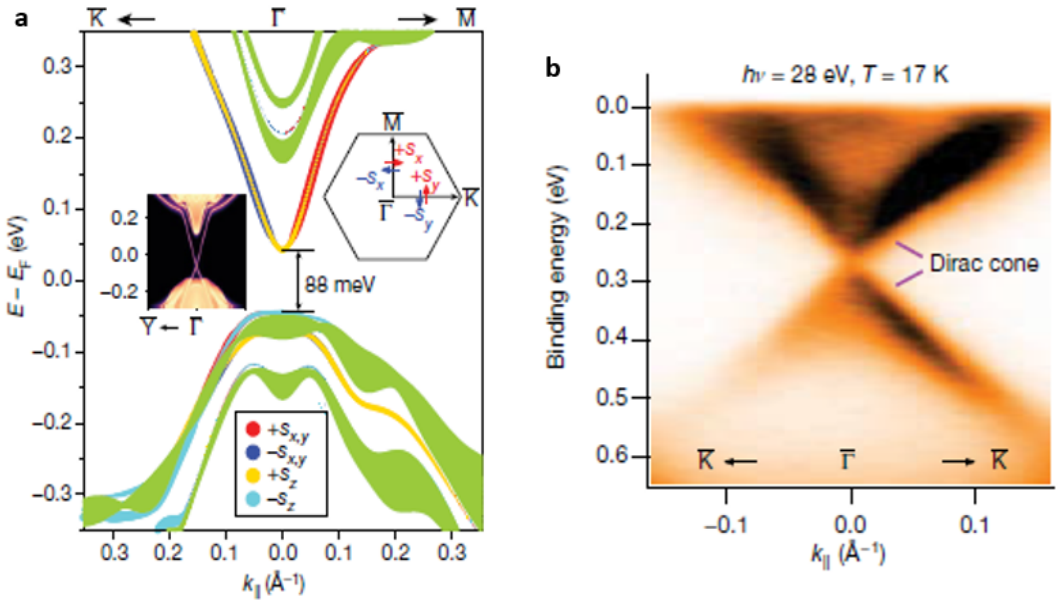

Figure 3.3: (a) Spin-resolved electronic structure of the $MnBi_2Te_4$ calculated on the (001) surface. (b) Dispersion of $MnBi_2Te_4$ (0001) measured at 17 K with a photon energy of 28 eV (surface); taken from Ref. [48].

A-type antiferromagnetism breaks the symmetry known as C $=\mathcal{T}\ \mathcal{S}$, leading to the creation of a bandgap exclusively at the top and bottom surfaces, while the side surfaces, preserving C symmetry, remain gapless. The size and origin of the bandgap in $MnBi_2Te_4$ have sparked controversy, with various reports suggesting different gap sizes at different points in the Brillouin zone. Notably, predictions in Ref. [48, 124] indicate a top surface gap of nearly 90 meV and a bulk gap of 0.2 eV at the Γ point (see Fig. 3.3 a). In contrast, calculations in Ref. [109, 125] propose a bulk gap of 0.18 eV at Γ, accompanied by a reduced top surface gap of 32 meV.

Experimental measurements of the band gap using angle-resolved photoemission spectroscopy (ARPES) have also exhibited discrepancies. Initially, multiple groups observed a substantial-top surface gap ranging between 70–85 meV (Fig. 3.3 b) [48, 112, 126, 127], employing different methods. Some reports even asserted the persistence of the band gap at high temperatures above the magnetic transition, contradicting the antiferromagnetic origin [112]. On the other hand, certain studies claimed gapless top surface states [115, 119, 128–130] due to surface reconstruction of the magnetic moment or the emergence of multi-domains with different magnetization orientations. One of the most common reasons for the variation in the size of the Dirac gap is associated with different amounts of Mn/Bi cationic intermixing, where a few groups showed that the intermixing is responsible for the reduction in the gap [117, 131–133]. Hence, understanding the magnetism of the intermixing through local probes is crucial.

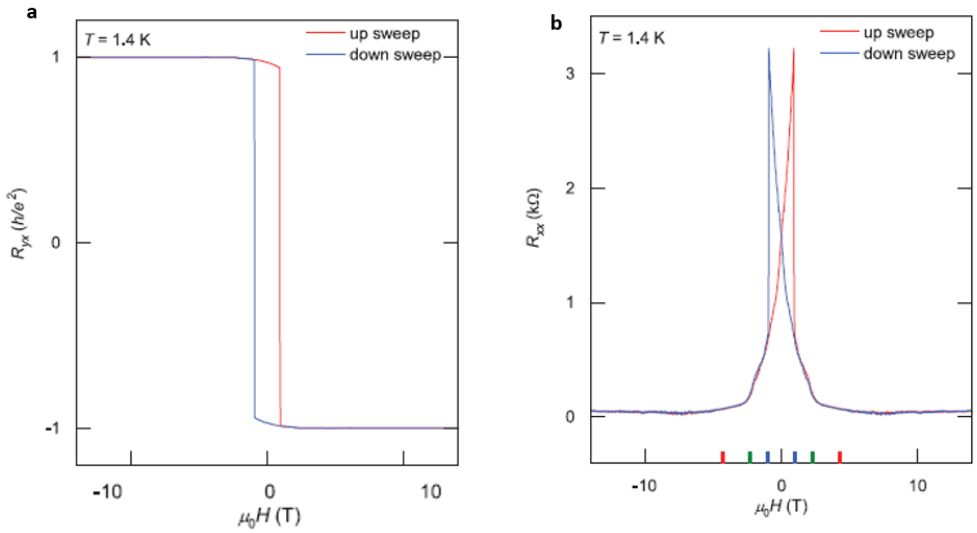

Figure 3.4: (a, b) Magnetic-field-dependent R_{yx} and R_{xx} acquired in the five-layer $MnBi_2Te_4$ sample at T = 1.4 K; taken from Ref. [134].

The distinctive feature of the magnetic topological insulator lies in the quantized anomalous Hall state, wherein the transverse resistivity (ρ_{xy}) approaches nearly h/e^2, and the longitudinal resistivity (ρ_{xx}) concurrently reaches zero. Deng et al.[134] first reported it in $MnBi_2Te_4$ in a five-septuple-layer specimen (5 SL) at T = 1.4 K (in zero field). This peculiar behavior arises due to the incomplete cancellation of magnetism in odd-layer flakes. The researchers observed layer-dependent magnetism, with the 3 and 5 SL flakes, leading to ferromagnetism, while the 4 SL maintained an antiferromagnetic state. Moreover, the transition temperature (T_N) shifted from 25 K in the bulk material to 18 K at 3 SL, attributed to increased thermal fluctuations as the system approaches the two-dimensional limit.

In addition, Deng et al. noted that at a bias voltage of -200V, the hall resistance (ρ_{xy}) attains $0.97h/e^2$, and at the same time, the longitudinal resistivity (ρ_{xx}) reduces to $0.061h/e^2$. Although not achieving perfection at zero fields, these observations provide unequivocal evidence of the QAH state and are equivalent to results obtained for the highest-quality thin films of magnetically doped topological insulators (TI). Furthermore, under a magnetic field of 2.5 T, when the field polarizes individual layers,

they observed the quantization of (ρ_{xy}) reaching $0.998h/e^2$, indicating significant improvement (shown in Fig. 3.4). This quantization persists, comprising only 3% of the resistance, even up to 6.5 K under a magnetic field of 7.6 T. On the other hand, for even-layered 6 SL $MnBi_2Te_4$ an axion-insulator state was reported. This state exhibited gapped bulk and surface states, along with a quantized magnetocaloric effect. Upon sweeping the magnetic field from -3.5 T to 3.5, the Hall resistance (ρ_{xy}) consistently remains at zero, while the corresponding longitudinal resistivity increases, reaching up to $7.5h/e^2$, in line with the spin flop transition. Beyond the spin-flop transition field, at 9 T, the emergence of a quantized Hall plateau at $0.974h/e^2$ was observed [122].

Similar to the spin Hall effect, the layer Hall effect was also detected in a six-layer configuration of $MnBi_2Te_4$ [135]. The application of an electric field modulates the Hall current within the top and bottom layers, inducing an imbalance by breaking $\mathcal{PT}$ symmetry. This perturbation splits the degenerate bands, resulting in variations in carrier concentration and, consequently, a substantial anomalous Hall conductance. Gao et al. observed a pronounced anomalous Hall effect (AHE) in a 6 SL specimen in the presence of an electric field, which was absent in its absence. The AHE vanished above the Neel temperature (T_N) and exhibited a reversed behavior when the direction of the electric field is reversed[135]. Notably, beyond these prominent experimental findings of quantized states, there were multiple reports of the anomalous Hall effect observed in both even and odd layer configurations[136, 137], as well as of quantized Hall effects under high magnetic fields[138].

Achieving the QAHE in thin layers not only needs to speed up the deposition of high-quality thin films and facilitate the observation of phenomena in the monolayer limit but also optimize crystal growth. Consequently, the materials community is actively seeking topological insulators with intrinsic ferromagnetism. Different approaches are presently considered in this material class: one involves increasing the gap between septuple layers by introducing a non-magnetic quintuple layer of Bi_2Te_3. Given the layered nature of the crystal structure, it is highly adjustable, potentially leading to the $MnBi_2Te_4$ $(Bi_2Te_3)_n$, n = 1, 2, family. This will be further discussed in the next section

3.2 $(MnBi_2Te_4)(Bi_2Te_3)_n$, n = 1, 2

In Fig. 3.5 the layered structure of the family compound and the direction of magnetic moments are illustrated. When n=0, it refers back to $MnBi_2Te_4$, while n=1 and n=2 correspond to $MnBi_4Te_7$ and $MnBi_6Te_{10}$. While the crystal structure remains consistent within the family, the magnetism undergoes significant changes due to altered exchange interactions. The AFM interlayer exchange tends to decrease with increasing the number of nonmagnetic layers (n) in the $MnBi_2Te_4(Bi_2Te_3)_n$, n = 1, 2, family. Increasing the layer count (n) beyond 3 significantly diminishes the interlayer interaction, resulting in a 2D ferromagnet [139]. Different terminations of the $MnBi_2Te_4$ SL and Bi_2Te_3 QL are also possible. This modification affects the electronic properties of the topological surface states and the gap at the Dirac point.

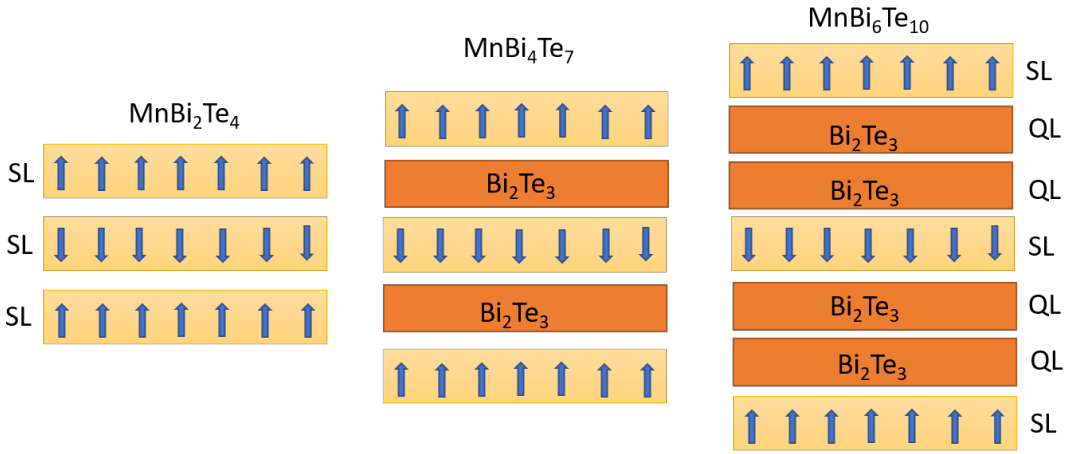

Figure 3.5: $(MnBi_2Te_4)(Bi_2Te_3)_n$, n=0,1,2 compounds consist of alternating five-layer (QL) and magnetic seven-layer (SL) blocks. The spin alignment (blue arrows) shown in each SL layer is based on Ref. [140].

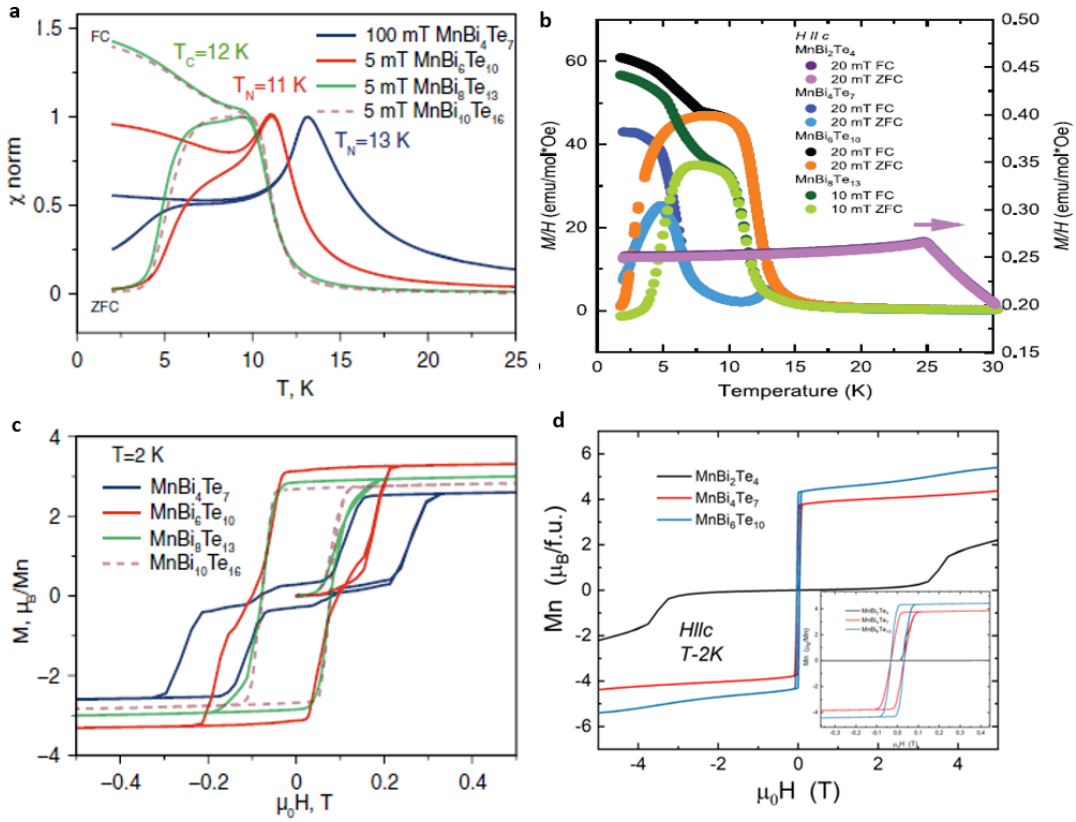

Figure 3.6: Magnetic properties of $MnBi_2Te_4$ family (a, b) Magnetic susceptibility as a function of temperature measured in small magnetic field in ZFC and FC conditions (c, d) Field-dependent magnetization curves taken at T = 2 K for $MnBi_2Te_4$ family compounds ; (a, c) taken from [140], (b) taken from Ref. [141] (d) replotted from Ref. [48, 141, 142].

Antiferromagnetic characteristics are reported in both $MnBi_4Te_7$ and $MnBi_6Te_{10}$ compounds, with respective Neel temperatures (T_N) of 13.2 K and 11.9 K, which were further suppressed upon applying a magnetic field, as evidenced by the temperature-dependent resistivity and magnetization curves in Ref. [140] (Fig.3.6a). The Curie-Weiss approximation for the $MnBi_4Te_7$ sample yields a θ_{CW} of 13.2 K, with a positive sign indicating a notable ferromagnetic contribution compared to the $MnBi_2Te_4$ sample, where θ_{CW} was relatively small, nearly 1 K, indicating that an additional non-magnetic layer reduces the antiferromagnetic interlayer exchange. Notably, the FC curve exhibits a slight divergence at low temperatures but is not discussed in Ref. [140]. Additional studies on different samples corroborated the presence of an antiferromagnetic ground state in $MnBi_4Te_7$ ([143]), along with the observation of a distinct metamagnetic-like transition at 6 K and a separate 13 K antiferromagnetic transition ([126, 144]) (shown in Fig.3.6). With n = 2, the (T_N) further decreased to 11.9 K (Fig.3.6a). This leads to an increased divergence between the ZFC and FC curves at lower temperatures, suggesting enhanced competition between ferromagnetism and antiferromagnetism [140]. It has to be noted, however, that contrary to these findings, various other reports suggested either exclusively ferromagnetic ground states in $MnBi_6Te_{10}$ (Fig.3.6b) [141, 145, 146] or the coexistence of both antiferromagnetic and ferromagnetic behavior ([147]).

Expanding to n = 3, 4, ferromagnetic-like behavior with a divergence between ZFC and FC curves just below the Curie temperature (T_C) of 12 K is observed (Fig.3.6 a,b). Lately, in the literature, these controversial findings were suggested to arise from different sample stoichiometries and/or amounts of antisite disorder, which has been further investigated in this PhD thesis. The isothermal magnetization behavior of $MnBi_4Te_7$ at T = 2 K exhibits antiferromagnetic characteristics, featuring a spin-flip transition reminiscent of $MnBi_2Te_4$ however, at much lower fields of $\approx$ 0.25 T, and hysteresis is evident at T = 2 K (refer to Fig. 3.6 c) [140]. The spin-flip transition is still present but further reduced to 0.07 T in $MnBi_6Te_{10}$. In other reports, both for $MnBi_4Te_7$ and $MnBi_6Te_{10}$ a pronounced hysteresis at low temperatures has been observed, associated with metamagnetic and ferromagnetic behavior in the samples, which is attributed to the intermixing that promotes ferromagnetism [126, 141, 144]. Furthermore, for n = 3, an almost ideal hysteresis loop, characteristic of ferromagnetic material, is demonstrated in [139, 140, 148].

The electronic structure and topological surface states within this material family, specifically for n = 1 and n = 2, exhibit variations depending on different surface terminations, whether it be the magnetic $MnBi_2Te_4$ SL on the surface or the non-magnetic Bi_2Te_3 layer on top [126, 140]. This distinction is also evident across different numbers of nonmagnetic layers. Notably, a more intricate electronic structure of surface states, valency band, and conduction band is observed with substantial differences in binding energy when the nonmagnetic quintuple layer (QL) is positioned on top [146, 149–152]. Moreover, when the magnetic SL layer is positioned on top, the electronic structure of $MnBi_4Te_7$ and $MnBi_6Te_{10}$ differs from that of $MnBi_2Te_4$ with additional branches of the conduction band emerging near the Dirac cone due to the hybridization of the top layer Dirac cone with the nonmagnetic bottom layer [150]. This effect is more pronounced in $MnBi_4Te_7$ than in $MnBi_6Te_{10}$. A Dirac point gap ranging from 34 meV to 54 meV has been observed in different samples of $MnBi_4Te_7$ [149, 150], while other reports contend that these materials exhibit gapless surface states [146, 151,

152]. A quantized Hall state has been observed in $MnBi_4Te_7$ at a relatively high temperature of T = 7 K and rises to h/e^2 for a self-organized, less disordered topological superlattice of thick 300 nm crystals [153]. Last but not least, more predictions, such as unconventional AHE states, layer-dependent Hall effect, and topological Hall states, are reported [144, 154–158].

3.3 $MnSb_2Te_4$

Another interesting approach to realizing a ferromagnetic topological insulator involves replacing Bi atoms with Sb atoms. $MnSb_2Te_4$ has the same crystal structure as its Bi counterpart. In its ideal crystal configuration, it is anticipated to exhibit an AFM ground state below 19 K and a non-topological band structure with an energy gap of 0.132 eV. However, introducing a mere 30% of Sb increase in the spin-orbit coupling (SOC) is predicted to induce band inversion, transforming it into an axion insulator [124]. By adjusting cation intermixing in the Mn and Sb positions, a ferromagnetic ground state and even a Weyl semimetal state may be achievable, as suggested by various studies [124, 159–162]. Further contradicting the initial prediction on the "ideal" material, it was reported by Eremiv et. al that this whole family member $(MnSb_2Te_4)$ $(Sb_2Te_3)_n$, n=0,1,2 of stoichiometric compounds are topologically nontrivial. In the ground state, the first three members of the family (n=0,1, 2) are 3D antiferromagnetic topological insulators, and due to a weak interlayer exchange coupling, these materials can be field-driven into the FM Weyl semimetal (n= 0) or FM axion insulator states (n$\geq$1). [163].

The magnetic ground state of $MnSb_2Te_4$ was proposed by Murakami et al. a few years back in 2019, who conducted a comprehensive investigation of the magnetic properties of powder samples through various techniques and first-principle calculations. Their findings suggested the emergence of spontaneous magnetization below 25 K, attributed to site intermixing between Mn and Sb sites, ultimately leading to a *ferrimagnetic* ground state [164]. Moreover, the intermixing involves the Mn atom, originally designated for the 3a sites (central site), with some occupying other cationic sites, particularly the 6c site of Sb. Similarly, Sb exhibits partial occupancy of the Mn 3a site. This site intermixing phenomenon was further substantiated in single crystals by Liu et al. [165]. They started to study the profound impact of intermixing, the consequences of synthesis, and the growth conditions of different samples, noting a change in the interlayer magnetic coupling from AFM with a transition temperature (T_N) of 19 K to ferromagnetic coupling with a T_C of 34 K (shown in Fig 3.7). Their electronic structure analysis, based on band structure calculations, indicated that this intermixing not only promotes ferromagnetic coupling but also plays a crucial role in inducing band inversion within the system. The insights provided by these studies contribute to a deeper understanding of the complex magnetic and electronic behavior exhibited by $MnSb_2Te_4$, shedding light on the role of site intermixing in shaping its ground state properties. Contradicting these results, a glassy ground state has been proposed by Li et. al. [166] in the $MnSb_2Te_4$ sample owing to the higher amount of intermixing in the system. The transition temperature has been reported to be 24 K, like in the powder samples. From an experimental standpoint, the findings are intricate. In contrast to $MnBi_2Te_4$, which exhibited a highly stable ground state and transition temperature, there are indications of complexity in the magnetic properties of $MnSb_2Te_4$. The synthesis procedures differ across reports, impacting both magnetic order and cation

intermixing. Given that the magnetism in the system is attributed to Mn^{2+}, the quantity and exact positions of Mn in the crystallographic structure become pivotal factors influencing the magnetic exchange coupling.

Despite the initial anticipation of $MnSb_2Te_4$ having a trivial band structure and an AFM ground state in its ideal crystal configuration, certain experiments have indicated the presence of a finite band gap at the Dirac point. This observation suggests the potential for $MnSb_2Te_4$ to be a ferromagnetic topological insulator. Wimmer et al. [167] propose that introducing a small percentage of excess Mn beyond the ideal stoichiometry could effectively double the transition temperature to a range of 45–50 K. Their thin film samples exhibit the necessary out-of-plane anisotropy and spin polarization. The two-dimensional Dirac cone is positioned proximate to the Fermi level, and scanning tunneling spectroscopy (STS) reveals the closure of an induced magnetic bandgap above the observed Curie temperature [167]. Further, the proposed Weyl state was observed in the spin-polarized state of the $MnSb_2Te_4$ [168], where they observe a single pair of Weyl points setting near the Γ point at the Fermi level without band intermixing. Their AHE measurements were further assisted by the first principle calculations, and similar transport measurements were also reported by [169]. Note that these studies were undertaken in parallel to our own work and are in overall agreement with our results on the magnetic ground state and the impact of intermixing on the magnetic properties.

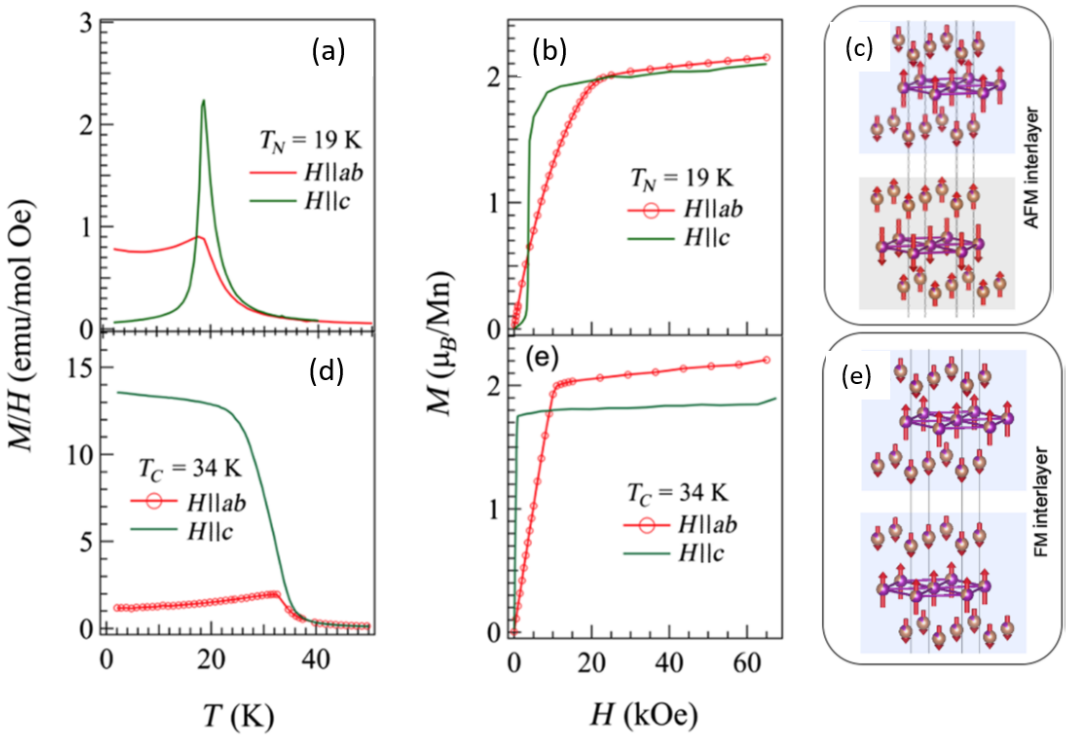

Figure 3.7: $MnSb_2Te_4$ single crystal properties (a,d) DC susceptibility along both $H \parallel ab$ and $H \parallel c$ for both AFM and FM samples; (b,e) Isothermal magnetization for both AFM and FM samples; (c,e) AFM and FM structure for from neutron diffraction; taken from [165]

3.4 Challenges and aims

The major challenge of this family of samples is the intermixing between the Mn (3a) site and the Bi/Sb (6c) site, which is unavoidable in this family of materials due to similar ionic radii. While some studies suggest that the Mn antisite aligns antiparallel to the main Mn site in $MnSb_2Te_4$, this phenomenon isn't thoroughly investigated and understood within the $(MnBi_2Te_4)(Bi_2Te_3)_n$, n=0,1,2 , likely due to limited intermixing detectable by neutron diffraction alone. Consequently, alternative methods are necessary to gain deeper insights into the magnetism of these Mn antisite configurations and to correlate them with the real crystallographic structure and composition of the actual compound. Furthermore, the exact impact of intermixing on strengthening magnetic ordering or amplifying ferromagnetism remains elusive since more factors besides pure intermixing change the magnetic and electronic ground states, such as Mn excess/off-stoichiometry. Many studies in the literature have been undertaken on "arbitrary crystals without thorough and detailed crystallographic characterization."

- To assess the relevance of its isostructural analog, $MnSb_2Te_4$, as a potential QAH candidate, the roles of Mn/Sb site mixing and cationic vacancies need to be clarified. Recent findings have shown that non-stoichiometry in $Mn_{1\pm x}Sb_{2\mp x}Te_4$ is an efficient tuning knob to achieve a net spin-polarized state and to raise the magnetic ordering temperature well above that of $MnBi_2Te_4$. Hence, the main focus of the next two chapters is to understand the magnetic interactions and ground state of $MnSb_2Te_4$ single crystalline samples and the tuning of the magnetic ordering by increasing the Mn stoichiometry, which has not been discussed in detail in the literature up to now. The primary objective for these compounds has always been to enhance the T_C so that QAHE could be observed at an elevated temperature. This goal will be achieved via a comprehensive study of high-quality single crystals that have been thoroughly characterized using different structural techniques before the magnetization investigations.

- The second major aim of this thesis is to understand the role of intermixing on magnetic properties through a comprehensive study of synthesis and local spectroscopic techniques like NMR and μSR in powder samples of $MnSb_2Te_4$ and $(MnBi_2Te_4)(Bi_2Te_3)_n$, n=0,1,2 to find a universal picture within the whole family of compounds.

Chapter 4

Tuning the magnetic order of $MnSb_2Te_4$

The conflicting findings regarding the magnetic ground state of $MnSb_2Te_4$ along with the insufficient examination of anti-site intermixing within each sublattice and its impact on the magnetic properties, called for detailed structural and magnetic assessments coupled with theoretical computations. This endeavor aims to gain a comprehensive understanding of the interplay between disorder and magnetic properties in this compound. Some of the findings presented in this chapter have already been published in our own previous work, Ref. [5].

4.1 Crystal structure of $MnSb_2Te_4$

All the samples used in this chapter are synthesized and structurally characterized by the group of Dr. Anna Isaeva at the Technical University of Dresden. Single-crystalline $MnSb_2Te_4$ samples are synthesized using the solid-state method. The first sample will be denoted as Sample 1 (S1), which was synthesized by annealing precise quantities of MnTe and Sb_2Te_3 at 630 °C in an evacuated quartz tube for 10 days, followed by quenching in water. After quenching, the ampules contained ingots of solidified melt that were cracked open to give two types of samples. On the one hand, the resulting metallic crumbs were either ground for powder diffraction or pressed into pellets for magnetic measurements. On the other hand, the crumbs were inspected through an optical microscope, and flat specimens with mirror-like surfaces were selected for single-crystal diffraction and energy-dispersive X-ray spectroscopy. These samples were then measured on a Rigaku SuperNova four-circle diffractometer, fitted with a molybdenum tube and an AtlasS2 detector. The data was subsequently indexed and integrated in the respective diffractometer software CrysAlisPro and the crystal structures were solved and refined with SUPERFLIP and JANA2006. Upon inspection of reciprocal space reconstructions, neither data set showed any sign of diffuse scattering or superstructure reflections. Constraints EXYZ were used to place both Mn and Sb atoms at the same position, and EADPs were fixed to be equivalent. The total occupancy of each shared position was fixed to a total of 1 but the occupancies of each element were allowed to freely vary. However, neither of the samples showed any significant change in occupancies after this, indicating that no vacancies could be found in the data sets. As a consequence, the refined compositions are electroneutral.

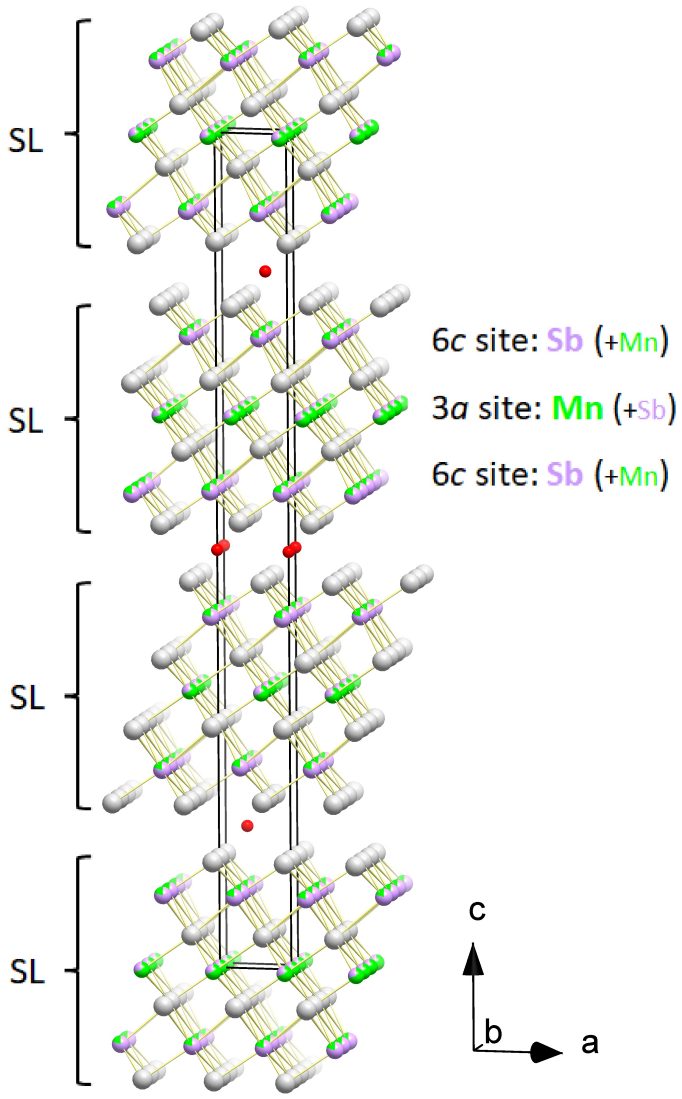

Figure 4.1: The crystal structure of $Mn_{1+x}Sb_{2-x}Te_4$: SL – septuple layer; grey circles - tellurium, lilac circles - antimony, green circles - manganese. The red circles indicate the 3b site that is partially populated in the x $\simeq$ 1.0 crystals (see text); taken from own publication, Ref. [5].

$MnSb_2Te_4$ crystallizes in the centrosymmetric space group $R3\bar{m}$ (number 166), with lattice parameters a = 4.2 Å and c = 40.8(2) Å. Similar to its sister compound based on Bi, the structure is composed of septuple layers of Te–Sb–Te–Mn–Te–Sb–Te arranged along the c-axis and separated by van der Waals gaps (illustrated in Fig. 4.1). In the ideal unit cell, Mn occupies the Wyckoff position 3a (0, 0, 0), while Sb and Te are located at the 6c Wyckoff positions; however, refinements on crystal S1 have shown that each septuple layer exhibits a Te–Sb–Te–Mn–Te–Sb–Te sequence with intermixing of Mn and Sb on Mn 3a and Sb 6c sites. Although there is experimental evidence suggesting vacancies, such as an incomplete site filling at the 3a and 6c sites, the quantities remain a subject of debate. According to theory, vacancies, having the highest formation energy among all defects, are less likely to occur.

Cation intermixing, a predominant occurrence, is primarily attributed to the closely matched atomic radii of Mn (2.05 Å) and Sb (2.2 Å). Noticeable differences in angles,

particularly around the central 3a position, can be linked to the size differences between Mn and Sb, as well as their respective occupancy variations [6]. The next task was to quantify this intermixing quantitatively. Accurate structural analysis is challenged by the simultaneous possibility of two types of defects. There is a correlation between the determined Mn-to-Sb ratios and the amount of vacancies in a refinement procedure, so just one scattering probe cannot yield a meaningful quantification for both parameters. This correlation depends on the magnitudes of the scattering amplitudes and is, therefore, different for x-rays and neutrons. Thus, a joint analysis using single-crystal data obtained by room-temperature x-ray diffraction on sample S1 and a combined Rietveld refinement from x-ray (297 K) and constant-wavelength neutron (60 K) powder diffraction data on a polycrystalline sample with a very similar stoichiometry was performed. The results from the different techniques with their constraints helped in quantifying the exact amount of intermixing, i.e., the 3a site is occupied by 70% Mn/30 % of Sb, and the 6c site has 19% Mn/81% of Sb with an overall composition of $Mn_{1.08}Sb_{1.92}Te_4$. Separately, EDX analysis has been performed on the same crystal, which leads to an average composition of $Mn_{1.05(1)}Sb_{2.01}$ Te_4, in good agreement with the refined composition from the single-crystal measurement. More details on the synthesis procedure and structural analysis were published in our own publication, Refs. [5, 6].

4.2 DC magnetic properties of $MnSb_2Te_4$

This sample has been further investigated using a Quantum Design SQUID vibrating sample magnetometer for studying the bulk magnetic properties and for elucidating the magnetic ground state and transition temperature of $MnSb_2Te_4$.

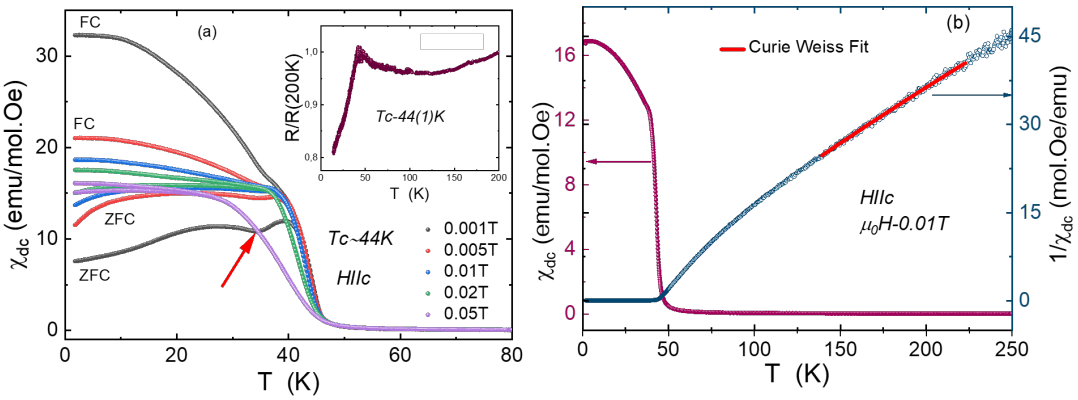

Figure 4.2: Magnetic DC susceptibility of sample S1 as a function of temperature for applied magnetic fields 1 mT $\leq \mu_0 H \leq$ 50 mT parallel to the *c* direction. Inset: longitudinal resistance normalized at T = 200 K as a function of temperature. (b) Temperature dependence of the magnetic susceptibility of S1 up to 250 K together with its inverse for $\mu_0 H$ = 10 mT applied parallel to the *c* direction. The red line shows the Curie-Weiss fit; taken from own publication, Ref. [5].

The temperature dependence of the DC magnetic susceptibility of Sample S1 (shown in Fig. 4.2 a) was investigated along H$\|$ c for various magnetic fields between 1 mT

$\leq \mu_0$ H $\leq$ 50 mT. Both ZFC and FC measurement protocols were employed while sweeping temperatures from 1.8 K to 250 K. Upon decreasing the temperature, there is a notable sharp rise in the magnetic susceptibility at $T_C = 44$ K (where T_C is defined as the inflection point of the susceptibility curve), accompanied by a divergence between the ZFC and FC curves, indicating the emergence of long-range ferromagnetic-like order. Interestingly, for μ_0H$\geq$ 50 mT, (i) the curves are broadened, and the magnetic transition at T_C = 44 K shifts to a slightly lower temperature, which otherwise occurs when there is a competing antiferromagnetic order, and (ii) the bifurcation of the ZFC and FC data is fully suppressed. Apart from the bifurcation, a notorious dip is observed around 40 K in both ZFC and FC curves, although only for low magnetic fields μ_0 H $\leq$ 20 mT. The critical temperature was validated through measurements of the resistance versus temperature at zero magnetic fields, as depicted in the inset of Fig.4.2a.

The inverse magnetic susceptibility (Fig. 4.2(b)) was fitted in the paramagnetic region (140-220 K) with the modified Curie-Weiss Law:

$$\chi(T) = \chi_0 + \frac{C}{T - \theta_{CW}}, \tag{4.1}$$

where χ_0, C and θ_{CW} represent the temperature-independent magnetic susceptibility contribution (core diamagnetism and Pauli paramagnetism), the Curie constant, and the Curie-Weiss temperature, respectively.

From such a fit, χ_0 = 0.0049 emu/mol Oe and a positive θ_{CW} = 22(5) K deviating from the critical temperature T_C = 44 K have been obtained. This, along with the non-linear behavior of the inverse magnetic susceptibility curve below 140 K (see Fig. 4.2b), suggests the presence of competing AFM and FM interactions. Additionally, the effective magnetic moment was determined from the formula $C = N_A\mu_{\text{eff}}^2/3k_B$ yielding $\mu_{\text{eff}} = 5.6(1)\mu_B$/Mn, closely matching the theoretical value of $5.92\mu_B$ for high-spin Mn^{2+} (S = 5/2).

The temperature dependence of the magnetic susceptibility was also measured for magnetic fields applied in the *ab* plane, as shown in Fig. 4.3a. Again, a substantial bifurcation between the ZFC and FC curves is observed. Interestingly, instead of an additional increase of the magnetic susceptibility for T > T_C, a downturn is observed for H ∥ ab and for μ_0H > 10 mT. The T_C also decreases by increasing the applied magnetic field. the most likely scenario for the origin of the downturn in the magnetization curve for H ∥ ab is a continuous reorientation of the magnetization direction as a result of an interplay between the magnetocrystalline anisotropy, field, and temperature, as seen in other 2D materials like $Cr_2Ge_2Te_6$ [170]. The applied field in *ab* aligns the magnetization along the field direction; however, the magnetocrystalline anisotropy favors the magnetization to be along the c direction, which leads to tilting of the magnetization away from the field direction, resulting in a reduction in the H∥ *ab*. An important observation is the presence of a dip and a kink at around 40 K, just below the ordering temperature. This characteristic was also noted in other orientations, and it was explored further through AC susceptibility measurements (see below).

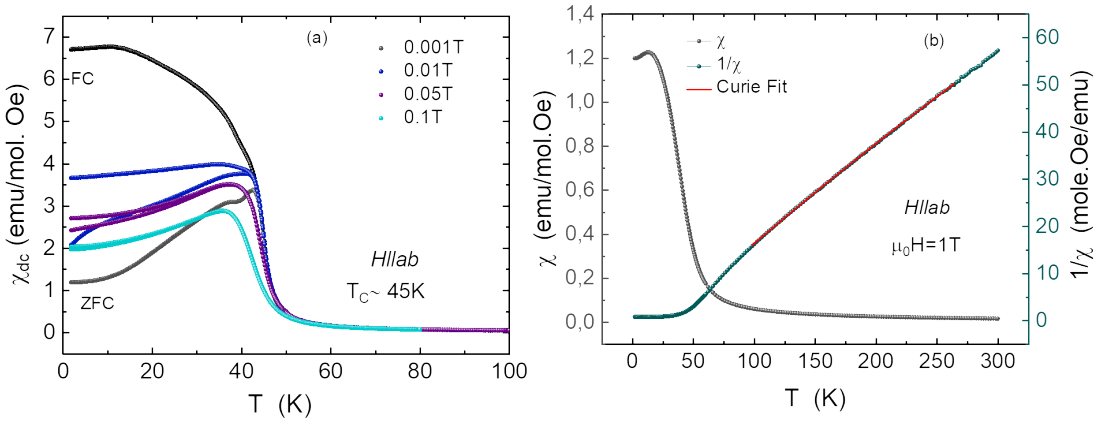

Figure 4.3: (a) DC magnetic susceptibility of S1 as a function of temperature for magnetic fields 1 mT $\leq \mu_0 H \leq$ 100 mT applied in the *ab*-plane. (b) Temperature dependence of the magnetic susceptibility of S1 up to 250 K together with its inverse for μ_0H = 10mT applied in the *ab* plane. The red line shows the Curie-Weiss fit.

Moreover, fitting the inverse susceptibility for H$\|$ ab with a Curie-Weiss model using Eq. 4.1 yields $\chi_0 = 0.00192$ emu/mol·Oe and $\theta_{CW} = 29(5)$ K, which again deviates from the critical temperature $T_C = 45$ K, confirming the competition between FM and AFM interactions in the sample. The effective magnetic moment μ_{eff} is determined to be 5.8(1) μ_B/Mn, closely aligning with the spin-only theoretical value. The similar θ_{CW} and μ_{eff} values along both directions indicate a rather isotropic behavior in the paramagnetic high-temperature regime.

The field dependence of the isothermal magnetization of Sample S1, with the magnetic field aligned parallel to both the crystallographic *c* direction and the *ab* plane, is presented in Fig. 4.4a,b for temperatures spanning from 2 K to 35 K. Despite a notable rise in magnetization, reaching approximately $1.5\mu_B$/Mn at low applied magnetic fields (< 1 T) as anticipated for a ferromagnetic material, the magnetization curves do not achieve complete saturation. Instead, they exhibit an S-shaped pattern up to at least 5 T, accompanied by an apparent coercive field of around 20 Oe, which, however, is very close to the limit of device resolution. At 7 T, the magnetization does not exceed 2 μ_B/Mn, indicating a loss in the magnetic moment associated with a possible ferrimagnetic [164] spin alignment of Mn ions on different crystallographic sites induced by anti-site disorder. It is worth emphasizing that the term *ferrimagnetic* is used here to account for the existence of two different (antiferromagnetically) coupled magnetic sublattices with the same spin value but of different size, i.e., high-spin Mn^{2+} ions on 3a sites and high-spin Mn^{2+} ions on 6c sites, which occupy differently sized sublattices in $MnSb_2Te_4$, as depicted in the lower inset of Fig. 4.4a. This observation has also been noted in several previous studies published parallel to our work [169, 171–173]. Estimating the manganese content at the 6*c* site could be achieved by employing the model proposed by Lai et al. in [173].

$$x = \frac{M_2 - M_1}{4m_0} \tag{4.2}$$

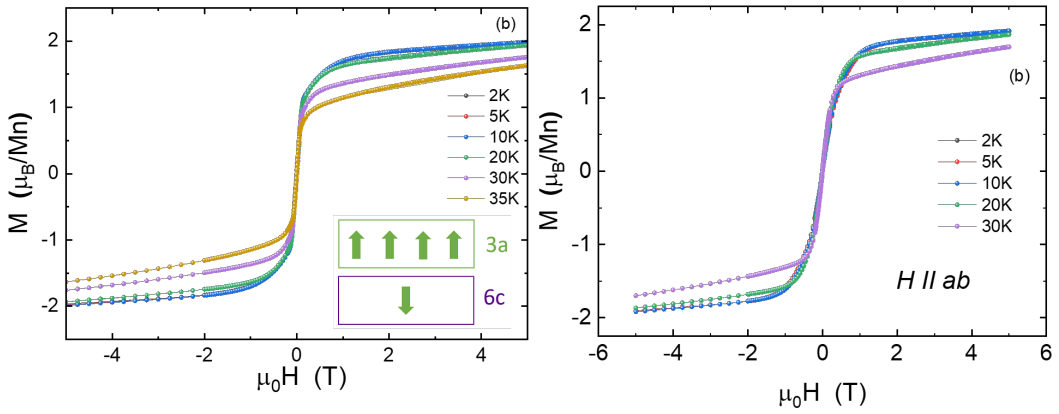

Figure 4.4: (a) Magnetization as a function of the magnetic field applied parallel to the *c*-axis and (b) for the *ab* plane for various temperatures 2 K $\leq T \leq$ 35 K of S1; taken from own publication Ref. [5].

where M_2 is the magnetization in the saturating region (60 T), M_1 is the magnetization at low field, and m_0 is the theoretical local magnetic moment. According to their findings, full saturation of $MnSb_2Te_4$ occurs at high fields, approximately near 60 T. To apply this model, the following rough approximations were made by considering (i) the saturation magnetization observed at (5 T, 2 K) as the low-field saturation plateau M_1, (ii) the absence of vacancies, and (iii) a local manganese moment $m_0 = 4.92\mu_B$, calculated from DFT. It's important to note that the samples investigated in Ref. [173] exhibit a T_C of 28 K, indicating differences with our samples. Despite these approximations, the estimated manganese content at the 6*c* site falls within the range of 15-19%, reasonably aligning with the amount of anti-site disorder identified in the $MnSb_2Te_4$ crystals. The isothermal magnetization measured along the *ab* plane shows similar S-shape behavior as measured along *c* direction; however, it requires a higher field to saturate due to out-of-plane anisotropy in the sample.

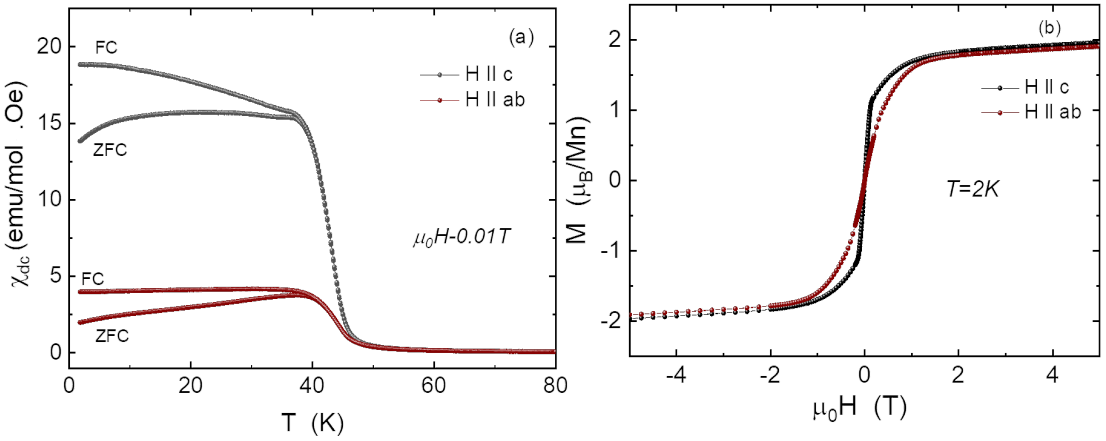

Figure 4.5: (a) Comparison of the magnetic susceptibility of S1 as a function of temperature for both $H \parallel c$ and $H \parallel ab$ (H = 100 Oe). (b) Comparison of the isothermal magnetization curves at T = 2 K for both $H \parallel c$ and $H \parallel ab$ plane; taken from own publication Ref. [5].

In order to better visualize the anisotropy in sample S1, the DC susceptibility and isothermal magnetization are compared for H|| c and H|| ab plane in Fig. 4.5. It is evident that the susceptibility along the *c* direction is four times higher than that along the *ab* plane, as shown in Fig. 4.5a. Additionally, the isothermal magnetization (Fig. 4.5b) along the *c* direction "saturates" more rapidly and achieves almost $1\mu_B$/Mn at 0.1 T than along the *ab* direction, where only $0.35\mu_B$/Mn are observed at 0.1 T, confirming the presence of an easy-axis anisotropy and out-of-plane magnetization. It should be emphasized that this is crucial for achieving the QAHE.

4.3 Ac susceptibility measurements

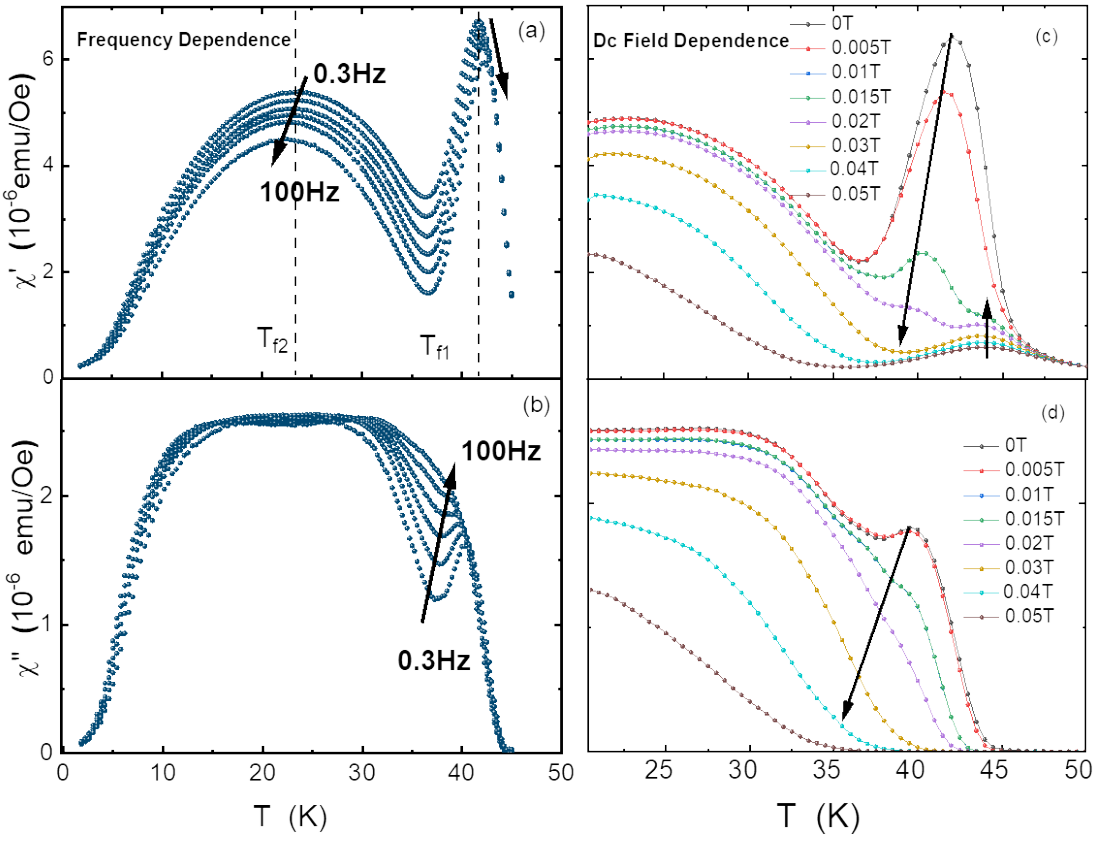

Figure 4.6: Temperature dependence of (a) χ' and (b) χ'' for different frequencies and at 10 Oe dc magnetic field (c) χ' and (e) χ'' at 10 Hz for different values of an applied dc magnetic field (H_{AC} = 10 Oe applied along *c* direction); taken from own publication Ref. [5].

To further investigate the dip observed in the DC magnetic susceptibility around 40 K, the magnetic response of the sample against a perturbation caused by a fixed AC magnetic field H_{AC} = 10 Oe is applied along the *c* direction for temperatures below T_C. AC magnetic susceptibility measurements were performed for several frequencies 0.3 Hz $\leq f <$ 100 Hz and for applied DC magnetic fields 0 Oe $\leq H_{DC} \leq$ 500 Oe. The temperature dependence of the real part of the AC susceptibility χ' is represented in Fig. 4.6 (a) for different frequencies.

Interestingly, two anomalies are present at T_{f1} = 42 K and T_{f2} = 23 K (for 0.3 Hz) showing a weak frequency dependence, pointing towards a "glassy" behavior in this temperature region. While the sharp peak at T_{f1} shifts towards higher temperature with a decrease in its magnitude upon increasing frequency, the broad anomaly at T_{f2} is also suppressed but shifts to lower temperature, pointing at a different origin/state of the two anomalies. For higher frequencies $>$ 100 Hz no clear shift is observable anymore. Both features are not detected in the DC magnetic susceptibility (see Fig. 4.2), where instead a phase transition is observed at slightly higher temperature T_C = 44 K together with a dip around 40 K. Notably, the frequency dependence of each anomaly differs, as highlighted by the black arrows, suggesting different underlying origins. In addition, a large non-zero χ'' (T) was detected for $T < T_C$ confirming the presence of dissipation via slow magnetic relaxation in the compound. Remarkably, for small frequencies, χ'' shows a plateau-like temperature dependence for 15 K $\leq$ T $\leq$ 30 K and drops to zero for both $T \rightarrow T_C$ and $T \rightarrow$ 2 K. For higher frequencies, however, a two-peak structure is observed, similar to χ' . This behavior is presently not well understood.

Characteristic parameters to differentiate between various possible scenarios leading to dissipation were examined further. In long-range ordered magnets, effects contributing to losses and therefore relaxation usually stem from irreversible domain wall displacements (e.g. due to dynamic wall pinning/depinning), irreversible magnetization rotation (hysteresis losses), eddy currents, or diffusion of electrons or defects. In superparamagnetic or spin-glass systems, relaxation usually originates from blocked magnetic moments in irreversible and metastable states. Considering the large values for χ'' for temperatures between 2 K $< T <$ T_C, however, glassy dynamics of larger objects, including more than a single spin, such as domain walls or large spin clusters, seem to be responsible for the magnetic relaxation in our case.

The Mydosh parameter (K), which defines the relative peak shift δT_f per log δf, is given by [174]

$$K = \frac{\delta T_f}{T_f log(\delta f)}. \tag{4.3}$$

For the sharp peak at T_{f1}, K is calculated to be about 0.004, which lies two orders of magnitude lower than those found in systems with purely Arrhenius relaxation, such as non-interacting superparamagnetic particles, and which lies in the lower end of typical values found in canonical spin glass systems [175–179].

After establishing the frequency dependence of the AC susceptibility, we investigated its sensitivity to DC fields while maintaining a constant AC excitation (H_{AC} = 10 Oe, f = 10 Hz), as outlined in Figures 4.6(c,d). Both the real and imaginary components of the susceptibility exhibit significant responsiveness to applied DC fields, extending up to 50 mT. The peak at T_{f1} suppresses upon increasing the field and vanishes at 30 mT. Notably, in the magnetic transition region around T_C = 44 K, a field-independent peak emerges upon suppression of the sharp peak at T_{f1}. This field-independent peak is most likely the initiation of long-range magnetic order at T_C and likely persists even at lower or zero dc magnetic fields, possibly being masked by the prominent frequency-dependent peak at T_{f1} for $\mu_0 H \leq$ 15 mT. The observed "double-peak" feature is consistent with findings in various members of the $MnBi_2Te_4$ family, including Sb-doped $MnBi_2Te_4$ [180], and is indicative of anti-site disorder within this family of compounds.

Magnetic relaxation measurement

To explore the dissipation observed in χ'', primarily attributed to slow relaxation, time-dependent magnetization was investigated, tracking the evolution of $M(t)$ (refer to Fig.4.7). Various relaxation curves were recorded at a constant temperature, each with different waiting periods of 60 s, 120 s, and 180 s. A typical relaxation study involved cooling the sample from 100 K to a specific temperature below T_C in a 10 Oe magnetic field applied parallel to the *c* direction, followed by a waiting period ranging from 60 to 180 s. Subsequently, the magnetic field was turned off, and the field-cooled remanent magnetization was measured at the specified temperatures for 7200 s. The analysis of the time-dependent magnetic moment employed a well-established stretched exponential model[181–183]:

$$M = M_1 \pm M_0 \times e^{(-t/\tau)^{\beta}} \tag{4.4}$$

where $\pm$ denotes FC and ZFC curves, respectively, M_1 represents the ferromagnetic component, M_0 signifies the time-dependent element of the sample's magnetic moment, τ indicates the average relaxation time and β serves as the stretching exponent, reflecting the distribution of relaxation times in the system when $\beta \neq 1$. It's noteworthy that, for all temperatures spanning $2 - 38$ K, the data reveals a finite component, M_0, and $\beta < 1$, indicating slow magnetic relaxation behavior in the magnetization curves below T_C (see Fig. 4.7).

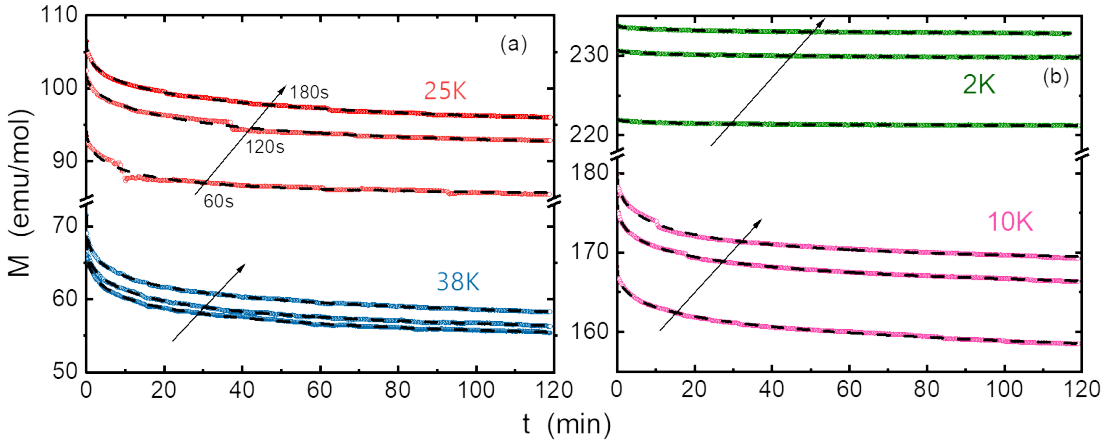

Figure 4.7: (a,b) Magnetization as a function of time $M(t)$ of S1 for temperatures between 2 K and 38 K with different waiting periods (60 s, 120 s, 180 s, the arrow represents increasing order); the dotted line refers to the fitting using Eq. 4.4; taken from own publication Ref. [5].

The timescale for relaxation exhibits strong temperature dependence, ranging from 10-20 minutes at temperatures down to 10 K. Relaxation becomes significantly slower at 2K, reaching orders of magnitude smaller values that pose challenges for detection using this method. These findings align with similar observations of slow magnetic relaxation in other members of the $MnBi_2Te_4$ family [180, 184].

Final insights into the dynamics of the magnetization process were achieved through magnetic memory measurements performed in FC mode at two different fields: $\mu_0 H_1$ = 1 mT (where the dip in magnetization is visible) and $\mu_0 H_2$ = 50 mT (where the dip in magnetization is already suppressed). In the FC procedure, the sample underwent

careful cooling in the presence of a 10 Oe magnetic field aligned parallel to the c axis, descending from 300 K to 100 K at a cooling rate of 10 K/min. Subsequently, the cooling rate was decreased to 1 K/min for cooling from 100 K down to 1.8 K. The measurement sequence involved two waiting periods at T_1 = 40K and T_2 = 20K, each lasting 21600 s. During these waiting periods, the applied field was removed to allow for magnetization relaxation. Following each waiting period, the field was reapplied, and the cooling process resumed.

The outcomes are depicted in Fig. 4.8(a,b). The magnetization recorded during this process, denoted as $M^{\text{int}}_{\text{fcc}}$, exhibits a step-like feature after each pause. Upon reaching 1.8 K, the sample was promptly heated at the same rate and under the same magnetic field conditions, but without interruptions, and the magnetization $M^{\text{mem}}_{\text{fcw}}$ was measured up to 60 K (where FCW stands for field-cooled warming). For comparison, the system was again cooled down to 1.8 K under the same conditions as before but without any waiting periods, resulting in $M^{\text{ref}}_{\text{fcc}}$. The irreversibility apparent in the FC and FCW curves at $T = 20$ K and $T = 40$ K at $\mu_0 H = 1$ mT distinctly indicates magnetic relaxation behavior, a phenomenon that diminishes at modest external magnetic fields around 50 mT, aligning with the findings in the time-dependent magnetization study.

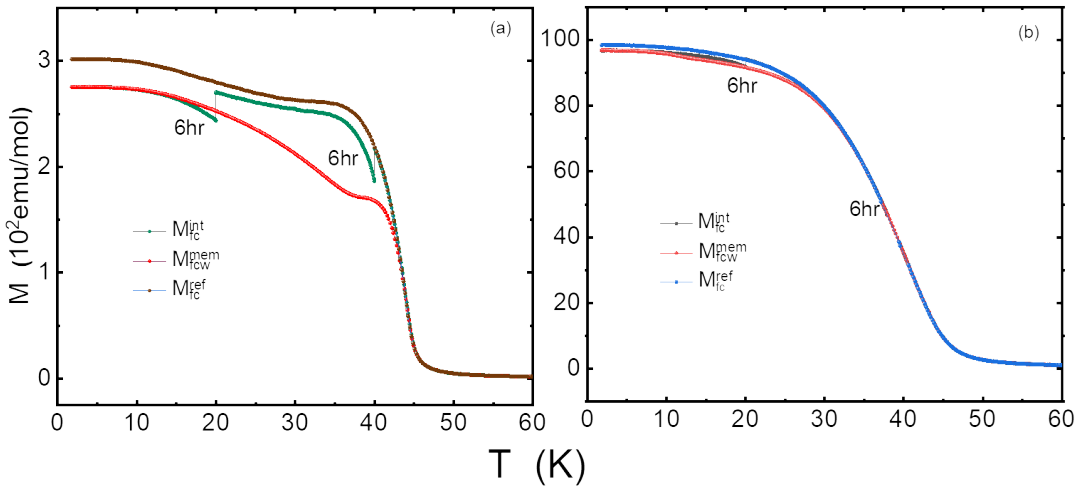

Figure 4.8: Magnetic memory effect in sample S1, while field-cooling at 1 mT (a) and 50 mT (b) for $H||c$. Two waiting periods at T = 40 K and T = 20 K were included in the sequence, where the applied magnetic field was removed for 21600 s; for details, see text; taken from own publication Ref. [5].

Altogether, the combined magnetic relaxation, memory effect, and AC susceptibility studies support "glassy" behavior in the high-T_C disordered $MnSb_2Te_4$ single crystal. Since the magnetic relaxation and frequency-dependent peaks in the AC susceptibility already disappear for very small DC magnetic fields of about 300 Oe, however, we can rule out a canonical spin-glass state in $MnSb_2Te_4$ for which much larger DC fields are typically necessary for a suppression of the spin-glass state [185, 186]. The strong dissipation recorded in χ'' for temperatures 2 K $< T <$ 42 K suggests larger objects, such as soft domain walls or large spin clusters, to account for the observed glassiness in small magnetic fields.

Recently, the origin of the relaxation behavior in $MnBi_2Te_4$ and Sb-doped $MnBi_2Te_4$ was attributed to irreversible domain movements via magneto-optical measurements, and a double-peak behavior in the temperature-dependent AC susceptibility in small DC fields was ascribed to a very soft ferromagnetic domain formation [180]. If this scenario also accounts for the results found for this high-quality $MnSb_2Te_4$ sample S1 with anti-site disorder and a ferrimagnetic ground state, it cannot be pinpointed from current data. Alternative scenarios considering clusters of magnetic spins that randomly orient and freeze just below T_C, where the majority of spins are already ordered in a long-range manner, cannot be ruled out at this point and also depend on the existence of the "additional" third peak observed in χ' for dc magnetic fields below 300 0e. Note that Li *et al.* [187] reported a disordered glassy magnetic ground state of $MnSb_2Te_4$ below a freezing temperature of 24 K, which enters a field-induced ferromagnetic state at H = 1000 Oe, in stark contrast to the results on high-T_C single crystals $Mn_{1.08}Sb_{1.92}Te_4$. For more clarification and a solid conclusion about the spin alignment in the different temperature ranges, a systematic neutron diffraction study is highly desirable.

4.4 Electron spin resonance measurement

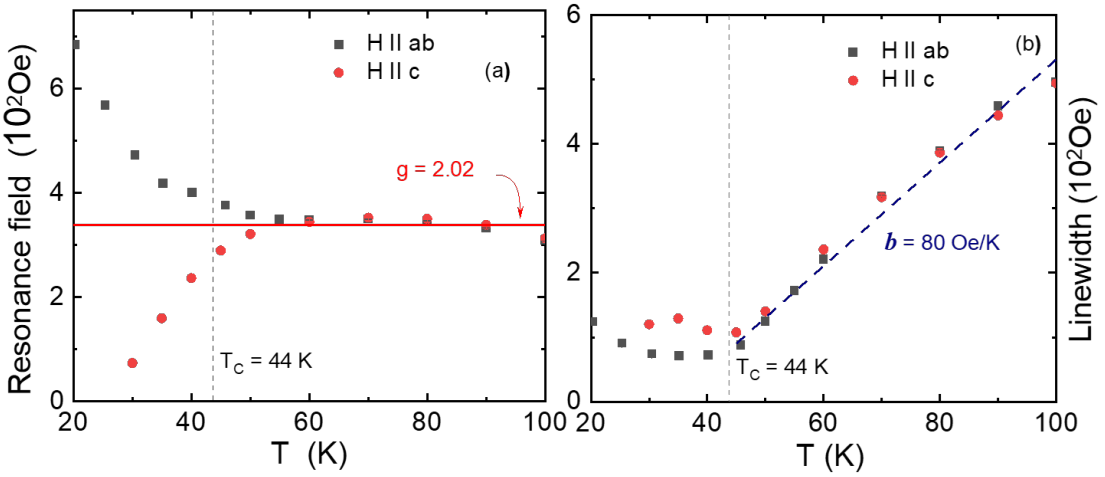

Figure 4.9: (a,b) Temperature dependence of the ESR resonance field and linewidth along H$\|$ ab and H$\|$ c for sample S1; taken from own publication Ref. [5].

The observed spin dynamics in MST called for further (microscopic) methods, such as electron spin resonance (ESR), to gain more insight into the dynamics of this interesting compound. The temperature dependence of the ESR response (see Fig. 4.9) of sample S1 was measured and analyzed by Dr. Alexey Alfonsov and other members of Dr. Vladislav Kataev's group at the IFW Dresden. These measurements were conducted at an X-band frequency of $\nu = 9.56$ GHz, with a magnetic field aligned parallel to both the *ab* plane and the c axis. The primary ESR line was modeled using the asymmetric Dysonian line shape profile commonly observed in conducting samples [188, 189]. The fitted results are depicted in Figures 4.9 (a,b). Notably, we observe that the resonance field remains nearly constant above approximately 50 K, indicating an uncorrelated paramagnetic state of $MnSb_2Te_4$ within this temperature range. As

depicted in Fig. 4.9b, the broadening of initial line A (ΔH) exhibits a notable and consistent increase with temperature above $T \sim 50$ K, indicative of a Korringa relaxation mechanism affecting the Mn spins through interactions with charge carriers, akin to the behavior observed in $MnBi_2Te_4$ compounds [190]. Notably, the Korringa slope $b = 80$ Oe/K, characterizing the linear temperature dependence of the ESR linewidth, $b \propto \Delta H(T)/T \propto [D(E_F)J_{s-d}]^2$, remains constant for both magnetic field orientations, H$\|$ ab and H$\|$ c. Here, $D(E_F)$ represents the Density of states (DOS) at the Fermi level, and J_{s-d} signifies the exchange coupling constant between the Mn d-electrons and mobile charge carriers (electrons or holes). This uniformity of b across different magnetic field directions mirrors the behavior observed in $MnBi_4Te_7$ reports, in contrast to the anisotropic Korringa slope observed in $MnBi_2Te_4$ [190].

In Ref. [190] such anisotropy was attributed to the sensitivity of the DOS to the specific orientation of the Mn magnetic moments under applied fields, particularly at low charge carrier densities $n \sim 10^{19}$ cm^{-3}. DFT calculations suggest the isotropic Korringa slope in $MnSb_2Te_4$ likely arising from the reduced spin-orbit coupling observed in this compound, a feature also noted in the above-shown DC magnetic measurements.

Decreasing the temperature below ~ 50 K leads to a shift of the A-line to smaller fields if the external magnetic field is applied along the c axis, and to higher fields if the magnetic field is in the ab plane. Interestingly, the ESR line starts to shift at a temperature only somewhat larger than T_C determined by magnetization and resistivity measurements (see section 4.2). This behavior is quite different from $MnBi_2Te_4$ and $MnBi_4Te_7$ compounds [190, 191], where the ESR line starts to shift already at $T \sim 60$ K, whereas the ordering temperature is of the order of only ~ 20 K. The closeness of the onset temperature of the line shift and of T_C in $MnSb_2Te_4$ suggests a more 3D-like character of the magnetic order in this compound, which is likely caused by the high degree of the Mn-Sb intermixing, mediating an effectively *ferromagnetic* and stronger in magnitude exchange path between the layers in the c direction as compared to a weaker antiferromagnetic interlayer coupling in $MnBi_2Te_4$.

At temperatures below the ordering temperature $T_C = 44$ K the shift of the resonance line A suggests a transformation of the paramagnetic response into a ferromagnetic one. Remarkably, the spectra contain an additional prominent line B, which corresponds to the second ferromagnetic mode. Below $T = 20$ K for H$\|$ ab and below $T = 30$ K for H$\|$ c the ESR signal cannot be detected anymore because the signals shift out of the available field range $0 - 0.9$ T due to the opening of the ferromagnetic excitation gap exceeding the X-band frequency of 9.56 GHz. The presence of this second mode, together with the opposite shifts of the resonance position of the main line A for two configurations of the magnetic fields (Fig. 4.9a), are typical for an easy-axis (c axis) ferro- or ferrimagnet [190, 191]. Note that due to a relatively small frequency and correspondingly small magnetic fields available in the employed ESR setup it is not possible to elucidate whether the observed resonance response at $T < T_C$ corresponds to the ferro- or ferrimagnetic state of Sample S1.

4.5 Theoretical model

Having comprehensively explored the magnetic properties of sample S1 through experimental means, insights into its magnetic ground state were further achieved via density functional calculations. As discussed in Chapter 3, several reports have elucidated the

impact of Mn/Sb intermixing on the ground state of $MnSb_2Te_4$, generally favoring ferri- or ferromagnetic ground states over the uniaxial antiferromagnetic configuration. Intriguingly, the samples grown for this work exhibit Mn excess relative to the ideal stoichiometry, together with intermixing, introducing a novel dimension for manipulating the magnetic ground state and associated properties.

The density-functional calculations for various structural models were carried out by Dr. Jorge I. Facio from the IFW Dresden. The structural models are given by (see Fig. 4.10)

- S_0 is the Mn deficient model. The Mn in the 2*b* Wyckoff site is replaced by an extra Sb atom.
- S_1, S_2, S_3 are overall stoichiometric models and S_1 represents an idealized, non-mixed case whereas the model S_2 features the Mn in the 4*e* site swapping place with the Sb in one 4*i* site. In the structural model S_3 the Mn atoms in the 2*a* and 2*b* sites are switching places with the Sb atoms in 4*i*.
- S_4, S_5 and S_6 are over stoichiometric structural models, S_4 and S_5 are constructed by Mn populating one of the two available 4*i* sites instead of Sb, while Sb goes into the 2*b* position. The most Mn-rich model S_6 model contains Mn in the 2*a*, 2*b*, 4*e*, and 4*i* sites amounting to the equal concentration of Mn and Sb.

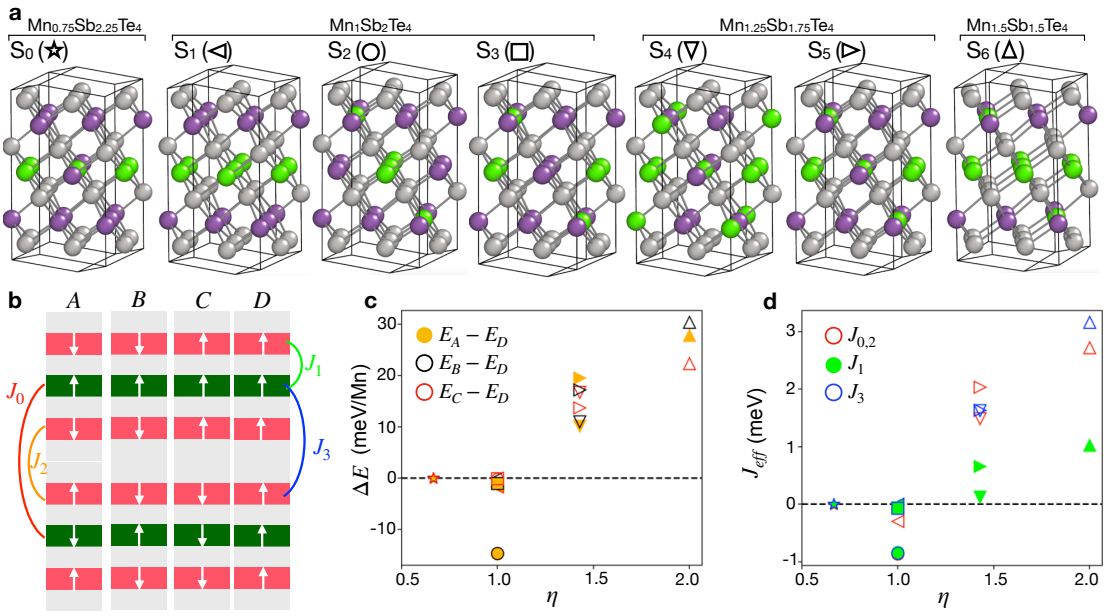

Figure 4.10: (a) Considered structural models comprising one septuple block per unit cell. (b) Models of magnetic order. (c) Total energies of the different magnetic models plotted with respect to the energy of the fully ferromagnetic model D for the different structural models as a function of $\eta = 2\#\mathrm{Mn}/\#\mathrm{Sb}$. (d) Exchange couplings for the different structural models. Each structural model is presented by the symbol specified in panel (a); taken from own publication Ref. [5].

In order to quantify the off-stoichiometry of the different models, the parameter η is defined as:

$$\eta = \frac{2\#\mathrm{Mn}}{\#\mathrm{Sb}}, \tag{4.5}$$

Here, Mn and Sb represent the count of Mn and Sb atoms per unit cell, respectively. The structure was examined for $0.75 \leq \eta \leq 2$, where $\eta = 1$ corresponds to the stoichiometric limit. Various magnetic arrangements were explored, as illustrated in Fig. 4.10b, for which the DFT total energies were computed.

Fig. 4.10c, depicts the variations in total energy among different magnetic orders relative to the fully ferromagnetic structure for each structural model. The plotted data, presented as a function of η, indicates a tendency toward a ferromagnetic ground state for larger values of η. Models without any defects and those with only one Mn replaced by Sb exhibit a preference for antiferromagnetic coupling between the Mn layers.

Nevertheless, the introduction of Mn into the original Sb positions induces significant alterations, the specifics of which depend on the particular structural model. In the case of overall stoichiometric models (where the Sb quantity in the 3*a* site equals the Mn swapped in the 6*c* site), either the magnetic ground state A (for S_2) or B (for S_3) are observed, with the difference $E_A - E_B$ being very small (less than 1 meV). On the other hand, the structure models S_3, S_4, and S_5, featuring an excess of Mn in the native Sb layer, exhibit a preference for the fully ferromagnetic configuration.

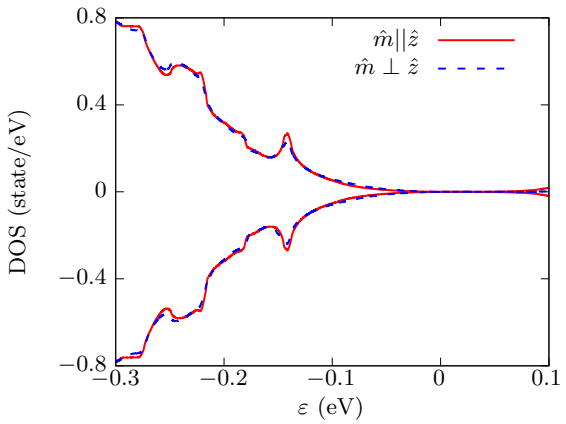

Figure 4.11: a)Density of states for model S1 in the presence of spin-orbit coupling and for different directions of the Mn magnetic moments: along the polar axis z or perpendicular to z; taken from own publication Ref. [5].

In Fig. 4.10d, the computed exchange couplings for various structural models are illustrated, with additional details available in Ref. [5]. Ferromagnetic in-plane coupling in each layer was assumed and $J_0 - J_3$ represents the different interlayer couplings (see Fig. 4.10 b. For the majority of the models, the exchange couplings between Mn atoms in different layers surpass the J_0 value observed in the defect-free model S_1. Essentially, the DFT findings support the notion that Mn atoms occupying native Sb positions promote a more three-dimensional magnetic order. This observation is qualitatively consistent with the comparison of ESR experiments conducted between $MnBi_2Te_4$ and $MnSb_2Te_4$. Further, the DOS calculation with isotropic spin-orbit coupling consistently aligns with the ESR results, indicating negligible anisotropy in the Korringa slope. Fig.

4.11 illustrates the DOS for model 'S_1' with magnetic model A', considering Mn magnetic moments along the polar axis $\hat{z}$ or perpendicular to it. These results, incorporating spin-orbit coupling, demonstrate that the DOS for $MnSb_2Te_4$ remains essentially independent of the direction of Mn magnetic moments.

Overall, the calculations uncover interesting limits raising open questions for further investigations. It is important to elucidate the range $1 < \eta < 2$ in more detail. As follows from Fig. 4.10c,d, there is a progressive change in the sign of various exchange couplings between the layers which may foster a particularly rich magnetic phase diagram.

4.6 Enhancing the magnetic order in Mn-rich $MnSb_2Te_4$

Now, to confirm the theoretical prediction, our collaborators attempted to increase the Mn content in the $MnSb_2Te_4$ samples. Surprisingly, Mn-rich crystals cannot be obtained by slow cooling from melts, and temperature gradients as well as long tempering at constant temperatures do not favor them. Instead, these crystals appear as a small fraction within powdered samples annealed at constant temperatures below the melting point of $MnSb_2Te_4$ (i.e. 640 deg C) for less than 7 days. Crystals with the Mn-enriched fraction have an anisotropic, flattened shape and are on average 100-200 μm in diameter. They are thicker and visually far less layered than the typical $MnSb_2Te_4$ crystals; they also often show triangular facets and intergrown terraces thereof on the largest facets. The EDS studies of several individual, mechanically separated crystallites (50-300 μm) revealed their compositional homogeneity with the record-high Mn content ranging from Mn 23.0(9), Sb 21.6(9), Te 55.4(6) at. % ($Mn_{1.66}Sb_{1.56}Te_4$) to Mn 26.8(5), Sb 18.4(4), Te 55.8(6) at. % ($Mn_{1.92}Sb_{1.32}Te_4$). For the magnetic studies, we used a crystal with the averaged composition 25.0(6) at. % of Mn, 20.1(6) at. % of Sb, and 55.0(4) at. % of Te (determined by EDS). This specimen is denoted S2. It was possible to conduct a Single crystal X-ray diffraction (SCXRD) experiment on an extracted flake of the Mn-enriched composition. The structure refinement converged to the outmost Mn-rich composition of $Mn_{2.01(1)}Sb_{1.19(1)}Te_4$. Upon increasing Mn content, the unit cell retains the trigonal symmetry, contracts in the ab plane, and expands in the c direction. This slightly modified lattice derives from the $MnSb_2Te_4$ structure type by partially filling up an additional crystallographic position, the 3b (1/3 2/3 1/6) site in the middle of the van der Waals gap (see the red circles in Fig. 4.1). The refinement gives a population of ca. 20 %, which is responsible for the more 3D-like shape of the crystals. The cationic intermixing is present in all other cationic positions and amounts to 84 % Mn and 16 % Sb in the 3a site, and 42 % Sb and 58 % Mn in the 6c position within the septuple layer. It was not possible to verify the refined composition by an independent EDS measurement on this same crystal. The discrepancies between the Mn content as per SCXRD and EDS may originate from the semi-qualitative nature of the non-calibrated EDS measurements on crystals and/or varying, partial occupancy of the 3b Wyckoff position.

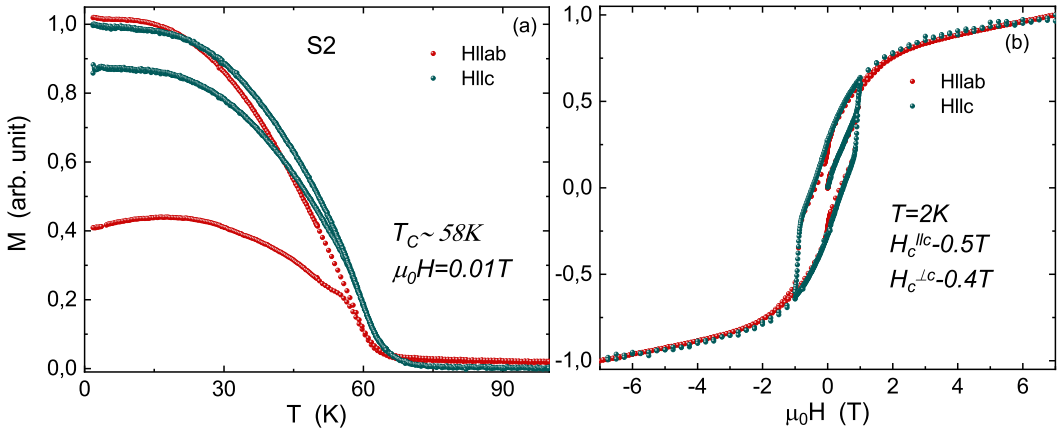

Figure 4.12: (a) Magnetization as a function of temperature and field (b) for S2 parallel to the *c*-axis and the *ab*-plane; taken from own publication Ref. [5].

The temperature and field dependence of the magnetization measured on S2 (for applied magnetic fields parallel to the *c*- axis and *ab*-plane) is shown in Fig. 4.12 a,b. Due to the small mass of the crystal, the mass of the sample could not be measured with the available balance; hence, the magnetization here is discussed only by normalizing to 1 and shown in arb. units. Remarkably, the T_C increases to $\approx$ 58 K (for H$\|$ c) and 59 K(for H$\|$ ab), which indicates enhanced ferromagnetic interaction, supporting the theoretical prediction. This illustrates how sensitive the magnetic behavior (in particular the transition temperature) is, not only to the intermixing pattern but also to the Mn content. Figure 4.12 b shows a comparison of the field dependence of the isothermal magnetization for sample S2 for magnetic fields applied along the c axis and parallel to the ab plane. As expected from the theoretical calculation, a substantial increase in the coercive fields up to 500 mT (H$\|$ c) and 400 mT (H$\|$ ab) is observed. The shape of the hysteresis curve is completely different than that of sample S1, where almost no coercive field was observed. The hysteresis curve shows pot-bellied type behavior (i.e. the width becomes broader as the magnetization goes to zero and then closes down again). Generally, these specific shapes can arise if two ferromagnetic materials with different coercivities and switching field distributions are coupled antiferromagnetically [192].

Further exploiting the temperature profile the collaborators found that further modifications could yield crystals with even higher Mn content, reaching up to $30 - 32$ at.%. However, these crystals undergo a structural transformation, i.e. they no longer remain layered but the van der Waals gap is completely occupied by Sb, and the crystal structure changes to cubic, with a space group Fd-3m, a = 11.9147(6) ÅṪhe DC magnetization performed on different pieces of this batch shows varying T_C between 65 K-70 K (as illustrated in Fig. 4.13 a.) which mostly is attributed to the different distribution of the Mn in the sublattices. The coercivity of these samples has also increased significantly, reaching up to 1 T, as presented in Table 4.1. The shape of the hysteresis loop resembles a pot-bellied type, the same as in the previous sample S2, most probably because of the same reason.

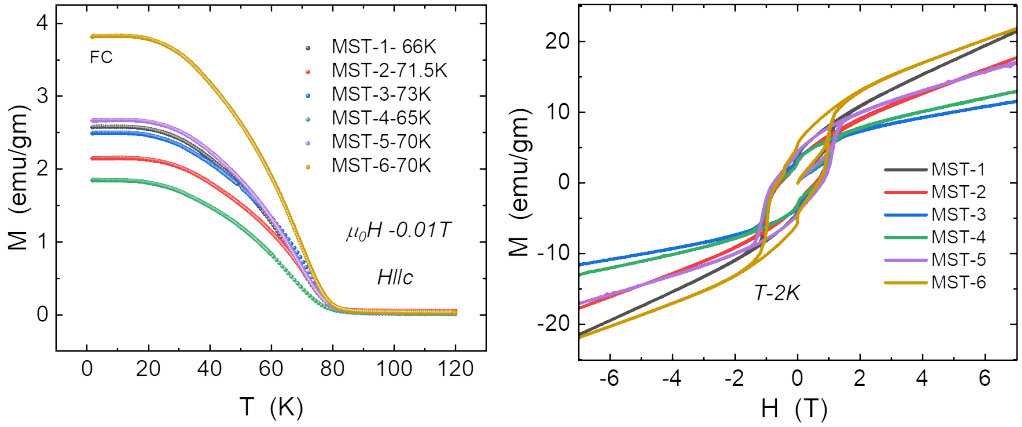

Figure 4.13: (a) Temperature dependence of the magnetization at $\mu_0 H = 10$ mT (b) Isothermal magnetization at $T = 2$ K of different Mn-rich samples $MnSb_2Te_4$ with a cubic structure.

Sample	T_C (K)	$H_C(T)$
MST1	66	0.58
MST2	71.5	0.55
MST3	73	0.78
MST4	65	0.62
MST5	70	0.78
MST6	70	0.65

Table 4.1: Different $MnSb_2Te_4$ samples with their $T_C$and H_C

The substantial inclusion of Sb cations into the Te-terminated van der Waals gaps was not considered in the initial calculations. A preliminary assessment by Dr. Jorge Facio (IFW Dresden) involving the calculation of the total DOS for a structured model where one-third of the 3*b* site is occupied, along with a fully ferromagnetic configuration, suggests that this alteration may induce a metallic state (as illustrated in Fig. 4.14). Such a property could potentially serve as a crucial limiting factor for the QAHE. However, the comprehensive exploration of this aspect together with a thorough determination of the crystallographic structure of this variant goes beyond the scope of the current thesis work and will be discussed in [7].

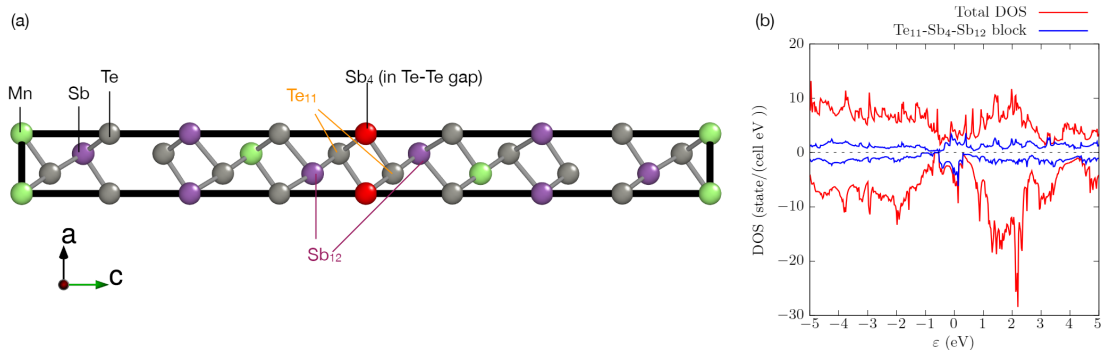

Figure 4.14: (a) Structural model considered to study the effects of Sb atoms in the van der Waals gap. (b) DOS was obtained for ferromagnetic configuration. The figure shows the total DOS and its projection on Te and Sb atoms next to the added Sb atom; taken from own publication Ref. [5].

4.7 Enhancement of magnetic ordering in $MnSb_2Te_4$ by applying pressure

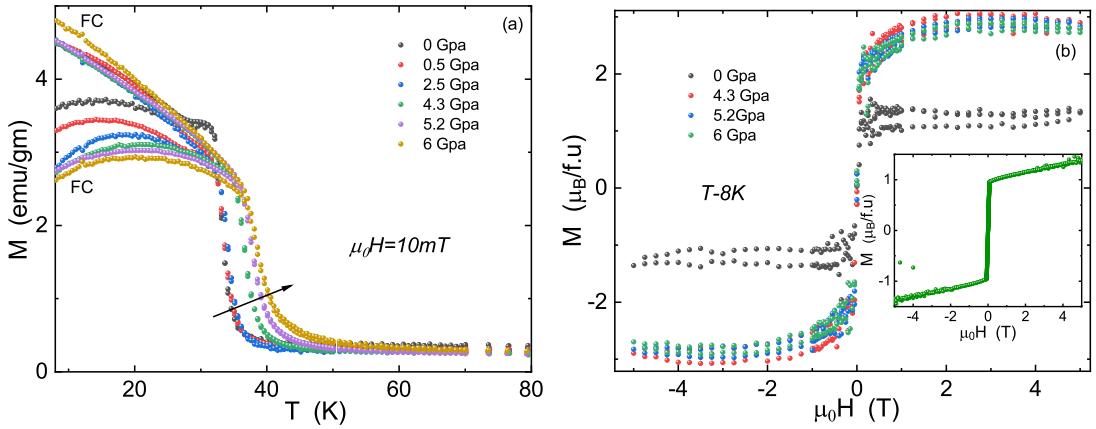

Figure 4.15: a) Temperature dependence of the magnetization in $MnSb_2Te_4$ sample measured at 0.01 T field and different pressures until 6 GPa c) Isothermal magnetization measured at 8 K and similar pressures

Adjusting the stoichiometry of Mn has proven to be an effective method for manipulating the magnetic properties of $MnSb_2Te_4$, enhancing ferromagnetic interactions, and elevating transition temperature. However, this approach comes at the expense of altering the original crystal structure due to the introduction of Sb into the van der Waals gap. In the quest for alternative methods to fine-tune the transition temperature, the influence of hydrostatic pressure has been extensively explored as a successful means of modulating the magnetism of 2D van der Waals materials, as evidenced by various studies [87, 193–198].

Along this line, the hydrostatic pressure control of the magnetization in $MnSb_2Te_4$ samples was achieved in this work. Notably, a thin, flake-like sample with a transition temperature of 33 K at a magnetic field of 0.01 T was used.

Figure 4.15 illustrates the impact of temperature on magnetization, observed in both FC and ZFC modes, with an applied magnetic field of 0.01 T along the c-axis, and varying applied pressures up to 6 GPa. The black dot represents the magnetization curve without any applied pressure, exhibiting a transition temperature of 33.12 K, consistent with the M-T measurements conducted without the pressure cell in SQUID VSM. it is observed that the T_C increases with increasing pressure $\frac{dT}{dP} > 0$. The rate of change $\frac{dT}{dP}$ remains small (0.5 K/GPa) up to 2.5 GPa, but notably escalates to nearly 1 K/GPa as the pressure reaches 6 GPa. Additionally, the curve broadens, and the magnitude of magnetization slightly increases. The T_C is determined by analyzing the derivative dM/dT curve. The same has also been measured at an applied field of 0.05T, a similar observation with an increase in T_C has been observed however the absolute value of the magnetization decreases.

The Isothermal magnetization is depicted in Figure 4.15 b, corresponding to the same pressure values as outlined in the temperature dependencies. To overcome the impact of imperfect background signal subtraction from the pressure cell at lower temperatures, the measurements were conducted at T = 8 K, a temperature sufficiently low to capture the characteristic behavior of the FM state and above the Pb superconducting transition. Only the diamagnetic subtraction has been performed at the higher fields. The M-H dataset in Figure 4.15 b includes (inset) a reference measurement performed at ambient pressure on a larger single crystal (mass approximately 0.2 mg) and without the pressure cell. The ambient pressure data reveal a moment (M_s) of 1.5 μ_B/Mn at 5 T and T=2 K. Surprisingly, with increasing pressure, M_s jumps to approximately 3 μ_B/Mn at 5.3 GPa and remains constant (within the error bar) until 6 GPa.

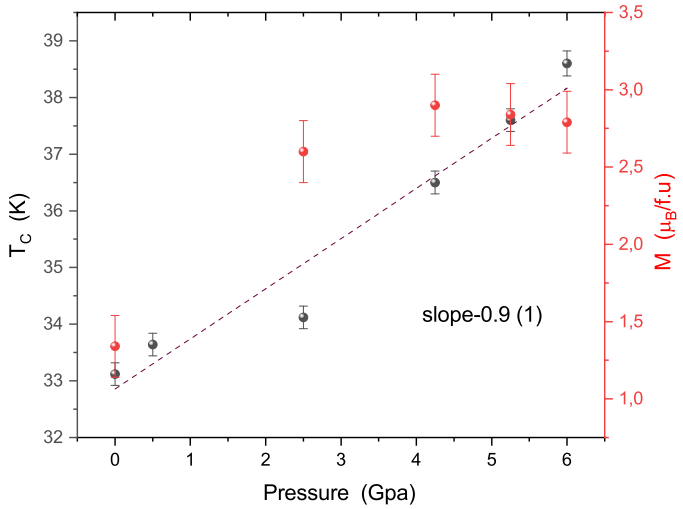

Figure 4.16: Pressure dependence of the T_C and M_S. Thw dashedline is a guide to the eye.

Finally, the obtained parameters are depicted in Figure 4.16, where T_C and M_S

(magnetization at 5T) are plotted alongside their respective error bars with respect to the applied pressure. As mentioned earlier, both T_C and M_S demonstrate an increase under applied pressure. The ferromagnetic exchange interactions in both intra-layer and interlayer increase by compressing the lattice parameter, hence applying hydrostatic pressure. The M_S increased until 4.3 GPa and remains constant at higher pressure whereas the T_C still increases at higher pressures, indicating the FM intralayer increase suppressing all the AFM interactions, however, the FM interlayer interactions keep increasing by reducing the lattice parameter. Moreover, applying pressure to the $MnSb_2Te_4$ samples could enhance the T_C , giving another parameter to tune for future applications. Further, a thorough calculation of the exchange parameter by applying pressure and X-ray diffraction under pressure could be beneficial in understanding the underlying mechanism. Pressure-dependent resistivity will also be required to verify the proposed Weyl semimetal state in the FM $MnSb_2Te_4$ samples.

4.8 Conclusions

Addressing the aim mentioned in chapter 3, an in-depth investigation on $MnSb_2Te_4$ single crystalline samples has been performed. This chapter delves deeply into the impact of site intermixing and the distribution of Mn on magnetic order. By accurately quantifying the intermixing, an aspect that was missing in the previous reports, this study reveals that both Mn over-stoichiometry and specific Mn/Sb distributions contribute to enriching ferromagnetism in the system and enhancing magnetic ordering temperature. The comprehensive investigation, combining bulk magnetic measurements and DFT studies, suggests an enhancement of ferromagnetic interactions as the Mn content increases in the 3*a* layers. Further, the possibility of tuning the magnetic ordering temperature was also observed by increasing cation intermixing between Mn and Sb sites, along with Mn-over-stoichiometry, while preserving the magnetic ground state up to the exceptional Curie temperature T_C = 58 K in bulk crystals. Further, DFT and ESR results reveal a quasi-2D to a more 3D-like magnetic ordering character due to the presence of Mn in the native Sb positions. An in-depth investigation into AC susceptibility and nonequilibrium measurements confirm the existence of large spin clusters below the ordering temperatures. Moreover, an additional rise in T_C up to 73 K is demonstrated with increasing Mn concentration. However, this enhancement comes at a cost as it loses the quasi-2D character of the crystal structure. Beyond a certain compositional threshold, Sb begins to occupy the van der Waals gap. This structural transformation induces a metallic character in the electronic spectrum, as discerned through DFT calculations. Although the precise Mn concentration triggering the magnetic state change is not quantifiable, trends are evident through DFT modeling. The electronic band topology of this modified system, however, remains unexplored.

In addition to manipulating the intermixing partner and Mn stoichiometry, pressure was investigated as an effective tool for increasing magnetic interaction and transition temperature without compromising the original crystal structure, which had never been observed before in these family materials. Fabrication of a Mn-rich $MnSb_2Te_4$ system resembling a stable natural heterostructure coupled with pressure tuning enhances its potential for practical applications and broadens the materials platform for advancing high-T QAHE. Consequently, $MnSb_2Te_4$ holds promise for yielding tunable layered magnets with diverse magnetic profiles.

Chapter 5

Role of Mn/P intermixing on the magnetism of MnP_2Te_4 (P=Bi, Sb)

In the previous chapter, the influence of Mn-over stoichiometry on the magnetism and fine-tuning of magnetic ordering in the $MnSb_2Te_4$ single crystalline samples were investigated. This chapter redirects its focus toward a comprehensive exploration of Mn/P, P=Bi, and Sb intermixing in all the $(MnBi_2Te_4)(Bi_2Te_3)_n$, n=0,1,2 and $MnSb_2Te_4$ samples, which could be manipulated through synthesis conditions, and subsequently understanding its impact on both bulk magnetic properties through SQUID and localized magnetization through nuclear magnetic resonance (NMR) and muon spin spectroscopy (μSR).

Within the scope of this study, previously reported $(MnBi_2Te_4)(Bi_2Te_3)_n$, n=0,1,2 samples and several $MnSb_2Te_4$ powder samples have been prepared under different synthesis conditions. The ensuing analysis entails a quantitative evaluation of composition through Energy Dispersive X-ray Spectroscopy (EDx) as well as a determination of the concentrations of Mn and Sb achieved using Neutron Powder Diffraction (NPD). Moreover, a nuanced investigation into the local magnetic properties of these samples will be conducted on all the samples, employing sophisticated techniques such as NMR and μSR. This examination aims to unravel the intricate interplay between Mn/P intermixing and the resultant magnetic attributes, offering a comprehensive understanding of the synthesis-dependent magnetic ordering and the impact of intermixing in this family of compounds. Part of this chapter has already been published in own publication Ref. [8–10]

5.1 Synthesis of $(MnBi/Sb_2Te_4)(Bi_2Te_3)_n$, n=0,1,2

All the samples investigated in this chapter are prepared by the group of Dr. Anna Isaeva in TU Dresden. Further structural analyses like EDx were also done by her group. Polycrystalline samples of $(MnBi_2Te_4)(Bi_2Te_3)_n$, n=0,1,2 and $MnSb_2Te_4$ were prepared by high-temperature solid-state reactions, kept as non-compacted powders for NMR experiments, and pressed into pellets for the μSR experiments. Two $MnBi_2Te_4$, (denoted α and β) powdered samples were obtained by two distinct high-temperature annealing routes.

The $MnBi_2Te_4$ α-sample was prepared from a mixture of pre-synthesized MnTe and Bi_2Te_3 taken in the ratio 0.87:1.05. The powders were handled in an argon-filled dry glovebox (MBraun), homogenized in a dry ball mill (Retsch, MM400) at 20 Hz for 20 min and then pressed into a 6-mm pellet (2 tons, 30 sec). The pressing was

placed into a quartz ampoule, sealed off under dynamic vacuum (3×10^{-3} mbar), and annealed in a temperature-controlled tube furnace (Reetz GmbH) following the procedure developed in [111]. The $MnBi_4Te_7$ and $MnBi_6Te_{10}$ samples were obtained from a corresponding, stoichiometric mixture of the powdered binaries, which were handled similarly to the ones above. The former was annealed at 585 °C for 10 days (heating rate 1 °C/ h) and the latter was annealed at 575 °C for 4 days (heating rate 90 °C/ h). Both samples were water-quenched.

The $MnBi_2Te_4$ β-sample was synthesized by co-melting of pre-synthesized MnTe and Bi_2Te_3 in an evacuated quartz ampoule at a temperature of about 980 °C for 12 h, followed by slow cooling down to 580 °C at the rate of 5 °/h. This temperature was kept for 12 h followed by air-quenching. Then, the polycrystalline sample was ground into a fine powder and converted into a pellet, which was then sealed in a quartz container under a pressure of 10^{-4} Pa. The ampoule was further heated up to 585 °C for 8 h, then kept at this temperature for about 240 h followed by air-quenching. The grinding and annealing processes were repeated twice to achieve a homogenized, phase-pure compound.

Three groups of $MnSb_2Te_4$ powder samples have been prepared by slightly varying annealing temperature and time.

Group 1 :FL_AP series:

This series denotes stoichiometric mixtures of the elements Mn, Sb, and Te ball-milled at 40 Hz for 20 min, pelletized, and annealed at a constant temperature for much longer to ensure thermodynamic equilibrium and then quenched.

Group 2 :FL_AV series:

The series were prepared with a starting 2.5 at% Te deficiency (with respect to the total amount of Te in the ideal formula $MnSb_2Te_4$), i.e. with the starting $MnSb_2Te_{3.9}$ (equivalent to $Mn_{1.02}Sb_{2.05}Te_4$) composition of the elemental mixture. The milling and heating treatments were similar to those above.

Group 3 :FL_A series: This series has been prepared following a similar initial stoichiometry of Group 1 but annealed at lower temperatures and for a short period.

Several samples have been prepared, and the detailed structural analysis will be reported in Ref. [10]. A few samples have been chosen to discuss the magnetic properties and their possible connection with the Mn concentrations at different sites. The details of all the annealed temperatures, times, and then their composition determined from the standard Edx are listed in tab. 5.1. The growth conditions and powder XRD for all the $(MnBi_2Te_4)(Bi_2Te_3)_n$, n=0,1,2 samples are reported in [111, 141, 142, 199] and the details of the $MnSb_2Te_4$ samples will be reported in [10].

Sample	Synthesis conditions	EDX with standards
FL_AP_01c :P1	640 °C ,7days	$Mn_{1.02(2)}Sb_{1.90(1)}Te_{4.00(1)}$
FL_AP_01a :P2	630°C ,7days	$Mn_{0.985}Sb_{1.99}Te_4$
FL_AV_07a_1 :P3	594°C, 5 days	$Mn_{0.98(2)}Sb_{2.01(2)}Te_{4.00(1)}$
FL_AV_07a_3 :P4	594°C, 8 days	$Mn_{0.992(5)}Sb_{2.016(4)}Te_{4.00(1)}$
FL_A_05a :P5	550 °C, 4 days	$Mn_{0.98(1)}Sb_{1.964(2)}Te_{4.00(1)}$
FL_A_05a_1 :P6	550 °C, 8 days	$Mn_{0.86(1)}Sb_{2.04(1)}Te_{4.00(1)}$

Table 5.1: $MnSb_2Te_4$ samples used for magnetic (P1-P6) with their synthesis conditions and composition from EDX

5.1.1 DC magnetization

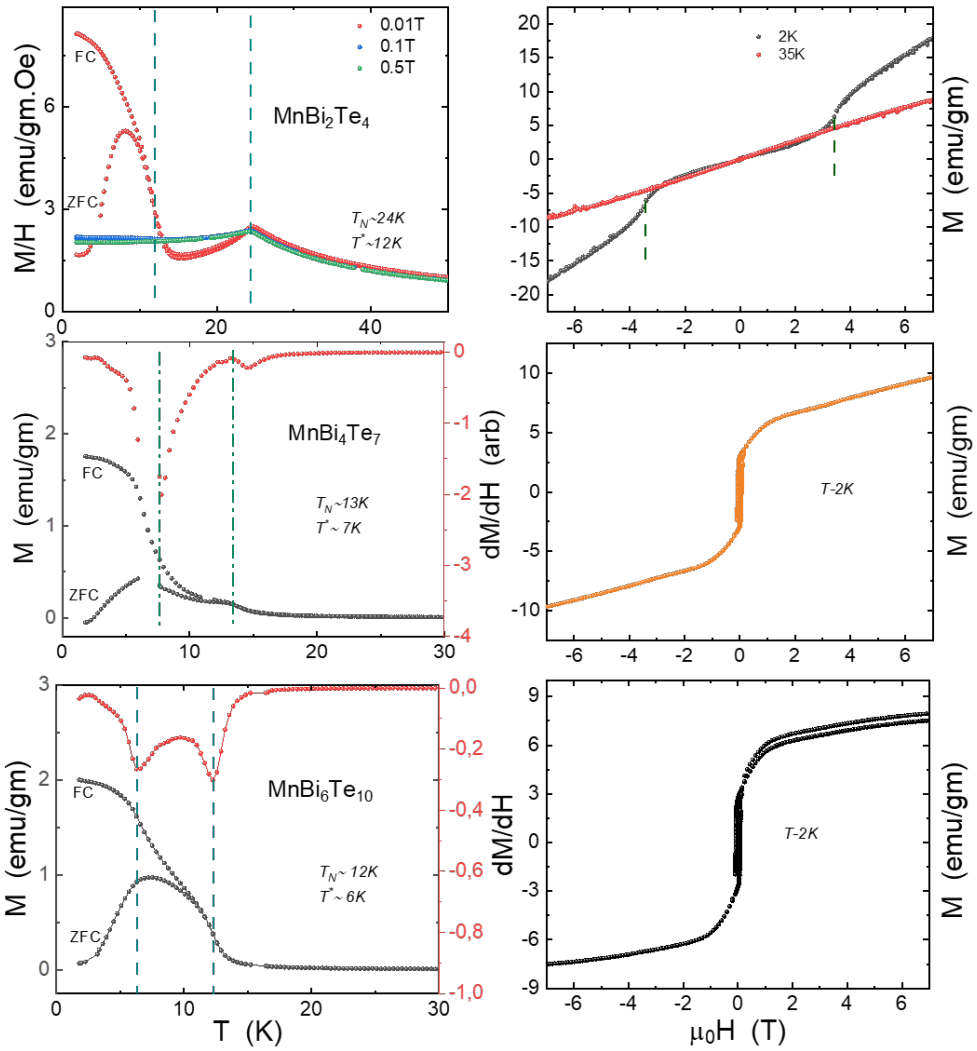

Figure 5.1: Temperature dependence of magnetization at 0.01 T(with the dashed line showing two transitions) and isothermal magnetization at T = 2 K for $(MnBi_2Te_4)(Bi_2Te_3)_n$, n=0,1,2.

The powder samples were measured employing a Quantum Design SQUID-VSM. The temperature-dependent magnetization was measured in both ZFC and FC modes, spanning the temperature range from 1.8 K to 300 K Additionally, isothermal magnetization measurements were conducted at two different temperatures, 2 K and 35 K.

The temperature dependence of the magnetization and isothermal magnetization for all the $(MnBi_2Te_4)(Bi_2Te_3)_n$, n=0,1,2 is shown in Fig. 5.1. In the $MnBi_2Te_4$ sample, for $\mu_0 H$= 10 mT, a cusp is observed at $T_N \simeq$ 24.6 K (see fig 5.1 a), indicating the onset of long-range antiferromagnetic order. Upon further cooling, both FC and ZFC curves exhibit an anomaly, appearing first as an upturn below 15 K, while below 11.5 K the ZFC and FC curves separate, denoting the onset of a ferromagnetic-like character at T^* = 11.5 K, as indicated by a peak in dM/dT. This double-peak behavior was not observed in the previous report. This second transition for $MnBi_2Te_4$ starts suppressing

above 0.1 T and is completely suppressed at 0.5 T indicating a field-induced behavior. The isothermal magnetization at 2 K reveals a small hysteresis confirming this ferromagnetic-like behavior however the overall interaction remains AFM with a spin flop field around 3.4 T which is again suppressed at high temperatures and becomes paramagnetic above T_N. A similar double transition is evidenced by the double peak in dM/dT observed in $MnBi_4Te_7$ at (13 K and 6 K) and in $MnBi_6Te_{10}$ (12 K and 6 K) as well (see Fig. 5.1 c,e). The AF cusp is not directly detected in the $MnBi_6Te_{10}$sample (see Fig. 5.1 e). The isothermal magnetization in both samples does not have a spin-flop transition, but rather a ferromagnetic-like S shape loop with small hysteresis.

Further, selected $MnSb_2Te_4$ samples were also investigated. The temperature-dependent magnetic susceptibility curve of several $MnSb_2Te_4$ powder samples is depicted in Fig. 5.2. As the temperature gradually decreases, a notable sharp rise in magnetic susceptibility is evident at $T_C = 46$ K for P1, where T_C denotes the inflection point of the susceptibility curve. This rise is accompanied by a divergence between the ZFC and FC curves, signifying the onset of long-range ferromagnetic-like order.Comparable temperature dependence of the DC susceptibility in Sample P2 is also shown in Fig 5.2a. Notably, the initiation of magnetic order from the paramagnetic state commences at a temperature lower than that observed in Sample P1. The susceptibility curve exhibits divergence starting at T_C = 33 K, and a corresponding bifurcation between the ZFC and FC curves is observed.

The curie Weiss fit in the paramagnetic region (150–250 K) measured at 0.0 1T using the below equation and parameters are presented in Table-4 and Fig. 5.2 b

$$\chi(T) = \chi_0 + \frac{C}{T - \theta_{CW}}, \tag{5.1}$$

where χ_0, C and θ_{CW} represent the temperature-independent susceptibility contribution (core diamagnetism and Pauli paramagnetism), the Curie constant, and the Curie Weiss temperature, respectively. Further, the effective magnetic moment calculated from the formula $C = N_A\mu_{eff}^2/3k_B$ was found to be $\mu_{eff} = 5.0(2)\mu_B$/Mn in all the samples which is lower than the theoretical value 5.92 μ_B for high-spin Mn^{2+} (S = 5/2).

The isothermal magnetization of Sample P1, P2 is illustrated with the magnetic field shown in Fig. 5.2c, at 2K. Similar to the $MnSb_2Te_4$ single crystal sample [5], the net magnetization in this case does not reach complete saturation until 7 T. Instead, it exhibits an S-shaped behavior, accompanied by an apparent coercive field of approximately 0.05 T Oe, which was not observed in the single crystal. At 7 T, the magnetization does not exceed $2\mu_B$/Mn, indicating a reduction in the magnetic moment associated with the competing FM and AFM interactions. It is noteworthy that in the previous chapter, it was discussed, the overall ferrimagnetic behavior arising from an unequal number of Mn^{2+} ions within the septuple layer at Mn_{3a} and Sb_{6c} sites. Addressing this hypothesis is imperative for a more profound comprehension of the system's ground state, which will be discussed in the upcoming section. An intriguing observation is the distinct presence of a spin-flop-like transition, a noteworthy characteristic that has not been reported in previous studies on $MnSb_2Te_4$ powder samples.

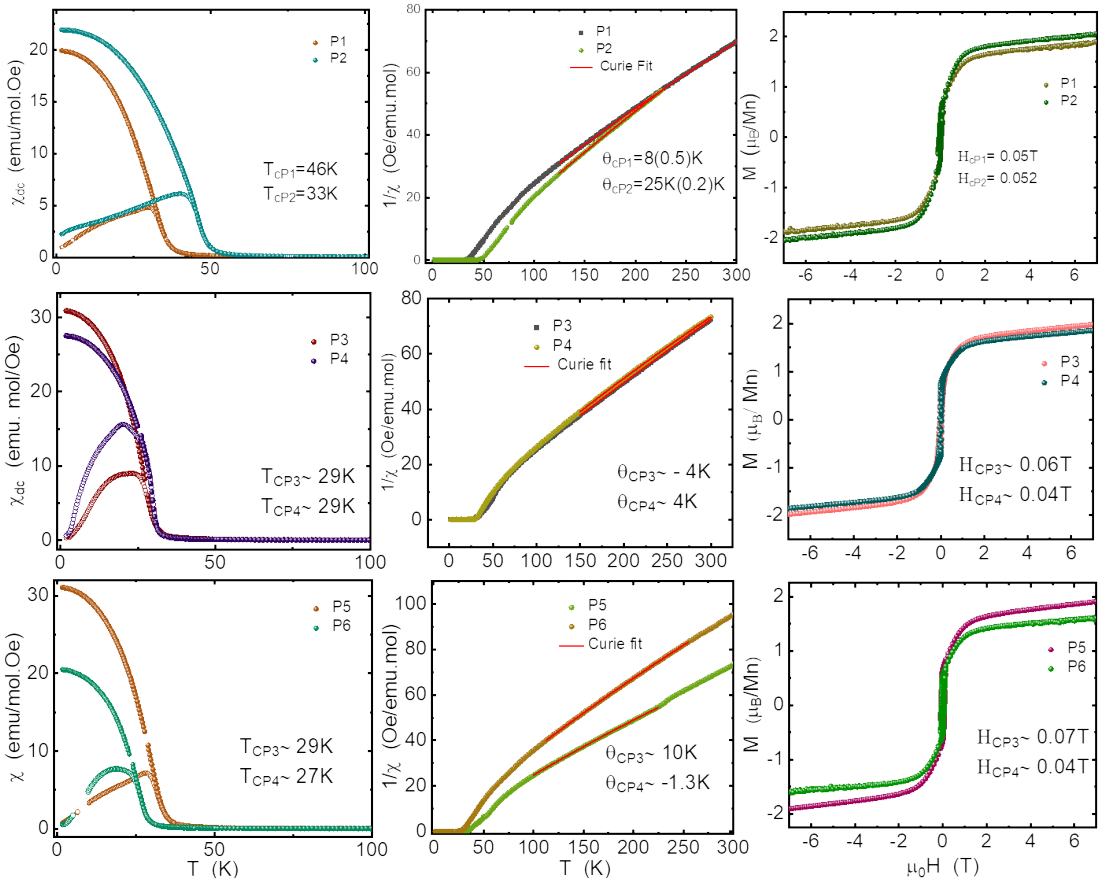

Figure 5.2: DC magnetic susceptibility (a,d,g), Curie Weiss fit (b,e,h) and isothermal magnetization (c,f, i) for P1, P2, P3, P4, P5, P6

Continuing with the examination of another set of samples, which were prepared at a lower temperature compared to the previous ones, Fig 5.2 d, depicts the temperature dependence of the DC susceptibility for samples P3 and P4. In these samples, the divergence in the DC susceptibility occurs at an even lower temperature, approximately $T_C = 30$ K. The Curie temperature (θ_c) is correspondingly lower, and the saturation magnetization from the isothermal magnetization is reduced compared to samples P1 and P2. Additionally, a spin-flop-like transition is also observed in these samples, with a value slightly distinct from the previous samples.

The last set of samples, grown at even lower temperatures and featuring a slight Te deficiency from the original composition, were measured. The temperature dependence of susceptibility for the selected samples P5 and P6 is illustrated in Fig 5.2g, where T_C is the lowest at around 27-29 K.

Interestingly, the annealing temperature appears to exert a detrimental effect on the magnetic ordering temperatures, with samples grown at temperatures above 630 °C exhibiting higher T_C compared to those annealed below 600 °C, which has T_C values lower than 30K. The isothermal magnetization behavior, depicted in Fig. 5.2 (i), mirrors a similar trend, featuring lower saturation magnetization (M_S) at 7T. Notably, sample P6 displays the lowest T_C and the minimum M_S. It is noteworthy that, contrary to the findings reported in [165] regarding the synthesis conditions associated with AFM and FM ground states, the observations reveal substantial disparities and modulation in magnetism even within the Ferromagnetic (FM) and Ferrimagnetic (FiM) ground

states. This variability underscores the critical role of synthesis conditions in tuning the magnetism of potential magnetic topological insulators for future advancements.

The comprehensive results from magnetization measurement for these samples from different batches are listed in the tab. 5.2

Label	$T_C(K)$	$\mu_{eff}(\mu_B$/Mn)	θ_C(K)	H_C (T)	M_s (μ_B/Mn)
P1	46	5.0(2)	28K(4)	0.05	1.9
P2	33	5.1(2)	7.5(3)	0.052	2.1
P3	29	5.3(2)	-4	0.06	1.98
P4	30	5.2(2)	4(2)	0.04	1.85
P5	29	5.1(2)	10(3)	0.07	1.98
P6	27	5.0(2)	-1(3)	0.04	1.61

Table 5.2: Comparison of μ_{eff} and θ_C calculated using equation 1 for selected samples.

Most of these samples were then further characterized using NMR and μSR to get more insight into the antisite intermixing, their effect on the local magnetism, and thermodynamic transition. This will be discussed in detail in the upcoming sections.

5.2 Anti-site detection in NMR

Site intermixing was most commonly reported in the $MnSb_2Te_4$ samples; however, there were a few reports briefly discussing this issue, also present in all the $MnBi_2Te_4$ family samples[111, 116, 117, 173]. Intermixing, indeed, plays a crucial role in the Dirac gap debate in $MnBi_2Te_4$ samples. Hence, extensive ^{55}Mn NMR measurements were performed, both in ZF and in applied field, on all the $(MnBi_2Te_4)(Bi_2Te_3)_n$,-n=0,1,2 and on different $MnSb_2Te_4$ samples. The interpretations were further supported by DFT calculation.

In ZF-NMR, ^{55}Mn nuclear spins (gyromagnetic ratio $^{55}\gamma/2\pi = 10.576$ MHz/T) precess around a very large hyperfine field $B_{\rm hf}$, between 40 and 45 T at 1.4 K. $B_{\rm hf}$ is primarily due to the negative coupling, $-\mathcal{A}$, to the on-site moment $-g\mu B\mathbf{S}$, with much smaller positive couplings $\mathcal{B}$ to six nearest neighbors Mn_{3a} moments, and even smaller distant dipole contributions, so that in first approximation, assuming parallel $\mathbf{S}$ in the layer, the NMR frequency is

$$^{55}\nu = {}^{55}\gamma(\mathcal{A} - 4\mathcal{B})\mu_{\rm B}S \tag{5.2}$$

A 3D view of the spectra for polycrystalline samples of $MnBi_2Te_4$, $MnBi_4Te_7$ and $MnBi_6Te_{10}$ at T = 1.4 K, in the frequency range 350 to 500 MHz, is shown in Fig. 5.3a-c with ZF at the back and increasing fields $\mu_0 H$ towards the front. They all show two broad peaks, each centered at a distinct frequency: $\nu_{\rm a,c} = {}^{55}\gamma\,|{}^{55}\mathbf{B}_{\rm a,c}|$. Therefore two distinct Mn sites experience a different total local field modulus $^{55}B_{\rm a,c}$, i.e. different values of $B_{\rm hf}$, as it would be expected for the main site Mn_{3a} and the anti-site Mn_{6c}. The 5-10% width of the frequency peaks is due to disorder in their vicinity, producing small variations of the local electronic environment, reflected in $B_{\rm hf}$. The spectra are fitted with one or more Gaussian components using equation 2.43 to determine the peak

position. When more than one component is used, the mean frequency is computed from the corresponding weights using equation 2.44.

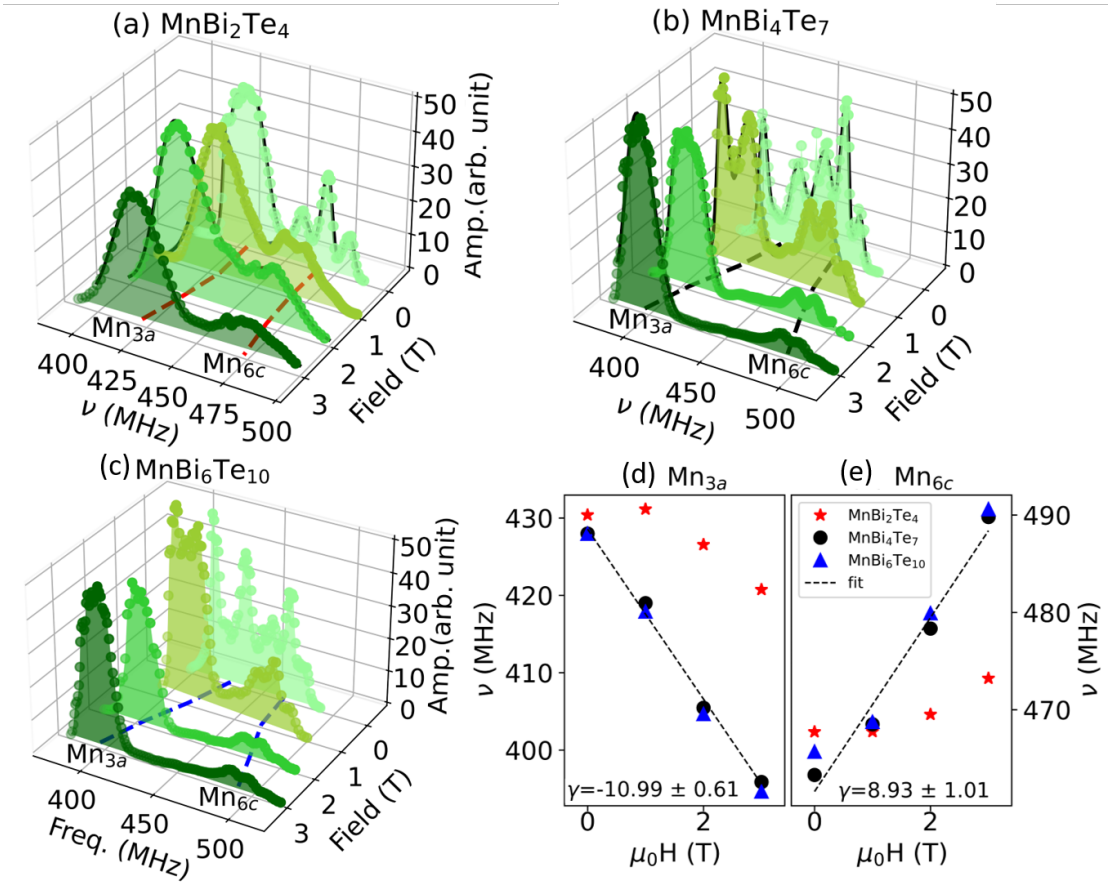

Figure 5.3: (a,b,c) ^{55}Mn NMR spectra measured at T=1.4K in increasing applied fields, starting from ZF together with their best fit,(d,e) field dependence of the Mn_{3a} and Mn_{6c} mean frequency peaks for the $(MnBi_2Te_4)(Bi_2Te_3)_n$, n=0,1,2; taken from own publication Ref. [9].

The relative area under the two peaks at 3T assigns the lower-frequency, majority peak to Mn_{3a} and the minority peak to Mn_{6c} (Fig. 5.3a-c, the proportionality of the signal amplitude with the number of nuclei may not be guaranteed in ZF but it is recovered in 3T). The frequencies confirm the assignment, since the six non-negligible transferred couplings $\mathcal{B}$ of Mn_{3a} and the three nearly vanishing ones for Mn_{6c} are both opposite to the on-site coupling $\mathcal{A}$, hence it is expected the minority peak to shift to a higher frequency as it is the case. This simple argument is confirmed by DFT simulations of the hyperfine coupling at the Mn sites discussed below 5.3.2.

The 3D representations in Fig. 5.3 additionally demonstrate the splitting of the mean frequency for both peaks as the field is increased, by the field vector composition $^{55}\mathbf{B} = \mu_0\mathbf{H} + \mathbf{B}_{\mathrm{hf}}$

In straightforward scenarios, the relative local orientation of the magnetic moments of Mn_{3a} and Mn_{6c} can be readily deduced from the vector composition depicted in chapter 2 Fig. 2.8 (a-c).

In the collinear antiferromagnetic (AFM) case, which was explained in chapter 2 equation 2.35, both the $Mn_{3a}$and Mn_{6c}frequencies don't shift at low fields, as shown in

5.3 a. Whereas in ref 5.3 b,c, the majority peak (Mn_{3a}) shifts towards lower frequencies, showing the case of FM as explained in 2.35 and shown in Fig. 2.8 b. Conversely, the peak associated with Mn_{6c} shifts to a higher frequency, indicating an opposing alignment to Mn_{3a}, as $\mathbf{B}_{\mathrm{hf}} \parallel \mathbf{H}$ (shown in Fig. 2.8c)

Figure 5.3 d displays the shifts versus the applied field for the $MnBi_2Te_4$ family samples. The predominant Mn_{3a} peak of $MnBi_2Te_4$ (depicted by red stars) remains unaltered with field up to 1 T, aligning with the AFM behavior predicted by Eq. 2.35. Its slight shift in the range $2 \leq H \leq 3$ T corresponds to a recognized canted AFM behavior (CAF) above the spin flop field [112–114].

In contrast, $MnBi_4Te_7$ and $MnBi_6Te_{10}$ (illustrated by black and blue symbols, respectively) exhibit a ferromagnetic (FM) behavior. The opposing spin alignment of the Mn_{6c} antisite is directly evidenced by Figure 5.3 e across all $MnBi_2Te_4$ family materials, as indicated by their positive slope values. These values are slightly diminished by an average canting angle θ between the sublattice magnetization and $\gamma = {}^{55}\gamma \cos\theta$. This angle is small for the other materials but quite substantial for $MnBi_2Te_4$, reflecting the extensive angle between the magnetization of its canted Mn_{3a} sublattices and the applied magnetic field. Unfortunately, NMR could not provide information on the temperature-dependent behavior of the spectra, due to short T_2. $MnSb_2Te_4$ samples display comparatively high, sample dependent T_C, which motivated us to perform the same NMR measurements on a few selected $MnSb_2Te_4$ samples.

5.3 Anti-site detection in $MnSb_2Te_4$

Distinct magnetic ordering has been observed in various samples, synthesized under slightly different conditions, implying potential variations in both the overall Mn concentration and the concentration at intermixing sites. The anti-site Mn_{6c} peak in all $(MnBi_2Te_4)(Bi_2Te_3)_n$, n=0,1,2 samples has been identified. According to the reports, the $MnSb_2Te_4$ samples naturally have more intermixing so hopefully will be simpler to identify and understand if the opposite alignment also holds here.

From all the six $MnSb_2Te_4$ samples characterized by DC magnetometer, four samples have been chosen, at least one from each batch, and having different magnetic ordering means different amounts of Mn at the antisite (6c) position. The purpose of this is not only, to identify the anti-site Mn and how it is coupled to the central (3a) Mn here in $MnSb_2Te_4$ samples but also to quantify the amount of Mn_{6c} using NMR as a local probe.

Figure 5.4 illustrates a three-dimensional representation of the spectra corresponding to samples P1, P2, P3, and P6 within the frequency range of 350 to 500 MHz. The depiction includes the zero-field (ZF) condition positioned at the back, with increasing magnetic fields (H) progressing toward the front. Notably, both samples exhibit similar two broad peaks, each centered at distinct frequencies denoted as $\nu = {}^{55}\gamma {}^{55}B_{a,c}$. Similar to the previous compounds, the assignment of the majority peak to Mn_{3a} and the minority peak to Mn_{6c}, respectively, and the DFT prediction for the frequencies are also similar (shown in Fig. 5.6 and Fig. 5.7).

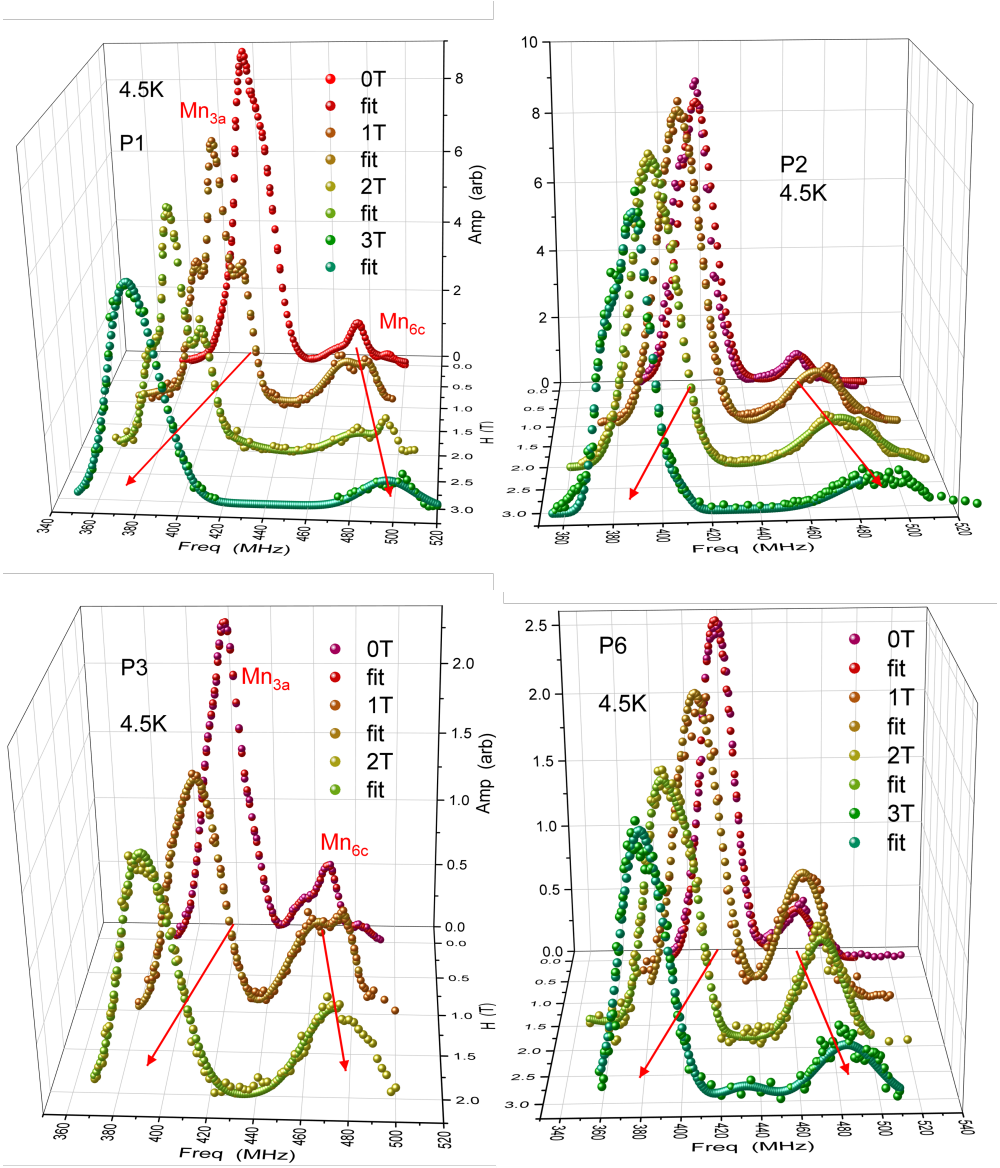

Figure 5.4: ^{55}Mn NMR spectra measured at T=4.5 K in increasing applied fields, starting from ZF together with the best fit for $MnSb_2Te_4$ samples **P1, P2, P3, P6**

The field dependence of frequencies of the majority peak (α i.e due to Mn_{3a}) and minority peak (i.e. due to Mn_{6c}) have been presented individually for all samples. The coupling of ^{55}B at the α peak attributed to Mn_{3a} aligns ferromagnetically with $B_{\rm hf}$ in nearly all samples, similar to the case of $MnBi_6Te_{10}$ and $MnBi_4Te_7$ (shown in Fig. 5.5a). The slope of the linear fit (γ) for these alignments is consistent, with γ being approximately equal to $-^{55}\gamma$ within the range of error bars.

Figure 5.5b demonstrates the opposite spin alignment of the Mn_{6c} antisite for all $MnSb_2Te_4$ samples through positive slope values. These values are slightly diminished by an average canting angle θ between the sublattice magnetization and **H**, as indicated by $\gamma = {}^{55}\gamma \cos\theta$. The deviation of γ from $^{55}\gamma$ in different samples reflects the canting of spins away from parallel or anti-parallel alignment. Further, the fraction of Mn

at the 6c position (x) from the ratio of the NMR peak areas in the high field at low temperatures has been estimated.

A comprehensive summary of the field behavior of Mn_{3a} and Mn_{6c}, their apparent γ, and the corresponding canting angles (from θ) is provided in table 5.3. The data are compatible (within error bars) with $\theta_{3a} = 0$, corresponding to the behavior expected for an FM (or, equivalently, the large magnetization sublattice of an FIM) and to a large angle, close but not quite 180 degrees, for θ_{6c}, which implies canting close to the FIM configuration for the anti-site.

Label	x (%)	γ_{3a}	γ_{6a}	θ_{3a}(deg)	θ_{6a}(deg)
P1	12	-12.94(1.54)	8.35(0.9)	0	142(5)
P2	17	-10.58(0.32)	6.44(0.75)	0	127(4)
P3	20	-11.05(1.2)	8.2(0.8)	0	144(50
P6	22	-12.09(0.36)	5.4(1.5)	0	121(5)

Table 5.3: Comparison of fraction of Mn at 6c and slope of the linear fit and canting angle calculated for P1, P2, P3, P6

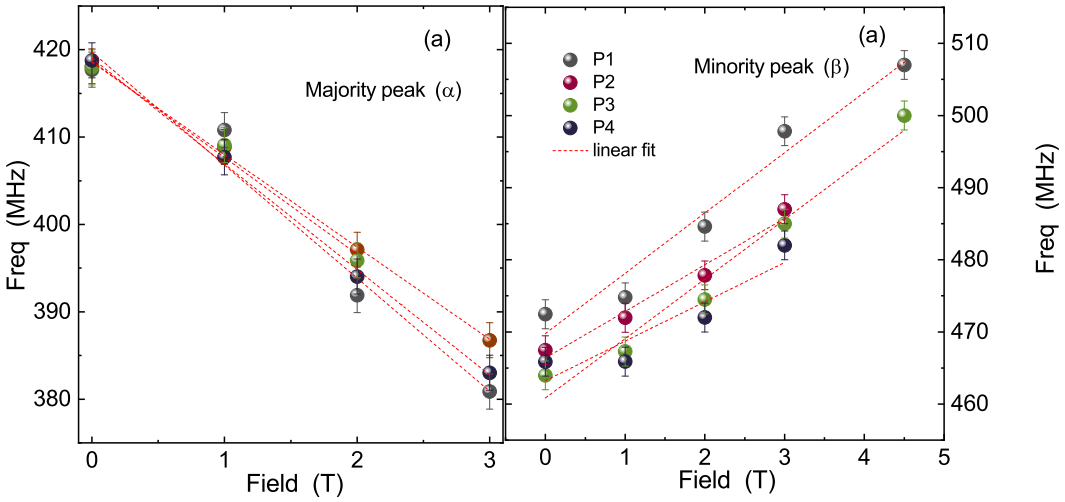

Figure 5.5: field dependence of the $Mn_{3a}$and Mn_{6c}mean frequency peaks for the $MnSb_2Te_4$ samples

5.3.1 Hyperfine field from DFT in $MnSb_2Te_4$

All the DFT calculations in this chapter have been performed by Dr. Ifeanyi John Onuorah, University of Parma. The hyperfine fields were computed for the perfect crystal structure of $MnSb_2Te_4$ to check the interpretation of the NMR experiment at the Mn_{3a} nucleus, employing a fully relativistic approach (ELK code) that includes spin-orbit coupling. The result is a hyperfine field value of 45.5 T. The calculation highlights the prevailing influence of the Fermi contact term, corresponding to NMR frequencies of 482 MHz. The computed value demonstrates very good concordance with experimental findings, falling within 15% of the experimental values illustrated in Fig. 5.4 for the four investigated samples, where the majority peak is centered at 420 MHz in ZF for all four sample.

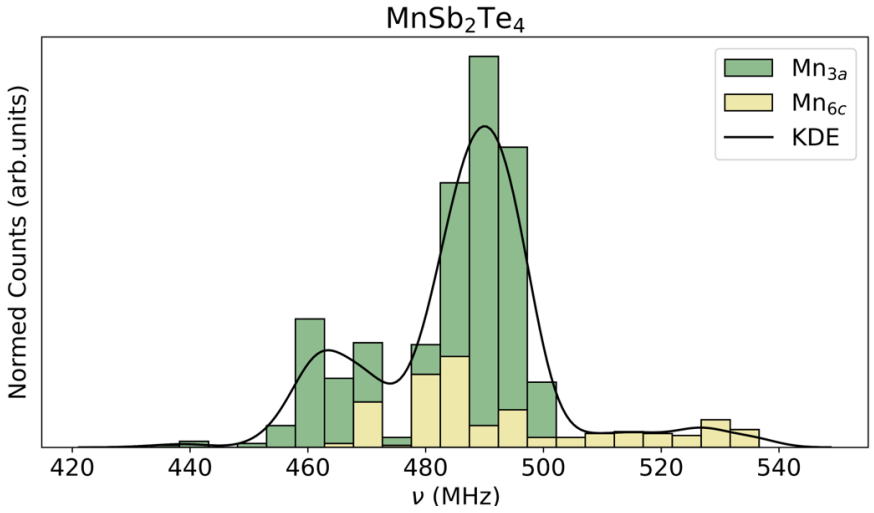

Figure 5.6: ^{55}Mn-hyperfine spectra calculated by DFT in $MnSb_2Te_4$, distinguishing the contributions from Mn_{3a} (green bars) and Mn_{6c} (yellow bars)

In order to represent the intermixing of Mn/Sb in $Mn_{3a}$and Mn_{6c}sites, a supercell approach (GIPAW code) was applied to simulate many random configurations. The resulting distribution of hyperfine fields is shown in Fig.5.6. The distribution is broad and the mean Mn_{6c} value is larger than the mean Mn_{3a} value as observed in the experiment. Further details of the calculation are provided in [9].

5.3.2 Hyperfine field from DFT in $MnBi_2Te_4$

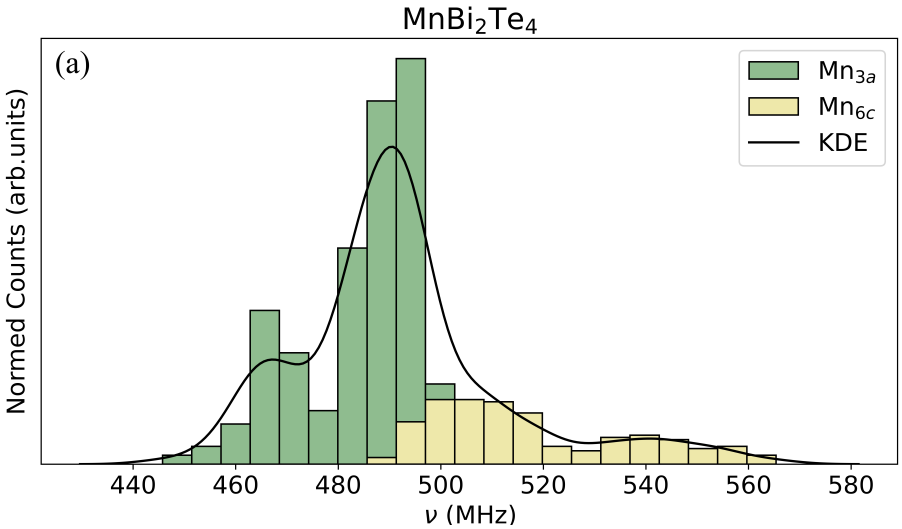

Figure 5.7: ^{55}Mn-hyperfine spectra calculated by DFT in $MnBi_2Te_4$, distinguishing the contributions from Mn_{3a} (green bars) and Mn_{6c} (yellow bars)

The hyperfine field at the Mn_{3a} nucleus was also calculated within the same approach in the ideal $MnBi_2Te_4$ crystal, yielding a consistent with that of $MnSb_2Te_4$, 45.6 T,

corresponding to an NMR frequency of 483 MHZ, respectively. The distribution of hyperfine fields considering cationic intermixing in the GIPAW approach is shown in Fig. 5.7. Similar consideration apply: the predicted spectrum is as broad as the measured one, the Mn_{6c} mean ZF-NMR frequency is higher than the Mn_{3a} mean frequency by an amount close to the experimental splitting (few tens of MHz). This supports the NMR peak assignment also in the entire $(MnBi_2Te_4)(Bi_2Te_3)_n$, n=0,1,2 family.

5.3.3 Temperature dependence of the antisite magnetic moment

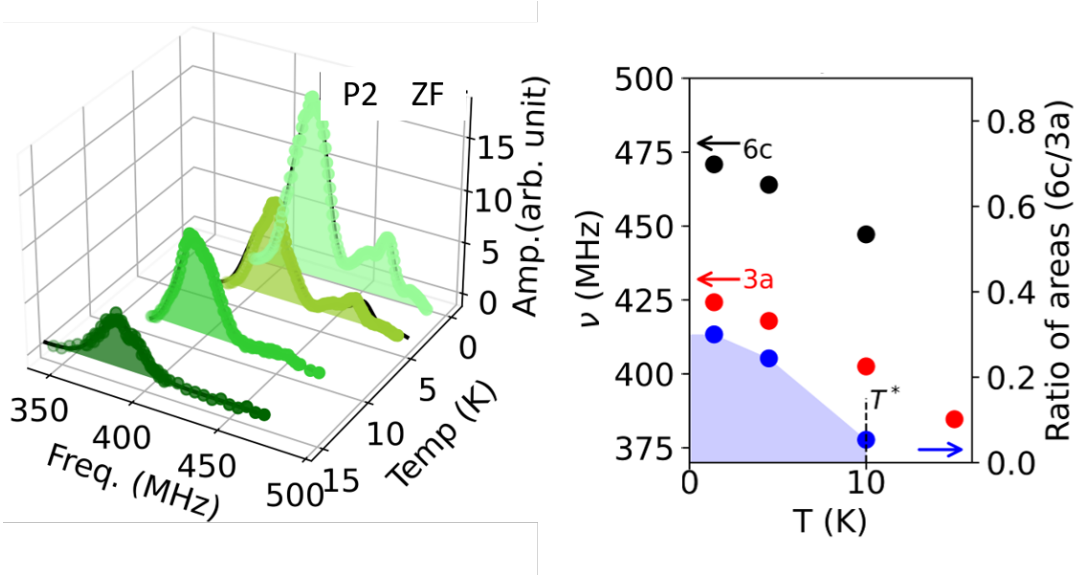

Figure 5.8: (a)Temperature-dependent of the NMR spectra for sample P2 (b) Frequency and ratio of areas plotted at different temperatures taken from own publication Ref. [9].

A short T_2 at the base temperature of HyReSpect ($T = 1.4$ K) generally evolves to even shorter rates as the temperature is increased. Fortunately, the temperature dependence of the ZF NMR spectra for all the $MnSb_2Te_4$ samples could be investigated. Only the results for sample P2 are presented here, in Fig. 5.8a. At the base temperature, the two distinct peaks are observed, but as the temperature increases their amplitude diminishes due to T_2 reduction. The measurement becomes very difficult for $t = T/T_C < 0.6$.. In this range, their mean frequency decreases also, as expected from the reduction of the order parameter $m(T)$. The outcome is summarized in the right panel, Fig. 5.8b, where the two ZF NMR peaks (Mn_{3a} and $Mn_{6c}$are represented by red and black symbols, respectively. Notice that the maximum reduction is less than 10%.

In contrast, the ratio of their peak areas (depicted by blue symbols) diminishes much more rapidly, reaching zero at around $t = 0.4$. This implies that the Mn_{6c} peak disappears in a first-order-like manner at a temperature T^* well below the T_C=33 K. The first-order disappearance of the Mn_{6c} signal (by amplitude reduction) means that the hyperfine field fluctuates in the missing sites, and suggests an earlier decoupling of the antisite sublattice, already below T_C. No such anomaly at T^* has been observed in bulk magnetization for the $MnSb_2Te_4$ samples. However, an unassigned anomaly at comparably low reduced temperatures is indeed present in the $(MnBi_2Te_4)(Bi_2Te_3)_n$,

n=0,1,2 samples [141, 142], as it was shown in Fig. 5.1. Unfortunately, the short T_2 of the $(MnBi_2Te_4)(Bi_2Te_3)_n$, n=0,1,2 samples does not allow a similar temperature-dependent investigation and the disappearance of the hyperfine field at the Mn_{6c} antisite below T_C could not be verified for them as well.

This further motivated us to investigate all our samples with alternative local spectroscopic techniques such as μSR.

5.4 μSR perspective on the site intermixing

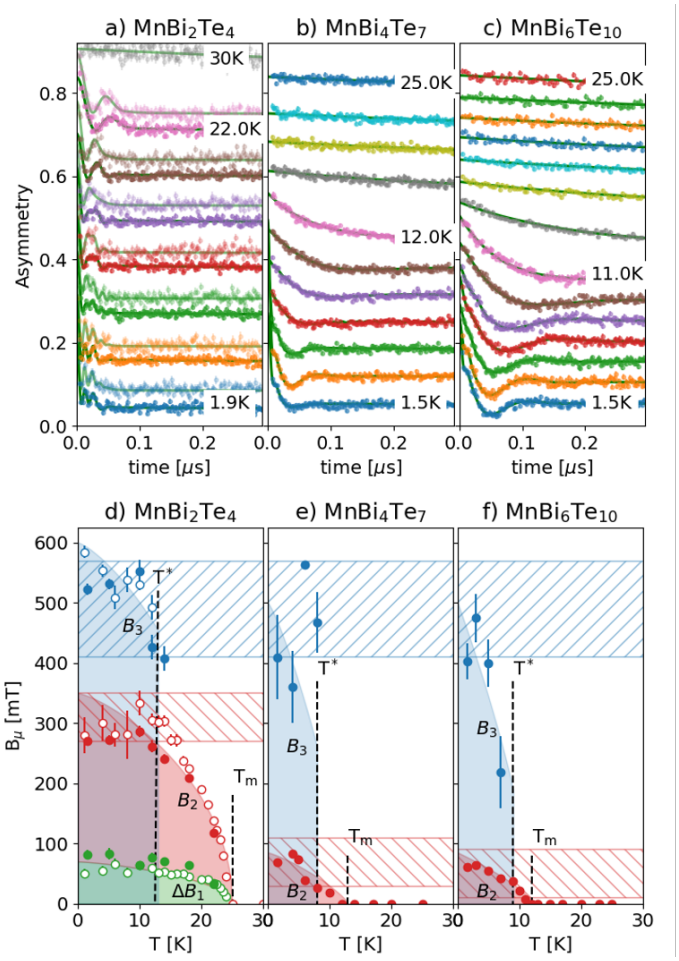

Figure 5.9: ZF μSRfor $(MnBi_2Te_4)(Bi_2Te_3)_n$, n=0,1,2 (a-c) Early time ZF asymmetries at various temperatures with best fits (solid curve), displaced vertically for clarity; (d-f) Temperature dependence of the internal fields $\Delta B1$, B_2, B_3 (green, red, blue symbols, respectively), the hatched bands show the values predicted by DFT at T = 0, shaded areas are guides to the eye; open points are sample β; taken from own publication Ref. [9].

Muon spin spectroscopy is a complementary method to NMR, since, unlike NMR, it allows measurements across the transition temperature (details can be found in the μSR section in chapter 2).

The μSR experiments were carried out on the GPS spectrometer at the Paul Scherrer Institute, Villigen, Switzerland. Both ZF μSR and WTF μSR experiments have been performed using a ^{4}He-flow cryostat on pressed polycrystalline powder samples of $(MnBi_2Te_4)(Bi_2Te_3)_n$, n=0,1,2 and $MnSb_2Te_4$ mounted on standard sample holders in the temperature range between 1.5 K and 50 K.

5.4.1 Zero field μSR in the $MnBi_2Te_4$ family

Fig. 5.9 a,b,c represents the ZF-μSR asymmetry $A(t)$ together with the best fit to eq. 5.3 for the $(MnBi_2Te_4)(Bi_2Te_3)_n$, n=0,1,2 samples across their entire ordered state. Let's start describing those of $MnBi_2Te_4$, panels a) and d). The asymmetry displays up to four components, as I describe below

- A slow relaxing component that is clearly the cumulative longitudinal fraction (the long time tail in Fig. 5.9 a)
- A very fast initial relaxation, in the first few ns, with an internal field B_1 smaller than its width ΔB_1, $0 \lesssim B_1 < \Delta B_1$ (overdamped)
- Two damped oscillation with two distinct internal fields: a low field $B_2 > \Delta B_2$ easily distinguished at high-temperature Fig. 5.9 a and a high field $B_3 > \Delta B_3$, the faster oscillation discernible at low temperatures.

A minimal choice for the best-fit function of the time domain ZF asymmetry for $MnBi_2Te_4$ is the following:

$$A_{ZF}(t) = A_0\left[f_{t1}\, e^{-\sigma_1^2 t^2/2} + \sum_{i=2}^{3} f_{ti}\, \cos(\gamma_\mu B_1 t)\, e^{-\sigma_i^2 t^2/2} + + f_l\, e^{-t/T_1}\right] \qquad (5.3)$$

Compare this expression to eq. 2.59 for reference. The three components with fractions f_{ti} are assigned to the transverse polarization due to their fast Gaussian relaxation, whereas the slow relaxing longitudinal fraction cannot be distinguished in as many components and is represented by the single term f_l. Here, $\sum_i f_{ti} + f_l = 1$ and the maximum experimental asymmetry, A_0, is calibrated at high temperature.

The three transverse components are those described in the bullet list above.

To validate this behavior, experiments with two different $MnBi_2Te_4$ samples, α, β, have been conducted. The two samples are represented by closed (α) and open (β) symbols in Fig. 5.9 d, both exhibiting similar patterns. The appropriateness of the model for both samples is highlighted in the expanded Fig. 5.10 a, which shows the separate contribution of components 1, 2, and 3 at base temperature.

This model describes the internal field distribution probed by muons as having three Gaussian components with very broad widths, ΔB_i. Importantly, the field distributions have similar temperature dependence in all the samples, as shown in 5.9 d,e,f. Let us consider, for example, that the $MnBi_2Te_4$ sample shows the ΔB_1, and B_2 follows as the magnetic order parameter until the second-order magnetic transition $T_N = 24K$. However, B_3 vanishes abruptly, well below T_N, at T^* = 12K without any corresponding anomaly in ΔB_1 or B_2. This abrupt disappearance is reminiscent of the antisite disordering detected by ^{55}Mn-NMR in $MnSb_2Te_4$.

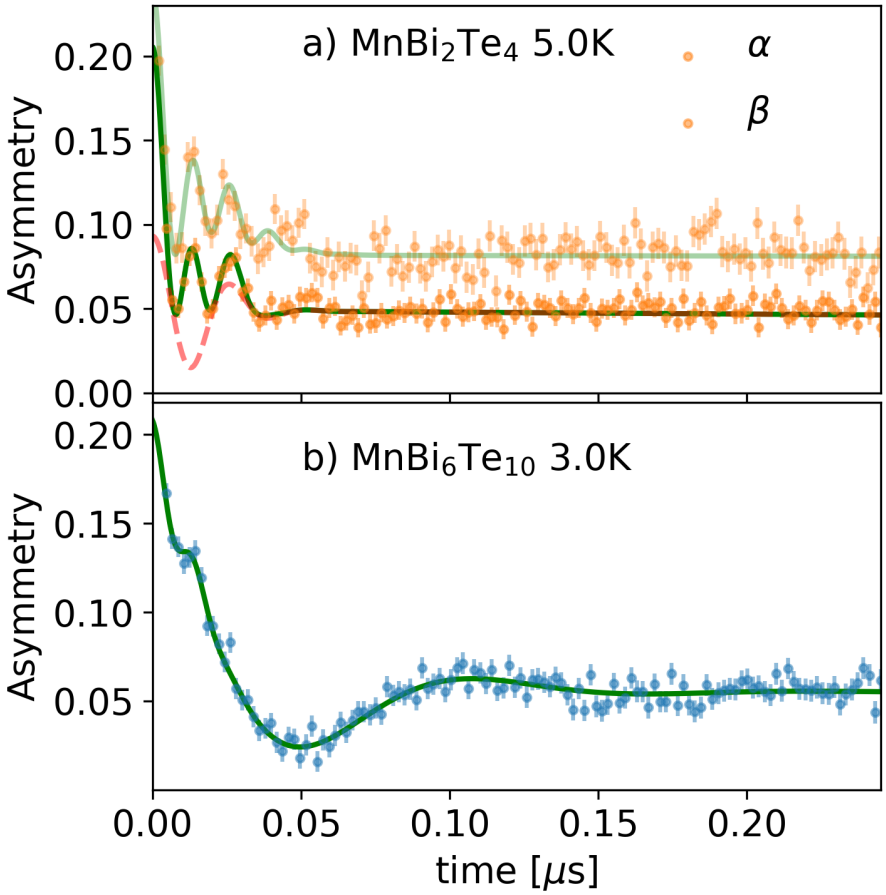

Figure 5.10: Best fits Eq. 2, at low temperature for a) $MnBi_2Te_4$ α and β samples (dashed curve: best fit with components 1 and 3 are set to zero amplitude to highlight component 2), and b) $MnBi_6Te_{10}$, with reduced χ^2 = 1.00, 0.98, 0.98, respectively; taken from own publication Ref. [9].

Let's not go back to $MnBi_4Te_7$ and $MnBi_6Te_{10}$ to underline the differences and similarities with $MnBi_2Te_4$. In FIg. 5.9 b,c, the asymmetry displays

- No overdamped fast relaxing component 1.
- Two similar damped oscillations with comparable internal fields: a low field $B_2 > \Delta B_2$ and a high field $B_3 > \Delta B_3$.

In these two other samples, B_2 also follows the order parameter until the transition temperature, and similarly, the higher field B_3 vanishes abruptly below $T^* = 6$ K. The disappearing component, which now coincides with the magnetometry anomaly for the same samples (Fig. 5.1), fully supports the identification of this phenomenon within the vanishing NMR antisite amplitude observed in the $MnSb_2Te_4$ sample in Fig. 5.8. It is tempting to link both to a first-order decoupling of the magnetic moments at the antisites, Mn_{6c}. However, this remains to be proven, first of all by consistency, and, possibly, by DFT site assignment.

Let's consider magnetic volume fractions m_i that are also derived (as it was shown qualitatively in Fig. 2.18) from the ZF normalized fractions (t each internal field B_i, using the equation

$$m_t = \sum_{i=1}^{3} m_i \qquad m_i = \frac{f_{ti}}{f_{t0}} \tag{5.4}$$

where $f_{t0} = \lim_{T\to 0} \sum_i^3 f_i(T)$ and independently, the total magnetic volume fraction m_l is obtained from the longitudinal amplitude

$$m_l = \frac{3}{2}(1 - f_l(T)) \tag{5.5}$$

where the last equation neglects muon stopping outside the sample, and is only valid in the ordered phase.

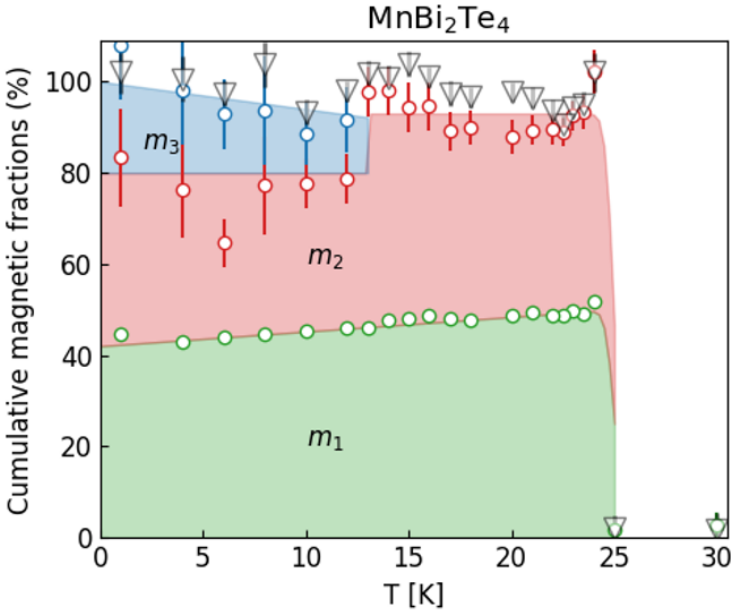

Figure 5.11: ZF transverse cumulative magnetic fractions m_1 (green circles), $m_1 + m_2$ (red circles) and $m_1 + m_2 + m_3$ (blue circles), plus longitudinal magnetic fraction m_l (grey triangles); taken from own publication Ref. [9].

These fractions are displayed in Fig. 5.11: the colored symbols and are the cumulative sum of the three transverse fractions for $MnBi_2Te_4$ -β. The shaded areas represent each of them, separately. The grey symbols show m_l. While $m_l, m_1 + m_2$ (grey, red and green symbols) drop sharply at the transition, m_3 (blue symbols) vanishes abruptly at T^*, suggesting that this component originates from muon sites sensitive to the subtle change that takes place across that point. This is again reminiscent of the vanishing B_3 at T^* and the vanishing NMR amplitudes in the $MnSb_2Te_4$ ZF-NMR results.

Now, let's check if the same phenomenon takes place in $MnSb_2Te_4$. the P6 has been selected. $MnSb_2Te_4$ sample, since it displays the closest transition temperature ($T_C = 27$ K) to $MnBi_2Te_4$, it is characterized both by NMR and magnetometry, it has the highest Mn_{6c} contribution, as estimated from NMR. Furthermore, this is precisely the sample where the NMR anomaly was observed, it is also important to confirm the presence of a high frequency oscillation in ZF-μSR with a similar temperature dependence.

5.4.2 Zero field μSR in the P6 $MnSb_2Te_4$ samples

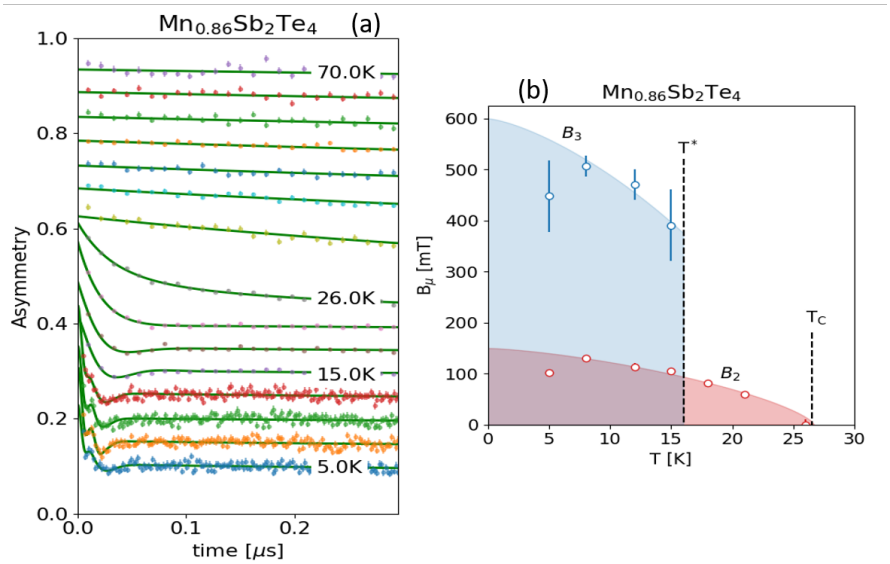

Figure 5.12: ZF μSRfor $MnSb_2Te_4$ (a) Early time ZF asymmetries at various temperatures with best fits (solid curve), displaced vertically for clarity; (b) Temperature dependence of the internal fields B_2, B_3 (red, blue symbols), shaded areas are guides to the eye; taken from own publication Ref. [9].

Fig 5.12 a shows the asymmetry measured in the temperature range $5 < T < 70$ K. The best fit obtained to the asymmetry using the same equation 5.3. At first sight, it looks similar to the results of $MnBi_4Te_7$, $MnBi_6Te_{10}$: no fast relaxing component B_1, exhibiting solely the damped oscillating components B_2 and B_3. The local field distributions are even broader, as is expected in view of an increased degree of cationic site intermixing, demonstrated by diffraction and presumably stemming from the closer ionic radii of Mn and Sb with respect to Mn and Bi. The temperature dependence of the local field presented in Fig. 5.12 b shows indeed a similar early vanishing of the higher field component B_3 at T^*, well below the ordering temperature T_C. This further supports the hypothesis that the Mn_{6c} moment is undergoing fast (paramagnetic-like) reorientations above T^*. But there is still a lack of convincing explanation in terms of muon sites. Before checking that out by DFT, let's consider what happens above T^*, according to μSR.

5.4.3 Weak transverse field μSR in $(MnBi_2Te_4)(Bi_2Te_3)_n$, n=0,1,2

As qualitatively described in Ch. 2 (Sec. 2.3), wTF-μSR provides the amplitude of the spin precession in a small applied field ($\mu_0 H \ll \Delta B_1, B_2, B_3$), well below the magnetic transition at T_m this amplitude is proportional to the small fraction of muons implanted outside the sample that do not experience any hyperfine field. Above the transition, the sample is paramagnetic, and the fast fluctuating moments produce just a small relaxation, with the total initial asymmetry A_0. The step around the second-order transition is sharper or broader, depending on the width of the inhomogeneous distribution of T_m values.

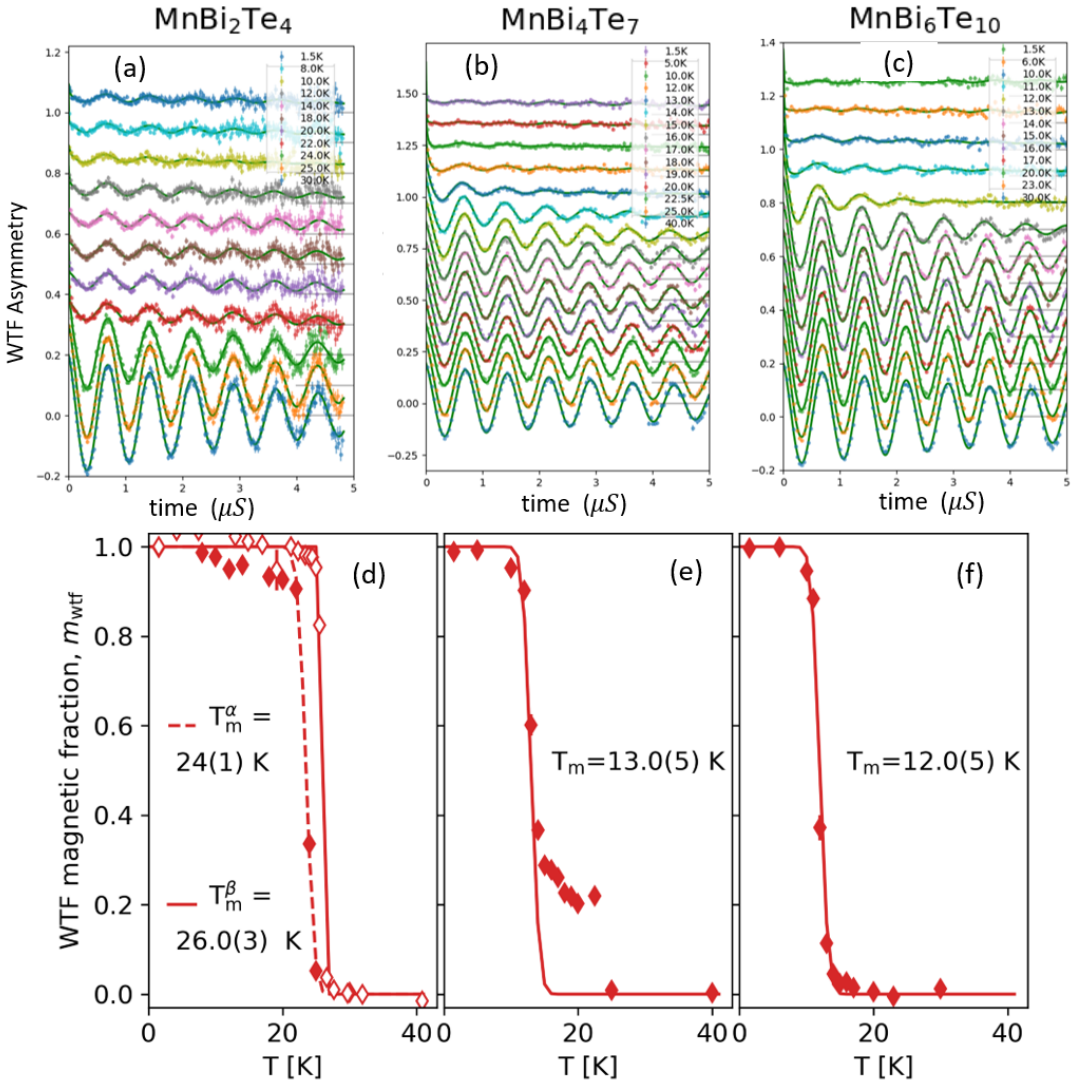

Figure 5.13: wTF-μSR in $(MnBi_2Te_4)(Bi_2Te_3)_n$, n=0,1,2(a-c) wTF asymmetry at different temperatures (d-f) temperature dependence of the wTF magnetic volume fraction; d, closed (open) symbols for sample α (β); taken from own publication Ref. [9].

WTF measurements in 10 mT in a wide temperature range have been performed. Fig. 5.13 a,b,c shows the asymmetry recorded for the $(MnBi_2Te_4)(Bi_2Te_3)_n$, n=0,1,2 samples. The prominent oscillations are due to the precession of the muons around the applied field without static magnetic ordering in the paramagnetic region. The weak field is, however, much smaller than internal fields in the ordered phase, where it does not alter the distinction between transverse (t) and longitudinal (l) components, leading to just a tiny wTF precession from the marginal fraction of muons stopping outside the sample. The best fit for the asymmetry is given by

$$A_{\mathrm{wTF}}(t) = A_0 \left[f_p \cos(\gamma B + \phi)\, e^{-\lambda_p t} + f_t\, e^{\sigma_t^2 t^2/2} + f_l\, e^{-\lambda_l t} \right] \tag{5.6}$$

where ϕ is an initial phase and f_p is the muon fraction that does not experience strong local hyperfine fields, which includes both muons stopping outside the sample

and inside paramagnetic microdomains around T_m. The former corresponds to the low-temperature residual value f_{p0}, whereas for $T \gg T_m$, one has $f_p = 1, f_t = f_l = 0$. The magnetic volume fraction d-f is obtained from the equation

$$m_{\mathrm{wtf}}(t) = \frac{f_p(T) - f_{p0}}{1 - f_{p0}}. \tag{5.7}$$

It is shown in Fig. 5.13 demonstrating that $MnBi_2Te_4$ and $MnBi_6Te_{10}$ undergo very sharp transitions at T_{m}, respectively (width $\Delta T < 1$ K for a 90%-10% volume reduction), despite their relatively large atomic disorder. Due to slightly different preparation conditions the α and β $MnBi_2Te_4$ samples show distinguishable transitions, both very sharp (T_{N} = 24(1), 26.0(3) K). The $MnBi_4Te_7$ sample displays a sharp transition as well, but a 20% contribution of the MBT phase, possibly due to $n = 0$ intergrowths, is also visible.

5.4.4 WTF μSR results for $MnSb_2Te_4$ sample

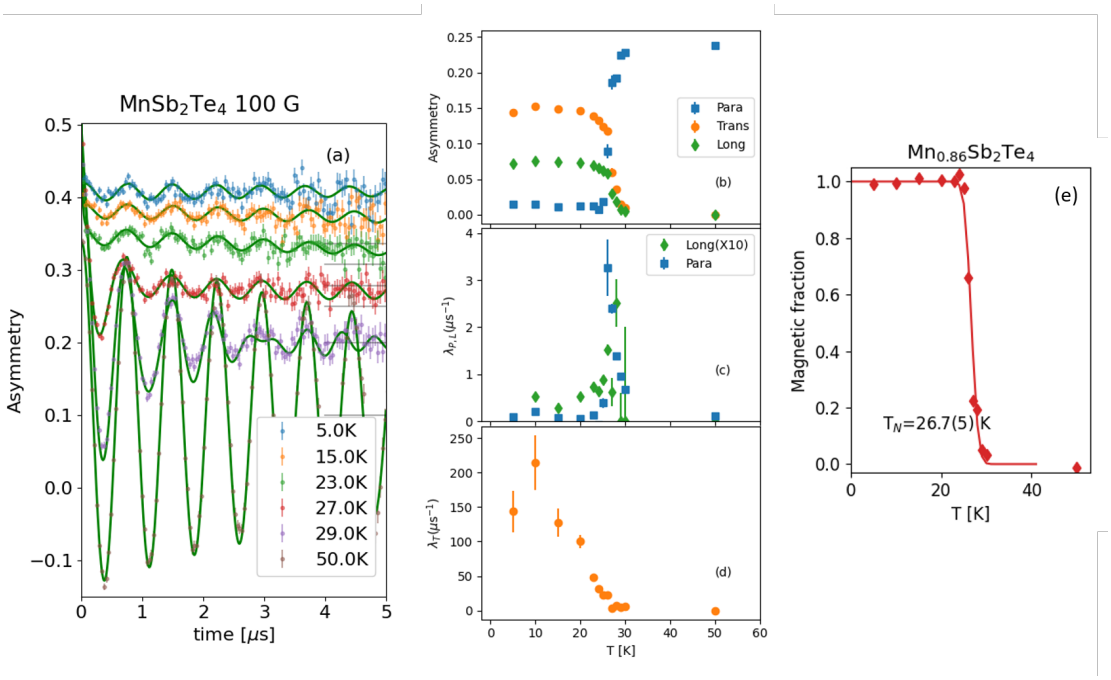

Figure 5.14: ,wTF-μSRin P6 $MnSb_2Te_4$: (a) wTF asymmetry and best fit to eq. 5.6 at selected temperatures; temperature dependence of (b-d) best fit parameters, (e) WTF magnetic volume fraction (eq. 5.7; taken from own publication Ref. [8].

Similar results were obtained for $MnSb_2Te_4$ sample P6. Fig. 5.14 a shows a representative subset of μSR asymmetries vs. time , both above and below $T_N = 27K$, together with best fits to the function of eq. 5.6 The best-fit parameters are plotted in panels b-d, and the magnetic volume fraction in panel e shows a relatively sharp transition. The same arguments of the $(MnBi_2Te_4)(Bi_2Te_3)_n$, n=0,1,2 samples apply.

Furthermore, below the transition, the rate λ_t, panel (d), represents both the mean internal field and the width of its distribution, which grows with decreasing T like an

order parameter. The transition is also marked by a relatively sharp divergence of the slow relaxation rates in panel c λ_p and λ_l. The latter is an approximation to $1/T_1$, so a divergence indicates a proper second-order transition. (details are published in Ref. [8]).

5.4.5 Magnetic transitions.

The transitions observed in $(MnBi_2Te_4)(Bi_2Te_3)_n$, n=0,1,2 and $MnSb_2Te_4$ samples, as measured by μSR and DC magnetometer (illustrated in Fig. 5.1), are summarized in Tab. 5.4. The agreement between bulk and local magnetic ordering is quite good. This suggests that the presence of significant antisite intermixing in these samples does not impact the bulk thermodynamic transition. This is crucial in identifying these samples as intrinsic magnetic TI, where atomic inhomogeneity does not play a role in the magnetic state, at least just below the transition. It is noteworthy that, despite having a wide

	T_C [K]		T^* [K]	
Sample	SQUID	μSR	SQUID	μSR
$MnBi_2Te_4$ α	24.6(1)	24(1)	11.5(1)	12(1)
$MnBi_4Te_7$	13.7(1)	13(1)	6.4(1)	6(1)
$MnBi_6Te_{10}$	12.3(1)	12(1)	6.5(1)	6(1)
$MnSb_2Te_4$	26.6(1)	26.7(5)	-	-

Table 5.4: Transition temperatures obtained from bulk magnetization and from μSR.

distribution of internal fields, due to the many different local configurations introduced by cationic intermixing, all the samples, from $MnBi_2Te_4$ and its $n = 1, 2$ descendents to $MnSb_2Te_4$, display a well defined, unique second-order magnetic transition temperature, T_m, as revealed by wTF-μSR. This contrasts, e.g. with typical *bad metal* oxides, like cuprates, where local inhomogeneity corresponds to very broad distributions of T_m.

5.4.6 Muon site calculation from DFT

After the μSR experiments, it was crucial to identify the muon sites for further insights. All calculations were conducted by Dr. I J. Onurah, University of Parma. DFT calculations were carried out on a magnetic supercell, incorporating an additional impurity hydrogen atom. The sampling of initial impurity supercell coordinates, along with lattice relaxation through force minimization, resulted in determining the minimum total energy sites and their spin couplings, allowing the computation of the local field. The protocols for determining the muon implantation sites (colloquially DFT + μ) and the local field B_μ in magnetic compounds are described in [200–203]. The details of the present calculations are reported in [9]

DFT+U calculations were performed in the antiferromagnetic unit of $MnBi_2Te_4$, wih cell size doubled along the c-axis, initially neglecting any atomic intermixing of atomic sites. To simulate the influence of an implanted muon, a hydrogen pseudopotential was placed in a larger $2 \times 2 \times 1$ supercell. For this 57-atom unit, a $3 \times 3 \times 1$ k-point grid was employed to determine the most stable arrangement of atoms and to

obtain the hyperfine field, fine-tuning the positions of atoms keeping the lattice parameters constant, until the force on each atom reached a specified low threshold value of 1×10^{-3} a.u (Ry/Bohr) and the numerical accuracy on the total energy was below 10^{-4} Ry.

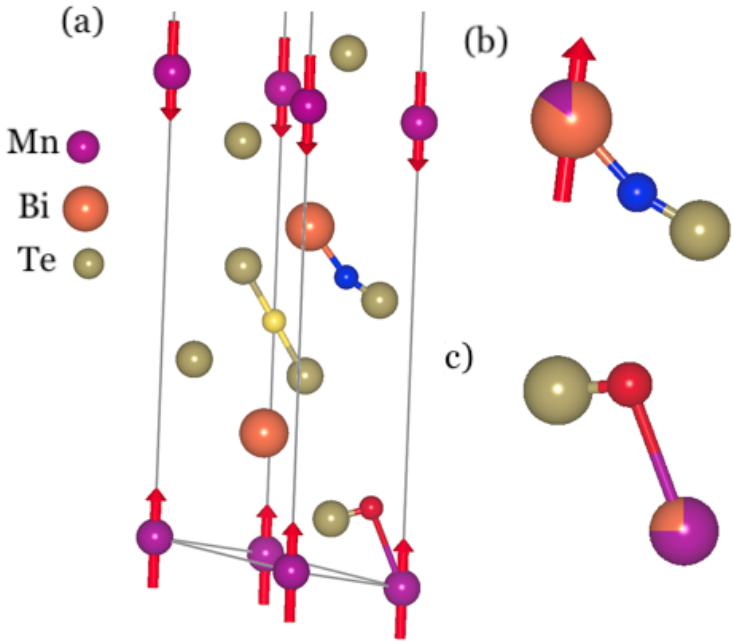

Figure 5.15: Representative muon sites as small colored atoms in $MnBi_2Te_4$ (and $MnSb_2Te_4$) by DFT+μ:Te-μ-Mn (red), Te-μ-Bi (blue atom), Te-μ-Te (yellow); taken from own publication Ref. [9].

Three muon sites have been identified in the ideal crystal: they are μ_{Te}, μ_{Bi} , and μ_{Mn}, shown in Fig. 5.15 by the small red, blue and yellow spheres, respectively. When considering site intermixing at both the Mn_{3a} and the Bi_{6c} positions, the muon sites nearest neighbor (nn) to these atoms are modified, This may happen to μ_{Bi}, and labeling the modified version $\mu_{Mn@Bi}$ when the nn 6c site is occupied by Mn. It may also happen to μ_{Mn}, and again labeling the modified version $\mu_{Bi@Mn}$ when the nn 3a site is occupied by Bi.

Of course, if the nn antisite Mn_{6c} becomes paramagnetic as hypothesized, then $\mu_{Mn@Bi}$ must become identical to μ_{Bi} again. In order to check our hypothesis we must then compare predicted and measured local fields, bearing in mind that more sites may contribute to the same field distribution from the data fit.

5.4.7 Local field calculation for $MnBi_2Te_4$

Recalling eq. 2.54, the total local magnetic field at the muon site is

$$\mathbf{B}_\mu = \mathbf{B}_\mathrm{C} + \mathbf{B}_\mathrm{dip} + \mu_0 \frac{\mathbf{M}}{3} \tag{5.8}$$

where the Lorentz term (the last) has been included, for further simulations on the FM structures. The isotropic contact contribution $\mathbf{B}_\mathrm{c}$, necessitates a quantum treatment of the electronic wavefunction obtained here by DFT [202]. The final two components

Muon site label	nn antisite	$DFT+\mu$ B_μ (mT)	Experiment B_i (mT)	i
μ_{Mn}	-	314	290(10)	2
μ_{Bi}	-	93	0(80)	1
μ_{Te}	-	0		
$\mu_{Mn@Bi}$	Mn_{6c}	527	550(30)	3
$\mu_{Bi@Mn}$	Bi_{3a}	95	0(80)	1

Table 5.5: local field at the representative muon sites from experiment and DFT, the color atom shows the sites shown in the fig 5.15

are derived by summing up long-range dipolar fields in real space within the Lorentz sphere and adding the Lorentz term if macroscopic **M** is non-zero [201]. Let's perform the comparison initially on antiferromagnetic $MnBi_2Te_4$, in which the Lorentz term vanishes. The contributions and the total $\mathbf{B}_\mu$, calculated for each muon site (with 4.3 μ_B on Mn, as obtained from NMR), are reported in Tab. 5.5 together with the experimental values.

The experimental B_2 field value closely matches the calculated field for the μ_{Mn} site. Similarly, B_3 corresponds well with the field computed for $\mu_{Mn@Bi}$- Finally, B_1, which has a larger width ΔB_1 than other fit components, agrees within its width with the calculations for μ_{Bi}, μ_{Te} and $\mu_{Mn@Bi}$ as well.

This agreement is already encouraging, but, furthermore, it agrees with the prediction that the high field B_3, originating from $\mu_{Mn@Bi}$ vanishes if Mn_{6c} becomes paramagnetic. The presence of the intermixing, which produces many slightly different local configurations, justifies all the broad field distributions. The field values exhibit a strong agreement with experimental values well within the accuracy of the DFT + μ, within a 25% margin.

This surprisingly good agreement for a complex material strongly supports the conclusion that the ^{55}Mn6a indeed decouples at T^*, based on the disappearance of the B_3 fit component above that temperature. Let's now check that the same picture holds for the other materials.

5.4.8 Local field for $MnBi_6Te_{10}$,$MnBi_4Te_7$ and $MnSb_2Te_4$

Let's first compare the DFT predictions for $MnBi_4Te_7$ and $MnBi_6Te_{10}$. First of all fields must be recalculated because of the additional Lorentz term for FM configurations (although the FM ground state in true ZF may not be given for granted).

In order to redo the field calculations, re-assigning the muon sites, assuming that two of them, μ_{Mn} and μ_{Bi} are the same as in $MnBi_2Te_4$, since the family shares the same structure close to these sites. This implies that the sites modified by a nn antisite, $\mu_{Mn@Bi}$ and $\mu_{Bi@Mn}$, also remain the same. The third unperturbed site, μ_{Te}, may change and actually give rise to more inequivalent minima in the larger unit cells. However, these sites are far removed both from the magnetic moments located at Mn_{3a} and at the antisite Mn_{6c}, so they will continue to contribute to the low field distribution.

The detailed calculation requires vector compositions, but its qualitative description is simple. The Lorentz field amounts to 40 and 30 mT for $MnBi_4Te_7$ and $MnBi_6Te_{10}$, respectively, and it contributes negligibly to the large field at $\mu_{Mn@Bi}$, and it reduces

significantly the total field value for μ_{Mn}. In contrast, it increases the values of μ_{Bi}, $\mu_{Bi@Mn}$ and of the farther removed sites, whose local fields tend to coalesce around $\mathbf{B}_L = \mu_0\mathbf{M}/3$. The exact calculation justifies two field distributions, one centered at B_3, due solely to $\mu_{Mn@Bi}$, the second due to all the other sites and centered around the Lorentz field. The DFT predictions are represented by the hatched regions in Fig. 5.9 d-f, and they compare extremely well with $T = 0$ experimental data (symbols of the same color). The overall agreement is truly remarkable. The same arguments substantially hold for $MnSb_2Te_4$ as well.

5.5 Discussion

5.5.1 NMR results on $MnBi_2Te_4$ and $MnSb_2Te_4$ samples

An important result from NMR is the size of the moment on Mn obtained from the hyperfine field, in first approximation proportional to the on-site coupling $\mathcal{A}$, which is roughly 10 T/μ_B for all 3d ions and for ^{55}Mn in particular [204, 205]. An estimate of this coupling comes from the ZF NMR frequency of Mn_{3a}, Mn_{6c}. Taking the value of the latter for its much smaller transferred terms $\mathcal{B}$, and, conservatively, half their difference as the uncertainty, getting roughly the same moment for all three $(MnBi_2Te_4)$-$(Bi_2Te_3)_n$, n=0,1,2 samples, $\mu_{\mathrm{Mn}} = 4.3(2)\mu B$, in agreement with neutron diffraction [206].

Most importantly, NMR identifies the antisite Mn_{6c} in all the samples and demonstrates its nearly antiparallel spin alignment to the spin of the main Mn_{3a} site. This was already suggested on the basis of neutron diffraction results for $MnSb_2Te_4$ [164, 165]. This finding extends to the whole $(MnBi_2Te_4)(Bi_2Te_3)_n$, n=0,1,2 family has been confirmed, where the magnetic role of the antisites was not established yet, despite extensive neutron diffraction data [143, 197, 206] (likely because of the much lower levels of intermixing as compared to $MnSb_2Te_4$). An indirect suggestion for an AFM coupling between the Mn_{6c} and Mn_{3a} was already provided by $MnBi_2Te_4$ high-field magnetization [173]. The NMR results provide a direct demonstration of the relative spin alignment, thanks to the positive identification of the antisite NMR signal.

The fraction x of Mn_{6c} in each sample may be estimated from the ratio of the area under the two NMR peaks in the high field at 1.4K and from the f_3 fraction experiencing the average field B_3 at 1.5 K in μSR. Both are due to the presence of static Mn_{6c} moments, this being a lower limit, very close to the true atomic occupancy. The results agree and are summarized in Tab. 5.3. It is noteworthy that the fraction of Mn_{6c} in the $MnBi_2Te_4$ sample is comparable to that of some $MnSb_2Te_4$ samples, which varies depending on preparation conditions,

sample	x (NMR)	x (μSR)
$MnBi_2Te_4$	0.2(1)	0.2(1)
$MnBi_4Te_7$	0.11(1)	0.10(5)
$MnBi_6Te_{10}$	0.13(1)	0.10(5)

Table 5.6: Fraction x of Mn_{6c} antisites.

Importantly, NMR reveals a magnetic order-disorder transition in the Mn_{6c} sublattice of $MnSb_2Te_4$ well below $T_{\mathrm{m}} = 27$ K. This clearly discriminates two regions in

the $MnSb_2Te_4$ magnetic phase diagram: (i) $T < T^* < T_C$, when the Mn_{6c} and Mn_{3a} moments are coupled antiferromagnetically; and (ii) $T^* < T < T_C$, when the Mn_{6c} sublattice is paramagnetic-like, whereas the Mn_{3a} one sustains its intra- and interlayer orders. The same could not be confirmed in the $(MnBi_2Te_4)(Bi_2Te_3)_n$, n=0,1,2 samples because of the smaller T_2 also they had a small T_C compared to the $MnSb_2Te_4$ samples.

5.5.2 μSR results on $MnBi_2Te_4$ and $MnSb_2Te_4$ samples

Above T^*all the $(MnBi_2Te_4)(Bi_2Te_3)_n$, n=0,1,2 samples, and the $MnSb_2Te_4$ sample as well, reveal the same vanishing of the high internal field B_3. This component is attributed by DFT to $\mu_{Mn@Bi}$, the muon site closest to Mn_{6c}. The magnetic fraction f_3 is small (small probability for a muon to end up there) but appreciable below T^* and it abruptly vanishes above, as shown in Fig. 5.11. Since the antisite is stable and DFT indicates that the muon site is also stable, the hyperfine field is averaged to zero when the Mn moment starts to fluctuate. Therefore, above $T^*$the $\mu_{Mn@Bi}$ site becomes magnetically equivalent to μ_{Bi}, and, indeed, m_2, the magnetic fraction to which this site contributes, displays a step-like increase at T^*. A similar conclusion can be drawn in all three compositions and in $MnSb_2Te_4$ as well.

No other fit parameter changes significantly across T^*, in particular, relaxation rates behave smoothly, therefore this point is not accompanied by slowing down of fluctuations. This aspect agrees with the $MnSb_2Te_4$ NMR results of Fig. 5.8, which suggests that, as the temperature increases, clusters of Mn_{6c} spins progressively decouple from the magnetic lattice and start to fluctuate. This shows up also as an anomaly at T^* is in the magnetization data of Fig. 3.6.

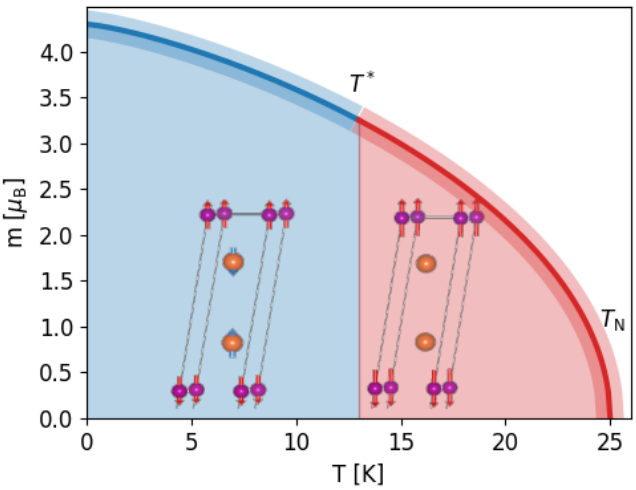

Figure 5.16: Phase diagram summary: staggered order parameter from $B_{1,2}$ and NMR hyperfine fields , magnetic moment on Mn_{3a}, for $MnBi_2Te_4$. Insets: magnetic structures; taken from own publication Ref. [9].

Fig. 5.16 summarizes the findings in a phase diagram for the A-type antiferromagnet $MnBi_2Te_4$, where the $T = 0$ magnitude of the static Mn moment is taken from

NMR and its temperature behavior from the ZF μSR fields $B_1(T), \Delta B_2(T)$ of Fig. 5.9 d, interpolated by Eq. 5.9.

$$b(T) = \left[1 - \left(\frac{T}{T_m}\right)^{\gamma}\right]^{\delta} \tag{5.9}$$

The blue region is characterized by the static ordering of the diluted Mn_{6c} moments, aligned antiparallel to the main Mn_{3a} moments, as NMR demonstrates. The static moment at Mn_{6c} vanishes in the red region. The red-filled high-temperature phase is characterized by a very sharp second-order transition, as it is witnessed in all samples by the abrupt vanishing of the entire magnetic volume fraction, both by WFT and ZF μSR (Fig. 5.13). The unique ability of μSR, as opposed to both magnetometry and neutron scattering, to distinguish the reduction of the magnetic moment, encoded in the local field, from the volume fraction, encoded in the amplitude of the signal is remarkable. Local disorder, like that expected from magnetically coupled, random antisites, could yield a distribution of transition temperatures, hence a more progressive reduction of the volume fraction than that displayed by all the samples. This suggests that from a magnetic point of view, the high-temperature ordered phase approaches closely the ideal, intermixing-free material. This provides both the antiferromagnetic and the ferromagnetic versions of a close-to-ideal magnetic topological insulator.

5.6 Conclusion

The intricate details of the intermixing in the anti-site position have been investigated thoroughly using local spectroscopic techniques. The NMR measurements confirm the opposite alignment between the Mn magnetic moments on native sites and anti-sites in the ground state of $MnSb_2Te_4$ and for the first time directly show the same alignment in $(MnBi_2Te_4)(Bi_2Te_3)_n$, n=0,1,2. Moreover, for all compounds, the static magnetic moment of the Mn antisite sublattice disappears well below the intrinsic magnetic transition temperature, leaving a homogeneous magnetic structure undisturbed by the intermixing.

The discovery of the loss of the Mn_{6c} sublattice magnetic ordering is highly relevant in the context of the crucial role that Mn-Bi intermixing plays in the reduction of the $MnBi_2Te_4$ Dirac point gap [115, 117, 129, 131–133]. Early sublattice decoupling is well documented, for instance in intermetallic compounds, [207–209] and it often involves exchange coupling frustration, which may also play a role in the present case [187]. Since intermixing is a common feature for all materials including cation species with similar radii, speculating that early antisite disordering may take place more often than one thinks, and the findings may have a more general impact than just on the present materials.

Chapter 6

Helical to conical ground state in $M_{1/3}XY_2$, observed through NMR

6.1 Introduction

Following the study of materials hosting momentum space topological order and an out-of-plane long-range magnetic order, this section will focus on materials that possess real space topological texture and exhibit a complex magnetic order undergoing various phases under the influence of a magnetic field. Among these phases is the topological texture soliton phase, previously introduced in the beginning. Solitons represent 1D spin chains characterized by topological robustness, resembling skyrmions in 2D or 3D. Despite being proposed in 1964, with numerous theoretical works outlining intriguing particle-like properties and topological robustness [50–53, 210, 211], it wasn't until 2012 that experimental realization of solitons was achieved in $Cr_{1/3}NbS_2$ [212] though polycrystalline samples were synthesized in 2009 [213].

Beginning with an investigation into the crystal structure of the material, the magnetic interactions that determine various magnetic phases will be highlighted, supported by a brief review of relevant literature on the phase diagram. Following this, the focus will turn to the related sister compound, expecting similar properties that have yet to be observed. The core objective of this thesis is to perform NMR measurements on these two samples to understand the unique phases that emerge in the ordered state when exposed to a magnetic field.

6.1.1 Crystal structure of $M_{1/3}NbS_2$, M=Cr,Mn

A diverse range of materials can be generated by inserting 3D transition metals into hexagonal-layered transition metal dichalcogenides (TMDC). The intercalated atoms take up octahedral 2c or 2d Wyckoff positions located between the trigonal prismatic layers, separated by a van der Waals gap. This configuration is denoted by the generic formula $M_{1/3}XY_2$, where M represents the intercalated transition metal (e.g., Cr, Mn, V, Ti, Co, Fe), X can be either Nb or Ta, and Y can be S or Se. Consequently, a vast array of materials with diverse topological and magnetic properties becomes accessible for various applications. The crystal structure depends on the amount of intercalation, with the parent compound XY_2 adopting a centrosymmetric $P6_3/mmc$ structure and transitioning into the noncentrosymmetric $P6_322$ structure only when the intercalant concentration reaches a critical level, i.e., $M_{1/3}XY_2$. It is crucial for the intercalant to exclusively occupy either the 2c or 2d Wyckoff position rather than being evenly distributed between both sites [214–217] shown in Fig. 6.1 a.

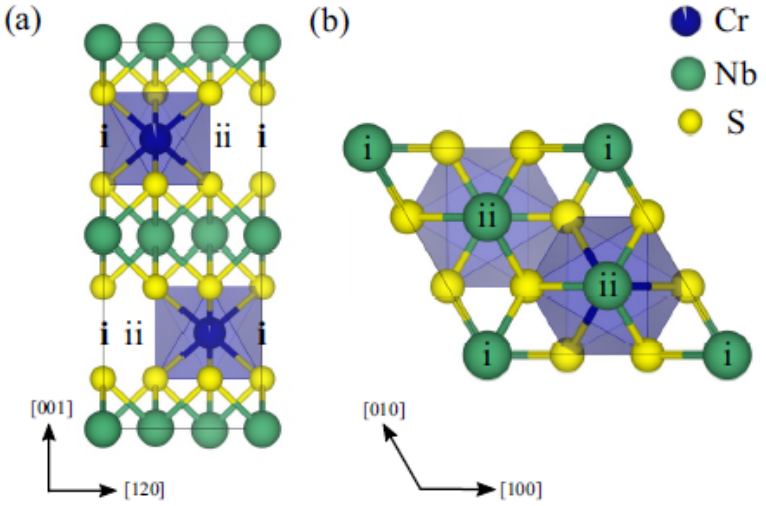

Figure 6.1: Crystal structure of $Cr_{1/3}NbS_2$ viewed along (a) the *a* axis and (b) *c* axis, with S atoms shown in yellow, Nb atoms shown in green, and Cr atoms shown in blue. The octahedral sites of the 2c Wyckoff position are shown by blue polyhedra. The projection of the 2b and 2d sites as seen from each direction is indicated using i and ii, respectively; taken from Ref. [214].

Within this broad class of materials, complicated magnetism is observed in $Cr_{1/3}NbS_2$ due to the placement of Cr atoms in the 2c position. This modification influences the arrangement of neighboring sulfur atoms, inducing a chiral axis along the c direction, owing to the absence of inversion symmetry and a mirror plane. The resulting chirality introduces a significant contribution from the antisymmetric exchange, known as the Dzyaloshinskii-Moriya (DM) interaction, to the magnetic Hamiltonian [212, 215, 217, 218]. These magnetic interactions will be discussed in detail in the next section.

6.1.2 Magnetic interactions in $Cr_{1/3}NbS_2$

Several magnetic interactions are present in the Cr compound and the Hamiltonian may be written as[218]

$$H = \sum_i [-J\mathbf{S}_i \cdot \mathbf{S}_j - \mathbf{D} \cdot (\mathbf{S}_i \times \mathbf{S}_j) + KS_{iz}^2 + g\mu_B \mathbf{B} \cdot \mathbf{S}_i] \tag{6.1}$$

Where the four terms are Heisenberg exchange interaction with J as the nearest neighbor parameter, DM interaction where D is the monoaxial DM vector along the *c* axis, magnetocrystalline anisotropy with A as the anisotropy constant, and Zeeman energy with μ_B is the Bohr magnetron. [219, 220]. These interactions are described in Chapter 1 and they simply recalled here in the context of the compounds under investigation.

The Heisenberg interaction, with coupling J, originates from the Coulomb repulsion between electrons when the ground state is an antisymmetric wavefunction. The dominant term is usually that between nearest neighbor spins within the layer, $J_{\parallel}$, and the next one still between nearest neighbors across two layers, $J_{\perp}$ In the $Cr_{1/3}NbS_2$

sample, they both contribute to the magnetic ordering, which takes place below T_C = 110–130 K. [221]

The Dzyaloshinskii-Moriya interaction emerges from spin-orbit coupling (SOC) when the inversion crystal symmetry is broken in the system [215]. While the Heisenberg interaction prefers spins to align parallel to neighboring spins, the DM interaction prefers spins to be perpendicular to the DM vector with a fixed angle relative to each other The competition between these two interactions results in a helical alignment of spins. The angle between spins can be determined from the DMI and intralayer Heisenberg interaction as $\theta = \arctan(D/J_{\parallel})$, 9 degrees in $Cr_{1/3}NbS_2$. The sign of the DM vector **D** dictates the chirality, which is left-handed due to a negative sign in this sample [212, 218].

The magnetocrystalline anisotropy, with coupling constant K, represents the simplest (uniaxial) interaction favoring the spin alignment along a specific crystalline lattice direction, if K is negative, indicating the preferred orientation of magnetization, known as the magnetic easy axis. In the case of $Cr_{1/3}NbS_2$, it exhibits a negative (easy plane) anisotropy K, stemming from its hexagonal crystal structure. Consequently, the chiral axis aligns with the c axis, fostering a long wavelength spin helix configuration and giving rise to the hosting of chiral topological spin texture, specifically solitons.

The Zeeman interaction aligns the spins in the direction of the field and is directly proportional to the field strength. Competition between the Zeeman term and the other three interactions leads to distinct phase transitions for different field directions and magnitudes.

6.1.3 Magnetic phases in $Cr_{1/3}NbS_2$

In the absence of a magnetic field, the system's ground state adopts a chiral helimagnetic (CHM) configuration due to the competition of the Heisenberg and DM interactions. The helical axis is along the c direction. The spins align within the ab plane like in a ferromagnet but rotate from plane to plane along $\hat{c}$ with left-hand chirality (illustrated for 10 unit cells in Fig. 6.2b). The chiral period in zero magnetic fields is calculated to be $L(0) = 2\pi aJ/D \approx 48$ nm, where a is the lattice constant. [212] The CHM phase for $Cr_{1/3}NbS_2$ is depicted in Fig. 6.2c with one representative spin per ab plane along the chiral axis. When a magnetic field is applied perpendicular to the direction of the helical axis, there is a competition between the Zeeman and the DM interactions. The first favors commensurate ferromagnetic (FM) domains,the second prefers the incommensurate chiral helimagnetic (CHM) state. This competition disrupts the periodicity of the CHM, leading to the emergence of the chiral soliton lattice (CSL) phase. The CSL phase, illustrated in figure 6.2d, is a magnetic superlattice comprising ferromagnetic domains periodically separated by 360 degree magnetic domain walls. The nonlinear CSL phase is determined by the chiral sine-Gordon (nonlinear) model, and the period increases with the applied magnetic field until it reaches a critical field, beyond which the spins align in the direction of the field, resulting in a state known as the forced ferromagnetic state (FFM) [212, 214, 218], depicted in Fig. 6.2f. This phenomenon may be controlled and utilized for various topological applications. Moreover, when a magnetic field is directed along the helical axis, it causes the spins to deviate from the ab plane and incline towards the field direction. This results in the development of the chiral conical (CC) phase due to the interplay between anisotropy

and the DM interaction, as depicted in Figure 6.2e. It is crucial for the field to be applied sufficiently close to the *c* axis; otherwise, it may induce the formation of another phase known as the tilted CSL phase. This also occurs only until a critical field and the spins then polarized to form FFM phase. Our focus will be primarily on the CC phase, and a more detailed discussion will follow.

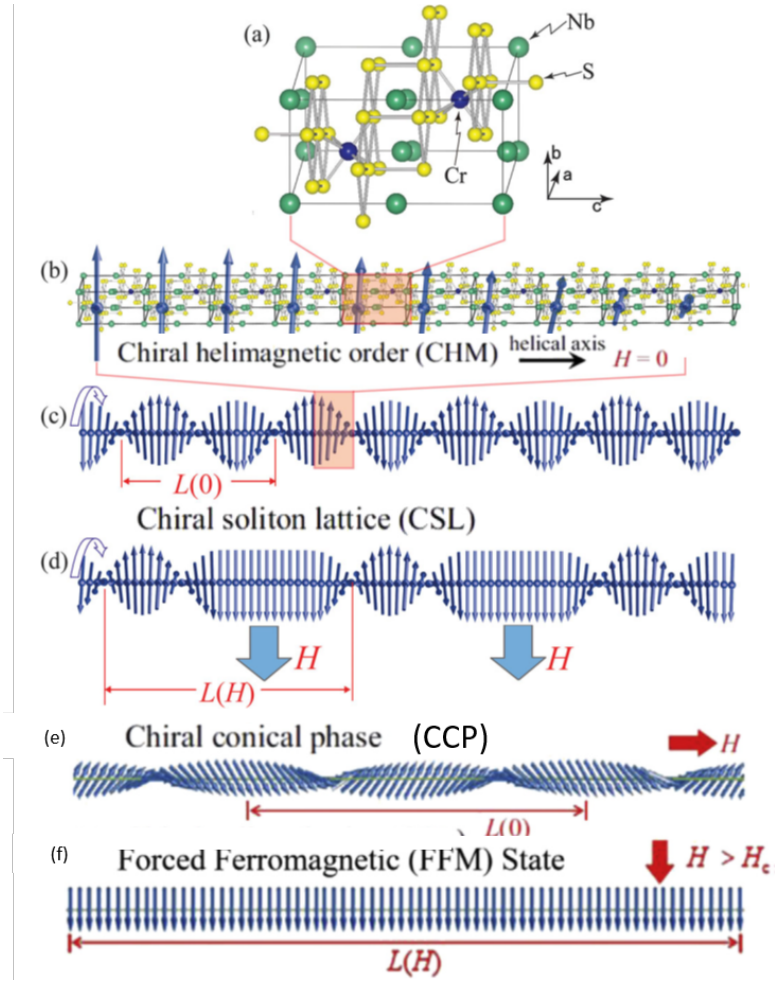

Figure 6.2: Schematic diagram of crystalline and magnetic structures of $Cr_{1/3}NbS_2$. (a) A unit cell of the crystal. A part of left-handed CHM is schematically drawn in ten unit cells in (b), whereas a whole left-handed CHM in (c). (d) In magnetic fields perpendicular to the helical *c* axis, CHM continuously transforms into CSL. (e) In magnetic fields parallel to the helical *c* axis, CHM continuously transforms into CCP. (f) Forced ferromagnetic (FFM) state under the magnetic field above the critical field; taken from Ref. [212, 218]

6.1.4 Experimental observation of magnetic phases in $Cr_{1/3}NbS_2$

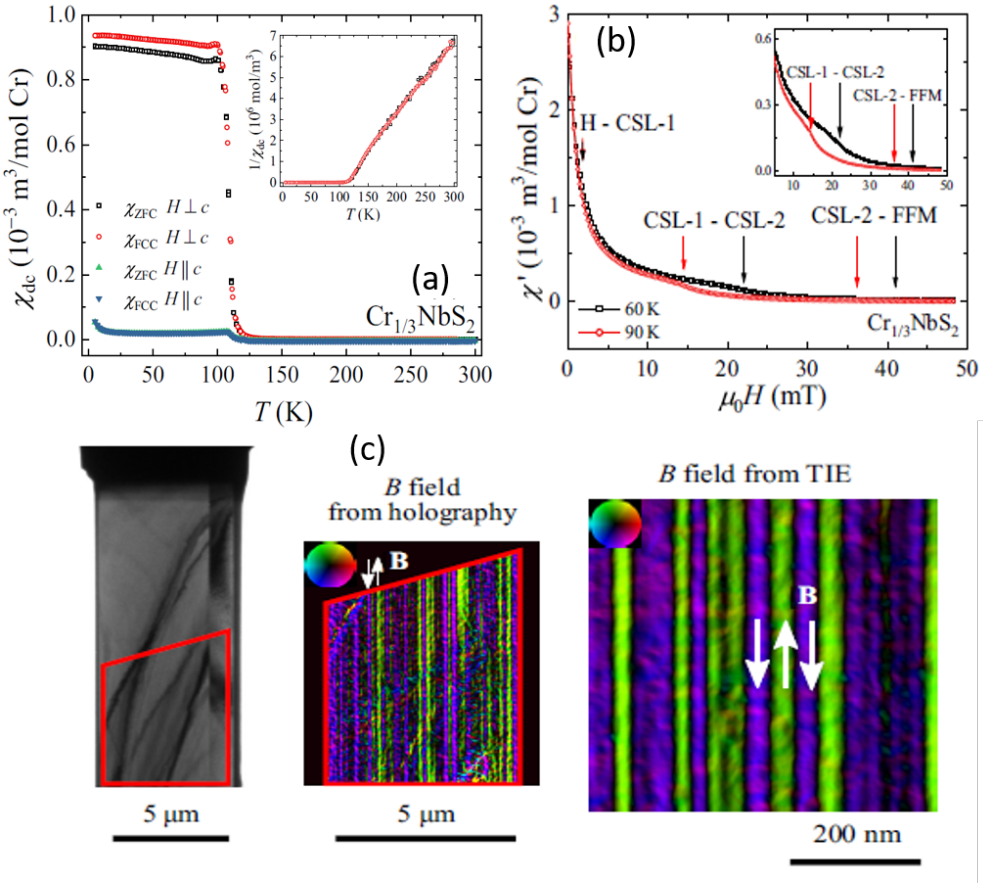

Figure 6.3: $Cr_{1/3}NbS_2$. (a) Temperature dependence of the DC susceptibility. (b) In-phase component of the ac susceptibility χ' as a function of dc field H directed perpendicular to the c axis. (c) Transmission electron micrographs infocus image, together with the projected B field at 92 K in $H = 0$ obtained using off-axis holography from the area outlined in red; taken from Ref. [214].

Figure 6.3 illustrates the magnetic phases reported [214] by our collaborators, who generously provided the samples used in this thesis. Figure 6.3a shows the static magnetization observed in the $Cr_{1/3}NbS_2$ sample under a magnetic field of 0.01T, applied parallel and perpendicular to the crystallographic c-axis ($H \parallel c$ and $H \perp c$). Below the critical temperature T_C = 111K, a ferromagnetic ordering is evident, with spins favoring alignment within the ab plane. The lower T_C, compared to other reports, can be attributed mainly to substitutional disorder[222].

From the Curie-Weiss fitting with $H \perp c$ a spin-only effective magnetic moment ($\mu_{\text{eff}} = 3.94(13)\mu_B$/Cr) is reported, consistent with the expected value for Cr^{3+} ($\sqrt{15}$) within errors. Figure 6.3b displays the in-phase component of the ac susceptibility (χ') obtained by varying the magnetic field at two different temperatures (60K and 90K) in the same sample. The noticeable decline in χ' with an increasing magnetic field signifies the transition between the chiral helimagnetic (CHM) and the chiral soliton lattice-1 (CSL-1) phases. Beyond the critical field of 40 mT, the curve saturates, marking the

transition to the spin-polarized ferromagnetic (FFM) phase, although this transition is somewhat challenging to identify.

Additionally, the first observation of the chiral soliton lattice (CSL) phase was obtained by Lorentz transmission microscopy (LTEM). [212] A structure made of thin magnetic stripes is evident n Fig. 6.3c, taken on our $Cr_{1/3}NbS_2$ sample, deviating from the conventional magnetic domains that are typically observed. This finding suggests the presence of a CSL within the material. However, it is noteworthy that the periodicity of these strips is not uniform, contrasting with the observations made in [212]. This non-uniformity is attributed to structural disorder, which not only affects the periodicity but also contributes to lowering the transition temperature and field value associated with the phase transition.

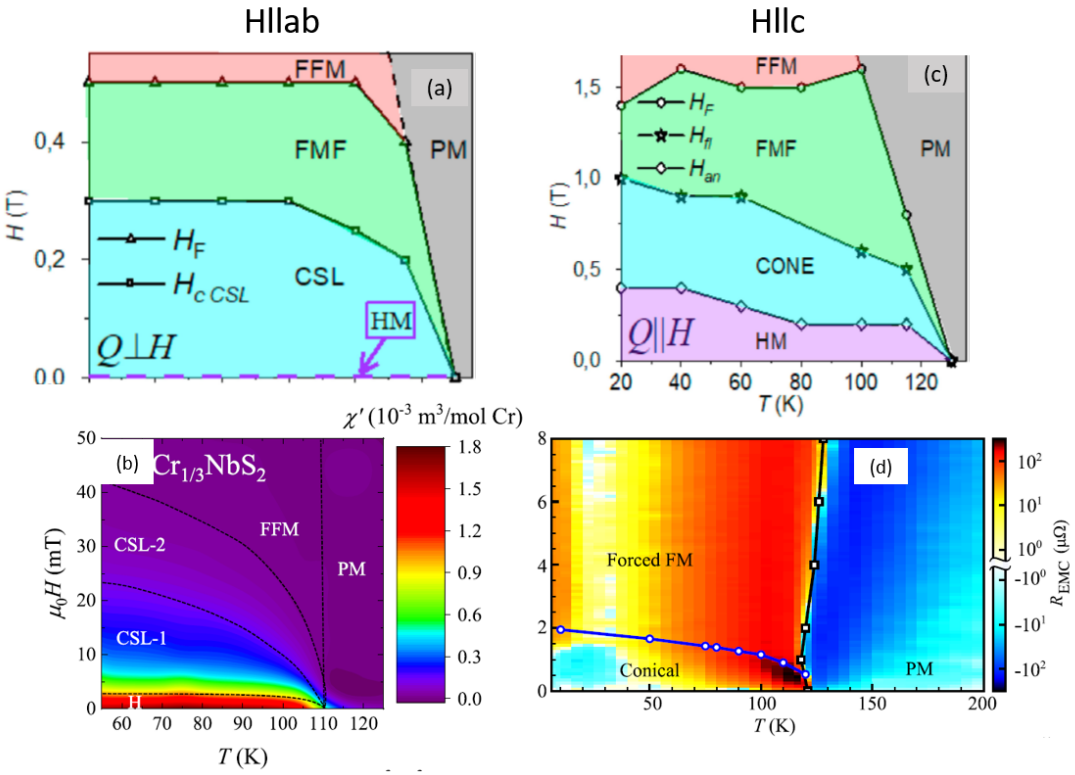

Figure 6.4: Phase diagram of $Cr_{1/3}NbS_2$. (a [223], b [216] with $H \parallel ab$) ; (c [223], d [224]) with $H \parallel c$.

Moreover, several research groups have undertaken efforts to map the phase diagram, illustrating the transitions between different phases and highlighting the phase boundaries [216, 223–227]. Figure 5.16 displays the phase diagram as reported by [214, 223, 224], considering both parallel and perpendicular orientations of the magnetic field. The critical field for these phase transitions exhibits a slight dependence on the degree of structural disorder within the system. However, the CSL phase is observed to manifest between 0.2 mT and 0.5 mT, approximately depicted in Fig. 6.4a, b. Figure 6.4a represents a phase diagram derived from integral intensity as a function of temperature and field, measured using small-angle neutron scattering (SANS) [223]. Figure 6.4b is constructed from an ac susceptibility study [214], revealing the presence of CHM for negligible or very small fields, followed by the evolution of the CSL phase

with a slightly applied field. The period of the CSL phase increases rapidly with the rising field, and beyond 0.5 mT, the spin-polarized FFM phase emerges. Similarly, for the field applied along the c-direction, as illustrated in Figure 6.4c, d, Figure 6.4c is derived from the same SANS measurement [223]. It demonstrates the CH to CC phase transition at a relatively substantial field of 0.4 mT, followed by the occurrence of a ferromagnetic fluctuation phase (FMF), and eventually, the FFM phase appears above 1.5 T at 20K. Figure 6.4d is based on resistance measurements from an electrical magnetochiral study conducted by [224]. This figure depicts the transition from the CCP phase to the FFM phase observed above 2T at the base temperature.

While all these reports confirm the phase transition from CHM to CSL and CC phases in the $Cr_{1/3}NbS_2$ sample, the isostructural $Mn_{1/3}NbS_2$ is still elusive and there are only few reports, inconclusive on whether the same magnetic scenario applies to the $Mn_{1/3}NbS_2$ sample, despite the similar crystal structur, belonging to the same space group of the Cr sample.

6.1.5 Magnetic phases in $Mn_{1/3}NbS_2$ and the challenges

Both the $Cr_{1/3}NbS_2$ and $Mn_{1/3}NbS_2$ samples were suggested to belong to the CHM family and synthesized in 2009 [213]. However, the exploration and establishment of the chiral helimagnet with its CSL and CCP phases were exclusively completed in the $Cr_{1/3}NbS_2$ sample. In this discussion, Let's focus on the few results reported for the $Mn_{1/3}NbS_2$ sample in [216, 228–230], along with the motivation behind our work. Figure 6.5a illustrates the direct current (dc) magnetization measured by our collaborators, as reported in [214]. It reveals a similar ferromagnetic ordering below the critical temperature (T_C= 45K), with the dc susceptibility along both field directions showing analogous easy-plane anisotropy. The Curie-Weiss fit provides a calculated effective magnetic moment (μ_{eff}) value of 5.43(1) μ_B/Mn along the $H \perp c$ direction, corresponding to an intermediate spin-only value, in between those appropriate for Mn^{3+} ($2\sqrt{6}$) and Mn^{2+} ($\sqrt{35}$).

The AC susceptibility in Fig. 6.5b, measured at 18 K and 36 K, exhibits a similar drop. Different phases, labeled as I and II, are identified. To assign these phases, Lorentz transmission electron microscopy (LTEM) was performed, as depicted in Figure 6.5c. The observed pattern resembled the findings by Karna et al. [228], yet interpretations varied. Karna et al. believed these patterns indicated helimagnetism and magnetic solitons, while Hall et al. contended that they were trivial magnetic domains separated by 180 deg domain walls as the difference between them is critical. The domain sizes along the *c* axis were approximately 250nm, consistent with previous observations [229] through neutron diffraction. However, confirmation of whether the anomaly observed in the ac susceptibility resulted from noncollinear behaviors or the rearrangement of domain walls remained elusive. Consequently, both research groups mapped out the phase diagram with a field applied along the ab plane, as depicted in Figure 6.5d, e, and f. All reports indicated a phase change around 30–40 mT, but no clear attribution to the CSL phase was possible. Neutron diffraction studies in this material could not resolve the structure, proposing either a large pitch-length magnetic modulation or a short-range ferromagnetic (FM) order with a domain size of 250 nm. They suggested this as the helimagnetic pitch length, $\lambda = 250$ nm ($q \approx 0.0025 \text{Å}^{-1}$)

[229], which is almost one order of magnitude smaller and larger, respectively, than the $Cr_{1/3}NbS_2$ values ($q \approx 0.015$Å^{-1}, pitch length 42 nm) [212].

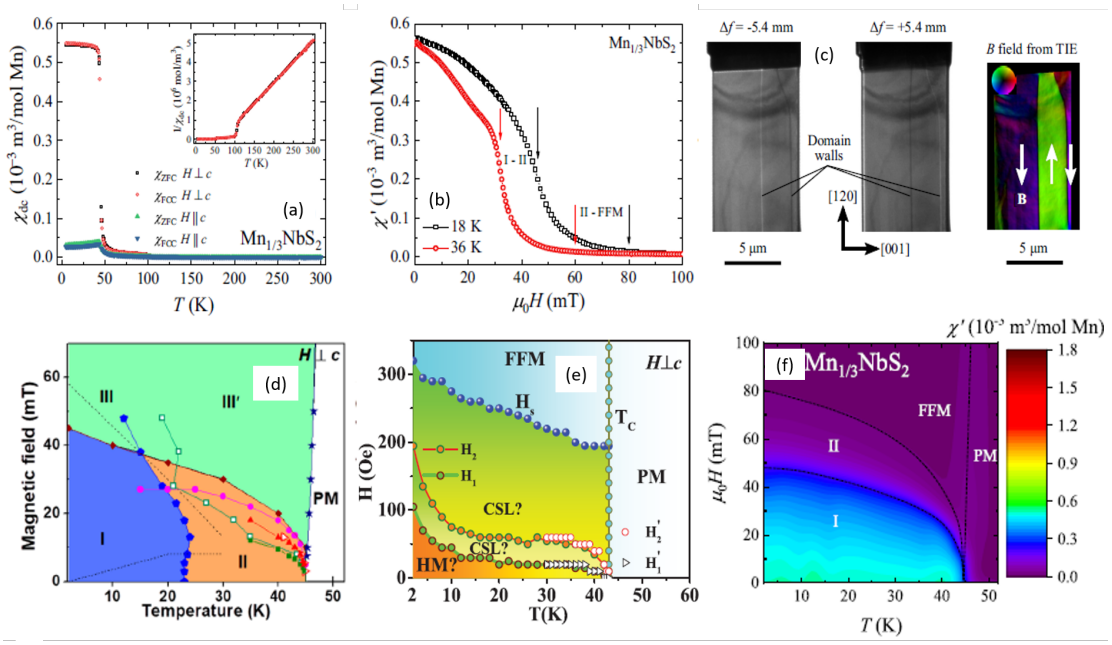

Figure 6.5: $Mn_{1/3}NbS_2$. (a) Temperature dependence of the DC susceptibility. (b) In-phase component of the AC susceptibility as a function of DC field H directed perpendicular to the c axis; and (c) transmission electron micrographs acquired at 35 K in a field of 63 mT, applied normally to the plane. White arrows and colors indicate the direction of the B field according to the inset color wheel (d, e, f) Phase diagram with $H \parallel ab$; taken from Ref. [214, 229].

Aim of our work

Distinguishing between the topologically trivial domains, and those with 360 deg domain walls in the nontrivial magnetic soliton phase poses a great experimental challenge. While the CSL phase in the $Cr_{1/3}NbS_2$ sample has been well established by various research groups, factors such as structural disorder and crystal quality have the potential to modify the periodicity and critical field for phase boundaries. [214, 222] This is particularly relevant the $Mn_{1/3}NbS_2$ sample, given the volatile nature of Mn. The intercalation of Mn occupying both 2c and 2d Wyckoff positions could potentially transform the noncentrosymmetric structure into a centrosymmetric one, eliminating the DM interaction and consequently suppressing helimagnetism and other nontrivial phases. The crystals by Karna *et. al.* [229], are reported to have 2b Mn occupancy of 15% and Hall *et. al.* also reported a small contribution from the $Mn_{1/3}NbS_2$ phase [214]. Additionally, the larger pitch length of $Mn_{1/3}NbS_2$ is at the limit of LTEM capabilities, while thickness-dependent effects might contribute to the observed patterns. Recently, μSR has helped to identify different phases by analyzing the amplitude of the magnetic fraction in both zero fields and applied fields, suggesting the presence of a helimagnetic phase below 50K [231].

This motivated us to complement magnetometry, μSR, neutron scattering and electron microscopy by investigating the various spin structures and magnetic phases of

both samples by ^{53}Cr,^{93}Nb and ^{55}Mn NMR. Previously, zero-field ^{55}Mn NMR has been employed trying to identify the various valency states resulting from disorder in the $Mn_{1/3}NbS_2$ compound[232, 233].

Specifically, the less disordered $Cr_{1/3}NbS_2$ will be studied first to benchmark NMR and to compare the $Mn_{1/3}NbS_2$ results with this well-established case, hoping to clarify to what extent the latter may be considered a CHM.

6.2 NMR results

An extensive set of zero-field (ZF) and field-dependent ^{53}Cr, ^{93}Nb and ^{55}Mn NMR measurements were performed on the Cr and Mn powders, as well as in single crystals, in two different field orientations.

6.2.1 Samples

The single crystal and polycrystal samples of $Cr_{1/3}NbS_2$ and $Mn_{1/3}NbS_2$ used for the NMR measurements were grown by Prof. Geetha Balakrishna's group from Warwick, UK. The single crystals were obtained in the form of platelets, approximately 3 mm in length. The phase purity of the polycrystalline materials was checked using X-ray powder diffraction. Single-crystal X-ray diffraction was used to ascertain the non-centrosymmetric space groups of the single crystals. X-ray Laue back-reflection studies were carried out to establish the crystalline quality as well as to check the crystallographic orientations of the single crystals obtained. The details of the synthesis and basic characterization were reported in [214].

6.2.2 Commonalities of the NMR spectra.

The properties of nuclear isotopes ^{53}Cr, ^{55}Mn and ^{93}Nb are summarized in Tab. 6.1.

isotope	I	γ (MHz/T)	Q fm^2	natural abundance
^{53}Cr	$\frac{3}{2}$	2.4115	-15(5) [234] -8.4 [235]	0.095
^{55}Mn	$\frac{5}{2}$	10.5763	33(1)	1.0
^{93}Nb	$\frac{9}{2}$	10.4523	32(2)	1.0

Table 6.1: Nuclear spin, gyromagnetic ratios, quadrupole moments and natural abundance of ^{53}Cr,^{55}Mn,^{93}Nb

The single-crystal low-temperature NMR spectra from these nuclear spins are due to a similar hierarchy of hyperfine and quadrupole couplings. Each spectrum is qualitatively understood considering that the cylindrical, nearly isotropic hyperfine field tensor $\mathbf{B}_{\rm hf}$ dominates on the smaller quadrupole coupling ($\nu_{\rm Q} \ll \nu_{hf} = \gamma B_{\rm hf}$), producing a pattern of $2I$ equally spaced frequencies (See Fig. 2.9, centered at the Larmor frequency corresponding to the internal field at the nucleus, as it was discussed in Sec. 2.2.6. Since to hyperfine and quadrupole tensors share the same principal axis, $\hat{z} = \hat{c}$, the two simple

experimental conditions are with **H** either parallel or perpendicular to $\hat{z}$. They produce the following frequency patterns in first-order perturbation

$$\nu_m^{\perp}(H) = \gamma|B_{\rm hf}^x - \mu_0 H| + \Delta\nu_m(0), \tag{6.2}$$

where the transition label is $-\frac{2I-1}{2} \leq m \leq \frac{2I-1}{2}$ and $\mathbf{B} = \mu_0\mathbf{H}$ is the applied magnetic field. For **B** along the c axis

$$\nu_m^{\parallel}(H,\theta) = \gamma B_{\rm loc} + \Delta\nu_m(\theta), \tag{6.3}$$

where

$$B_{\rm loc} = \left((B_{\rm hf}^x \cos\theta)^2 + (B_{\rm hf}^z \sin\theta - \mu_0 H)^2\right)^{\frac{1}{2}},$$
$$\Delta\nu_m(\theta) = m\nu_{\rm Q}\frac{3\sin^2\theta - 1}{2}, \tag{6.4}$$

and the relative sign of H and $B_{\rm hf}$ is due to the electron moment being opposite to the electron spin. Equations 6.2-6.4 predict $2I = 3$, 5, and 9 lines for Cr, Mn and Nb, respectively and the field dependence is close to the exact one, but best fits of the data are refined by numerical diagonalization of the full spin Hamiltonian 2.38, beyond first-order approximation.

6.2.3 ^{53}Cr NMR in $Cr_{1/3}NbS_2$.

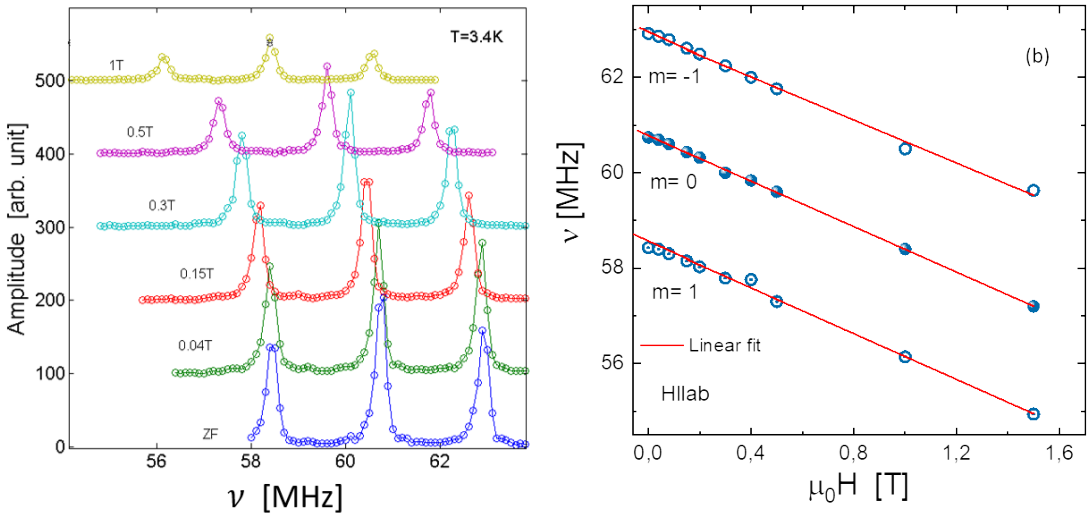

Figure 6.6: ^{53}Cr NMR spectra measured at T=3.4 k at different applied fields until 1T along $H \parallel ab$. (b) Mean peak frequency plotted to the applied field for $Cr_{1/3}NbS_2$.

Figure 6.6a shows the expected triplet of NMR lines obtained in zero applied field (ZF) for the Cr single crystal, together with the shifted spectra measured with $\mathbf{H} \perp \hat{c}$ at 3.4 K. The ZF central frequency is around 61 MHz (i.e. $|B_{\rm hf}| = 25.34$ T). Triplet spectra are fitted to a minimal set of Gaussian components. The peak position for each of the

three components is defined as its center of gravity (the first moment, see Eq. 2.44). The rigid shift of these triplet peaks towards lower frequencies, shown in Fig. 6.6b for this crystal orientation, with slope equal to $^{53}\gamma$, indicates that the applied and internal field add collinearly according to Eq. 6.2 in the forced ferromagnetic phase expected for this easy plane chiral magnet [236]. The slight deviation at very low fields is compatible with the CSL phase, but clearly, NMR is not suited to investigate further this phase.

The more complex pattern predicted by Eq. 6.3 for the other crystal orientation, $\mathbf{H} \parallel \hat{c}$ is indeed displayed in Fig. 6.7. The peak positions are shown in Fig. 6.8a vs. field. Notably, the triplet splitting vanishes at the angle $\theta = \sin^{-1}\frac{1}{3}$, in agreement with Eq. 6.4. The peak positions are shown in Fig. 6.8a vs. field. In the first order, they agree with Eq. 6.3, but the global best fit (dashed line) is obtained by numerical diagonalization, optimizing the common hyperfine and quadrupolar parameters reported in Tab. 6.2, together with a separate, local angle $\theta(H)$ for the three data points at each experimental field value. This global fit was performed with the program developed by Prof. Giuseppe Allodi, University of Parma. The fitted angles for each field, are displayed in Fig. 6.8 b and agree [236] with the mean-field prediction

$$\theta(H) = \frac{\pi}{2} - \cos^{-1}\left(\frac{H}{H_c}\right) \tag{6.5}$$

where $H_c = 2S(\sqrt{J^2 + D^2} - J + K) = 2.9(1)$ T, J, D, K are the Heisenberg, DM exchange and the easy plane (negative) anisotropy constants, respectively.

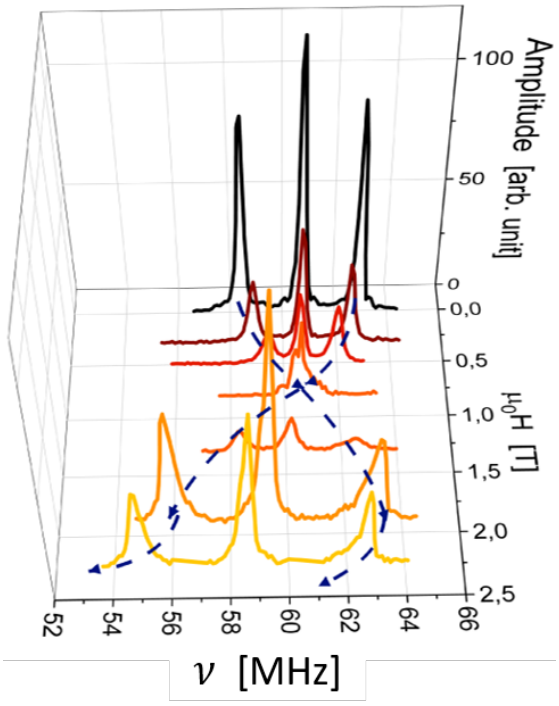

Figure 6.7: ^{53}Cr NMR spectra measured at T=3.4 k at different applied fields along $H \parallel c$

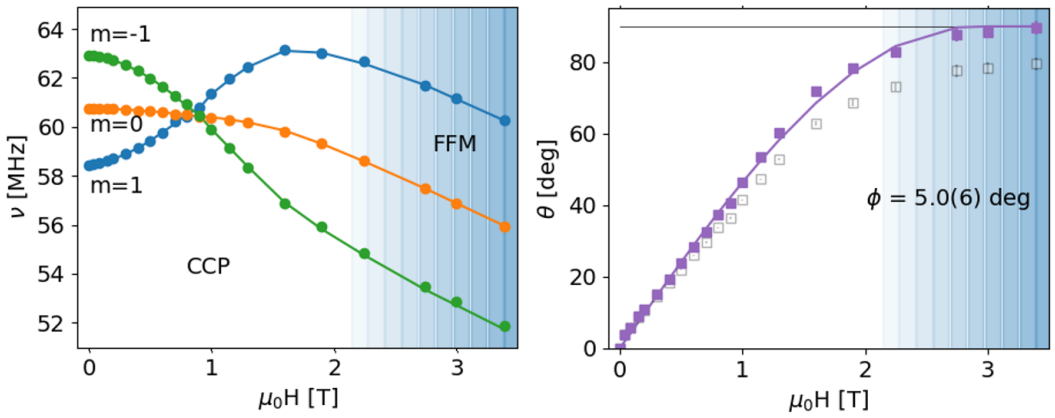

Figure 6.8: (a) ^{53}Cr peak frequencies vs. field from the $\mathbf{H} \parallel \hat{c}$ spectra of Fig. 6.7, with best fit curves (solid lines). (b) Field dependence of the best fit conical angles $\theta(H)$ with (purple) and without (gray) correction for experimental misalignment ϕ between the field direction and $\hat{c}$ (symbols), with the best fit eq. 6.5

ν_Q [MHz]	B^x_{hf} [T]	B^z_{hf} [T]	ϕ [deg]
4.49(3)	25.172(3)	26.63()	5.0(6)

Table 6.2: ^{53}Cr global best fit parameters for Fig. 6.8.

Let's turn now to the microscopic magnetization, measured by the hyperfine field dominated by the on-site contact contribution $B_{hf} = \mathcal{A}S$ (see below eq. 2.34), proportional to the average electronic spin. Typical values in transition metal ions are $\mathcal{A} \approx 10$ T/μ_B, therefore the hyperfine field value of 26 T at 3.4 K in Tab. 6.2 roughly corresponds to 2.6μ_B. The ZF frequency of the central peak, $\nu_0 = {}^{53}\gamma B^x_{hf}(T)$ from eq. 6.2, is plotted in Fig. 6.9a and it changes with temperature proportionally to the order parameter, the atomic moment $\mu(T)$ on Cr. The lower panel b in the same figure shows the temperature dependence of the area under the central peak, the amplitude $A(T)$. It is more or less constant up to 70 K, then it increases due to magnetic anisotropy reduction, which provides larger ferromagnetic enhancement, to finally rapidly decrease within few degrees of the Curie point. This behavior is typical of a first-order transition where paramagnetic domains start developing well below T_C, whereas the order parameter $\mu(T)$ in the residual ordered domains remains large (the hyperfine field at T_C is still more than half of its zero temperature value).

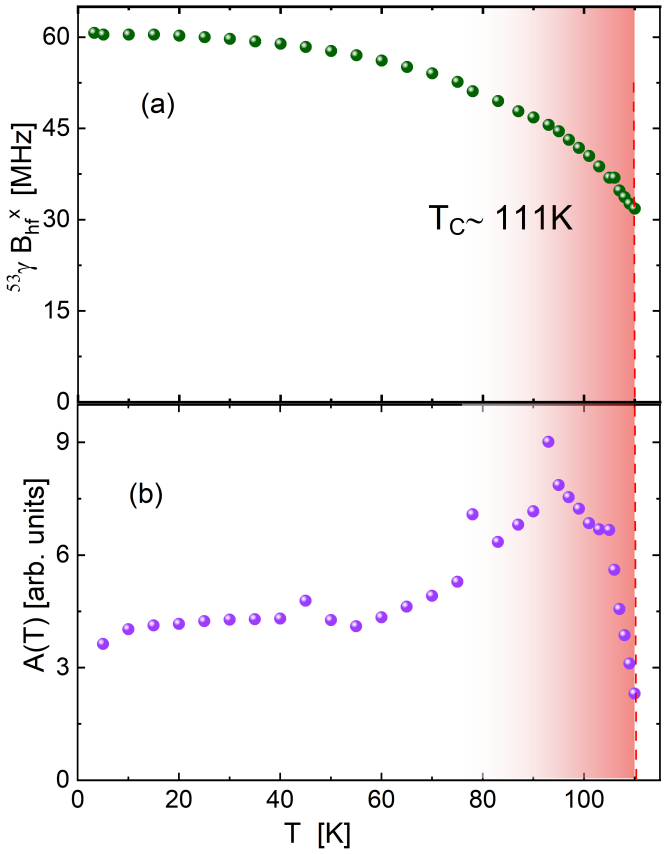

Figure 6.9: Temperature dependence of: (a) the ^{53}Cr hyperfine frequency $^{53}\gamma B_{\rm hf}^{x} \propto \mu(T)$; (b) its NMR amplitude $A(T)$, corrected for the nuclear Curie law.

6.2.4 ^{93}Nb NMR in $Cr_{1/3}NbS_2$

Nb nuclei resonate in ZF due to the presence of a spontaneous hyperfine field, i.e. a core spin polarization at the Nb nucleus, induced by Cr. Even for nominally nonmagnetic Nb this interaction is larger than the nuclear quadrupole interaction. The blue curve in Fig. 6.10 a shows the polycrystalline ZF NMR spectrum of ^{93}Nb. By inspection, two replicas of the nine quadrupolar transitions predicted by Eq. 6.2 have been identified for nuclear spin $I = \frac{9}{2}$, which could be attributed to the two inequivalent sites Nb 2a and 2b, in the ratio 1:2 per cell. The separation of the two nonuplets is proportional to the difference of their hyperfine fields $^{93}B_{2b} - {}^{93}B_{2a} \approx 0.5$ T, roughly 0.8 and 1.3 T, respectively. These fields are too large to be due to distant dipoles on Cr ions (a very rough estimate yields 0.2T). The larger field value indicates a dominant contribution from a local moment on Nb, due to Cr-Nb hybridization.

The best-fit curves in Fig. 6.10 require pairs of Nb sites with occupancies in the ratio 1:2, as per Wyckoff sites 2a and 2b in crystal group 181. The simplest model, with just these two main sites (Tab. 6.3) corresponds to the gray curve. Its residues are above the noise level and a second pair of sites with much smaller occupancy significantly improve the fit quality (orange curve), but it does not change the previous parameters (details provided in our own publication Ref. [11]).

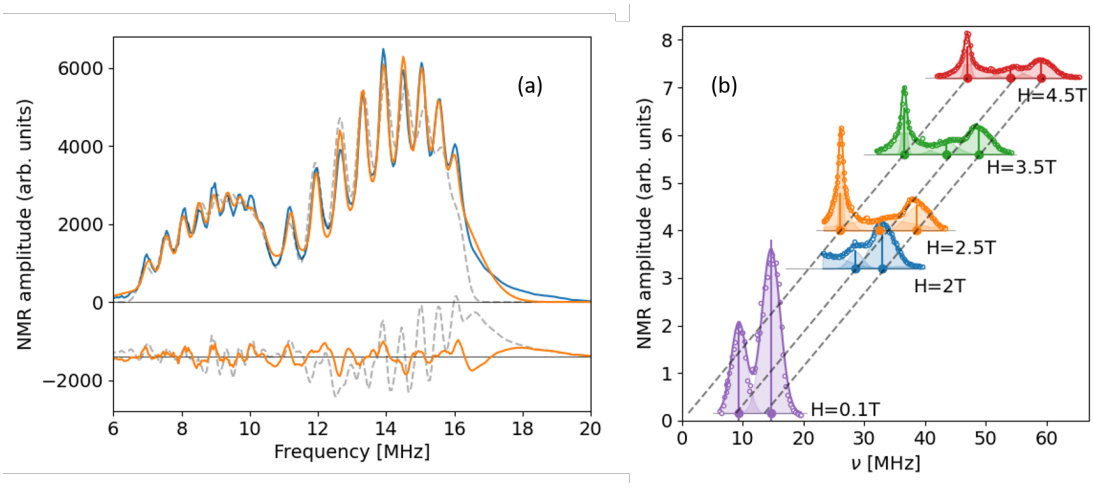

Figure 6.10: (a) ZF (blue curve) ^{93}Nb NMR spectrum at $T = 1.3$ K in $Cr_{1/3}NbS_2$ with a 2-site (gray dashed) and a 4-site (orange solid) best fit. The residues are plotted in the same colors with a negative offset. (b) ^{93}Nb NMR spectra in applied fields H at $T = 1.3$ K, shifted along the vertical axis proportionally to H. The lines correspond to $^{93}\gamma\mu_0 H + \nu_{\mathrm{hf}}$

Wyckoff site	fraction	ν_{Q} [MHz]	ν_{hf} [MHz]	$\delta\nu$ [MHz]
2a	0.33	0.9	8.9	0.19
2b	0.67	1.23	13.8	0.21

Table 6.3: ^{93}Nb quadrupolar and hyperfine parameter of the 2-site best fit in Fig. 6.10.

Figure 6.10 b shows NMR polycrystalline spectra in increasing external fields larger than any FFM critical field, hence, they obey the condition $\mathbf{S} \parallel \mathbf{H}$. The entire spectra shift almost rigidly to higher frequencies, according to $^{93}\gamma(\mu_0 H + B_{\mathrm{hf}})$, where the two main hyperfine fields detected in ZF NMR are recognizable. The positive shift demonstrates that the small spin on ^{93}Nb is always opposite to the main spin on ^{53}Cr, which displays a negative shift..

A third peak appears in the higher field spectra, which extrapolates to zero frequency, $B_{\mathrm{hf}} = 0$, for $H = 0$. This peak indicates the presence (at least in this more disordered power sample) of a substantial fraction of Nb sites with vanishing hyperfine fields. Partial Nb Cr intermixing may be responsible for this component since Nb in the Cr 2c site would have no Nb-Cr hybridization. The large apparent amplitude may be artificially amplified by uncorrected different relaxation rates.

6.2.5 ^{55}Mn NMR in $Mn_{1/3}NbS_2$

The single crystal experiments like those reported above for ^{53}Cr, searching for ^{55}Mn-NMR signals in the $Mn_{1/3}NbS_2$ single crystal, have been reproduced.

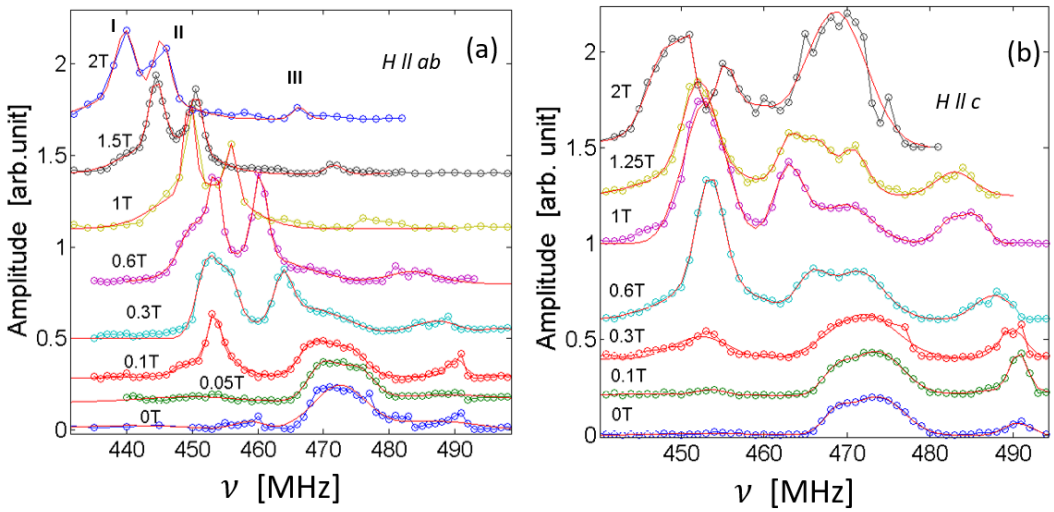

Figure 6.11: $Mn_{1/3}NbS_2$ single crystal ^{55}Mn NMR spectra in zero and applied fields (a) $\mathbf{H} \perp \hat{c}$. (b) $\mathbf{H} \parallel \hat{c}$

Figure 6.11 a and b show a selection of the corresponding NMR spectra, obtained at $T = 1.7$ K, ranging from ZF up to $\mu_0 H = 2$ T, with $\mathbf{H} \perp \hat{c}$ and $\mathbf{H} \parallel \hat{c}$, respectively. ZF spectra are centered around 470 MHz and span the range of 440-490 MHz. More prominent peaks appear with the field in both orientations and change shape while gradually shifting towards lower frequencies for increasing field value.

In comparing with ^{53}Cr data, Fig. 6.6 a and Fig. 6.7 for the two field orientations, preliminarily a few important experimental differences have been noticed. First of all, in ZF and up to 0.1 T the lower frequency portion of the ^{55}Mn spectra, below 460 MHZ, is affected by very fast T_2^{-1} relaxation, which suppresses the 450 MHz component.[1] Furthermore, the much larger gyromagnetic ratio of ^{55}Mn (roughly a factor four with respect to ^{53}Cr, see Tab. 6.1) and the larger Mn moment per ion (roughly a factor two) lead to eight times larger hyperfine frequencies, in agreement with the experimental ratio of about 470 MHz to 60 MHz. This modifies the prediction of Eqs. 6.2, 6.3, implying that any local magnetic inhomonegeity produces eight times larger inhomogeneous linewidths. The ^{53}Cr linewidths of 0.3 MHz would correspond to 2.4 MHz on ^{55}Mn. The observed linewidth is even broader than this in $Mn_{1/3}NbS_2$, well in excess of 5 MHz, which completely hides the quadrupolar quintuplets of the ^{55}Mn $I = 5/2$ nucleus. In this condition, if $Mn_{1/3}NbS_2$ were another textbook case like $Cr_{1/3}NbS_2$, a *single broad* line would be expected, with a field dependence similar to that of the central $^{53}\nu_0$ (Fig. 6.6b, filled symbols, and Fig. 6.7 red symbols).

However, the ^{55}Mn spectra show more than one broad component, and they are separated by up to 35 MHz, a much larger and diverse splitting than that expected for the quadrupole pattern. The quadrupolar quintuplets are convoluted by the larger magnetic inhomogeneous broadening, hence hidden within the linewidth. The origin of the multimodal distributions of hyperfine fields must stem from magnetically different

[1] When T_2 is comparable to the dead-time of our NMR probe, the signal becomes marginal and difficult to reliably correct for relaxation.

local surroundings. Notice in this respect that 35 MHz is only 7% of the mean hyperfine frequency, 450 MHz, which is compatible with local changes in the hyperfine couplings.

Let's concentrate on Fig. 6.11 a, $\mathbf{H} \perp \hat{c}$, where three main components are identified: two more intense at lower frequencies, originating in ZF at 455 and 475 MHz, labeled I and II, respectively, and a much weaker peak around 490 MHz, labeled III in Fig. 6.11 a. Its higher frequency indicates a fractionally larger valence and a comparably larger magnetic moment.

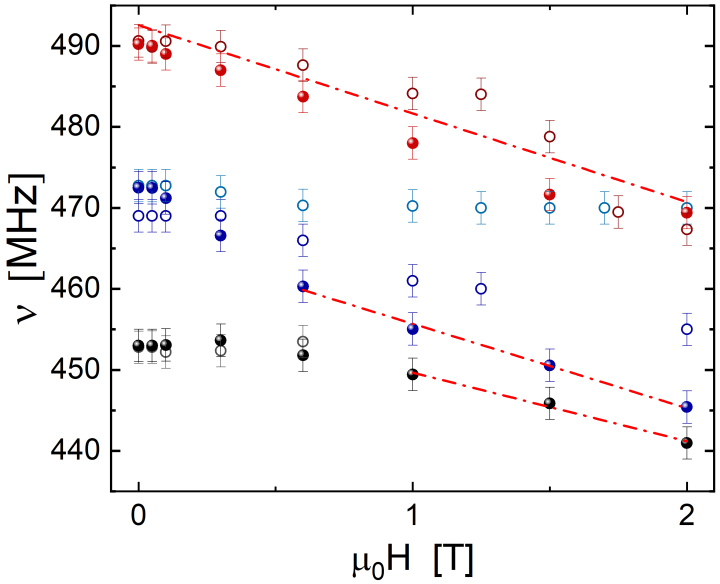

Figure 6.12: Field dependence of the frequencies center of gravity for $\mathbf{H} \perp \hat{c}$ (full symbols) and $\mathbf{H} \parallel \hat{c}$ (open symbols);

Despite the larger error bars, we can compare the field dependence of their first moments in Fig. 6.12b with those of ^{53}Cr. For $\mathbf{H} \perp \hat{c}$ peak III (green solid circles) shifts to lower frequency with a slope in agreement with $^{55}\gamma$ (dashed-dotted red line). This is expected in an easy plane ferromagnet when the spin aligns along $\mathbf{H}$ and the magnetic moment (hence the hyperfine field) aligns opposite to $\mathbf{H}$. Peak III is thus identified as a small $Mn_{1/4}NbS_2$ fraction, characterized by mean valence Mn^{2+}. [237].

Figure 6.12 further shows that components I and II follow at high field a similar behavior for $\mathbf{H} \perp \hat{c}$ (solid blue, black symbols), in agreement with Eq. 6.2, $m = 0$. They assign this higher field range to a FFM phase. They depart from the linear field dependence at lower fields, where a chiral soliton phase would be expected in this orientation.

Finally for $\mathbf{H} \parallel \hat{c}$ the field dependence of components I and II (which actually splits in two) qualitatively agrees with the nonlinear behavior of Eqs. 6.3, **??** in the whole field range, deviating from the red dash-dotted guides for the other field orientation, in analogy with the ^{53}Cr $m = 0$ transition of Fig. 6.8. This behavior of components I and II follows the distinctive mark of the CCP phase.

Summarizing the results for both orientations, components I and II have been attributed to the majority $Mn_{1/3}NbS_2$ structure, in two distinct, possibly defect-free and defect-related-configuration, as discussed in Sec. 6.2.6 and 6.3.2. At the same time, they imply that $Mn_{1/3}NbS_2$ is a CHM.

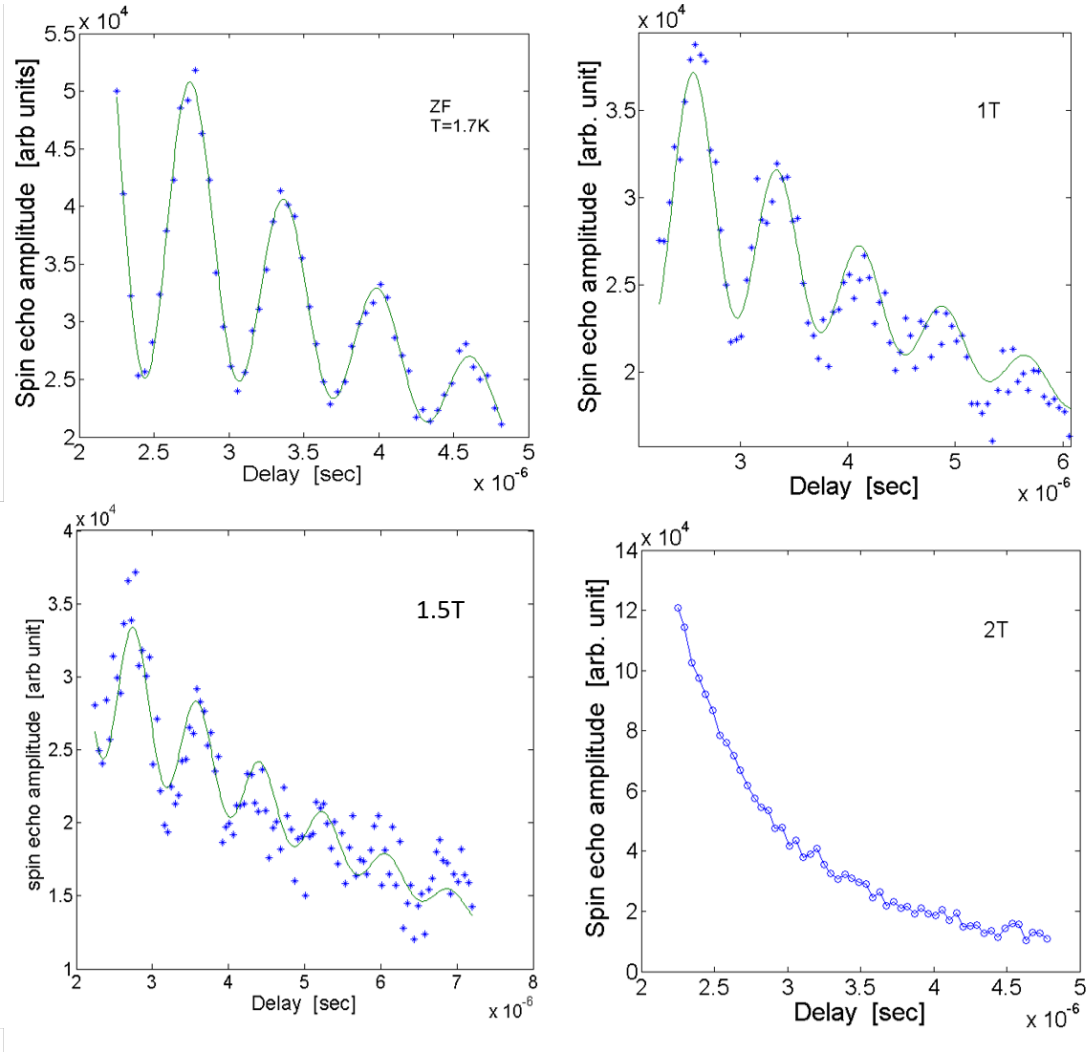

Figure 6.13: Oscillating spin echo amplitude vs. pulse delay at $T = 1.7$ K in $\mu_0 H = 0, 1, 1.5, 2$ T, $\mathbf{H} \parallel \hat{c}$, at 472 MHz;

This assignment is strongly supported by the peculiar spin-echo (T_2) relaxation of peak II, shown in Fig. 6.11 d, which shows large amplitude oscillations with a relaxing envelope, deviating strongly from the normal simple exponential behavior of T_2 relaxation. The oscillations also appear in peaks I, ZF, and moderate fields. The phenomenon is well known in the NMR literature (see Ref. [238] and references therein) and quite generic. In this case, it arises from coherent beatings of pairs of quadrupole lines, originating from the same individual nuclear spin. The oscillating amplitude is particularly large, an indication of rather sharp quadrupole lines hidden in the magnetic inhomogeneous width: all of the lines in the single crystal are separated by the same ^{55}Mn quadrupole splitting $\Delta_1(\theta)$ (Eq. 6.4), which depends on the spin angle $\theta = \theta(H)$. Therefore whenever two of them fall within the spectral width of the NMR probe, they contribute to the beatings according to the delay of the echo pulse sequence. The field

dependence of the splitting obtained from these beatings are compared in Fig. 6.14 (left panel) to $|\Delta\nu(\theta)|$ from eq. 6.4, providing $\nu_Q = 1.57(2)$ MHz and the six values of $\theta(H)$ plotted in the same figure (right panel). The field dependence of these initial angles is that predicted by the monoaxial helical chiral model of Ref. [236] and Eq. 6.5. The good agreement confirms the presence of a CC phase in $Mn_{1/3}NbS_2$ for components I and II, i.e. their assignment to the bulk crystal. The guides to the eye would predict a critical field for the FFM phase $H_c = 10(1)$ T but the oscillations are lost well before reaching this value.

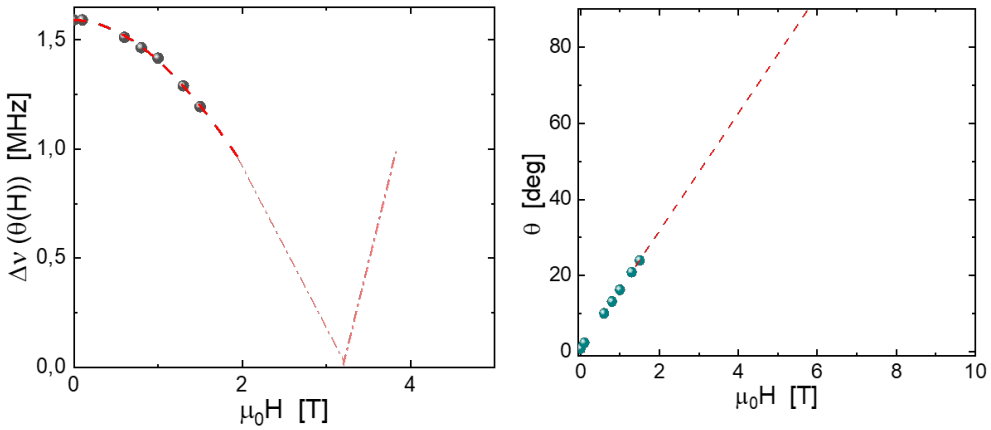

Figure 6.14: $Mn_{1/3}NbS_2$, left: quadrupole splitting $|\Delta\nu(\theta(H))|$ (Eq. 6.3), from the T_2 oscillations of Fig. 6.13, (dash-dotted line: absolute value of eq. 6.4); right: angle θ between **S** and $\hat{c}$, (red dotted line eq. 6.5; both lines are a guide to the eye.

6.2.6 DFT calculations

In order to confirm the NMR interpretation *ab-initio* simulations have been performed with full potential collinear formalism to determine both the EFG and the hyperfine field at the Cr and Mn nuclei. These calculations were performed by Dr. Pietro Bonfà, University of Parma. The details of the calculations are provided in Ref. [11]. The resulting ground state is assumed FM and the calculated magnetic moment is $3\mu_B$/Crfor $Cr_{1/3}NbS_2$ and and $4.2\mu_B$/Mn for $Mn_{1/3}NbS_2$, in good agreement with experiments. The EFG has the principal axis for the largest component aligned with the c lattice parameter and $\eta = 0$ for $Cr_{1/3}NbS_2$. Values of $\nu_Q \sim 4.3$ MHz ($Cr_{1/3}NbS_2$) and 1.7 MHz ($Mn_{1/3}NbS_2$) are obtained, which compare very well with the experimental ones provided in Tab. 6.2 and Fig. 6.14, respectively. Finally, the hyperfine field is predicted to be 16 T and 34.5 T for $Cr_{1/3}NbS_2$ and $Mn_{1/3}NbS_2$, respectively, which are in very reasonable agreement with the experimentally observed value. In $Cr_{1/3}NbS_2$ a small moment is found on Nb, opposite to that of the neighbor Cr ions.

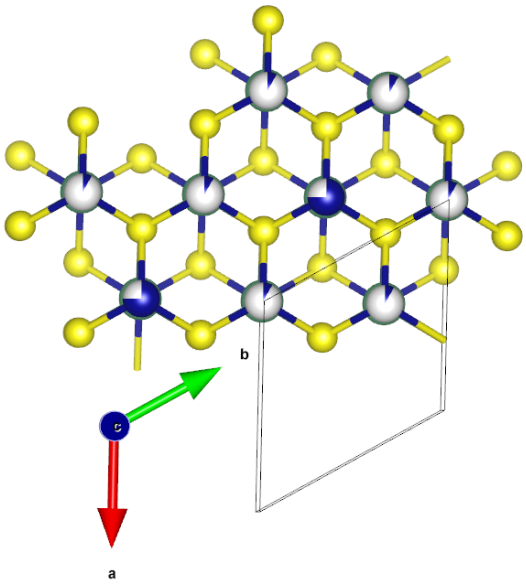

Figure 6.15: Partial occupancy (blue fractions) of Mn 2c site (0.85), 2b (0.08) and 2d (0.02) [214].

Simple simulations with the binomial distribution on the sites of Fig. 6.15, assuming the refined occupancies of Ref. [214] (0.85, 0.08 and 0.02 at 2*c*, 2*b*, and 2*c* respectively), indicate that two main environments are most probable: those with no nearest neighbor (nn) defects ($p = 0.73$) and those with one nn defect ($p = 0.24$). A DFT simulation of the symmetry-allowed configurations in 2x2x2 cell evidence a bipartite distribution of hyperfine fields with a 3% difference in their values that compares rather well with the experimental ratio $({}^{55}\nu_{II} - {}^{55}\nu_I)/\overline{{}^{55}\nu} = 0.043$ for components I and II. This supports the observation of two groups of resonances in single crystal $Mn_{1/3}NbS_2$ in Fig. 6.11.

6.3 Discussion

6.3.1 $Cr_{1/3}NbS_2$

Simple ^{53}Cr quadrupole triplet patterns have been detected in both single crystal and powders. This pattern was obscured in previous polycrystal data [233], probably owing to sample quality, while it was discerned in more recent results on an isostructural Cr compound $Cr_{1/3}NbSe_2$ [232, 239]. The on-site contact hyperfine field ($T \to 0$) provides an estimated magnetic moment of 2.6 μ_B on Cr, with a 13% reduction over the spin-only Cr^{3+} value of $3\mu_B$. DFT predicts a Cr moment somewhat closer to the spin-only value.

A small nonvanishing moment on Nb, opposite to that of Cr, was suggested in Ref. [239], as shown in Fig. 6.16. This moment is demonstrated by the presence of a ZF ^{93}Nb spectrum, which is quantified in 0.1-0.15 μ_B. The opposite alignment to Cr is witnessed by the positive rigid shift of the spectra in large applied fields. DFT attributes this moment to Nb-Cr hybridization and confirms its direction.

Hyperfine and quadrupolar tensors for Cr sharing a common principal axes reference frame and negligible deviations from cylindrical symmetry are demonstrated by

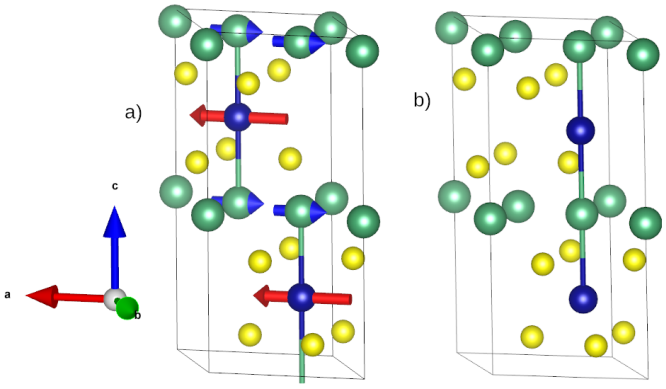

Figure 6.16: a) Spin structure in $Cr_{1/3}NbS_2$, including the small magnetic moment on Nb (not to scale); b) stacking fault along $\hat{c}$.

the relatively sharp ^{53}Cr-NMR peaks and are reproduced also quantitatively by DFT calculation (within the expected accuracy of the approach). A prior study [214] shows that $\mathbf{H} \perp \hat{c}$ generates the expected 2π domain walls corresponding to magnetic solitons (CSL), giving way to the FFM phase around $\mu_0 H = 40$ mT. In our data, this is a tiny field compared to the very large B_{hf}= 25 T, and it barely shows as a flattening of the shifts (Fig. 6.6 b) towards $H = 0$.

The transition of from the CH to the CC phase by applying the field along the chiral axis ($\mathbf{H} \parallel \hat{c}$) is neatly witnessed by the fit of Fig. 6.8, panel a, and the simultaneous agreement of the extracted conical angle $\theta(H)$ of panel b with the mean-field theory. [213] This provides a more precise measurement of the boundary to the FFM phase ($\mu_0 H = 3$ T) than the achievement of saturation of magnetization. The overall agreement of our NMR findings with the CHM model confirms that our samples belong to the $P6_322$ space group.

The first-order nature of the transition at T_N is very clearly shown by NMR, a local probe that can distinguish the decrease of the ordered volume from that of the average local moment, a separation that is difficult to ascertain but from diffraction and from macroscopic techniques. This finding is consistent with mean field predictions [240] and a previous analysis of the entropy change at the transition [241] in a work that attributes the difficulty of observing experimental behavior to a weakly first-order nature. The NMR convincing signature is a more direct assessment of this weak first-order nature.

In summary, the ^{53}Cr NMR data from the single crystal and polycrystal samples is classified as the textbook case for an ideal monoaxial chiral helimagnet.

6.3.2 $Mn_{1/3}NbS_2$

Our more interesting findings are on the $Mn_{1/3}NbS_2$ material, whose magnetic phase diagram is still controversial. [214] The three component NMR spectra are assigned to a minority $Mn_{1/4}NbS_2$ inclusion and to two structural variations of the dominant $Mn_{1/3}NbS_2$ phase. DFT calculations show that the distribution of hyperfine fields is in qualitative agreement with the local configurations originated by a sizable occupancy of the Mn 2b and 2d Wyckoff sites. Notice that the hyperfine coupling eight times larger

than in the Cr textbook case makes the hyperfine field distribution dominant and hides the quadrupole interaction in the spectra.

A qualitative agreement with the CHM model can be recognized comparing the field dependence of these spectra, showing the linear shifts expected of a FFM for $\mathbf{H} \perp \hat{c}$ and strong deviations from lienarity in the $\mathbf{H} \perp \hat{c}$ case.

This qualitative attribution is confirmed by the behavior of the homogeneous, coherent quadrupole splitting observed through the spin echo oscillations for $\mathbf{H} \parallel \hat{c}$ (Fig. 6.13), well-known in NMR when homogeneous quadrupolar and inhomogeneous magnetic interactions coexist. The field dependence of this quadrupole splitting is identical to that displayed directly in ^{53}Cr NMR spectra in the CC phase and strongly supports the presence of the same phase in the $Mn_{1/3}NbS_2$ crystal. However, the coherent oscillations in the T_2 relaxation are lost for conical angles larger than 25 degrees, at about 2T. The critical field for the FFM phase can only be extrapolated from the early part of the mean-field behavior, checked to be valid in the Cr case, to the value of 10 T, but the region above 2 T could not be directly investigated.

6.4 Conclusions

The detailed analysis further allows us to draw conclusions by comparison with the $Cr_{1/3}NbS_2$, which has been established as a textbook case of a chiral monoaxial helimagnet and the determination of its CC-to-FFM phase boundary at $T = 0$ has been refined. This allows us to establish a detailed model for the NMR of a CHM, and leveraging on this, further, it has been shown that, in the more controversial case of $Mn_{1/3}NbS_2$, where substantial site disorder blurred the signature of the CHM for most experimental techniques. For this reason, the ground state of $Mn_{1/3}NbS_2$ was still under debate until now. Specifically, the coherent oscillations measured in the T_2 NMR relaxation allow us to extract field-dependent quadrupole splittings also for the ^{55}Mn nuclei, hidden in the NMR spectra by inhomogeneous magnetic broadening. These splittings reveal the same field behavior as the $Cr_{1/3}NbS_2$ textbook case and support the assignment of $Mn_{1/3}NbS_2$ to the same category of chiral helimagnets.

Chapter 7

Summary

This chapter summarizes all the results obtained in this thesis work.

Chapter 4 describes the investigation of the structural and magnetic properties of the recently proposed $MnSb_2Te_4$ material, mostly performed on single crystalline samples. It is shown that ferromagnetism is displayed with enhanced Curie temperature, and a thorough structural analysis of the site intermixing is reported. By accurately quantifying the intermixing, which in previous reports was still missing information, the study reveals that both Mn over-stoichiometry and specific Mn/Sb distributions contribute to promoting ferromagnetism and increasing the magnetic ordering transition temperature up to T_C=58 K (the highest reported till now). However, Mn over-stoichiometry beyond a certain compositional threshold affects the original crystal structure, which loses the quasi-2D character. These over-stoichiometric crystals require further investigations to understand the electronic band topology as well as their magnetic properties. In addition to these stoichiometric strategies, pressure also demonstrated to be an effective tool for increasing magnetic interaction and transition temperature without compromising the original crystal structure.

Chapter 5 illustrates the importance of intermixing and, in particular, the role of the magnetic Mn in the anti-site position, which has been investigated using local spectroscopic techniques. Our NMR measurements directly assess the opposite alignment between the Mn magnetic moments on the native sites and those at the antisites in the $T = 0$ ground state for all the members of the $(MnBi_2Te_4)(Bi_2Te_3)_n$, n=0,1,2 family, as well as for $MnSb_2Te_4$. A further important result is the demonstration, first suggested by NMR evidence in $MnSb_2Te_4$, and positively supported by μSR in all materials, that the static magnetic moment of the Mn in the antisite sublattice starts to fluctuate at T^*, well below the magnetic transition temperature of the main magnetic lattice. This leaves a homogeneous magnetic structure above T^*, undisturbed by magnetic disorder in the antisite. This may solve some inconsistencies in the observation of the Dirac gap and QAHE in different specimens of these MTI candidates. Since intermixing is a common feature for all materials, it is speculated that early antisite disordering may take place more often; hence, these findings may have a more general impact than just on the present material.

Chapter 6 reports our investigation of a second class of materials, candidates for real space topological spin texture. The first one, $Cr_{1/3}NbS_2$, was already established to display a helimagnetic ground state and three further characteristic textures, a chiral soliton lattice, or CSL phase, and a chiral conical, or CC phase, these two selected by the direction of the applied field, and both followed by a forced ferromagnetic or FFM phase. In this case, we demonstrated that ^{53}Cr NMR clearly identifies from the interplay of the hyperfine and quadrupole coupling of ^{53}Cr at least two of these, the CC

and the FFM phase, providing a wealth of quantitative information, including the size of the Cr magnetic moment and the mapping of the conical angle with the applied field. This configures $Cr_{1/3}NbS_2$ as the textbook CHM case for NMR.

Such a detailed analysis further allows us to draw conclusions by comparison in the more controversial case of $Mn_{1/3}NbS_2$, where substantial site disorder blurred the signature of the CHM for most experimental techniques. For this reason, the ground state of $Mn_{1/3}NbS_2$ was still under debate until now. Specifically, the coherent oscillations measured in the T_2 NMR relaxation allow us to extract field-dependent quadrupole splittings also for the ^{55}Mn nuclei, hidden in the NMR spectra by inhomogeneous magnetic broadening. These splittings reveal the same field behavior as the $Cr_{1/3}NbS_2$ textbook case and support the assignment of $Mn_{1/3}NbS_2$ to the same category of chiral helimagnets.

Moreover, this thesis highlights the importance of studying detailed magnetism, especially a comprehensive study of the native defects, through local and bulk probes in 2D van der Waals magnetic materials, which also host topological nontriviality.

Chapter 8

Appendix

8.1 Quadrupole-perturbed NMR, 2nd order perturbation theory

$$\nu_m = \nu_L - \frac{4\nu_Q^2}{\nu_L}[(I=1/2)^2-1][2\mathcal{B}(\theta,\phi)-\mathcal{C}(\theta,\phi)] - \nu_Q\mathcal{A}(\theta,\phi)m + \frac{12\nu_Q^2}{\nu_L}[4\mathcal{B}(\theta,\phi)-\mathcal{C}(\theta,\phi)]m^2 \tag{8.1}$$

Expansions vs. satellite order $m(m = [-(I-1/2), -(1-1/2)+1, .., (I-1/2)])$:

$$\nu_m = \nu^{(0)} + \nu^{(1)}m + \nu^{(2)}m^2 \tag{8.2}$$

where

$$\nu^{(0)} \equiv \nu_L - \frac{4\nu_Q^2}{\nu_L}[(I=1/2)^2-1][2\mathcal{B}(\theta,\phi)-\mathcal{C}(\theta,\phi)] \tag{8.3}$$

$$\nu^{(1)} \equiv \nu_Q\mathcal{A}(\theta,\phi) \tag{8.4}$$

$$\nu^{(2)} \equiv \frac{12\nu_Q^2}{\nu_L}[4\mathcal{B}(\theta,\phi)-\mathcal{C}(\theta,\phi)] \tag{8.5}$$

and

$$\mathcal{A}(\theta,\phi) = \frac{1}{2}(3\cos^2\theta) - 1 + \eta\sin^2\theta\cos 2\phi \tag{8.6}$$

$$\mathcal{B}(\theta,\phi) = \frac{1}{144}\sin^2\theta[\cos^2\theta(9-6\eta\cos 2\phi+\eta^2\sin^2 2\phi)+\eta^2\sin^2 2\phi] \tag{8.7}$$

$$\mathcal{C}(\theta,\phi) = \frac{1}{576}9\sin^4\theta + 6\eta\sin^2\theta(1+cos^2\theta)\cos 2\phi + \eta^2[\cos^2 2\phi + 2\cos^2\theta(1+sin^2 2\phi)$$

$+\cos^4\theta\cos^2 2\phi]$(8.8)

Powder average:

$\langle\mathcal{A}\rangle = 0$ $\langle\mathcal{B}\rangle = \langle\mathcal{C}\rangle = \frac{1}{120}(1+\frac{\eta^2}{3})$

and 2nd-order quadrupole shift, central line

$$\langle \nu_0 \rangle - \nu_L = \frac{\nu_Q^2}{30\nu_L}[(I+1/2)^2 - 1](1+\frac{\eta^2}{3})$$

BIBLIOGRAPHY

Bibliography

[49] Jiadong Zang, Vincent Cros, and Axel Hoffmann. *Topology in magnetism*. Vol. 192. Springer, 2018 (cit. on pp. 13, 14).

[56] Stephen Blundell. *Magnetism in condensed matter*. OUP Oxford, 2001 (cit. on pp. 15, 16).

[77] Dante Gatteschi, Roberta Sessoli, and Jacques Villain. *Molecular nanomagnets*. Vol. 5. Oxford University Press, USA, 2006 (cit. on p. 24).

[90] Charles P Slichter. *Principles of magnetic resonance*. Vol. 1. Springer Science & Business Media, 2013 (cit. on p. 28).

[91] Anatole Abragam. *The principles of nuclear magnetism*. 32. Oxford university press, 1961 (cit. on pp. 28, 33).

[104] Alain Yaouanc and Pierre Dalmas de Réotier. *Muon spin rotation, relaxation, and resonance: applications to condensed matter*. International series of monographs on physics. Oxford: Oxford Univ. Press, 2011. URL: https://cds.cern.ch/record/1385534 (cit. on p. 47).

[105] Stephen J. Blundell, Roberto De Renzi, Tom Lancaster, and Francis L. Pratt. *Muon Spectroscopy: An Introduction*. Oxford University Press, 2021 (cit. on p. 47).

[175] John A Mydosh. *Spin glasses: an experimental introduction*. CRC Press, 1993 (cit. on p. 69).

Bibliography

[1] Xiaoming Zhang, Xiaotian Wang, Tingli He, Lirong Wang, Wei-Wang Yu, Ying Liu, Guodong Liu, and Zhenxiang Cheng. “Magnetic topological materials in two-dimensional: theory, material realization and application prospects”. In: *Science Bulletin* 68.21 (2023), 2639–2657 (cit. on p. 2).

[2] Gaojie Zhang, Hao Wu, Liang Zhang, Li Yang, Yuanmiao Xie, Fei Guo, Hongda Li, Boran Tao, Guofu Wang, Wenfeng Zhang, et al. “Two-Dimensional Van Der Waals Topological Materials: Preparation, Properties, and Device Applications”. In: *Small* 18.47 (2022), 2204380 (cit. on p. 2).

[3] Yafei Ren, Zhenhua Qiao, and Qian Niu. “Topological phases in two-dimensional materials: a review”. In: *Reports on Progress in Physics* 79.6 (2016), 066501 (cit. on p. 2).

[4] B Andrei Bernevig, Claudia Felser, and Haim Beidenkopf. “Progress and prospects in magnetic topological materials”. In: *Nature* 603.7899 (2022), 41–51 (cit. on p. 2).

[5] M Sahoo, MC Rahn, E Kochetkova, O Renier, LC Folkers, A Tcakaev, ML Amigó, FM Stier, V Pomjakushin, and Kand others Srowik. “Tuning strategy for Curie-temperature enhancement in the van der Waals magnet Mn1+ xSb2-xTe4”. In: *Materials Today Physics* 38 (2023), 101265 (cit. on pp. 3, 62–64, 67, 68, 70–72, 74, 75, 77, 79, 85).

[6] Laura C Folkers, Laura Teresa Corredor, Fabian Lukas, Manaswini Sahoo, Anja UB Wolter, and Anna Isaeva. “Occupancy disorder in the magnetic topological insulator candidate Mn1- x Sb2+ x Te4”. In: *Zeitschrift für Kristallographie-Crystalline Materials* 237.4-5 (2022), 101–108 (cit. on pp. 3, 64).

[7] E. Kochetkova, M. Sahoo, M.C. Rahn, F. Tardieux, O. Pabst, I. Renier, K. Aguilera, A.U.B. Wolter, L.T. Corredor, and A. Isaeva. “"Mn-enrichment in magnetic topological insulators: synthesis, cubic crystal structure and ferromagnetism of bulk $Mn_{2.72}Sb_{1.28}Te_4$"”. In: *In preparation* (2024) (cit. on pp. 3, 78).

[8] M Sahoo, Z Salman, G Allodi, A Isaeva, L Folkers, AUB Wolter, B Büchner, and R De Renzi. “Impact of Mn-Pn intermixing on magnetic properties of an intrinsic magnetic topological insulator: the μSR perspective”. In: *Journal of Physics: Conference Series*. Vol. 2462. 1. IOP Publishing. 2023, p. 012040 (cit. on pp. 3, 82, 100, 101).

[9] M Sahoo, IJ Onuorah, LC Folkers, EV Chulkov, MM Otrokov, ZS Aliev, IR Amiraslanov, AUB Wolter, B Büchner, LT Corredor, et al. “Ubiquitous order-disorder transition in the Mn antisite sublattice of the (MnBi _2 Te _4)(Bi _2 Te _3) _n magnetic topological insulators”. In: *arXiv preprint arXiv:2402.06340* (2024) (cit. on pp. 3, 82, 88, 92–94, 96–99, 101, 102, 105).

[10] E. Kochetkova, M. Sahoo, M. Rahn, O. Renier, L. C. Folkers, I.J. Onuorah, B. Büchner, A.U.B. Wolter, L.T. Corredor, G. Allodi, R. De Renzi, and A. Isaeva. "Tweaking magnetism in the magnetic topological insulators $Mn_{1-x}Sb_{2+x}Te_4$ by adjusting the Mn/Sb ratio". In: *In preparation* (2023) (cit. on pp. 3, 82, 83).

[11] M. Sahoo, Bonfà P., A. E. Hall, D. A. Mayoh, L. T. Corredor, A. U. B. Wolter, B B üchner, G. Balakrishnan, R. De Renzi, and G. Allodi. "Helical to conical order in $M_1/3\ NbS_2$ (M=Cr, Mn), detected by Cr, Mn NMR". In: *In preparation* (2024) (cit. on pp. 3, 119, 124).

[12] K v Klitzing, Gerhard Dorda, and Michael Pepper. "New method for high-accuracy determination of the fine-structure constant based on quantized Hall resistance". In: *Physical review letters* 45.6 (1980), 494 (cit. on p. 4).

[13] David J Thouless, Mahito Kohmoto, M Peter Nightingale, and Marcel den Nijs. "Quantized Hall conductance in a two-dimensional periodic potential". In: *Physical review letters* 49.6 (1982), 405 (cit. on p. 4).

[14] Mahito Kohmoto. "Topological invariant and the quantization of the Hall conductance". In: *Annals of Physics* 160.2 (1985), 343–354 (cit. on p. 4).

[15] M Zahid Hasan and Charles L Kane. "Colloquium: topological insulators". In: *Reviews of modern physics* 82.4 (2010), 3045 (cit. on pp. 4–6, 8).

[16] Michael Victor Berry. "Quantal phase factors accompanying adiabatic changes". In: *Proceedings of the Royal Society of London. A. Mathematical and Physical Sciences* 392.1802 (1984), 45–57 (cit. on p. 4).

[17] F Duncan M Haldane. "Model for a quantum Hall effect without Landau levels: Condensed-matter realization of the" parity anomaly"". In: *Physical review letters* 61.18 (1988), 2015 (cit. on pp. 5, 6).

[18] B Andrei Bernevig, Taylor L Hughes, and Shou-Cheng Zhang. "Quantum spin Hall effect and topological phase transition in HgTe quantum wells". In: *science* 314.5806 (2006), 1757–1761 (cit. on p. 7).

[19] Markus Konig, Steffen Wiedmann, Christoph Brune, Andreas Roth, Hartmut Buhmann, Laurens W Molenkamp, Xiao-Liang Qi, and Shou-Cheng Zhang. "Quantum spin Hall insulator state in HgTe quantum wells". In: *Science* 318.5851 (2007), 766–770 (cit. on p. 7).

[20] David Hsieh, Dong Qian, Lewis Wray, Yiman Xia, Yew San Hor, Robert Joseph Cava, and M Zahid Hasan. "A topological Dirac insulator in a quantum spin Hall phase". In: *Nature* 452.7190 (2008), 970–974 (cit. on p. 7).

[21] Joel Moore. "The next generation". In: *Nature Physics* 5.6 (2009), 378–380 (cit. on p. 7).

[22] Yuqi Xia, Dong Qian, David Hsieh, L Wray, Arijeet Pal, Hsin Lin, Arun Bansil, DHYS Grauer, Yew San Hor, Robert Joseph Cava, et al. "Observation of a large-gap topological-insulator class with a single Dirac cone on the surface". In: *Nature physics* 5.6 (2009), 398–402 (cit. on p. 7).

[23] Haijun Zhang, Chao-Xing Liu, Xiao-Liang Qi, Xi Dai, Zhong Fang, and Shou-Cheng Zhang. "Topological insulators in Bi2Se3, Bi2Te3 and Sb2Te3 with a single Dirac cone on the surface". In: *Nature physics* 5.6 (2009), 438–442 (cit. on p. 7).

[24] YL Chen, James G Analytis, J-H Chu, ZK Liu, S-K Mo, Xiao-Liang Qi, HJ Zhang, DH Lu, Xi Dai, Zhong Fang, et al. "Experimental realization of a three-dimensional topological insulator, Bi2Te3". In: *science* 325.5937 (2009), 178–181 (cit. on p. 7).

[25] David Hsieh, Yuqi Xia, D Qian, L Wray, Fabian Meier, JH Dil, J Osterwalder, L Patthey, AV Fedorov, H Lin, et al. "Observation of time-reversal-protected single-Dirac-cone topological-insulator states in Bi 2 Te 3 and Sb 2 Te 3". In: *Physical review letters* 103.14 (2009), 146401 (cit. on p. 7).

[26] David Hsieh, Yuqi Xia, Dong Qian, L Wray, JH Dil, Fedorov Meier, J Osterwalder, L Patthey, JG Checkelsky, Nai Phuan Ong, et al. "A tunable topological insulator in the spin helical Dirac transport regime". In: *Nature* 460.7259 (2009), 1101–1105 (cit. on pp. 7, 8).

[27] Jieyi Liu and Thorsten Hesjedal. "Magnetic topological insulator heterostructures: A review". In: *Advanced Materials* 35.27 (2023), 2102427 (cit. on p. 8).

[28] Liang Fu and Charles L Kane. "Time reversal polarization and a Z 2 adiabatic spin pump". In: *Physical Review B* 74.19 (2006), 195312 (cit. on p. 8).

[29] Xiao-Liang Qi, Taylor L Hughes, and Shou-Cheng Zhang. "Topological field theory of time-reversal invariant insulators". In: *Physical Review B* 78.19 (2008), 195424 (cit. on p. 8).

[30] Yoshinori Tokura, Kenji Yasuda, and Atsushi Tsukazaki. "Magnetic topological insulators". In: *Nature Reviews Physics* 1.2 (2019), 126–143 (cit. on pp. 8, 10, 51).

[31] Rui Yu, Wei Zhang, Hai-Jun Zhang, Shou-Cheng Zhang, Xi Dai, and Zhong Fang. "Quantized anomalous Hall effect in magnetic topological insulators". In: *science* 329.5987 (2010), 61–64 (cit. on pp. 9, 11, 51).

[32] Zilong Jiang, Cui-Zu Chang, Chi Tang, Peng Wei, Jagadeesh S Moodera, and Jing Shi. "Independent tuning of electronic properties and induced ferromagnetism in topological insulators with heterostructure approach". In: *Nano letters* 15.9 (2015), 5835–5840 (cit. on p. 9).

[33] Adriana I Figueroa, Fréderic Bonell, MG Cuxart, Manuel Valvidares, Pierluigi Gargiani, G van der Laan, Aitor Mugarza, and Sergio O Valenzuela. "Absence of magnetic proximity effect at the interface of Bi 2 Se 3 and (Bi, Sb) 2 Te 3 with EuS". In: *Physical Review Letters* 125.22 (2020), 226801 (cit. on p. 9).

[34] Ryota Watanabe, Ryutaro Yoshimi, Minoru Kawamura, Masataka Mogi, Atsushi Tsukazaki, XZ Yu, Kiyomi Nakajima, Kei S Takahashi, Masashi Kawasaki, and Yoshinori Tokura. "Quantum anomalous Hall effect driven by magnetic proximity coupling in all-telluride based heterostructure". In: *Applied Physics Letters* 115.10 (2019) (cit. on p. 9).

[35] Rudro R Biswas and Alexander V Balatsky. "Impurity-induced states on the surface of three-dimensional topological insulators". In: *Physical Review B* 81.23 (2010), 233405 (cit. on p. 9).

[36] J Henk, A Ernst, SV Eremeev, Eugene V Chulkov, IV Maznichenko, and I Mertig. "Complex spin texture in the pure and Mn-doped topological insulator Bi 2 Te 3". In: *Physical Review Letters* 108.20 (2012), 206801 (cit. on p. 9).

[37] Jian-Min Zhang, Wenguang Zhu, Ying Zhang, Di Xiao, and Yugui Yao. "Tailoring magnetic doping in the topological insulator Bi 2 Se 3". In: *Physical review letters* 109.26 (2012), 266405 (cit. on p. 9).

[38] JB Staunton, Balazs L Gyorffy, J Poulter, and Paul Strange. "A relativistic RKKY interaction between two magnetic impurities-the origin of a magnetic anisotropic effect". In: *Journal of Physics C: Solid State Physics* 21.8 (1988), 1595 (cit. on p. 9).

[39] YS Hor, P Roushan, H Beidenkopf, J Seo, D Qu, JG Checkelsky, LA Wray, D Hsieh, Y Xia, S-Y Xu, et al. "Development of ferromagnetism in the doped topological insulator Bi 2- x Mn x Te 3". In: *Physical Review B* 81.19 (2010), 195203 (cit. on p. 10).

[40] Joseph G Checkelsky, Jianting Ye, Yoshinori Onose, Yoshihiro Iwasa, and Yoshinori Tokura. "Dirac-fermion-mediated ferromagnetism in a topological insulator". In: *Nature Physics* 8.10 (2012), 729–733 (cit. on p. 10).

[41] Paolo Sessi, Felix Reis, Thomas Bathon, Konstantin A Kokh, Oleg E Tereshchenko, and Matthias Bode. "Signatures of Dirac fermion-mediated magnetic order". In: *Nature communications* 5.1 (2014), 5349 (cit. on p. 10).

[42] Cui-Zu Chang, Jinsong Zhang, Xiao Feng, Jie Shen, Zuocheng Zhang, Minghua Guo, Kang Li, Yunbo Ou, Pang Wei, Li-Li Wang, et al. "Experimental observation of the quantum anomalous Hall effect in a magnetic topological insulator". In: *Science* 340.6129 (2013), 167–170 (cit. on pp. 11, 51).

[43] Cui-Zu Chang, Weiwei Zhao, Duk Y Kim, Haijun Zhang, Badih A Assaf, Don Heiman, Shou-Cheng Zhang, Chaoxing Liu, Moses HW Chan, and Jagadeesh S Moodera. "High-precision realization of robust quantum anomalous Hall state in a hard ferromagnetic topological insulator". In: *Nature materials* 14.5 (2015), 473–477 (cit. on pp. 11, 12).

[44] Inhee Lee, Chung Koo Kim, Jinho Lee, Simon JL Billinge, Ruidan Zhong, John A Schneeloch, Tiansheng Liu, Tonica Valla, John M Tranquada, Genda Gu, et al. "Imaging Dirac-mass disorder from magnetic dopant atoms in the ferromagnetic topological insulator Crx (Bi0. 1Sb0. 9) 2-xTe3". In: *Proceedings of the National Academy of Sciences* 112.5 (2015), 1316–1321 (cit. on p. 12).

[45] YL Chen, J-H Chu, JG Analytis, ZK Liu, Kyushiro Igarashi, H-H Kuo, XL Qi, Sung-Kwan Mo, RG Moore, DH Lu, et al. "Massive Dirac fermion on the surface of a magnetically doped topological insulator". In: *Science* 329.5992 (2010), 659–662 (cit. on p. 12).

[46] Roger SK Mong, Andrew M Essin, and Joel E Moore. "Antiferromagnetic topological insulators". In: *Physical Review B* 81.24 (2010), 245209 (cit. on pp. 12, 51).

[47] Mikhail M Otrokov, Tatiana V Menshchikova, Maia G Vergniory, Igor P Rusinov, A Yu Vyazovskaya, Yu M Koroteev, Gustav Bihlmayer, Arthur Ernst, Pedro M Echenique, Andrés Arnau, et al. "Highly-ordered wide bandgap materials for quantized anomalous Hall and magnetoelectric effects". In: *2D Materials* 4.2 (2017), 025082 (cit. on pp. 13, 51).

[48] Mikhail M Otrokov, Ilya I Klimovskikh, Hendrik Bentmann, D Estyunin, Alexander Zeugner, Ziya S Aliev, S Gaß, AUB Wolter, AV Koroleva, Alexander M Shikin, et al. "Prediction and observation of an antiferromagnetic topological insulator". In: *Nature* 576.7787 (2019), 416–422 (cit. on pp. 13, 51, 53–55, 57).

[49] Jiadong Zang, Vincent Cros, and Axel Hoffmann. *Topology in magnetism*. Vol. 192. Springer, 2018 (cit. on pp. 13, 14).

[50] Hans-Benjamin Braun. "Topological effects in nanomagnetism: from superparamagnetism to chiral quantum solitons". In: *Advances in Physics* 61.1 (2012), 1–116 (cit. on pp. 13, 107).

[51] David Finkelstein and Charles W Misner. "Some new conservation laws". In: *Annals of Physics* 6.3 (1959), 230–243 (cit. on pp. 13, 107).

[52] Ramamurti Rajaraman. "Solitons and instantons". In: (1982) (cit. on pp. 13, 107).

[53] LJ De Jongh. "Solitons in magnetic chains". In: *Journal of Applied Physics* 53.11 (1982), 8018–8023 (cit. on pp. 13, 107).

[54] Kostya S Novoselov, Da Jiang, F Schedin, TJ Booth, VV Khotkevich, SV Morozov, and Andre K Geim. "Two-dimensional atomic crystals". In: *Proceedings of the National Academy of Sciences* 102.30 (2005), 10451–10453 (cit. on p. 14).

[55] Andres Castellanos-Gomez, Xiangfeng Duan, Zhe Fei, Humberto Rodriguez Gutierrez, Yuan Huang, Xinyu Huang, Jorge Quereda, Qi Qian, Eli Sutter, and Peter Sutter. "Van der Waals heterostructures". In: *Nature Reviews Methods Primers* 2.1 (2022), 58 (cit. on p. 14).

[56] Stephen Blundell. *Magnetism in condensed matter*. OUP Oxford, 2001 (cit. on pp. 15, 16).

[57] CV Topping and SJ Blundell. "AC susceptibility as a probe of low-frequency magnetic dynamics". In: *Journal of Physics: Condensed Matter* 31.1 (2018), 013001 (cit. on pp. 16, 19, 22–24).

[58] Youngjun Ahn, Xiaoyu Guo, Suhan Son, Zeliang Sun, and Liuyan Zhao. "Progress and prospects in two-dimensional magnetism of van der Waals materials". In: *Progress in Quantum Electronics* (2024), 100498 (cit. on pp. 16, 17).

[59] N David Mermin and Herbert Wagner. "Absence of ferromagnetism or antiferromagnetism in one-or two-dimensional isotropic Heisenberg models". In: *Physical Review Letters* 17.22 (1966), 1133 (cit. on p. 18).

[60] Rudolf Peierls. "On Ising's model of ferromagnetism". In: *Mathematical Proceedings of the Cambridge Philosophical Society*. Vol. 32. 3. Cambridge University Press. 1936, pp. 477–481 (cit. on p. 18).

[61] Shucheng Xing, Jian Zhou, Xuanguang Zhang, Stephen Elliott, and Zhimei Sun. "Theory, properties and engineering of 2D magnetic materials". In: *Progress in Materials Science* 132 (2023), 101036 (cit. on p. 18).

[62] Bevin Huang, Genevieve Clark, Efrén Navarro-Moratalla, Dahlia R Klein, Ran Cheng, Kyle L Seyler, Ding Zhong, Emma Schmidgall, Michael A McGuire, David H Cobden, et al. "Layer-dependent ferromagnetism in a van der Waals crystal down to the monolayer limit". In: *Nature* 546.7657 (2017), 270–273 (cit. on p. 18).

[63] Cheng Gong, Lin Li, Zhenglu Li, Huiwen Ji, Alex Stern, Yang Xia, Ting Cao, Wei Bao, Chenzhe Wang, Yuan Wang, et al. "Discovery of intrinsic ferromagnetism in two-dimensional van der Waals crystals". In: *Nature* 546.7657 (2017), 265–269 (cit. on p. 18).

[64] Yujun Deng, Yijun Yu, Yichen Song, Jingzhao Zhang, Nai Zhou Wang, Zeyuan Sun, Yangfan Yi, Yi Zheng Wu, Shiwei Wu, Junyi Zhu, et al. "Gate-tunable room-temperature ferromagnetism in two-dimensional Fe3GeTe2". In: *Nature* 563.7729 (2018), 94–99 (cit. on p. 18).

[65] Ke-zhao Du, Xing-zhi Wang, Yang Liu, Peng Hu, M Iqbal Bakti Utama, Chee Kwan Gan, Qihua Xiong, and Christian Kloc. "Weak van der Waals stacking, wide-range band gap, and Raman study on ultrathin layers of metal phosphorus trichalcogenides". In: *ACS nano* 10.2 (2016), 1738–1743 (cit. on p. 18).

[66] Jae-Ung Lee, Sungmin Lee, Ji Hoon Ryoo, Soonmin Kang, Tae Yun Kim, Pilkwang Kim, Cheol-Hwan Park, Je-Geun Park, and Hyeonsik Cheong. "Ising-type magnetic ordering in atomically thin FePS3". In: *Nano letters* 16.12 (2016), 7433–7438 (cit. on p. 18).

[67] Cheng-Tai Kuo, Michael Neumann, Karuppannan Balamurugan, Hyun Ju Park, Soonmin Kang, Hung Wei Shiu, Jin Hyoun Kang, Byung Hee Hong, Moonsup Han, Tae Won Noh, et al. "Exfoliation and Raman spectroscopic fingerprint of few-layer NiPS3 van der Waals crystals". In: *Scientific reports* 6.1 (2016), 20904 (cit. on p. 18).

[68] Zhaowei Zhang, Jingzhi Shang, Chongyun Jiang, Abdullah Rasmita, Weibo Gao, and Ting Yu. "Direct photoluminescence probing of ferromagnetism in monolayer two-dimensional CrBr3". In: *Nano letters* 19.5 (2019), 3138–3142 (cit. on pp. 18, 51).

[69] Evan J Telford, Avalon H Dismukes, Kihong Lee, Minghao Cheng, Andrew Wieteska, Amymarie K Bartholomew, Yu-Sheng Chen, Xiaodong Xu, Abhay N Pasupathy, Xiaoyang Zhu, et al. "Layered antiferromagnetism induces large negative magnetoresistance in the van der Waals semiconductor CrSBr". In: *Advanced Materials* 32.37 (2020), 2003240 (cit. on p. 18).

[70] Dante J O'Hara, Tiancong Zhu, Amanda H Trout, Adam S Ahmed, Yunqiu Kelly Luo, Choong Hee Lee, Mark R Brenner, Siddharth Rajan, Jay A Gupta, David W McComb, et al. "Room temperature intrinsic ferromagnetism in epitaxial manganese selenide films in the monolayer limit". In: *Nano letters* 18.5 (2018), 3125–3131 (cit. on p. 18).

[71] Manuel Bonilla, Sadhu Kolekar, Yujing Ma, Horacio Coy Diaz, Vijaysankar Kalappattil, Raja Das, Tatiana Eggers, Humberto R Gutierrez, Manh-Huong Phan, and Matthias Batzill. "Strong room-temperature ferromagnetism in VSe2 monolayers on van der Waals substrates". In: *Nature nanotechnology* 13.4 (2018), 289–293 (cit. on p. 18).

[72] Qian-Qian Yuan, Zhaopeng Guo, Zhi-Qiang Shi, Hui Zhao, Zhen-Yu Jia, Qian-jin Wang, Jian Sun, Di Wu, and Shao-Chun Li. "Ferromagnetic MnSn monolayer epitaxially grown on silicon substrate". In: *Chinese Physics Letters* 37.7 (2020), 077502 (cit. on p. 18).

[73] Lixing Kang, Chen Ye, Xiaoxu Zhao, Xieyu Zhou, Junxiong Hu, Qiao Li, Dan Liu, Chandreyee Manas Das, Jiefu Yang, Dianyi Hu, et al. "Phase-controllable growth of ultrathin 2D magnetic FeTe crystals". In: *Nature communications* 11.1 (2020), 3729 (cit. on p. 18).

[74] Quantumdesign. "Fundamentals of magnetism and magnetic measurements". In: (). URL: https://qdusa.com/siteDocs/appNotes/FundPrimer.pdf (cit. on p. 20).

[75] Francesco Scaravaggi. "Electronic correlations and nematicity in 122 and 1111 Fe-based superconductors". In: (2021) (cit. on p. 20).

[76] Sam Mugiraneza and Alannah M Hallas. "Tutorial: a beginner's guide to interpreting magnetic susceptibility data with the Curie-Weiss law". In: *Communications Physics* 5.1 (2022), 95 (cit. on p. 22).

[77] Dante Gatteschi, Roberta Sessoli, and Jacques Villain. *Molecular nanomagnets*. Vol. 5. Oxford University Press, USA, 2006 (cit. on p. 24).

[78] Haiwen Xi, Kai-Zhong Gao, Jun Ouyang, Yiming Shi, and Yizhang Yang. "Slow magnetization relaxation and reversal in magnetic thin films". In: *Journal of Physics: Condensed Matter* 20.29 (2008), 295220 (cit. on p. 25).

[79] Rudolph Kohlrausch. "Theorie des elektrischen Rückstandes in der Leidener Flasche". In: *Annalen der Physik* 167.2 (1854), 179–214 (cit. on p. 25).

[80] K Jonason, E Vincent, J Hammann, JP Bouchaud, and P Nordblad. "Memory and chaos effects in spin glasses". In: *Physical Review Letters* 81.15 (1998), 3243 (cit. on p. 25).

[81] Jean-Philippe Bouchaud, Leticia F Cugliandolo, Jorge Kurchan, and Marc Mézard. "Out of equilibrium dynamics in spin-glasses and other glassy systems". In: *Spin glasses and random fields* 12 (1998), 161 (cit. on p. 25).

[82] Ph Refregier, E Vincent, J Hammann, and M Ocio. "Ageing phenomena in a spin-glass: effect of temperature changes below Tg". In: *Journal de Physique* 48.9 (1987), 1533–1539 (cit. on p. 26).

[83] E Vincent, JP Bouchaud, J Hammann, and F Lefloch. "Contrasting effects of field and temperature variations on ageing in spin glasses". In: *Philosophical Magazine B* 71.4 (1995), 489–500 (cit. on p. 26).

[84] Wolf Schottenhamel. "Aufbau eines hochauflösenden Dilatometers und einer hydrostatischen SQUID-Druckzelle sowie Untersuchungen an korrelierten Übergangsmetalloxiden". PhD thesis. Technische Universität Dresden, 2016 (cit. on p. 27).

[85] G Prando, R Dally, W Schottenhamel, Z Guguchia, S-H Baek, R Aeschlimann, AUB Wolter, SD Wilson, B Büchner, and MJ Graf. "Influence of hydrostatic pressure on the bulk magnetic properties of Eu 2 Ir 2 O 7". In: *Physical Review B* 93.10 (2016), 104422 (cit. on p. 27).

[86] Patricia Lebre Alireza and Gilbert George Lonzarich. "Miniature anvil cell for high-pressure measurements in a commercial superconducting quantum interference device magnetometer". In: *Review of Scientific Instruments* 80.2 (2009) (cit. on p. 27).

[87] T Sakurai, B Rubrecht, LT Corredor, R Takehara, M Yasutani, J Zeisner, A Alfonsov, S Selter, S Aswartham, AUB Wolter, et al. "Pressure control of the magnetic anisotropy of the quasi-two-dimensional van der Waals ferromagnet Cr 2 Ge 2 Te 6". In: *Physical Review B* 103.2 (2021), 024404 (cit. on pp. 27, 79).

[88] Riaz Hussain. "Spin spectroscopy of materials for quantum information processing, data storage and energy conversion". In: (2019) (cit. on pp. 28, 36).

[89] Marcello Mazzani. "Muons and Hydrogen in Graphene". PhD thesis. PhD thesis, Science and Technology of Innovative Materials-University of ..., 2011 (cit. on pp. 28, 36, 42).

[90] Charles P Slichter. *Principles of magnetic resonance*. Vol. 1. Springer Science & Business Media, 2013 (cit. on p. 28).

[91] Anatole Abragam. *The principles of nuclear magnetism*. 32. Oxford university press, 1961 (cit. on pp. 28, 33).

[92] E. L. Hahn. "Spin Echoes". In: *Phys. Rev.* 80 (4 1950), 580–594. DOI: 10.1103/PhysRev.80.580. URL: https://link.aps.org/doi/10.1103/PhysRev.80.580 (cit. on p. 32).

[93] Denninger Gert. "Hyperfine interaction". In: (). URL: https://www3.pi2.uni-stuttgart.de/official/g.denninger/GKMR2005/PDF/hyperfine_interaction.pdf (cit. on p. 33).

[94] Sara Bordignon. "Magnetic properties and Spin dynamics in magnetic Molecular Rings". In: (2016) (cit. on pp. 36, 42).

[95] G. Allodi, A. Banderini, R. De Renzi, and C. Vignali. "HyReSpect: A broadband fast-averaging spectrometer for nuclear magnetic resonance of magnetic materials". In: *Review of Scientific Instruments* 76.8 (2005), 083911. DOI: 10.1063/1.2009868. eprint: https://doi.org/10.1063/1.2009868. URL: https://doi.org/10.1063/1.2009868 (cit. on p. 37).

[96] E. Koster and B. G. Turrell. "NMR Studies of Fe2P and Fe3P". In: *Journal of Applied Physics* 42.4 (1971), 1314–1315. DOI: 10.1063/1.1660234. URL: https://doi.org/10.1063/1.1660234 (cit. on p. 42).

[97] Stephen J. Blundell, Roberto De Renzi, Tom Lancaster, and Francis L. Pratt. "336μSR versus other resonance and bulk techniques". In: *Muon Spectroscopy: An Introduction*. Oxford University Press, Nov. 2021. DOI: 10.1093/oso/9780198858959.003.0023. eprint: https://academic.oup.com/book/0/chapter/366299757/chapter-pdf/50191555/oso-9780198858959-chapter-23.pdf. URL: https://doi.org/10.1093/oso/9780198858959.003.0023 (cit. on p. 42).

[98] Richard L Garwin, Leon M Lederman, and Marcel Weinrich. “Observations of the failure of conservation of parity and charge conjugation in meson decays: the magnetic moment of the free muon”. In: *Physical Review* 105.4 (1957), 1415 (cit. on p. 42).

[99] Tsung D Lee and Chen Ning Yang. “Parity nonconservation and a two-component theory of the neutrino”. In: *Physical Review* 105.5 (1957), 1671 (cit. on p. 43).

[100] L Nuccio, L Schulz, and AJ Drew. “Muon spin spectroscopy: magnetism, soft matter and the bridge between the two”. In: *Journal of Physics D: Applied Physics* 47.47 (2014), 473001 (cit. on p. 44).

[101] Jeff E. Sonier. “Muon Spin roation-Relaxation-Resonance”. In: (). URL: https://cmms.triumf.ca/intro/musr/muSRBrochure.pdf (cit. on p. 45).

[102] A. "Amato and H." Luetkens. *"GPS User Guide"*. Tech. rep. "Paul Scherrer Institut", "2015". URL: "https://www.psi.ch/sites/default/files/import/smus/InstrumentGpsEN/User_Guide_present_version.pdf" (cit. on p. 47).

[103] S. J. Blundell. “Spin-polarized muons in condensed matter physics”. In: *Contemporary Physics* 40.3 (1999), 175–192. DOI: 10.1080/001075199181521. URL: http://dx.doi.org/10.1080/001075199181521 (cit. on p. 47).

[104] Alain Yaouanc and Pierre Dalmas de Réotier. *Muon spin rotation, relaxation, and resonance: applications to condensed matter*. International series of monographs on physics. Oxford: Oxford Univ. Press, 2011. URL: https://cds.cern.ch/record/1385534 (cit. on p. 47).

[105] Stephen J. Blundell, Roberto De Renzi, Tom Lancaster, and Francis L. Pratt. *Muon Spectroscopy: An Introduction*. Oxford University Press, 2021 (cit. on p. 47).

[106] Pinyuan Wang, Jun Ge, Jiaheng Li, Yanzhao Liu, Yong Xu, and Jian Wang. “Intrinsic magnetic topological insulators”. In: *The Innovation* 2.2 (2021) (cit. on p. 51).

[107] Emile DL Rienks, Sebastian Wimmer, Jaime Sánchez-Barriga, Ondřej Caha, Partha Sarathi Mandal, Jiří Ržička, Andreas Ney, Hubert Steiner, Valentine V Volobuev, Heiko Groiß, et al. “Large magnetic gap at the Dirac point in Bi2Te3/MnBi2Te4 heterostructures”. In: *Nature* 576.7787 (2019), 423–428 (cit. on p. 51).

[108] MM Otrokov, Igor P Rusinov, María Blanco-Rey, M Hoffmann, A Yu Vyazovskaya, SV Eremeev, Arthur Ernst, Pedro M Echenique, Andrés Arnau, and Eugene V Chulkov. “Unique thickness-dependent properties of the van der Waals interlayer antiferromagnet MnBi 2 Te 4 films”. In: *Physical review letters* 122.10 (2019), 107202 (cit. on p. 51).

[109] Jiaheng Li, Yang Li, Shiqiao Du, Zun Wang, Bing-Lin Gu, Shou-Cheng Zhang, Ke He, Wenhui Duan, and Yong Xu. “Intrinsic magnetic topological insulators in van der Waals layered MnBi2Te4-family materials”. In: *Science Advances* 5.6 (2019), eaaw5685 (cit. on pp. 51, 54).

[110] Shuai Li, Tianyu Liu, Chang Liu, Yayu Wang, Hai-Zhou Lu, and XC Xie. "Progress on the antiferromagnetic topological insulator MnBi2Te4". In: *National Science Review* 11.2 (2024), nwac296 (cit. on p. 51).

[111] Alexander Zeugner, Frederik Nietschke, Anja UB Wolter, Sebastian Gaß, Raphael C Vidal, Thiago RF Peixoto, Darius Pohl, Christine Damm, Axel Lubk, Richard Hentrich, et al. "Chemical aspects of the candidate antiferromagnetic topological insulator MnBi2Te4". In: *Chemistry of Materials* 31.8 (2019), 2795–2806 (cit. on pp. 52–54, 83, 87).

[112] Seng Huat Lee, Yanglin Zhu, Yu Wang, Leixin Miao, Timothy Pillsbury, Hemian Yi, Susan Kempinger, Jin Hu, Colin A Heikes, Patrick Quarterman, et al. "Spin scattering and noncollinear spin structure-induced intrinsic anomalous Hall effect in antiferromagnetic topological insulator MnB i 2 T e 4". In: *Physical Review Research* 1.1 (2019), 012011 (cit. on pp. 54, 55, 89).

[113] S-K Bac, K Koller, F Lux, J Wang, L Riney, K Borisiak, W Powers, M Zhukovskyi, T Orlova, M Dobrowolska, et al. "Topological response of the anomalous Hall effect in MnBi2Te4 due to magnetic canting". In: *npj quantum materials* 7.1 (2022), 46 (cit. on pp. 54, 89).

[114] Paul M Sass, Wenbo Ge, Jiaqiang Yan, D Obeysekera, JJ Yang, and Weida Wu. "Magnetic imaging of domain walls in the antiferromagnetic topological insulator MnBi2Te4". In: *Nano letters* 20.4 (2020), 2609–2614 (cit. on pp. 54, 89).

[115] Yu-Jie Hao, Pengfei Liu, Yue Feng, Xiao-Ming Ma, Eike F Schwier, Masashi Arita, Shiv Kumar, Chaowei Hu, Meng Zeng, Yuan Wang, et al. "Gapless surface Dirac cone in antiferromagnetic topological insulator MnBi 2 Te 4". In: *Physical Review X* 9.4 (2019), 041038 (cit. on pp. 54, 55, 106).

[116] J-Q Yan, Qiang Zhang, Thomas Heitmann, Zengle Huang, KY Chen, J-G Cheng, Weida Wu, David Vaknin, Brian C Sales, and Robert John McQueeney. "Crystal growth and magnetic structure of MnBi 2 Te 4". In: *Physical Review Materials* 3.6 (2019), 064202 (cit. on pp. 54, 87).

[117] Manuela Garnica, Mikhail M Otrokov, P Casado Aguilar, Ilya I Klimovskikh, Dmitry Estyunin, Ziya S Aliev, Imamaddin R Amiraslanov, Nadir A Abdullayev, Vladimir N Zverev, Mahammad B Babanly, et al. "Native point defects and their implications for the Dirac point gap at MnBi2Te4 (0001)". In: *npj Quantum Materials* 7.1 (2022), 7 (cit. on pp. 54, 55, 87, 106).

[118] Bing Li, J-Q Yan, Daniel M Pajerowski, Elijah Gordon, A-M Nedić, Y Sizyuk, Liqin Ke, Peter P Orth, David Vaknin, and Robert J McQueeney. "Competing magnetic interactions in the antiferromagnetic topological insulator MnBi 2 Te 4". In: *Physical review letters* 124.16 (2020), 167204 (cit. on p. 54).

[119] YJ Chen, LX Xu, JH Li, YW Li, HY Wang, CF Zhang, Hao Li, Yang Wu, AJ Liang, Cheng Chen, et al. "Topological electronic structure and its temperature evolution in antiferromagnetic topological insulator MnBi 2 Te 4". In: *Physical Review X* 9.4 (2019), 041040 (cit. on pp. 54, 55).

[120] Chaowei Hu, Anyuan Gao, Bryan Stephen Berggren, Hong Li, Rafał Kurleto, Dushyant Narayan, Ilija Zeljkovic, Dan Dessau, Suyang Xu, and Ni Ni. "Growth, characterization, and Chern insulator state in MnBi 2 Te 4 via the chemical vapor transport method". In: *Physical Review Materials* 5.12 (2021), 124206 (cit. on p. 54).

[121] Hao-Ran Ji, Yan-Zhao Liu, He Wang, Jia-Wei Luo, Jia-Heng Li, Hao Li, Yang Wu, Yong Xu, and Jian Wang. "Detection of magnetic gap in topological surface states of MnBi2Te4". In: *Chinese Physics Letters* 38.10 (2021), 107404 (cit. on p. 54).

[122] Chang Liu, Yongchao Wang, Hao Li, Yang Wu, Yaoxin Li, Jiaheng Li, Ke He, Yong Xu, Jinsong Zhang, and Yayu Wang. "Robust axion insulator and Chern insulator phases in a two-dimensional antiferromagnetic topological insulator". In: *Nature materials* 19.5 (2020), 522–527 (cit. on pp. 54, 56).

[123] Xiao Lei, L Zhou, ZY Hao, XZ Ma, C Ma, YQ Wang, PB Chen, BC Ye, L Wang, F Ye, et al. "Surface-induced linear magnetoresistance in the antiferromagnetic topological insulator Mn Bi 2 Te 4". In: *Physical Review B* 102.23 (2020), 235431 (cit. on p. 54).

[124] Dongqin Zhang, Minji Shi, Tongshuai Zhu, Dingyu Xing, Haijun Zhang, and Jing Wang. "Topological axion states in the magnetic insulator MnBi 2 Te 4 with the quantized magnetoelectric effect". In: *Physical review letters* 122.20 (2019), 206401 (cit. on pp. 54, 59).

[125] Jiaheng Li, Chong Wang, Zetao Zhang, Bing-Lin Gu, Wenhui Duan, and Yong Xu. "Magnetically controllable topological quantum phase transitions in the antiferromagnetic topological insulator MnBi 2 Te 4". In: *Physical Review B* 100.12 (2019), 121103 (cit. on p. 54).

[126] RC Vidal, Hendrik Bentmann, TRF Peixoto, Alexander Zeugner, S Moser, C-H Min, S Schatz, K Kißner, M Ünzelmann, CI Fornari, et al. "Surface states and Rashba-type spin polarization in antiferromagnetic MnBi 2 Te 4 (0001)". In: *Physical Review B* 100.12 (2019), 121104 (cit. on pp. 55, 58).

[127] DA Estyunin, Ilya I Klimovskikh, Alexander M Shikin, EF Schwier, MM Otrokov, A Kimura, S Kumar, SO Filnov, Ziya S Aliev, MB Babanly, et al. "Signatures of temperature driven antiferromagnetic transition in the electronic structure of topological insulator MnBi2Te4". In: *APL Materials* 8.2 (2020) (cit. on p. 55).

[128] Hang Li, Shun-Ye Gao, Shao-Feng Duan, Yuan-Feng Xu, Ke-Jia Zhu, Shang-Jie Tian, Jia-Cheng Gao, Wen-Hui Fan, Zhi-Cheng Rao, Jie-Rui Huang, et al. "Dirac surface states in intrinsic magnetic topological insulators EuSn 2 As 2 and MnBi 2 n Te 3 n+ 1". In: *Physical Review X* 9.4 (2019), 041039 (cit. on p. 55).

[129] Przemyslaw Swatek, Yun Wu, Lin-Lin Wang, Kyungchan Lee, Benjamin Schrunk, Jiaqiang Yan, and Adam Kaminski. "Gapless Dirac surface states in the antiferromagnetic topological insulator MnBi 2 Te 4". In: *Physical Review B* 101.16 (2020), 161109 (cit. on pp. 55, 106).

[130] Dan Nevola, Haoxiang X Li, J-Q Yan, RG Moore, H-N Lee, Hu Miao, and Peter D Johnson. "Coexistence of surface ferromagnetism and a gapless topological state in MnBi 2 Te 4". In: *Physical Review Letters* 125.11 (2020), 117205 (cit. on p. 55).

[131] Mengke Liu, Chao Lei, Hyunsue Kim, Yanxing Li, Lisa Frammolino, Jiaqiang Yan, Allan H Macdonald, and Chih-Kang Shih. "Visualizing the interplay of Dirac mass gap and magnetism at nanoscale in intrinsic magnetic topological insulators". In: *Proc. Natl. Acad. Sci. U.S.A.* 119 (2022) (cit. on pp. 55, 106).

[132] Felix Lüpke, Marek Kolmer, Jiaqiang Yan, Hao Chang, Paolo Vilmercati, Hanno H Weitering, Wonhee Ko, and An-Ping Li. "Anti-site defect-induced disorder in compensated topological magnet MnBi2-xSbxTe4". In: *Communications Materials* 4.1 (2023), 82 (cit. on pp. 55, 106).

[133] Hengxin Tan and Binghai Yan. "Distinct Magnetic Gaps between Antiferromagnetic and Ferromagnetic Orders Driven by Surface Defects in the Topological Magnet $MnBi_2Te_4$". In: *Phys. Rev. Lett.* 130 (12 2023), 126702. DOI: 10.1103/PhysRevLett.130.126702. URL: https://link.aps.org/doi/10.1103/PhysRevLett.130.126702 (cit. on pp. 55, 106).

[134] Yujun Deng, Yijun Yu, Meng Zhu Shi, Zhongxun Guo, Zihan Xu, Jing Wang, Xian Hui Chen, and Yuanbo Zhang. "Quantum anomalous Hall effect in intrinsic magnetic topological insulator MnBi2Te4". In: *Science* 367.6480 (2020), 895–900 (cit. on p. 55).

[135] Anyuan Gao, Yu-Fei Liu, Chaowei Hu, Jian-Xiang Qiu, Christian Tzschaschel, Barun Ghosh, Sheng-Chin Ho, Damien Bérubé, Rui Chen, Haipeng Sun, et al. "Layer Hall effect in a 2D topological axion antiferromagnet". In: *Nature* 595.7868 (2021), 521–525 (cit. on p. 56).

[136] Shuai Zhang, Rui Wang, Xuepeng Wang, Boyuan Wei, Bo Chen, Huaiqiang Wang, Gang Shi, Feng Wang, Bin Jia, Yiping Ouyang, et al. "Experimental observation of the gate-controlled reversal of the anomalous Hall effect in the intrinsic magnetic topological insulator MnBi2Te4 device". In: *Nano Letters* 20.1 (2019), 709–714 (cit. on p. 56).

[137] Yi-Fan Zhao, Ling-Jie Zhou, Fei Wang, Guang Wang, Tiancheng Song, Dmitry Ovchinnikov, Hemian Yi, Ruobing Mei, Ke Wang, Moses HW Chan, et al. "Even–odd layer-dependent anomalous Hall effect in topological magnet MnBi2Te4 thin films". In: *Nano letters* 21.18 (2021), 7691–7698 (cit. on p. 56).

[138] Jun Ge, Yanzhao Liu, Jiaheng Li, Hao Li, Tianchuang Luo, Yang Wu, Yong Xu, and Jian Wang. "High-Chern-number and high-temperature quantum Hall effect without Landau levels". In: *National science review* 7.8 (2020), 1280–1287 (cit. on p. 56).

[139] Chaowei Hu, Lei Ding, Kyle N Gordon, Barun Ghosh, Hung-Ju Tien, Haoxiang Li, A Garrison Linn, Shang-Wei Lien, Cheng-Yi Huang, Scott Mackey, et al. "Realization of an intrinsic ferromagnetic topological state in MnBi8Te13". In: *Science advances* 6.30 (2020), eaba4275 (cit. on pp. 56, 58).

[140] Ilya I Klimovskikh, Mikhail M Otrokov, Dmitry Estyunin, Sergey V Eremeev, Sergey O Filnov, Alexandra Koroleva, Eugene Shevchenko, Vladimir Voroshnin, Artem G Rybkin, Igor P Rusinov, et al. "Tunable 3D/2D magnetism in the (MnBi2Te4)(Bi2Te3) m topological insulators family". In: *npj Quantum Materials* 5.1 (2020), 54 (cit. on pp. 57, 58).

[141] Abdul-Vakhab Tcakaev, Bastian Rubrecht, Jorge I Facio, Volodymyr B Zabolotnyy, Laura T Corredor, Laura C Folkers, Ekaterina Kochetkova, Thiago RF Peixoto, Philipp Kagerer, Simon Heinze, et al. "Intermixing-Driven Surface and Bulk Ferromagnetism in the Quantum Anomalous Hall Candidate MnBi6Te10". In: *Advanced Science* 10.10 (2023), 2203239 (cit. on pp. 57, 58, 83, 94).

[142] Raphael C Vidal, Alexander Zeugner, Jorge I Facio, Rajyavardhan Ray, M Hossein Haghighi, Anja UB Wolter, Laura T Corredor Bohorquez, Federico Caglieris, Simon Moser, Tim Figgemeier, et al. "Topological electronic structure and intrinsic magnetization in MnBi 4 Te 7: a Bi 2 Te 3 derivative with a periodic Mn sublattice". In: *Physical Review X* 9.4 (2019), 041065 (cit. on pp. 57, 83, 94).

[143] J-Q Yan, YH Liu, DS Parker, Y Wu, AA Aczel, M Matsuda, MA McGuire, and BC Sales. "A-type antiferromagnetic order in MnBi 4 Te 7 and MnBi 6 Te 10 single crystals". In: *Physical Review Materials* 4.5 (2020), 054202 (cit. on pp. 58, 104).

[144] Aoyu Tan, Valentin Labracherie, Narayan Kunchur, Anja UB Wolter, Joaquin Cornejo, Joseph Dufouleur, Bernd Büchner, Anna Isaeva, and Romain Giraud. "Metamagnetism of weakly coupled antiferromagnetic topological insulators". In: *Physical Review Letters* 124.19 (2020), 197201 (cit. on pp. 58, 59).

[145] Chenhui Yan, Yanglin Zhu, Leixin Miao, Sebastian Fernandez-Mulligan, Emanuel Green, Ruobing Mei, Hengxin Tan, Binghai Yan, Chao-Xing Liu, Nasim Alem, et al. "Delicate ferromagnetism in MnBi6Te10". In: *Nano letters* 22.24 (2022), 9815–9822 (cit. on p. 58).

[146] Shangjie Tian, Shunye Gao, Simin Nie, Yuting Qian, Chunsheng Gong, Yang Fu, Hang Li, Wenhui Fan, Peng Zhang, Takesh Kondo, et al. "Magnetic topological insulator MnBi 6 Te 10 with a zero-field ferromagnetic state and gapped Dirac surface states". In: *Physical Review B* 102.3 (2020), 035144 (cit. on p. 58).

[147] Xiaolong Xu, Shiqi Yang, Huan Wang, Roger Guzman, Yuchen Gao, Yaozheng Zhu, Yuxuan Peng, Zhihao Zang, Ming Xi, Shangjie Tian, et al. "Ferromagnetic-antiferromagnetic coexisting ground state and exchange bias effects in MnBi4Te7 and MnBi6Te10". In: *Nature Communications* 13.1 (2022), 7646 (cit. on p. 58).

[148] Chaowei Hu, Lei Ding, Kyle N Gordon, Barun Ghosh, Haoxiang Li, Shang-Wei Lian, A Garrison Linn, Hung Ju Tien, Cheng Yi Huang, P Reddy, et al. "Realization of an intrinsic, ferromagnetic axion insulator in MnBi8Te13". In: *Preprint at https://arxiv. org/abs/1910.12847* (2019) (cit. on p. 58).

[149] Yong Hu, Lixuan Xu, Mengzhu Shi, Aiyun Luo, Shuting Peng, ZY Wang, JJ Ying, T Wu, ZK Liu, CF Zhang, et al. "Universal gapless Dirac cone and tunable topological states in (MnB i 2 T e 4) m (B i 2 T e 3) n heterostructures". In: *Physical Review B* 101.16 (2020), 161113 (cit. on p. 58).

[150] Xiao-Ming Ma, Zhongjia Chen, Eike F Schwier, Yang Zhang, Yu-Jie Hao, Shiv Kumar, Ruie Lu, Jifeng Shao, Yuanjun Jin, Meng Zeng, et al. "Hybridization-induced gapped and gapless states on the surface of magnetic topological insulators". In: *Physical Review B* 102.24 (2020), 245136 (cit. on p. 58).

[151] Xuefeng Wu, Jiayu Li, Xiao-Ming Ma, Yu Zhang, Yuntian Liu, Chun-Sheng Zhou, Jifeng Shao, Qiaoming Wang, Yu-Jie Hao, Yue Feng, et al. "Distinct topological surface states on the two terminations of MnBi 4 Te 7". In: *Physical Review X* 10.3 (2020), 031013 (cit. on p. 58).

[152] Ruie Lu, Hongyi Sun, Shiv Kumar, Yuan Wang, Mingqiang Gu, Meng Zeng, Yu-Jie Hao, Jiayu Li, Jifeng Shao, Xiao-Ming Ma, et al. "Half-magnetic topological insulator with magnetization-induced Dirac gap at a selected surface". In: *Physical Review X* 11.1 (2021), 011039 (cit. on p. 58).

[153] Haiming Deng, Zhiyi Chen, Agnieszka Wołoś, Marcin Konczykowski, Kamil Sobczak, Joanna Sitnicka, Irina V Fedorchenko, Jolanta Borysiuk, Tristan Heider, Łukasz Pluciński, et al. "High-temperature quantum anomalous Hall regime in a MnBi2Te4/Bi2Te3 superlattice". In: *Nature Physics* 17.1 (2021), 36–42 (cit. on p. 59).

[154] Jianhua Cui, Bin Lei, Mengzhu Shi, Ziji Xiang, Tao Wu, and Xianhui Chen. "Layer-Dependent Magnetic Structure and Anomalous Hall Effect in the Magnetic Topological Insulator MnBi4Te7". In: *Nano Letters* 23.5 (2023), 1652–1658 (cit. on p. 59).

[155] Bin Jia, Shuai Zhang, Zhe Ying, Hangkai Xie, Bo Chen, Muhammad Naveed, Fucong Fei, Minhao Zhang, Danfeng Pan, and Fengqi Song. "Unconventional anomalous Hall effect in magnetic topological insulator MnBi4Te7 device". In: *Applied Physics Letters* 118.8 (2021) (cit. on p. 59).

[156] Hongyi Sun, Bowen Xia, Zhongjia Chen, Yingjie Zhang, Pengfei Liu, Qiushi Yao, Hong Tang, Yujun Zhao, Hu Xu, and Qihang Liu. "Rational design principles of the quantum anomalous Hall effect in superlatticelike magnetic topological insulators". In: *Physical review letters* 123.9 (2019), 096401 (cit. on p. 59).

[157] Mingqiang Gu, Jiayu Li, Hongyi Sun, Yufei Zhao, Chang Liu, Jianpeng Liu, Haizhou Lu, and Qihang Liu. "Spectral signatures of the surface anomalous Hall effect in magnetic axion insulators". In: *Nature communications* 12.1 (2021), 3524 (cit. on p. 59).

[158] MZ Shi, B Lei, CS Zhu, DH Ma, JH Cui, ZL Sun, JJ Ying, and XH Chen. "Magnetic and transport properties in the magnetic topological insulators MnB i 2 T e 4 (B i 2 T e 3) n (n= 1, 2)". In: *Physical Review B* 100.15 (2019), 155144 (cit. on p. 59).

[159] Liqin Zhou, Zhiyun Tan, Dayu Yan, Zhong Fang, Youguo Shi, and Hongming Weng. "Topological phase transition in the layered magnetic compound MnSb 2 Te 4: Spin-orbit coupling and interlayer coupling dependence". In: *Physical review B* 102.8 (2020), 085114 (cit. on p. 59).

[160] Ping Li, Jiangying Yu, Ying Wang, and Weidong Luo. "Electronic structure and topological phases of the magnetic layered materials MnBi 2 Te 4, MnBi 2 Se 4, and MnSb 2 Te 4". In: *Physical Review B* 103.15 (2021), 155118 (cit. on p. 59).

[161] Huisheng Zhang, Wenjia Yang, Yingying Wang, and Xiaohong Xu. "Tunable topological states in layered magnetic materials of Mn Sb 2 Te 4, Mn Bi 2 Se 4, and Mn Sb 2 Se 4". In: *Physical Review B* 103.9 (2021), 094433 (cit. on p. 59).

[162] Li Chen, Dongchao Wang, Changmin Shi, Chuan Jiang, Hongmei Liu, Guangliang Cui, Xiaoming Zhang, and Xiaolong Li. "Electronic structure and magnetism of MnSb 2 Te 4". In: *Journal of Materials Science* 55 (2020), 14292–14300 (cit. on p. 59).

[163] Sergey V Eremeev, Igor P Rusinov, Yu M Koroteev, A Yu Vyazovskaya, M Hoffmann, Pedro Miguel Echenique, A Ernst, Mikhail M Otrokov, and Evgueni V Chulkov. "Topological magnetic materials of the (MnSb2Te4)·(Sb2Te3) n van der Waals compounds family". In: *The Journal of Physical Chemistry Letters* 12.17 (2021), 4268–4277 (cit. on p. 59).

[164] Taito Murakami, Yusuke Nambu, Takashi Koretsune, Gu Xiangyu, Takafumi Yamamoto, Craig M Brown, and Hiroshi Kageyama. "Realization of interlayer ferromagnetic interaction in MnS b 2 T e 4 toward the magnetic Weyl semimetal state". In: *Physical Review B* 100.19 (2019), 195103 (cit. on pp. 59, 66, 104).

[165] Yaohua Liu, Lin-Lin Wang, Qiang Zheng, Zengle Huang, Xiaoping Wang, Miaofang Chi, Yan Wu, Bryan C Chakoumakos, Michael A McGuire, Brian C Sales, et al. "Site mixing for engineering magnetic topological insulators". In: *Physical Review X* 11.2 (2021), 021033 (cit. on pp. 59, 60, 86, 104).

[166] Hao Li, Yaoxin Li, Yukun Lian, Weiwei Xie, Ling Chen, Jinsong Zhang, Yang Wu, and Shoushan Fan. "Glassy magnetic ground state in layered compound MnSb2Te4". In: *Science China Materials* 65.2 (2022), 477–485 (cit. on p. 59).

[167] Stefan Wimmer, Jaime Sánchez-Barriga, Philipp Küppers, Andreas Ney, Enrico Schierle, Friedrich Freyse, Ondrej Caha, Jan Michalička, Marcus Liebmann, Daniel Primetzhofer, et al. "Mn-Rich MnSb2Te4: A topological insulator with magnetic gap closing at high curie temperatures of 45–50 K". In: *Advanced Materials* 33.42 (2021), 2102935 (cit. on p. 60).

[168] Shuchun Huan, Dinghui Wang, Hao Su, Hongyuan Wang, Xia Wang, Na Yu, Zhiqiang Zou, Haijun Zhang, and Yanfeng Guo. "Magnetism-induced ideal Weyl state in bulk van der Waals crystal MnSb2Te4". In: *Applied Physics Letters* 118.19 (2021) (cit. on p. 60).

[169] Gang Shi, Mingjie Zhang, Dayu Yan, Honglei Feng, Meng Yang, Youguo Shi, and Yongqing Li. "Anomalous Hall effect in layered ferrimagnet MnSb2Te4". In: *Chinese Physics Letters* 37.4 (2020), 047301 (cit. on pp. 60, 66).

[170] Sebastian Selter, Gaël Bastien, Anja UB Wolter, Saicharan Aswartham, and Bernd Büchner. "Magnetic anisotropy and low-field magnetic phase diagram of the quasi-two-dimensional ferromagnet Cr 2 Ge 2 Te 6". In: *Physical Review B* 101.1 (2020), 014440 (cit. on p. 65).

[171] Ming Xi, Famin Chen, Chunsheng Gong, Shangjie Tian, Qiangwei Yin, Tian Qian, and Hechang Lei. "Relationship between antisite defects, magnetism, and band topology in MnSb2Te4 crystals with TC 40 K". In: *The Journal of Physical Chemistry Letters* 13.47 (2022), 10897–10904 (cit. on p. 66).

[172] DY Yan, M Yang, PB Song, YT Song, CX Wang, CJ Yi, and YG Shi. "Site mixing induced ferrimagnetism and anomalous transport properties of the Weyl semimetal candidate Mn Sb 2 Te 4". In: *Physical Review B* 103.22 (2021), 224412 (cit. on p. 66).

[173] You Lai, Liqin Ke, Jiaqiang Yan, Ross D McDonald, and Robert J McQueeney. "Defect-driven ferrimagnetism and hidden magnetization in $MnBi_2Te_4$". In: *Physical Review B* 103.18 (2021), 184429 (cit. on pp. 66, 67, 87, 104).

[174] JA Mydosh. "Spin glasses: redux: an updated experimental/materials survey". In: *Reports on Progress in Physics* 78.5 (2015), 052501 (cit. on p. 69).

[175] John A Mydosh. *Spin glasses: an experimental introduction*. CRC Press, 1993 (cit. on p. 69).

[176] Pallab Bag, PR Baral, and R Nath. "Cluster spin-glass behavior and memory effect in $Cr_{0.5}Fe_{0.5Ga}$". In: *Physical Review B* 98.14 (2018), 144436 (cit. on p. 69).

[177] VK Anand, DT Adroja, and AD Hillier. "Ferromagnetic cluster spin-glass behavior in $PrRhSn_3$". In: *Physical Review B* 85.1 (2012), 014418 (cit. on p. 69).

[178] GA Petrakovskii, KS Aleksandrov, LN Bezmaternikh, SS Aplesnin, B Roessli, F Semadeni, A Amato, C Baines, J Bartolomé, and M Evangelisti. "Spin-glass state in $CuGa_2O_4$". In: *Physical Review B* 63.18 (2001), 184425 (cit. on p. 69).

[179] D Samal, C Shivakumara, and PS Anil Kumar. "The incongruous observation of magnetic phase separation in $La_{0.85}Sr_{0.15}CoO_3$ spin glass system". In: *Journal of Applied Physics* 106.12 (2009), 123920 (cit. on p. 69).

[180] Chaowei Hu, Makariy A Tanatar, Ruslan Prozorov, and Ni Ni. "Unusual dynamic susceptibility arising from soft ferromagnetic domains in $MnBi_8Te_{13}$ and Sb − doped $MnBi_{2n}Te_{3n+1}$ (n = 2, 3)". In: *J. Phys. D: Appl. Phys.* 55 (2022), 054003 (cit. on pp. 69, 70, 72).

[181] Rahul Kumar, Premakumar Yanda, and A Sundaresan. "Cluster-glass behavior in the two-dimensional triangular lattice Ising-spin compound $Li_2Mn_3O_7$". In: *Physical Review B* 103.21 (2021), 214427 (cit. on p. 70).

[182] A Bhattacharyya, S Giri, and S Majumdar. "Spin-glass-like state in GdCu: Role of phase separation and magnetic frustration". In: *Physical Review B* 83.13 (2011), 134427 (cit. on p. 70).

[183] S Chattopadhyay, S Giri, and S Majumdar. "Structural domain and spin-ordering–induced glassy magnetic phase in single-layered manganite $Pr_{0.22}Sr_{1.78}MnO_4$". In: *EPL (Europhysics Letters)* 98.2 (2012), 27004 (cit. on p. 70).

[184] Jiazhen Wu, Fucai Liu, Can Liu, Yong Wang, Changcun Li, Yangfan Lu, Satoru Matsuishi, and Hideo Hosono. "Toward 2D magnets in the $(MnBi_2Te_4)(Bi_2Te_3)_n$ bulk crystal". In: *Advanced Materials* 32.23 (2020), 2001815 (cit. on p. 70).

[185] Johannes Kroder, Kaustuv Manna, Dominik Kriegner, AS Sukhanov, Enke Liu, Horst Borrmann, Andreas Hoser, Johannes Gooth, Walter Schnelle, Dmytro S Inosov, et al. "Spin glass behavior in the disordered half-Heusler compound IrMnGa". In: *Physical Review B* 99.17 (2019), 174410 (cit. on p. 71).

[186] Fan Wang, Jungho Kim, Young-June Kim, and GD Gu. "Spin-glass behavior in LuFe 2 O 4+ δ". In: *Physical Review B* 80.2 (2009), 024419 (cit. on p. 71).

[187] Hao Li, Yaoxin Li, Yukun Lian, Weiwei Xie, Ling Chen, Jinsong Zhang, Yang Wu, and Shoushan Fan. "Glassy magnetic ground state in layered compound $MnSb_2Te_4$". In: *Science China Materials* (2021), 1–9 (cit. on pp. 72, 106).

[188] George Feher and A. F. Kip. "Electron Spin Resonance Absorption in Metals. I. Experimental". In: *Phys. Rev.* 98 (2 1955), 337–348. DOI: 10.1103/PhysRev.98.337. URL: https://link.aps.org/doi/10.1103/PhysRev.98.337 (cit. on p. 72).

[189] Freeman J. Dyson. "Electron Spin Resonance Absorption in Metals. II. Theory of Electron Diffusion and the Skin Effect". In: *Phys. Rev.* 98 (2 1955), 349–359. DOI: 10.1103/PhysRev.98.349. URL: https://link.aps.org/doi/10.1103/PhysRev.98.349 (cit. on p. 72).

[190] A. Alfonsov, J. I. Facio, K. Mehlawat, A. G. Moghaddam, R. Ray, A. Zeugner, M. Richter, J. van den Brink, A. Isaeva, B. Büchner, and V. Kataev. "Strongly anisotropic spin dynamics in magnetic topological insulators". In: *Phys. Rev. B* 103 (18 2021), L180403. DOI: 10.1103/PhysRevB.103.L180403. URL: https://link.aps.org/doi/10.1103/PhysRevB.103.L180403 (cit. on p. 73).

[191] A. Alfonsov, K. Mehlawat, A. Zeugner, A. Isaeva, B. Büchner, and V. Kataev. "Magnetic-field tuning of the spin dynamics in the magnetic topological insulators $(MnBi_2Te_4)(Bi_2Te_3)_n$". In: *Phys. Rev. B* 104 (19 2021), 195139. DOI: 10.1103/PhysRevB.104.195139. URL: https://link.aps.org/doi/10.1103/PhysRevB.104.195139 (cit. on p. 73).

[192] Lawrence H Bennett and Edward Della Torre. "Analysis of wasp-waist hysteresis loops". In: *Journal of applied physics* 97.10 (2005) (cit. on p. 77).

[193] Tingxin Li, Shengwei Jiang, Nikhil Sivadas, Zefang Wang, Yang Xu, Daniel Weber, Joshua E Goldberger, Kenji Watanabe, Takashi Taniguchi, Craig J Fennie, et al. "Pressure-controlled interlayer magnetism in atomically thin CrI3". In: *Nature materials* 18.12 (2019), 1303–1308 (cit. on p. 79).

[194] Matthew J Coak, David M Jarvis, Hayrullo Hamidov, Andrew R Wildes, Joseph AM Paddison, Cheng Liu, Charles RS Haines, Ngoc T Dang, Sergey E Kichanov, Boris N Savenko, et al. "Emergent magnetic phases in pressure-tuned van der Waals antiferromagnet FePS 3". In: *Physical Review X* 11.1 (2021), 011024 (cit. on p. 79).

[195] Yueshao Zheng, Xing-xing Jiang, Xiong-xiong Xue, Jiayu Dai, and Yexin Feng. "Ab initio study of pressure-driven phase transition in FePS 3 and FePSe 3". In: *Physical Review B* 100.17 (2019), 174102 (cit. on p. 79).

[196] Zhisheng Lin, Mark Lohmann, Zulfikhar A Ali, Chi Tang, Junxue Li, Wenyu Xing, Jiangnan Zhong, Shuang Jia, Wei Han, Sinisa Coh, et al. "Pressure-induced spin reorientation transition in layered ferromagnetic insulator Cr 2 Ge 2 Te 6". In: *Physical Review Materials* 2.5 (2018), 051004 (cit. on p. 79).

[197] Shilei Ding, Zhongyu Liang, Jie Yang, Chao Yun, Peijie Zhang, Zefang Li, Mingzhu Xue, Zhou Liu, Guang Tian, Fuyang Liu, et al. "Ferromagnetism in two-dimensional Fe 3 Ge Te 2; Tunability by hydrostatic pressure". In: *Physical Review B* 103.9 (2021), 094429 (cit. on pp. 79, 104).

[198] Dante J O'Hara, Zachary E Brubaker, Ryan L Stillwell, Earl F O'Bannon, Alexander A Baker, Daniel Weber, Leonardus Bimo Bayu Aji, Joshua E Goldberger, Roland K Kawakami, Rena J Zieve, et al. "Suppression of magnetic ordering in Fe-deficient Fe 3- x Ge Te 2 from application of pressure". In: *Physical Review B* 102.5 (2020), 054405 (cit. on p. 79).

[199] Ziya S Aliev, Imamaddin R Amiraslanov, Daria I Nasonova, Andrei V Shevelkov, Nadir A Abdullayev, Zakir A Jahangirli, Elnur N Orujlu, Mikhail M Otrokov, Nazim T Mamedov, Mahammad B Babanly, et al. "Novel ternary layered manganese bismuth tellurides of the MnTe-Bi2Te3 system: Synthesis and crystal structure". In: *Journal of Alloys and Compounds* 789 (2019), 443–450 (cit. on p. 83).

[200] Pietro Bonfà and Roberto De Renzi. "Toward the computational prediction of muon sites and interaction parameters". In: *Journal of the Physical Society of Japan* 85.9 (2016), 091014 (cit. on p. 101).

[201] Pietro Bonfà, Ifeanyi John Onuorah, and Roberto De Renzi. "Introduction and a quick look at MUESR, the Magnetic structure and mUon Embedding Site Refinement suite". In: *Proceedings of the 14th International Conference on Muon Spin Rotation, Relaxation and Resonance (μSR2017)*. 2018, p. 011052 (cit. on pp. 101, 103).

[202] Ifeanyi John Onuorah, Pietro Bonfà, and Roberto De Renzi. "Muon contact hyperfine field in metals: A DFT calculation". In: *Physical Review B* 97.17 (2018), 174414 (cit. on pp. 101, 102).

[203] JS Möller, P Bonfà, D Ceresoli, Fabio Bernardini, SJ Blundell, T Lancaster, R De Renzi, N Marzari, I Watanabe, S Sulaiman, et al. "Playing quantum hide-and-seek with the muon: localizing muon stopping sites". In: *Physica Scripta* 88.6 (2013), 068510 (cit. on p. 101).

[204] Takeji Kubo, Akira Hirai, and Hisashi Abe. "Mn55 Nuclear Magnetic Resonance of the Mn3+ Ion Located at the B-Site in Manganese Ferrite Single Crystal—Anisotropic Hyperfine Field Due to the Local Jahn-Teller Distortion". In: *Journal of the Physical Society of Japan* 26.5 (1969), 1094–1109 (cit. on p. 104).

[205] Giuseppe Allodi, M Cestelli Guidi, Roberto De Renzi, and MW Pieper. "Inhomogeneous electronic state of low-doped insulating manganites: NMR and μSR evidence". In: *Journal of magnetism and magnetic materials* 242 (2002), 635–639 (cit. on p. 104).

[206] Lei Ding, Chaowei Hu, Feng Ye, Erxi Feng, Ni Ni, and Huibo Cao. "Crystal and magnetic structures of magnetic topological insulators MnBi 2 Te 4 and MnBi 4 Te 7". In: *Physical Review B* 101.2 (2020), 020412 (cit. on p. 104).

[207] F Cugini, S Chicco, F Orlandi, G Allodi, P Bonfá, V Vezzoni, ON Miroshkina, ME Gruner, L Righi, S Fabbrici, et al. "Effective decoupling of ferromagnetic sublattices by frustration in Heusler alloys". In: *Physical Review B* 105.17 (2022), 174434 (cit. on p. 106).

[208] F Damay, J Sottmann, F Lainé, L Chaix, M Poienar, P Beran, E Elkaim, F Fauth, L Nataf, A Guesdon, et al. "Magnetic phase diagram for Fe 3- x Mn x BO 5". In: *Physical Review B* 101.9 (2020), 094418 (cit. on p. 106).

[209] V Ovidiu Garlea, Liurukara D Sanjeewa, Michael A McGuire, Cristian D Batista, Anjana M Samarakoon, David Graf, Barry Winn, Feng Ye, Christina Hoffmann, and Joseph W Kolis. "Exotic magnetic field-induced spin-superstructures in a mixed honeycomb-triangular lattice system". In: *Physical Review X* 9.1 (2019), 011038 (cit. on p. 106).

[210] Hans-Benjamin Braun, Jiri Kulda, Bertrand Roessli, Dirk Visser, Karl W Krämer, Hans-Ulrich Güdel, and Peter Böni. "Emergence of soliton chirality in a quantum antiferromagnet". In: *Nature Physics* 1.3 (2005), 159–163 (cit. on p. 107).

[211] Jun-ichiro Kishine and AS Ovchinnikov. "Theory of monoaxial chiral helimagnet". In: *Solid State Physics* 66 (2015), 1–130 (cit. on p. 107).

[212] Y Togawa, T Koyama, K Takayanagi, S Mori, Y Kousaka, J Akimitsu, S Nishihara, K Inoue, AS Ovchinnikov, and J-i Kishine. "Chiral magnetic soliton lattice on a chiral helimagnet". In: *Physical review letters* 108.10 (2012), 107202 (cit. on pp. 107–110, 112, 114).

[213] Y Kousaka, Y Nakao, J Kishine, M Akita, K Inoue, J Akimitsu, et al. "Chiral helimagnetism in T {sub 1/3} NbS {sub 2}(T= Cr and Mn)". In: *Nuclear Instruments and Methods in Physics Research. Section A, Accelerators, Spectrometers, Detectors and Associated Equipment* 600 (2009) (cit. on pp. 107, 113, 126).

[214] AE Hall, JC Loudon, PA Midgley, AC Twitchett-Harrison, SJR Holt, DA Mayoh, JP Tidey, Y Han, Martin R Lees, and Geetha Balakrishnan. "Comparative study of the structural and magnetic properties of Mn 1/3 NbS 2 and Cr 1/3 NbS 2". In: *Physical Review Materials* 6.2 (2022), 024407 (cit. on pp. 107–109, 111–115, 125, 126).

[215] Kannan Lu, Deepak Sapkota, Lisa DeBeer-Schmitt, Yan Wu, HB Cao, Norman Mannella, David Mandrus, Adam A Aczel, and Gregory J MacDougall. "Canted antiferromagnetic order in the monoaxial chiral magnets V 1/3 TaS 2 and V 1/3 NbS 2". In: *Physical Review Materials* 4.5 (2020), 054416 (cit. on pp. 107–109).

[216] AE Hall, DD Khalyavin, P Manuel, DA Mayoh, F Orlandi, OA Petrenko, Martin R Lees, and Geetha Balakrishnan. "Magnetic structure investigation of the intercalated transition metal dichalcogenide V 1/3 NbS 2". In: *Physical Review B* 103.17 (2021), 174431 (cit. on pp. 107, 112, 113).

[217] LM Volkova and DV Marinin. "Role of structural factors in formation of chiral magnetic soliton lattice in Cr1/3NbS2". In: *Journal of Applied Physics* 116.13 (2014) (cit. on pp. 107, 108).

[218] Y Cao, Z Huang, Y Yin, H Xie, B Liu, W Wang, C Zhu, D Mandrus, L Wang, and W Huang. "Overview and advances in a layered chiral helimagnet Cr1/3NbS2". In: *Materials Today Advances* 7 (2020), 100080 (cit. on pp. 108–110).

[219] Daichi Yoshizawa, Yuya Sawada, Yusuke Kousaka, Jun-ichiro Kishine, Yoshihiko Togawa, Masaki Mito, Katsuya Inoue, Jun Akimitsu, Takehito Nakano, Yasuo Nozue, et al. "Anomalous spiked structures in ESR signals from the chiral helimagnet CrNb 3 S 6". In: *Physical review B* 100.10 (2019), 104413 (cit. on p. 108).

[220] Benjamin J Chapman, Alexander C Bornstein, Nirmal J Ghimire, David Mandrus, and Minhyea Lee. "Spin structure of the anisotropic helimagnet Cr1/3NbS2 in a magnetic field". In: *Applied Physics Letters* 105.7 (2014) (cit. on p. 108).

[221] Misako Shinozaki, Shintaro Hoshino, Yusuke Masaki, Jun-ichiro Kishine, and Yusuke Kato. "Finite-temperature properties of three-dimensional chiral helimagnets". In: *journal of the physical society of japan* 85.7 (2016), 074710 (cit. on p. 109).

[222] V Dyadkin, F Mushenok, A Bosak, D Menzel, S Grigoriev, P Pattison, and D Chernyshov. "Structural disorder versus chiral magnetism in Cr 1/3 NbS 2". In: *Physical Review B* 91.18 (2015), 184205 (cit. on pp. 111, 114).

[223] Alexey Anatol'evich Bykov, NM Chubova, EV Altinbaev, Yu Kousaka, AS Ovchinnikov, J Kishine, and SV Grigoriev. "Magnetic phase diagram of Cr1/3NbS2: SANS study". In: *Journal of Solid State Chemistry* 322 (2023), 123951 (cit. on pp. 112, 113).

[224] Ryuya Aoki, Yusuke Kousaka, and Yoshihiko Togawa. "Anomalous nonreciprocal electrical transport on chiral magnetic order". In: *Physical Review Letters* 122.5 (2019), 057206 (cit. on pp. 112, 113).

[225] Jun-ichiro Yonemura, Yusuke Shimamoto, Takanori Kida, Daichi Yoshizawa, Yusuke Kousaka, Sadafumi Nishihara, Francisco Jose Trindade Goncalves, Jun Akimitsu, Katsuya Inoue, Masayuki Hagiwara, et al. "Magnetic solitons and magnetic phase diagram of the hexagonal chiral crystal CrNb 3 S 6 in oblique magnetic fields". In: *Physical Review B* 96.18 (2017), 184423 (cit. on p. 112).

[226] K Tsuruta, M Mito, H Deguchi, J-i Kishine, Y Kousaka, J Akimitsu, and K Inoue. "Phase diagram of the chiral magnet Cr 1/3 NbS 2 in a magnetic field". In: *Physical Review B* 93.10 (2016), 104402 (cit. on p. 112).

[227] Hui Han, Lei Zhang, Deepak Sapkota, Ningning Hao, Langsheng Ling, Haifeng Du, Li Pi, Changjin Zhang, David G Mandrus, and Yuheng Zhang. "Tricritical point and phase diagram based on critical scaling in the monoaxial chiral helimagnet Cr 1/3 NbS 2". In: *Physical Review B* 96.9 (2017), 094439 (cit. on p. 112).

[228] Sunil K Karna, Madalynn Marshall, Weiwei Xie, Lisa DeBeer-Schmitt, David P Young, Ilya Vekhter, William A Shelton, Andras Kovács, Michalis Charilaou, and John F DiTusa. "Annihilation and control of chiral domain walls with magnetic fields". In: *Nano letters* 21.3 (2021), 1205–1212 (cit. on p. 113).

[229] Sunil K Karna, FN Womack, R Chapai, DP Young, M Marshall, Weiwei Xie, D Graf, Yan Wu, Huibo Cao, L DeBeer-Schmitt, et al. "Consequences of magnetic ordering in chiral M n 1/3 Nb S 2". In: *Physical Review B* 100.18 (2019), 184413 (cit. on pp. 113, 114).

[230] Yuhui Dai, Wei Liu, Yamei Wang, Jiyu Fan, Li Pi, Lei Zhang, and Yuheng Zhang. "Critical phenomenon and phase diagram of Mn-intercalated layered MnNb3S6". In: *Journal of Physics: Condensed Matter* 31.19 (2019), 195803 (cit. on p. 113).

[231] D Braam, C Gomez, S Tezok, EVL de Mello, L Li, D Mandrus, Hae-Young Kee, and JE Sonier. "Magnetic properties of the helimagnet Cr 1/3 NbS 2 observed by μ SR". In: *Physical Review B* 91.14 (2015), 144407 (cit. on p. 114).

[232] VV Ogloblichev, Yu V Piskunov, and FB Mushenok. "Magnetic order in the structurally disordered helicoidal magnet Cr 1/3 NbS 2: NMR at 53 Cr nuclei". In: *Journal of Experimental and Theoretical Physics* 125 (2017), 317–322 (cit. on pp. 115, 125).

[233] VV Ogloblichev, Yu V Piskunov, I Yu Arapova, and FB Mushenok. "The Valence State of Manganese in the Mn 1/3 NbS 2 Magnet According to 55 Mn-NMR Data". In: *Physics of Metals and Metallography* 119 (2018), 1056–1061 (cit. on pp. 115, 125).

[234] W. Ertmer, U. Johann, and R Mosmann. "Measurement of the Nuclear Quadrupole Moment of S3Cr by Laser-Rf Double Resonance". In: *Z. Phys. A - Atoms and Nuclei* 309 (1982) (cit. on p. 115).

[235] D. Stephenson and N. Singh. "53Cr, 17O and 14N nuclear quadrupole resonance in ammonium dichromate". In: *Hyperfine Interact.* 237, 118 (2016) (). DOI: https://doi.org/10.1007/s10751-016-1332-3 (cit. on p. 115).

[236] Jun-Ichiro Kishine and A.S. Ovchinnicov. "Theory of monoaxial chiral helimagnet". In: *Solid State Physics* 66 (2015), 1–130 (cit. on pp. 117, 124).

[237] Azizur Rahman, Majeed Ur Rehman, Muhammad Yousaf, Maryam Kiani, Hongze Zhao, Jianlin Wang, Yalin Lu, Keqing Ruan, Rucheng Dai, Zhongping Wang, et al. "RKKY-type in-plane ferromagnetism in layered Mn 1/4 NbS 2 single crystals". In: *Physical Review B* 105.21 (2022), 214410 (cit. on p. 122).

[238] H.-A. Krug von Nidda, N. Büttgen, and A. Loidl. "Magnetic resonance in quantum spin chains". In: *The European Physical Journal Special Topics* 180 (2010), 161–189. DOI: 0.1140/epjst/e2010-01217-0. URL: https://doi.org/10.1140/epjst/e2010-01217-0 (cit. on p. 123).

[239] VV Ogloblichev, NV Baranov, PA Agzamova, A Yu Germov, NM Nosova, Yu V Piskunov, EM Sherokalova, NV Selezneva, AF Sadykov, and AG Smolnikov. "Electronic states in ferromagnetic Cr x Nb Se 2 (x= 0.33, 0.5) studied by Cr 53 and Nb 93 NMR spectroscopy". In: *Physical Review B* 104.24 (2021), 245115 (cit. on p. 125).

[240] Victor Laliena, Javier Campo, and Yusuke Kousaka. "Understanding the $H-T$ phase diagram of the monoaxial helimagnet". In: *Phys. Rev. B* 94 (9 2016), 094439. DOI: 10.1103/PhysRevB.94.094439. URL: https://link.aps.org/doi/10.1103/PhysRevB.94.094439 (cit. on p. 126).

[241] Eleanor M Clements, Raja Das, Ling Li, Paula J Lampen-Kelley, Manh-Huong Phan, Veerle Keppens, David Mandrus, and Hariharan Srikanth. "Critical behavior and macroscopic phase diagram of the monoaxial chiral helimagnet Cr1/3NbS2". In: *Scientific reports* 7.1 (2017), 6545 (cit. on p. 126).